Textural Evolution of the Hellyer Massive Sulphide Deposit

Gary J. McArthur B.Sc. (U.N.S.W.)

Volume I - Text

A thesis submitted as fulfilment of the requirements for the degree of Doctor of Philosophy

Geology Department
University of Tasmania
August, 1996

Frontispiece

The magnificent textural variety of the Hellyer massive sulphide (60% actual size). This polished slab, collected from early 400 level development exposure, was originally prepared as part of a plaque to commemorate the official opening of the Hellyer Concentrator in April 1989.

The dust of antique time would lie unswept
And mountainous error be too highly heap'd
For truth to o'erpeer.

Shakespeare (Coriolanus)

Authority of Access

This thesis may be made available for loan and limited copying in accordance with the *Copyright Act 1968*.

_____

Signed: G.J.McArthur

2nd April 1997.

ABSTRACT

The Hellyer zinc-lead-silver deposit of western Tasmania is a well preserved example of a volcanic-hosted massive sulphide. The deposit is hosted by intermediate-basic lavas and volcaniclastics of the Que-Hellyer Volcanics, the uppermost volcanic unit of the Cambrian Mt.Read Volcanics. The complete deposit, including the footwall alteration stringer zone, is preserved. The current complex morphology of the massive sulphide is due to the combination of primary depositional irregularities, ductile Devonian folding and brittle Mesozoic faulting.

Statistical analysis of available mine sample assays and subsequent geostatistical 3D grade modelling has revealed a classic metal zonation pattern. Whilst Cu and Fe are enriched towards the footwall, proximal to the central feeder zone recognised by Gemmell and Large (1992); Zn, Pb, Ag, Au, As and Ba are gradually enriched towards the distal hangingwall. The current observed metal distribution is interpreted to be substantially the same as the Cambrian distribution; Devonian deformation resulted in only very local remobilisation.

Spatial analysis of macroscopic textures has shown a clear zonation, similar to the geometry of the metal distribution. Massive sulphide proximal to the central feeder zone is strongly recrystallised, but grades upwards and outwards to a featureless, massive texture and finally to strongly banded ores at the hangingwall contact.

A very detailed microtextural study of 174 polished thin sections was completed from samples selected on a 3D grid through the central part of the deposit. Two hundred and twenty-two different microscopic textures have been recognised, with their spatial occurrence and features documented in a comprehensive atlas. These textures have been placed into paragenetic groups ranging through early primitive deposition, in situ recrystallisation, intra-mound veining, upwards redeposition, thermal retraction, Devonian and Mesozoic deformation-related, and finally, surface weathering. These paragenetic groups are zoned, similar to the metal zoning and macroscopic textures, around the central feeder in the footwall. Various depositional and recrystallisation processes are postulated in an overall model for textural evolution.

Microprobe analyses of the major minerals from numerous samples have shown variation according to texture and position within the overall orebody zonation. Significantly, pyrite

shows considerable reduction in trace element content as crystallinity increases towards the proximal base of the sulphide mound. Early sphalerite has a higher Fe content than the late varieties, early tetrahedrite has a higher Ag content than later generations and carbonates show increasing CaO content and decreasing FeO content passing from early to late textural types. Other minerals show more complex compositional variability.

The classic metal and texture zonation patterns, together with evidence from detailed microprobe analysis lend support to a mound refining genetic model, similar to that proposed by Eldridge et al. (1983) for the Kuroko volcanic-hosted massive sulphide deposits. The Hellyer genetic model postulates that a hydrothermal system was focussed at the intersection of a normal graben fault with a transfer fault on the Cambrian seafloor. These faults tapped a deep heat source and as temperature increased, rising hot solutions saturated with base and precious metals and reduced sulphur, began to vent into the cold, oxygenated seawater. Initially, barite/anhydrite and cherty crusts were deposited on the seafloor overlying the core of the footwall alteration zone. These crusts, by partly capping the system, allowed higher temperature deposition of primitive melnikovite pyrite and sphalerite/wurtzite, by replacement of pre-existing sulphates, and within voids, just below the mound surface. As the mound grew, these depositional processes moved upwards and outwards, away from the central feeder. Much higher temperatures in the lower part of the mound, gradually recrystallised and refined the primitive pyrite, expelling contaminant trace elements to be redeposited in higher, cooler parts of the mound. The growing mound became unstable, depositing clastic massive sulphide in adjacent basins that were eventually enveloped by the expanding higher temperature hydrothermal system, recrystallising and partially destroying the original fragmental framework. When the mound reached its ultimate extent, rotation of the stress regime closed off access to the heat and fluid sources and temperatures in the system decreased. As volcaniclastic mass flows and pillow lavas buried and preserved the deposit, the waning phase led to further deposition of lower temperature mineralisation, increasingly deeper within the mound in available voids. Devonian deformation annealed and extended the ductile sphalerite-galena rich distal hangingwall zones and introduced tensile pull-apart fractures in the more proximal pyritic zones. All minerals, except pyrite, were locally remobilised into newly created voids. Mesozoic brittle wrench faulting brecciated pyritic areas causing minor remobilisation of minerals into late narrow cracks that cut across all earlier textural features.

ACKNOWLEDGMENTS

Firstly, I would like to offer my sincere thanks to my present employer, Aberfoyle Resources Limited, for the generous financial support given to my research. This has been in the form of the costs involved in section preparation, assaying, photography, digital scanning and thesis production, notwithstanding the occasional extended periods of normal worktime spent on this research. I thank my boss, Adrian Molinia in Melbourne head office, who somehow managed to divert or postpone my work commitments during final thesis preparation. I also thank all the geologists I have worked with, who provided virtually daily encouragement and valuable probing discussion: Tim Akerman, Ben Coutts, Chris Davies, Richard Downs, Ed Dronseika, Chris Drown, Mark Fleming, Tony Hespe, Rohan Hine, Graham Howard, Doug Jack, Henry Kurth, Rob Lewis, Alistair Miller, Andrew McNeill, Steve Richardson, Robina Sharpe, Hugh Skey, Dave Wallace and Chris Young. My good friend and first-class programmer Alan Kuipers provided FORTRAN programming support from start to finish and "Wallaby Wal" Wilson assisted with the core sampling and slab polishing. Special thanks to Bob Colson who first introduced me to Paradox database software in 1991 and to Rob Lewis who got me started on the data conversion to Microsoft Access. Rob often helped out with the many frustrating computing problems. Robina Sharpe kindly devoted some of her own scarce time to provide desperately needed help with calculation of probe detection limits. Dale Wagner provided timely help with the Access database listings, while Greg Cayzer provided valuable phone assistance in my battles with CAD drafting. Sharee Taylor is thanked for her helped with the probe photomicrographs appendix. Finally, it was Richard de Bomford, Aberfoyle's Burnie legend, who kept me sane when the going got tough towards the end.

I should also thank Aberfoyle (Hugh Skey) for initially inviting me to become involved with the Hellyer deposit, shortly after its discovery in 1983. My association with this outstanding deposit over almost 13 years has indeed been an honour professionally, and a personal pleasure. I can only marvel at the variety of geological wonder and curiosity that the Hellyer deposit has provided, and will continue to provide for generations of geologists to come.

Dr Bruce Gemmell and Prof. Ross Large from the CODES Key Centre at the University of Tasmania are thanked for their constant support, supervision, encouragement and criticism, over the rather lengthy punctuated course of my study. Dr Wiszlecw Jablonski of the Central Science Laboratory provided friendly assistance for the numerous lengthy sessions on the microprobe.

I thank my ex-wife Jo who provided support during the difficult times of the family tragedy that overwhelmed us both in the earlier part of my research.

Lastly, but certainly not least, I thank my new family; especially Susan, for her unwavering love, her constant encouragement and practical help with thesis collation which enabled me to finally complete this work.

TABLE OF CONTENTS

Page

VOLUME I

LIST OF FIGURES

[page number]

LIST OF PLATES

LIST OF TABLES

1. INTRODUCTION

1.1 Location

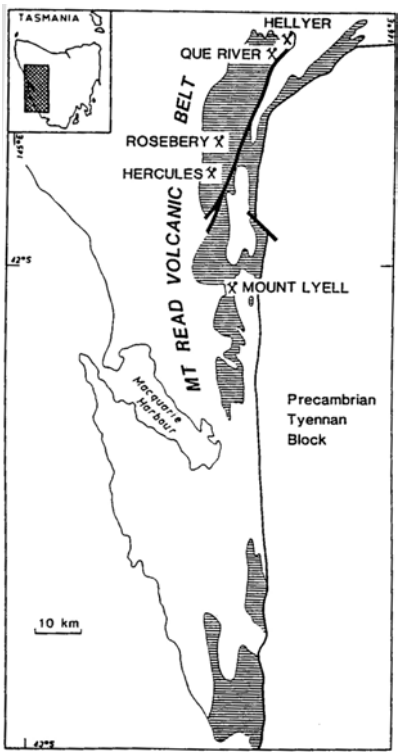

Figure 1 - Location of the Hellyer deposit (after Gemmell and Large, 1992)

The Hellyer volcanic-hosted massive sulphide (VHMS) deposit is located in Western Tasmania (Fig. 1) at 41° 34' 34" S, 145° 43' 15" E (5396500mN, 393400mE AMG).

The local topography consists of a rolling plateau 650-700m above sea level with local deep dissection by rivers draining south and west. The climate is typical of Western Tasmania, cool and wet. Average rainfall is 1980mm on 260 days/year and temperature varies between 2°C - 7°C in July and 8°C - 18°C in February. Snowfalls are common.

1.2 Author's involvement

The author has been involved with the Hellyer deposit through full-time employment with the mine operator, Aberfoyle Resources Limited. From 1983 to 1993 the author was the senior geologist based on site.

1.3 Previous studies of the Hellyer deposit

The Hellyer volcanic-hosted massive sulphide (VHMS) deposit has been the subject of many research studies and associated publications since its discovery in 1983.

Early papers aptly concentrate on the role electromagnetic geophysics played in the discovery. Sise and Jack (1984), Skey (1984), Eadie et al. (1985) and Silic et al. (1985) all cover this topic as brief abstracts authored by geoscientists involved in the actual discovery.

The first publication of any geological detail (McArthur, 1986) gives an account of the geological understanding as interpreted from early diamond drilling. Variation in macroscopic and microscopic texture is described, as well as the observed stratigraphic metal zonation pattern. The author suggests that the spatial arrangement of sulphide texture and metal about the interpreted footwall feeder system is very similar to that described by Eldridge at al. (1983) for the Kuroko VHMS deposits. McArthur's 1986 attempt to reconstruct the seafloor topography at the time of sulphide deposition ignored Devonian deformational effects.

Further papers on exploration geophysics cover aspects of the deposit's discovery regarding electromagnetic response (Eadie(1987,1988), Silic and Eadie (1989), Staff of Aberfoyle Resources (1989)); gravity response (Hudspeth (1986)) and reflection seismic response (Read, 1989).

Specific studies on more geological aspects of the Hellyer deposit include Warren (1989) which describes sulphide mineralisation within the hangingwall basalts; a general summary of Que River and Hellyer geology by Staff of Aberfoyle Resources (1990); an explanation of deformational variation around the Hellyer deposit based on the concept of strain partitioning by Drown and Downs (1990) and further general geological updates by Drown and Richardson (1990) and McArthur and Dronseika (1990). The latter paper illustrates average stratigraphic metal zonation trends and an example of grade variation around the interpreted footwall feeder zone in one cross-section reconstructed to a pre-faulting configuration. McArthur and Dronseika (1990)

envisage a mound refining genesis for Hellyer similar to that put forward by Eldridge et al. (1983) for the Japanese Kuroko massive sulphide deposits.

Ramsden et al. (1990) conducted quite a detailed electron microprobe study of core samples from three holes evenly spaced along the deposit. Whilst their study well documents the stratigraphic zonation in these holes, it ignores the three-dimensional aspect of zonation around the footwall alteration pipe. Some of their probe results are compared to results from this study under section 6.4.

Sharpe (1991) studied spatial relationships and textural features of the Hellyer siliceous and baritic caps and Downs (1993) reconstructed the seafloor topography at the time of Hellyer mineralisation by unfolding the Devonian deformation. Both these theses are discussed in relation to this study in later sections.

Volcanology of the Que River and Hellyer host rocks has been studied briefly by Scott (1988) and more extensively covered by Waters (1990, 1995), McPhie and Allen (1992) and Waters and Wallace (1992). This study could never hope to expand on the excellent description and interpretation of the volcanic rocks provided by these workers.

Strontium isotope studies have been undertaken by Whitford and Craven (1986) on host rocks and barite mineralisation at Que River and Hellyer whilst Gemmell et al. (1990) studied sulphur and lead isotopes from the Hellyer stringer zone. Jack (1989) in his thesis on the hangingwall alteration covers sulphur isotopes from the hangingwall and the massive sulphide itself.

Specific studies on the footwall alteration zone have been documented in a comprehensive way by Gemmell (1988, 1989, 1990b, 1991), Gemmell et al (1990), Gemmell & Large (1990a,b, 1992), and Khin Zaw and Gemmell (1996). Gemmell's elucidation of the core of the footwall alteration provides a direct connection with the metal and textural zonation found in this study (see section 4.4).

In a recent publication, Khin Zaw et al (1996) conducted a study of primary fluid inclusions in quartz and sphalerites from veins in the footwall alteration zone.

Perkins et al. (1992) provides dating estimates for the Hellyer host rocks and the

mineralisation by the $^{40}Ar/^{39}Ar$ method.

Aspects of Hellyer applied geology are covered by McArthur (1988), Downs (1990) and McArthur and Kuipers (1990).

1.4 This study

1.4.1 Research aims

The main aim of this research was to investigate the style and 3-dimensional geometry of metal concentration, mineralogy and microtextural distribution (i.e. the zonation) within the massive sulphide of the Hellyer deposit. A further aim was to formulate the evolution process for the massive sulphide purely by analysis and interpretation of the textural observations made.

1.4.2 Philosophy

The author has deliberately undertaken to adhere to a strict disciplined regime in order to maximise the unbiased representivity of samples, maximise objectivity of the microscopic observations and finally, maximise the use of latest technology pictorial representation to communicate the observations made.

An important part of this philosophy was to make an honest attempt to strongly resist the temptation of "collecting facts to fit the theory". In this regard the author has stuck rigidly to objectively collecting all the available textural observations *prior* to undertaking analysis and interpretation. As a consequence, some data collected proved in the end to be of no relevance to the final outcome. So be it.

In addition, the author, whilst making full acknowledgment of data gathered by other workers covering other branches of geological science, has come to the conclusions documented in this thesis, only from the restricted dataset of the author's own observations. The author feels that detailed conventional textural analysis is all too often underplayed. Traditional observational skills should be respected in providing data equally as valuable as that emanating from the more favoured modern technological analytical methods.

1.4.3 Methods

The methods employed to achieve the stated aims are:

- analysis of a 3-dimensional block grade model constructed by industry-accepted geostatistical interpolation to understand geometry of the metal zonation
- sampling of the massive sulphide on an arbitrary 3-dimensional grid from available drillcore to prepare polished thin sections
- point counting of minerals and mineral textures on these polished sections
- detailed microscopic observations of textures on the polished sections stored in a computer database
- colour slide photomicrography
- microprobe analyses of all minerals in selected samples
- analysis of the 3-dimensional spatial relationships of the microscopic features
- paragenetic interpretation from textural observations and microprobe analyses.

All of the methods used are described in detail in later sections.

1.5 Exploration History

1.5.1 Pre-1970 Early Exploration

In November 1828, early surveyor-explorer Henry Hellyer, in search of grazing land for the van Diemen's Land Company, records in his journal (Binks, 1980) how he traversed around Mt.Cripps and crossed the Southwell River to follow high ground SSW to Mt.Block (Fig.2).

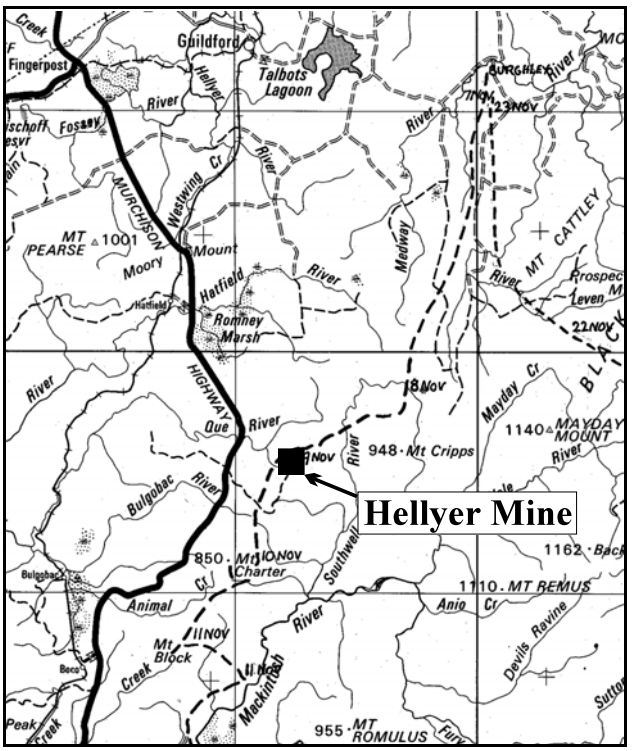

Figure 2 - Henry Hellyer's 1828 footsteps over the deposit (modified after Binks, 1980, p92.)

By his description of the landform we can confidently say Hellyer was the first European to walk across what was to become the Hellyer mining lease some 158 years later. Hence the Hellyer deposit was so named.

The first documented mining exploration of the Hellyer area is shown in early government records as having taken place in 1922 when Tom McDonald (discoverer of the Rosebery deposit) sank a 6m. shaft at Gold Hill just north of Que River (McArthur and Dronseika, 1990). Small amounts of gold associated with decomposed sulphide rock were found, but he did not locate the main Que River massive sulphide lenses. The area lay almost untouched until the 1960's when several companies realised the volcanics in the Que River/Hellyer area had similarities to the Mt.Lyell and Rosebery host rocks and undertook initial exploration, without any success.

1.5.2 1970-1982 Aberfoyle Exploration

Modern exploration really began in the Hellyer area in 1970 when Aberfoyle Resources Limited (ARL) in association with Cominco Limited of Canada began exploration on the Mackintosh Exploration Licence. Initial stream bed mapping and stream sediment sampling highlighted a complex volcanic succession with areas of anomalous Pb geochemistry (Webster and Skey, 1979). A 1972 helicopter-borne electromagnetic survey over 400 km^2 of exposed volcanics resulted in only a few good discrete anomalies, one of which coincided with an area of anomalous stream sediment geochemistry at Que River (Staff of Aberfoyle Resources, 1989). In 1973, actual sub-cropping massive sulphide of the Cu-rich S Lens was discovered during ground follow-up. The first drill hole in 1974 intersected significant Cu-rich and Zn/Pb/Ag-rich massive sulphide lenses thereby marking the discovery of the Que River deposit, some 3 km distant from what was to become Hellyer. The ensuing 6 years concentrated on drilling out and developing the Que River Mine prior to production commencing in 1980. This period of detailed data gathering provided local geologists with a valuable understanding of the mineralisation and alteration style in this local terrain that contributed significantly to Hellyer's discovery a few years later.

Shortly after Que River production commenced, renewed exploration activity included induced polarisation (IP) surveys over exposed volcanics in the Mackintosh area. A northerly-plunging IP anomaly 3km north of Que River coincident with spotty Pb geochemistry was considered worthy of follow-up. Drill hole MG1 (now renamed HL001) was drilled in 1982 on line 10200N[1], very close to the southern end of the now known Hellyer massive sulphide, only to find weak pyritic mineralisation in basalts.

1.5.3 1983-1985 Hellyer discovery and feasibility

Cominco of Canada introduced the University of Toronto Electromagnetic method (UTEM) of large loop time domain surveys to Aberfoyle in 1982 (Staff of Aberfoyle

[1] Throughout this thesis, reference is made to 3D location using Aberfoyle's Que River/Hellyer mine grid which has its origin at 5388687mN, 383973mE AMG. Australian Height Datum (AHD) is taken as 0 RL. Grid north is aligned at 022° 07' 20" AMG, approximately 009° magnetic. Note that all directional references also use this mine grid: e.g. grid north-south strike is equivalent to AMG NNE-SSW . The Hellyer deposit is located between 10200-11100N, 5600-6000E, 150-650RL.

Resources, 1989). This new method was tested at Que River and was found to detect the sphalerite-rich PQ lens missed by earlier EM methods. In anticipation that any other target orebody would be of similar conductivity to Que River, UTEM was applied over the northern two-thirds of outcropping volcanics during 1982/83.

At the extreme northern end of the UTEM grid on line 10300N, a moderate response was detected close to the previously drilled IP anomaly. Meanwhile, geological mapping of new exposures created by the construction of a HEC transmission line had revealed veins of barite and intense 'fuchsite'-carbonate alteration in basalt. This alteration was concentrated in the nose of a northerly plunging anticline some 300m north of the UTEM anomaly. The grid was therefore extended 400m to the volcanic/shale contact on line 10700N and subsequent detailed UTEM defined a deep, moderately conductive body, part of which lay directly beneath the most intense alteration. An attractive drill target supported by geological, geophysical and geochemical ingredients had been outlined.

The initial 3-hole diamond drill programme commenced in July 1983. The first hole was aimed at the strongest interpreted EM conductor on line 10400N. Drill hole MG3

Plate 1 - Cairn erected at the MG3 drillsite , admired by (from left) Exploration Manager Hugh Skey, Senior Geophysicist Tom Eadie, Senior Geological Technician Errol Smith, Chief Mine Geologist Gary McArthur, Senior Geologist Doug Jack

(now renamed HL003) intersected massive sulphides on 2nd August 1983 at 200m downhole depth, 100m below the surface (now historically marked by a cairn and plaque at the drillhole collar, Plates 1,2). The total discovery intersection was **23.1m** grading **0.25%Cu, 4.5%Pb, 13.0%Zn, 162 g/t Ag and 1.9 g/t Au.**

Follow-up drilling to the north during 1983 provided 5 additional massive sulphide intersections with underlying stringer vein mineralisation over a 500m strike length, thus confirming the discovery of a major deposit. The initial preference for a Que River-like vertically oriented body (as interpreted from the UTEM response) was eventually discarded as correlation of volcanic units progressed with the drilling. By the end of 1983 there was general acceptance for a sub-horizontal stratigraphy with only gentle folding in a northerly-plunging anticline, cut transgressively by a well developed footwall alteration zone beneath the massive sulphides. The author became involved with the Hellyer deposit in December 1983 during the drilling of HL016.

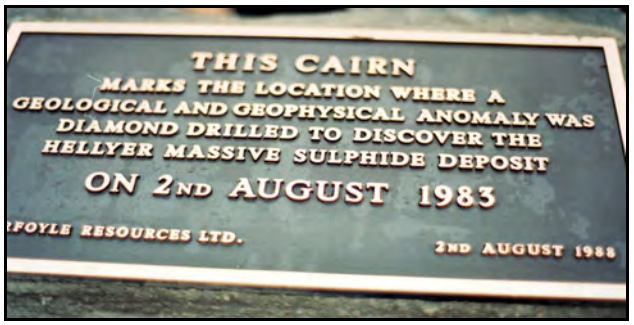

Plate 2 - Plaque commemorating Hellyer's discovery at the MG3 drillsite

Plate 3 - Diamond drilling during 1984, on sections 10850N, 10900N and 10950N

During 1984 an intensive exploration programme was mounted to drill out Hellyer on a nominal 50m X 50m pattern (Plate 3). This featured the

serendipitous discovery of the eastern half of the deposit (east of the Jack Fault) in drillhole HL037. By year end, a 15 Mt deposit had been outlined from the 28,171m drilled with 50 intersections over a 750m strike length (from 10300N to 11050N).

1985 saw preliminary mining and metallurgy feasibility studies undertaken while access to a proposed portal site in the adjacent Southwell River gorge was in progress. Actual tunnelling of a 1.3km horizontal adit through the hangingwall sequences to access the orebody commenced in May 1985 (Weston et al., 1988).

1.5.4 1986-1989 Hellyer Mine development

In June 1986 (Plate 4), the massive sulphide was first exposed in underground development on the 400 level (280m below the surface).

Plate 4 - The first ore shipment from Hellyer in 1986, amazingly anointed by a serendipitous rainbow

The next 12 months saw extensive development driving and crosscutting on the 400 level to provide a representative metallurgical bulk sample over a wide area of the deposit (10630-11030N) and to provide underground diamond drill sites. High quality 1:100 geological mapping of all exposed vertical faces was undertaken to further the understanding of all the deposit's characteristics as applicable to mining. Detailed wall chip sampling augmented the orebody grade database. Later development on the 360 and 440 levels provided further vertical confirmation of the zonation found on the 400 level.

Whilst the bulk sample for metallurgical testing was being mined, attempts were made to sort the ore into separate stockpiles according to macroscopic ore texture (Richmond and Lai, 1988). Even at this early stage, a good workable understanding of textural zonation was evident. In September 1986, 20m-spaced diamond drilling commenced from sites on the 400 level to delineate areas for initial stope exploitation.

This detailed drilling was to continue uninterrupted until August 1992 when the total deposit had been covered (Fig.3). Mostly these drillholes provided the samples for this study.

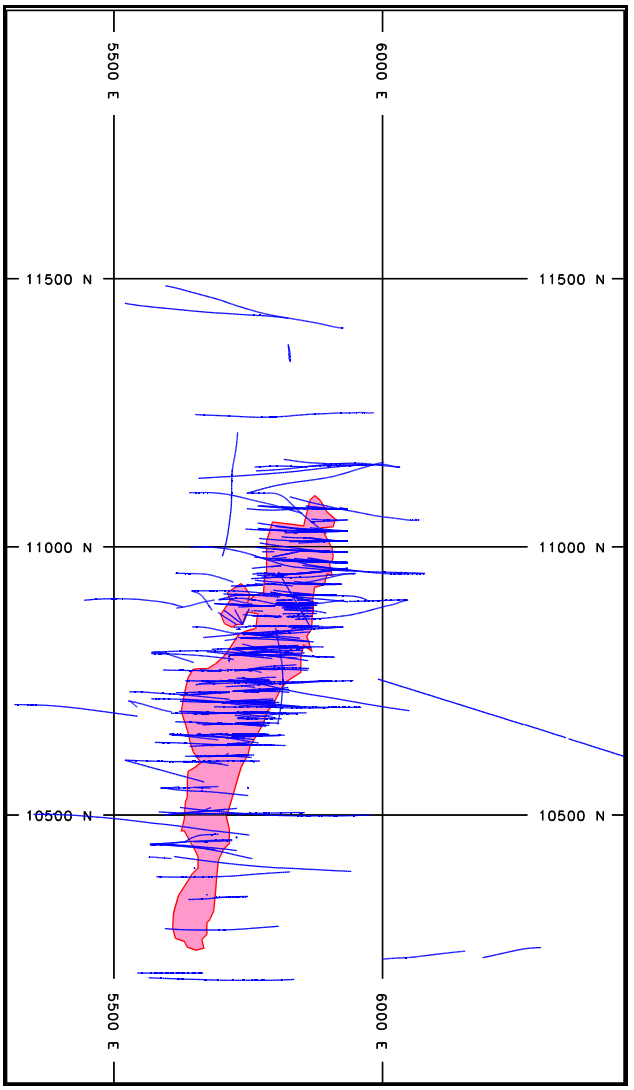

Figure 3 - Diamond drilling coverage by end-1989 when samples for this study were selected

While mine development and underground drilling was in progress, exploration drilling continued from the surface particularly at the northern end of the deposit. No additional economic mineralisation was found.

In 1988, a single drillhole (HL306) was collared on 400 level to drill as far as possible into the footwall stringer zone. This hole provided valuable sample material to initiate a Hellyer Stringer Zone post-doctoral research project (Gemmell, 1988,1989,1990).

1.5.5 1990-present Hellyer Mine production

Since the mine increased its output to full production (1 million tonnes/year) in 1989, geological understanding has evolved in concert with the increasing drill density (Fig. 4) and the rapidly expanding development exposure on all levels of the mine. Although the overall interpretation of the deposit and its host rocks has changed little over the years, some crucial milestones on the road to complete understanding stand

out, and deserve mention. These are discussed in more detail under later sections.

- recognition that much of the pyrite/(sphalerite-galena) layering is symmetric crustiform infill of complex multi-generation cracks that sometimes represent upward continuation of stringer veins
- recognition that some of the barite intersections are in fact late cross-cutting veins
- recognition that major footwall stringer veins occupy significant fracture systems that influenced seafloor topography and subsequent massive sulphide morphology (Downs, 1993)
- recognition of important late east-west structures (missed in surface drilling) that often displace ore contacts significantly
- recognition that strain partitioning during the Devonian had very important influences on the current massive sulphide morphology (Drown and Downs, 1990)
- recognition of a large WNW-ESE trending structure at the southern end of the deposit that coincides with a major regional gravity/magnetic lineament

The author has learnt much over the years due to his involvement with routine mill product microscopy . The discipline of detailed microscopic examination of fortnightly samples has not only improved his overall microscopy skills but more importantly demonstrated that the mineral associations and textures seen (in both whole rock sections and mill product grain mounts) play an extremely significant role in the ore's treatability and overall economic viability. The author has therefore personally experienced how basic scientific research can often lead to important economic applications.

Diamond drilling has continued up to the time of writing, testing for northern extensions and lower horizons deep in the footwall. To date none of this exploration has been successful. Drilling south of 10200N on the opposite side of the major WNW-ESE structure has intersected large thicknesses of barite but very little base

metal sulphide.

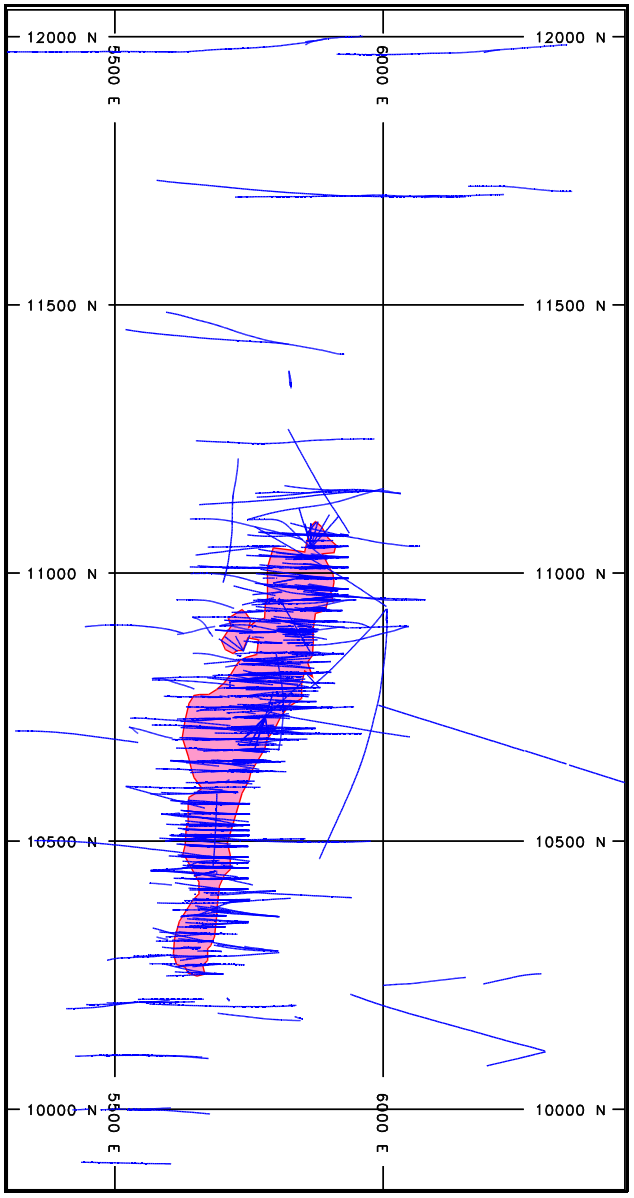

Figure 4 - Diamond drilling coverage mid-1996

2. STRATIGRAPHIC AND STRUCTURAL SETTING

2.1 Regional Geologic Setting

2.1.1 Volcanostratigraphy

The Hellyer massive sulphide deposit is located within the Mount Read Volcanics (MRV) belt of western Tasmania (Fig. 5). This 200- by 20-km belt of highly mineralised rocks strikes north from Elliott Bay on the south-west coast, through Queenstown and Rosebery and thence arcing north-east through Que River and Hellyer before passing beneath younger cover to strike east-west in the Sheffield region. The MRV lie at the eastern margin of the Dundas Trough between the Tyennan Precambrian block of central Tasmania and the Rocky Cape Precambrian block to the north-west.

Corbett (1992) has recognised seven lithological associations (Fig. 6) within the well known central part of the MRV. These can be summarised briefly as below (oldest to youngest):

Sticht Range Beds - up to several hundred metres of basal siliciclastic conglomerates and sandstone dipping west and lying unconformably on the Tyennan Precambrian rocks

Murchison Volcanics - a complex sequence of steeply west-dipping rhyolites, dacites, minor andesites and their volcaniclastic equivalents with porphyry intrusions and related granitoids in the Lake Dora to Mt. Farrell region

Central Volcanic Complex (CVC) - a sequence of dominantly feldspar-phyric lava-rich volcanics including abundant rhyolitic-dacitic lavas, pumiceous volcaniclastics and massive lava domes. These rocks ooccur in one belt east of the Henty Fault from Mt.Darwin to the Henty River and an

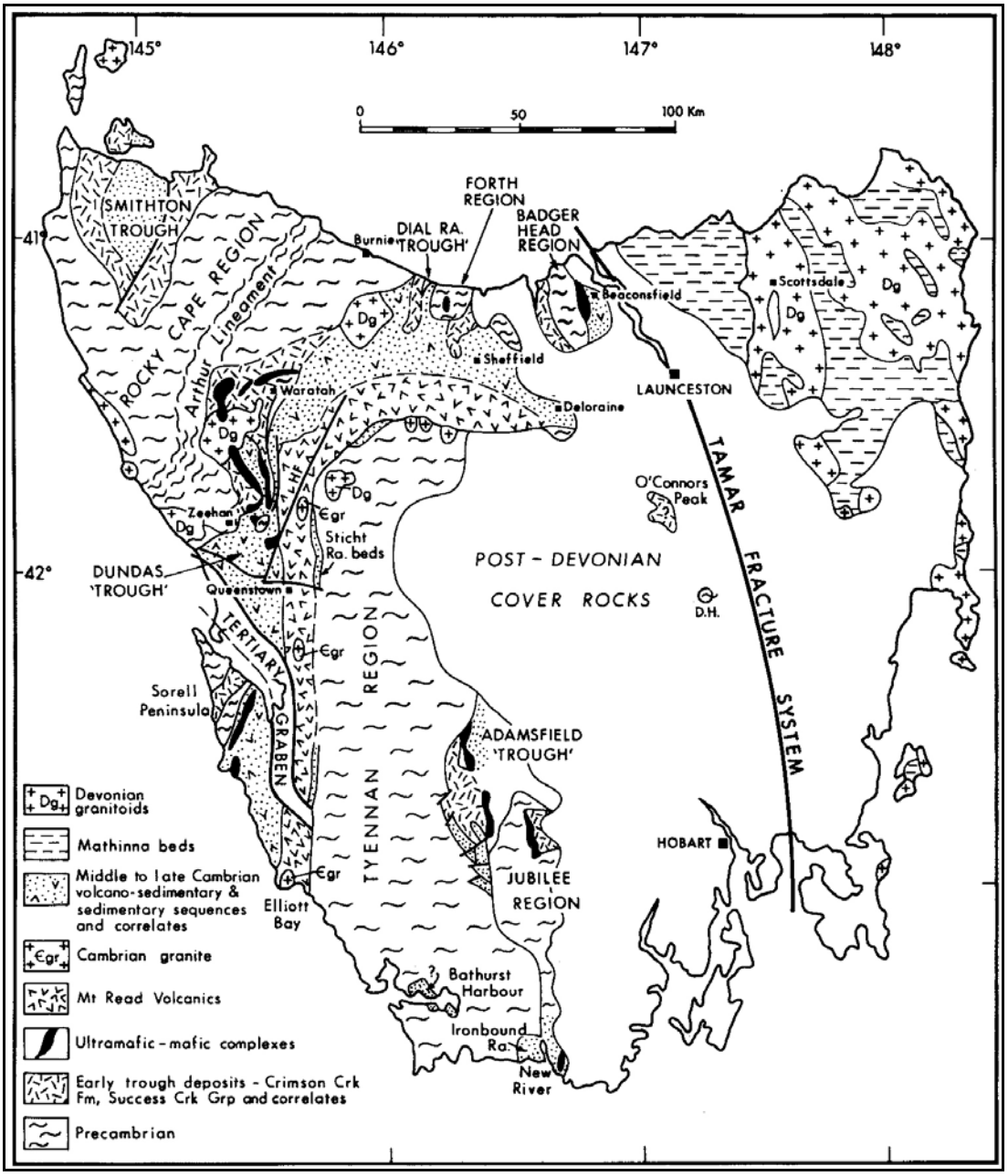

Figure 5 - Simplified map of early Palaeozoic geologic elements of Tasmania (after Corbett, 1992)

extensive area west of the Henty Fault from Mt.Read to Mt.Block. Interfingering relationships of the contained units have made strict stratigraphic definition of this sequence impossible.

Tyndall Group - a sequence of characteristic mass-flow breccias and sandstones and volcanolithic conglomerates occurring in a belt from

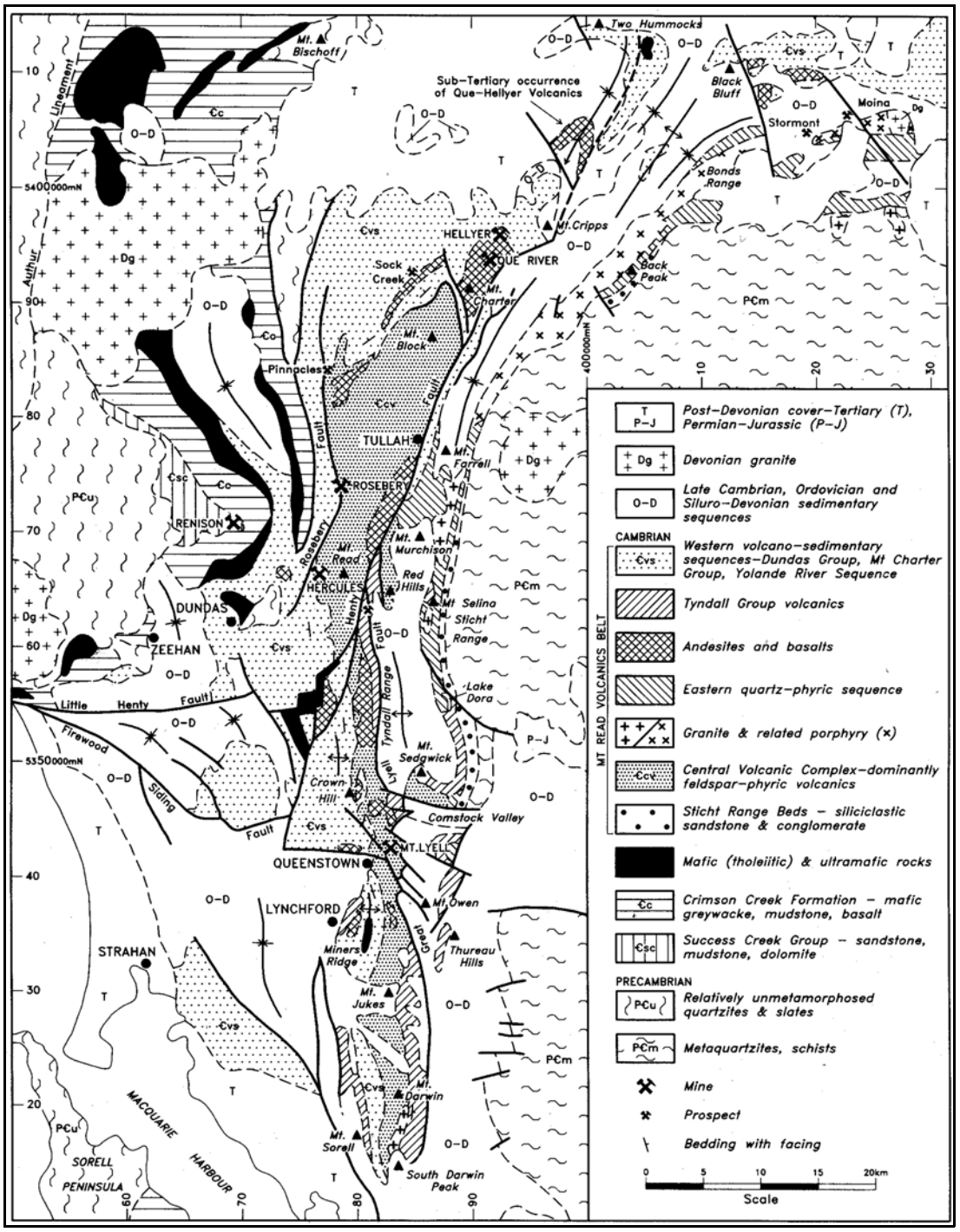

Figure 6 - Geology of the Queenstown-Hellyer region (after Corbett, 1992)

Queenstown to Red Hills. Abundant clasts of welded tuff in mass-flows in the lower units suggest a shallow-marine environment on the flanks of a partly subaerial volcanic chain.

Western volcano-sedimentary sequences - a broad classification of mixed rocks occurring on the western flanks over the entire length of the central MRV that includes:

(i) the **Yolande River sequence** in the Queenstown area, consisting of a basal tholeiitic basalt with overlying siliciclastic sandstone and andesitic/basaltic lavas and volcaniclastics. This sequence is intruded by sill-like bodies of quartz-feldspar porphyry.

(ii) the **Dundas Group** of volcanic debris sediments (mass-flows, conglomerates, greywackes, siltstones and shales) extending from Mt.Dundas to the Rosebery-Pinnacles area.

(iii) the **Mt.Charter Group** in the Mt.Charter to Hellyer region with basal mudstones and greywacke overlain by andesite-basalt lavas and volcaniclastics with dacite intrusives (Que-Hellyer Volcanics, QHV). The upper sequences contain the Que River black shale and felsic pumiceous volcaniclastics of the Southwell Subgroup.

(iv) the **Henty fault wedge sequence** in the Henty gorge region containing highly disrupted rocks having distinct similarities to the Mt.Charter Group.

Andesitic-basaltic volcanics - a loosely constructed grouping of scattered volcanics and associated intrusions occurring within or between the other lithostratigraphic associations of the MRV. The occurrence of quench-fragmented lavas and breccias strongly suggest submarine extrusion (Waters and Wallace, 1992).

Tholeiitic rocks - a group of tholeiitic basalts and andesites occurring in three main areas:

(i) strongly deformed ophitic basalts at **Miners Ridge** east of Lynchford that may be part of an upthrust basement tholeiite

(ii) porphyritic gabbros, basalts and andesites in the western part of the **Henty fault wedge** interfingering with calc-alkaline andesitic volcaniclastics

(iii) numerous basaltic, doleritic and gabbroic **dikes** occurring within the Central Volcanic Complex adjacent to the **Henty Fault**

The Mt.Lyell, Rosebery and Hercules deposits are hosted by the Central Volcanic Complex while the Que River and Hellyer deposits lie within the Que-Hellyer Volcanics of the Mt.Charter Group.

2.1.2 Lithogeochemistry

Crawford et al. (1992) have geochemically classified the MRV lithotypes into three calc-alkaline suites and two tholeiitic suites as briefly summarised in Table 1. These are also shown diagrammatically in section in Fig.7.

Table 1. Summary of MRV lithogeochemical affinities (modified from Crawford et al., 1992). CVC=Central Volcanic Complex, QHV=Que-Hellyer Volcanics, REE=rare earth elements.

Characteristic	Suite I	Suite II	Suite III	Suite IV	Suite V
Stratigraphic occurrence	Volumetrically abundant. CVC QHV footwall Henty Flt wedge Tyndall Group Murch. granitoid	Only south-east of Henty Fault. CVC top Yolande River Sequence	Yolande River Sequence QHV hanging wall basalt	Henty Flt wedge Henty dike swarm	Miners Ridge basalt
Petrology	augite-plag phyric andesites, plag phyric dacites, qtz+plag phyric rhyolites	hornblende phyric andesites/dacites, aug+plag phyric andesites with partly resorbed qtz phenocrysts	primitive xstal-rich oliv+chromite+cpx phyric basalts, more evolved cpx+plag phyric basalts/andesites	augite+plag phyric basalts, aphyric-ophitic basalts	aphyric-ophitic basalts with rare altered olivine phenocrysts
%SiO_2 range	58-78	58-68	48-57	50-54	48-52
P_2O_5/TiO_2 range	<0.4	0.3-0.7	0.2-1.2	<0.2	<0.2
FeO trend with differentiation	steady decrease	steady decrease	decrease	increase	increase
TiO_2 trend with differentiation	steady decrease	flat decrease	flat	increase	variable
Ti/Zr range	5-40	15-20	20-40	70-110	90-160
REE enrichment	moderate light REE enrichment	strong light REE enrichment	variable	weak light REE enrichment	weak light REE depletion
AFFINITY	medium-high K calc-alkaline	high K calc-alkaline	transitional medium-high K calc-alkaline, P-rich REE-rich shoshonites	tholeiitic	strongly magnesian tholeiitic

Crawford et al. (1992) also provide a summary of alternative tectonic models for the MRV. These are briefly summarised below (as per Downs, 1993):

(i) an intracontinental rift adjacent to an extensional plate boundary

(ii) an Andean-type arc over an east-dipping subduction zone, erupted on to the Precambrian Tyennan basement

(iii) a convergent plate boundary over a west-dipping subduction zone

(iv) an extensional setting within an active continental margin with associated strike-slip faulting

(v) localised in grabens along the eastern side of the Dundas Trough following an arc-continent collision in east-directed subduction. Fore-arc crust was thrust over the passive margin leading edge and extension related to relaxation rifting of the thickened crust exhumed the thinned Precambrian as the Tyennan region.

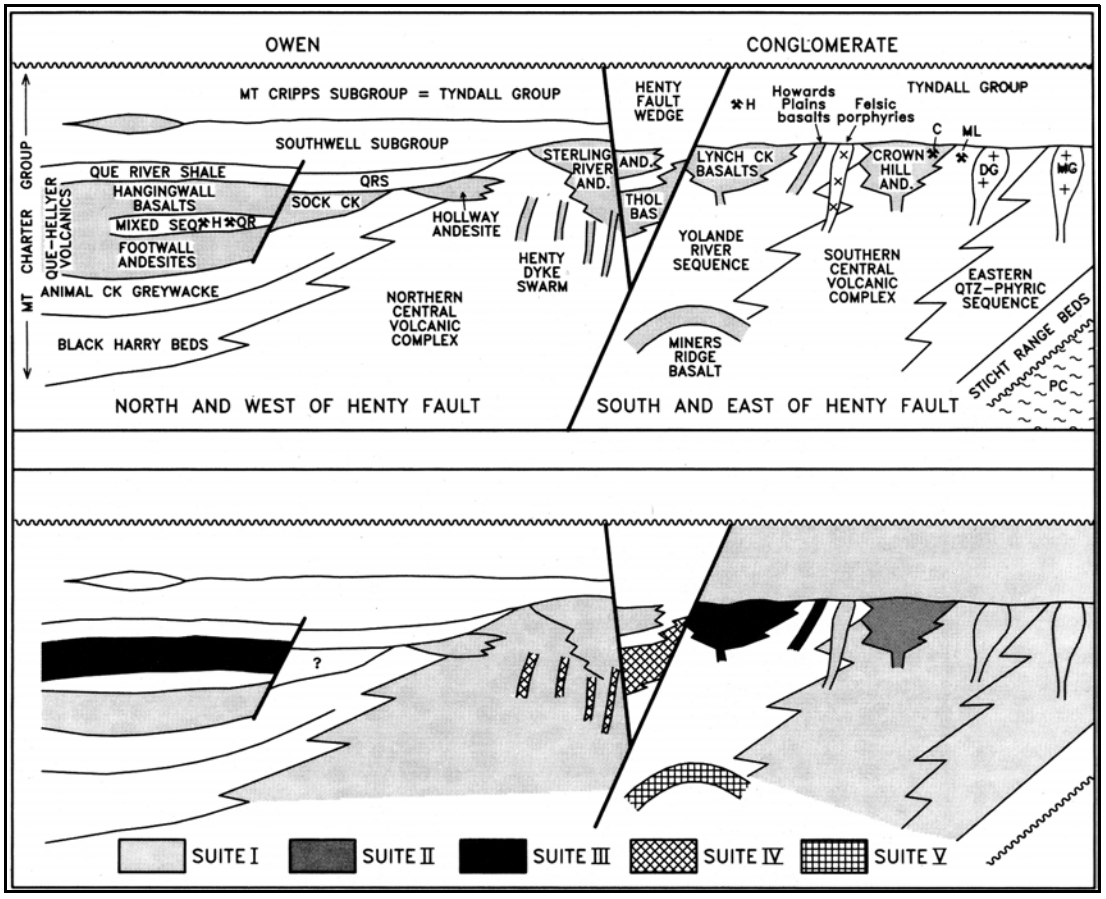

Figure 7 - Diagrammatic section showing major stratigraphic units and distribution of geochemical suites (after Corbett, 1992 and Crawford et al., 1992)

2.1.3 Major structural elements

The MRV volcanic sequences are disrupted by a number of major faults.

The Henty fault is the most prominent, running SSW-NNE (true) for 45 km from Mt.Read to Que River (Fig. 6). This west-dipping fault has a complex movement history (Berry, 1989), but simplistically represents a Cambrian fault reactivated during the Devonian Tabberabberan deformation. Two arcuate splay faults at the southern end enclose the Henty fault wedge which contains a unique combination of lithotypes, whilst at the northern end the Mt.Charter splay defines the northernmost outcrop of CVC.

The north-south trending Great Lyell fault intersects the Henty fault at Red Hills and is also a major Cambrian fault reactivated in the Devonian.

The relatively shallow east-dipping Rosebery fault (Devonian) forms the western limit of the main MRV in the Rosebery-Pinnacles area.

A cluster of WNW-ESE trending Devonian faults cuts through the Mt.Lyell region, converging towards the west coast.

2.1.4 Metamorphism

Regional metamorphism varies between prehnite-pumpellyite facies to the north and lower greenschist facies to the south (Offler and Whitford, 1992). In the Rosebery mine, metasomatic replacement assemblages (magnetite-biotite, pyrrhotite-pyrite and tourmaline-quartz) indicate a post-tectonic Devonian hydrothermal overprint emanating from granitoid plutons below (Lees et al., 1990).

2.2 Local Geologic Setting

The following description is summarised from McArthur and Dronseika (1990) and Corbett (1992) and refers only to that area covered by Aberfoyle's Mackintosh Exploration Licence surrounding the Que River and Hellyer deposits (Fig. 8).

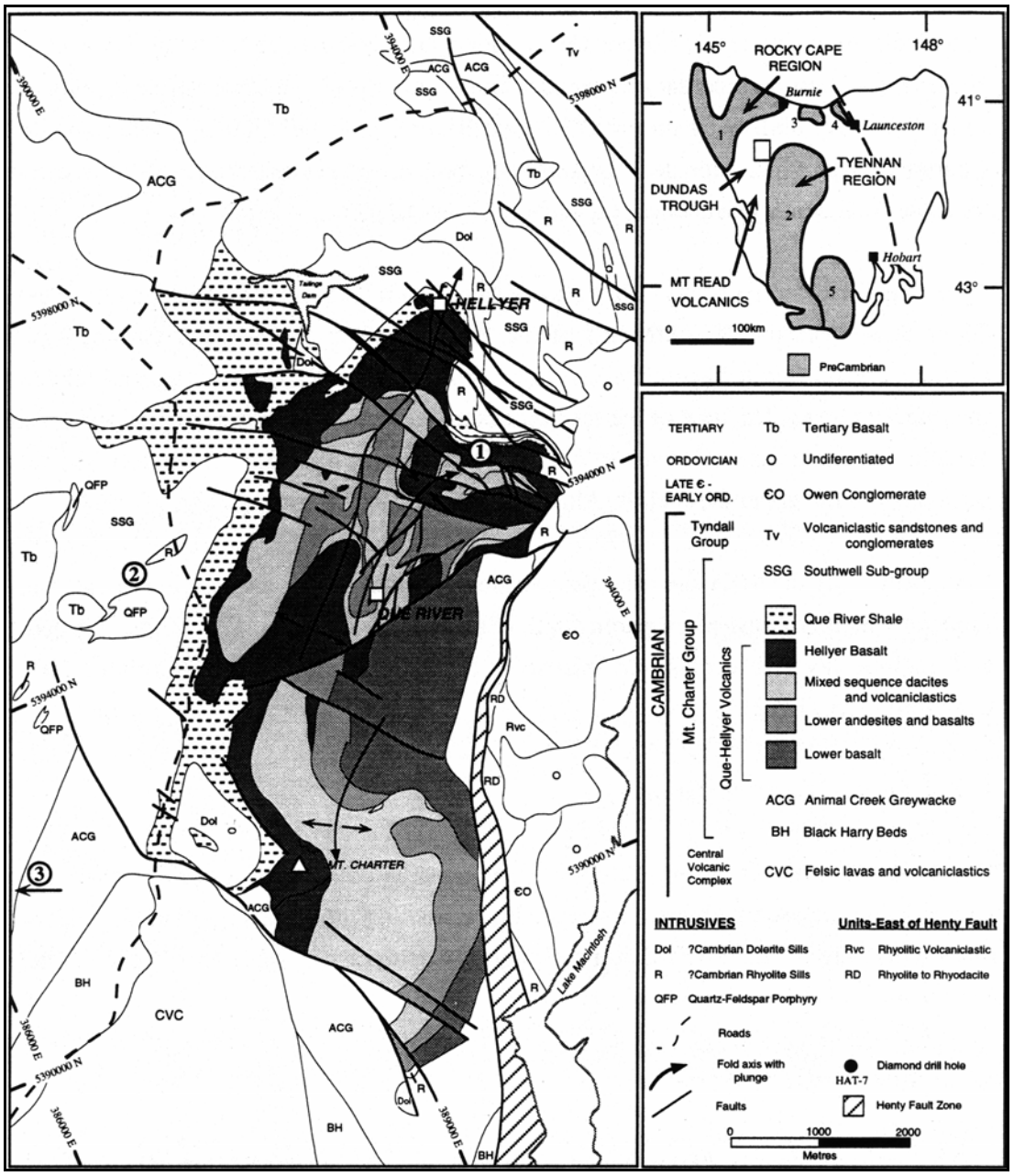

Figure 8 - Local geological map of the Que-Hellyer Volcanics (after Waters, 1995)

The QHV are exposed over a 9 km by 4km elliptical area with the long axis aligned NNE-SSW (mine grid). Maximum thickness is about 1 km at Que River but all units thin dramatically to the north-west.

2.2.1 Local stratigraphic succession

Central Volcanic Complex - massive felsic volcanics (suite I) restricted to the area south of the Mt.Charter fault. Several thin discontinuous dikes of basalt (Henty dike swarm) intrude the CVC adjacent to the Henty fault.

Mt.Charter Group

Black Harry Beds - at least 300m thickness of interbedded marine volcanic mudstones, tuffaceous sandstones, mass-flows and shales conformably overlying or faulted against the CVC. The upper contact is gradational. Restricted to the area south of the Mt.Charter fault on the Murchison Highway and to a small outlier 4 km WNW of Hellyer at Black Harry Road. This unit is not represented in Aberfoyle exploration drilling.

Animal Creek Greywacke - approximately 300m thickness of well-bedded (often beautifully cross-bedded) grey micaceous sandstones interbedded with dark grey siltstones and shales. Sandstone provenance appears to be the Precambrian with some chromite grains possibly sourced from ultramafics. Interbedded with the basalts above.

Que-Hellyer Volcanics (Fig.9)

"Lower basalt" - variable thickness of calc-alkaline (suite III?) dark grey-green basalts and volcaniclastics mainly known south of the Que Fault from poor surface exposure and several exploration drillholes. Occurrence and thickness appear to be

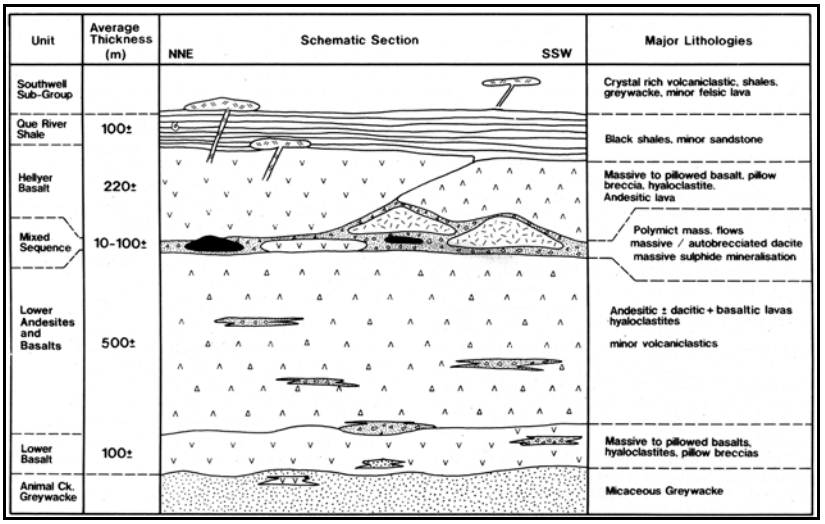

Figure 9 - Schematic stratigraphic section through the QHV (after Waters and Wallace, 1992)

rigidly controlled by subordinate basement faults. Gradational with andesites above but contact is sometimes marked by discontinuous polymictic mass-flow breccias.

"Feldspar-phyric sequence" (FPS) - highly variable thickness of calc-alkaline (suite I) grey andesite (minor basalt) lavas, autobreccias and volcaniclastics, occasionally vesicular. Very thick at Que River but thinning to only a few metres at the QHV western margin. Partially or completely absent where large dacite domes occur, e.g. Mt.Charter. Frequently cut transgressively by mineralised hydrothermal alteration zones (especially Que River and Hellyer). Generally has a sharp contact with the volcaniclastic unit above.

"Mixed sequence" or **"hangingwall volcaniclastic sequence" (HVS)** - up to 250m thickness of polymictic mass-flow breccias, ash volcaniclastics and minor shale with flows and dome-like bodies of feldspar phyric dacite. Hosts the Que River massive sulphide lenses and lies semi-conformably on the hangingwall of the Hellyer massive sulphide. Contains massive sulphide boulders, especially in the "switchback" area

south-east of Hellyer. There is a general trend for this unit to thin to the west but locally thickness is strongly controlled by seafloor topography. The upper contact with the basalts is very sharp and conformable.

"Upper basalt" or **"pillow lava sequence" (PLS)** - up to 400m of basalt and andesite (suite III) as sheet lavas, pillow lavas and hyaloclastite breccias (Waters, 1995) with minor shale. North and west of Hellyer this unit thins dramatically and interdigitates with Que River Shale. Hydrothermally altered above the Hellyer massive sulphide. This unit has a sharp semi-conformable contact with the overlying shales.

Que River Shale (QRS) - usual 100m thickness of well bedded black carbonaceous shale and siltstone that can be much thicker to the north of Hellyer where PLS is all but absent. Pyritic, especially in the lower parts near the basalt. Agnostid trilobite fossils indicate a Middle Cambrian age (Jago, 1979). Sinclair (1994) concludes from the presence of complete trilobites, carbonaceous pyritic content and degree of pyritisation (DOP) measurements that the QRS was deposited in quiet reducing conditions from an andesitic/basaltic loacl provenance. This unit marks a distinct hiatus between the basaltic/andesitic proximal volcanism below and the more distal felsic volcaniclastics above. The upper contact with the Southwell Subgroup is sharp and conformable.

Southwell Subgroup or **"upper rhyolitic sequence" (URS)** - about 1 km thickness of interbedded quartz-feldspar phyric pumiceous mass-flow breccia, sandstone, greywacke turbidite and massive shale with sill-like bodies of rhyolite lava (Scott, 1988 and Corbett and Komyshan, 1989).

Tertiary basalt - vesicular tholeiitic basalt lava unconformably overlying the QRS and URS north of Hellyer increasing in thickness further north. Basal gravels and wood debris are common in paleochannels (S.M.Richardson, pers.comm.).

2.2.2 Local structural elements

The south-eastern margin of the QHV block is controlled by the steep west-dipping Henty fault which appears offset by the Mt.Cripps/Que Fault north of Que River. The Mt.Charter fault in the south-west marks a distinct break, with clear thickness variations of equivalent units either side. Within the QHV basin, numerous Cambrian faults are interpreted to strongly control occurrence and thickness of the volcanic units (S.M.Richardson, pers.comm.). The QHV are thickest at Que River (approx. 1 km) but thin dramatically over several km to the north-west. Some of this thickening is due to Middle Devonian deformation. The significant fold axes are aligned NNE-SSW with a shallow NNE plunge common. An earlier open WNW-ESE crossfold has led to local plunge reversals, particularly west and north-west of Que River (Fig.8). Fold style varies from tight, often asymmetric forms in the east to open and symmetric in the west (partly due to strain partitioning in altered rocks).

A later, brittle deformation event in the Mesozoic (Berry, 1989) formed wrench faults in association with sinistral movement along the Henty fault.

All units of the QHV (apart from the strongly conductive massive sulphide bodies and mineralised footwall alteration zones) are geophysically non-responsive. The carbonaceous and pyritic QRS is moderately conductive as are the water-laden gravels basal to and interbedded with the Tertiary basalt, making deeper geophysical exploration difficult.

2.2.3 Metamorphism

Local metamorphic grade has been determined by Offler and Whitford (1992) to be prehnite-pumpellyite facies.

2.3 Hellyer Mine scale geologic setting

2.3.1 Mine stratigraphic succession

At Hellyer (Figure 10), the mine scale (1000m by 500m) volcanostratigraphic succession is (oldest to youngest):

"Feldspar phyric sequence" (FPS) - at least 400m of grey feldspar-porphyritic andesite lavas, autobreccias and volcaniclastics with vesicular basaltic units at the north end of the mine. Altered by the footwall alteration zone directly beneath the massive sulphide to various quartz-sericite-chlorite-pyrite assemblages (see section 3.7).

"Hangingwall volcaniclastic sequence" (HVS) - up to 30m of altered polymictic mass-flow breccias, basaltic lapilli and ash volcaniclastics and minor shale (Waters, 1990) directly overlying FPS, altered FPS or massive sulphide. Individual interbedded mass-flow/ash units can be correlated between drillholes over a reasonable distance, but overall there is considerable textural variety. From drillhole interpretation and actual exposure underground, the HVS is seen to onlap the massive sulphides/barite. In some areas over the thickest massive sulphide, the HVS is totally absent. McArthur (1986) demonstrates how HVS thickness varies systematically around the Hellyer sulphide mound.

"Pillow lava sequence" (PLS) - up to 300m of grey-green basalt showing great textural variety (Waters, 1994) with minor interflow and interpillow shale/siltstone. Vesicular pillowed lavas are dominant, with individual pillows

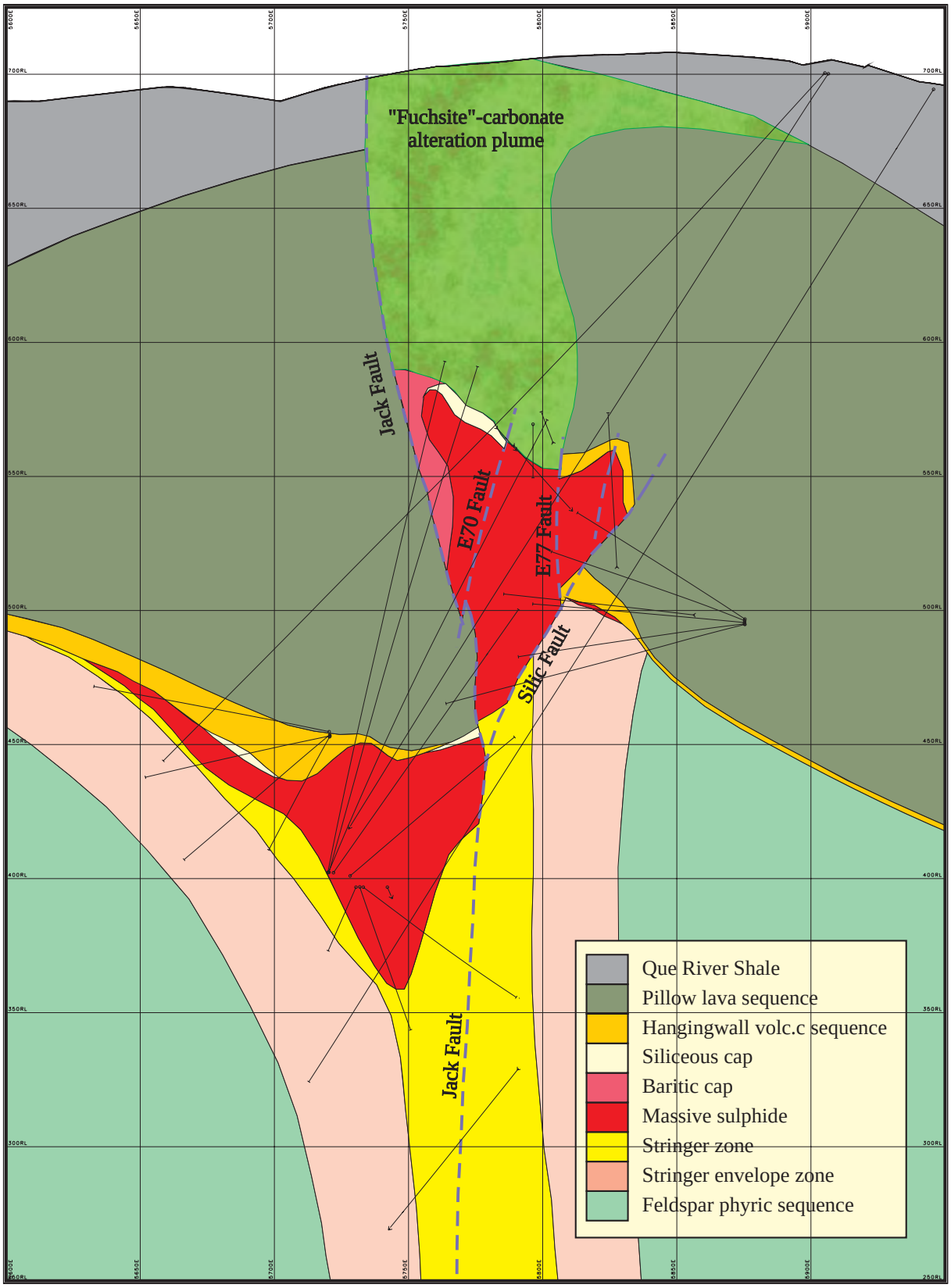

Fig. 10 - Cross-section 10750N, showing drill holes and stratigraphic/ structural interpretation (modified from company drawing)

up to 2m across showing increased vesicle concentration near the upper pillow margin. Interpillow regions contain shale, indurated shale or chert. Hyaloclastite breccias of infinite variety occur in irregular zones about the pillowed lavas. One characteristic correlatable pillow lava displays beautiful varioles (original glassy material) arranged symmetrically about the pillow margins. Non-vesiculated homogeneous sheet lavas are also common, often interbedded with pillowed forms. Within this unit, Jack (1989) has recognised a core basalt with distinctive geochemical composition. Downs (1993) demonstrates how PLS stratigraphy is configured proximally around a basalt dike in the footwall, strongly suggesting that a local vent was responsible for building the high-aspect volcanic edifice. The PLS is variably carbonate-"fuchsite"-pyrite altered (Warren, 1989 and Jack, 1990) above the thicker massive sulphide: pillowed forms are notably more susceptible to alteration due to increased permeability.

Que River Shale (QRS) - up to 100m thickness of black shale and lesser siltstone, only known from the mine in drillholes and the adit. The QRS is often pyritic, particularly in the basal 10m, where the frequency of narrow pyritic beds increases towards the basalt contact, possibly reflecting waning pulses of hydrothermal activity.

"Upper rhyolitic sequence (URS) - only known from drillholes and the mine adit where pumiceous felsic volcaniclastics, shales and greywacke turbidites predominate.

2.3.2 Structural components

Downs (1993) in his reconstruction of the Cambrian seafloor at the time of formation of the Hellyer massive sulphide concluded that east-west extension formed a north-south half graben with east-west striking transfer faults. Rotation of the extension direction to NW-SE then reactivated and dilated the transfer faults to allow hydrothermal flow (Fig.11) and later basalt eruption.

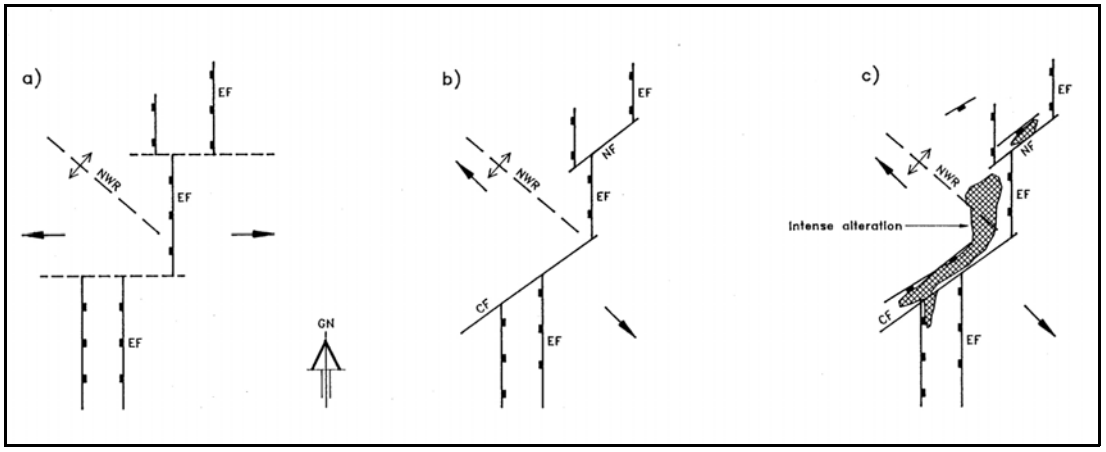

Figure 11 -Schematic plan view of Cambrian fault evolution (after Downs, 1993)

East-west compression associated with the Middle Devonian Tabberaberan Orogeny (Komyshan, 1986) produced open, upright folds at Hellyer plunging 20° NNE, with a steep east-dipping cleavage (S1). Intense strain was channeled to the ductile areas of the massive sulphide and underlying sericite/chlorite-rich portions of the footwall alteration system, whilst the pyrite-rich areas of the massive sulphide, the siliceous core of the footwall alteration zone and the unaltered host rocks display brittle structures (Drown and Downs, 1990 and Downs, 1993).

The sub-vertical **Jack Fault** strikes north-south, cutting acutely through the Hellyer massive sulphide and enclosing rocks with a measured sinistral displacement of 130m.(McArthur and Dronseika, 1990). It appears that the fault trace follows a pre-existing Cambrian NNE-SSW trending fault south of 10670N, but to the north strikes due north-south unrelated to any pre-existing Cambrian structure. Downs (1993) interprets the Jack Fault and its accompanying ESE-striking dextral faults were probably associated with the Mesozoic wrench movement on the Henty-Mt.Cripps Fault (Berry, 1989). The brittle cataclasite fault gouge indicates shallow depth of deformation.

3. THE HELLYER MASSIVE SULPHIDE

3.1 Size and shape

3.1.1 Morphology

The rather complex morphology seen in the Hellyer deposit[1] today has resulted from the superimposition of Cambrian depositional site irregularities, Devonian folding and Mesozoic faulting. The overall shape could be described as an irregular elongate lozenge plunging at 20° to the NNE, cut acutely into two equal sized halves with sinistral displacement by the north-south striking, sub-vertical Jack Fault. Two synclines with tightly folded footwall traces sit astride an open central anticline. Overall morphological variability is well shown in Fig.12. Local terminology has subdivided the deposit into 5 mining areas:

South End - south of 10600N, all west of the Jack Fault
Keel Zone - 10600-10850N, west of the Jack Fault
Poke's Reward - 10850-10930N, west of the Jack Fault
Cap Zone - 10680-10850N, east of the Jack Fault
North End - north of 10850N, east of the Jack Fault.

These geographic terms are used throughout the thesis.

3.1.2 Dimensions

The massive sulphide is totally preserved, the shallowest portion at the southern end being some 60m below the surface. The deepest parts of the northern end are at 500m depth. It has a known north-south extent of 830m (700m pre-Jack Fault), a maximum

[1] The term "deposit" used in this thesis refers to the combination at Hellyer of massive sulphide plus the baritic and siliceous caps. The stringer mineralisation beneath the Hellyer footwall will not be termed "massive sulphide".

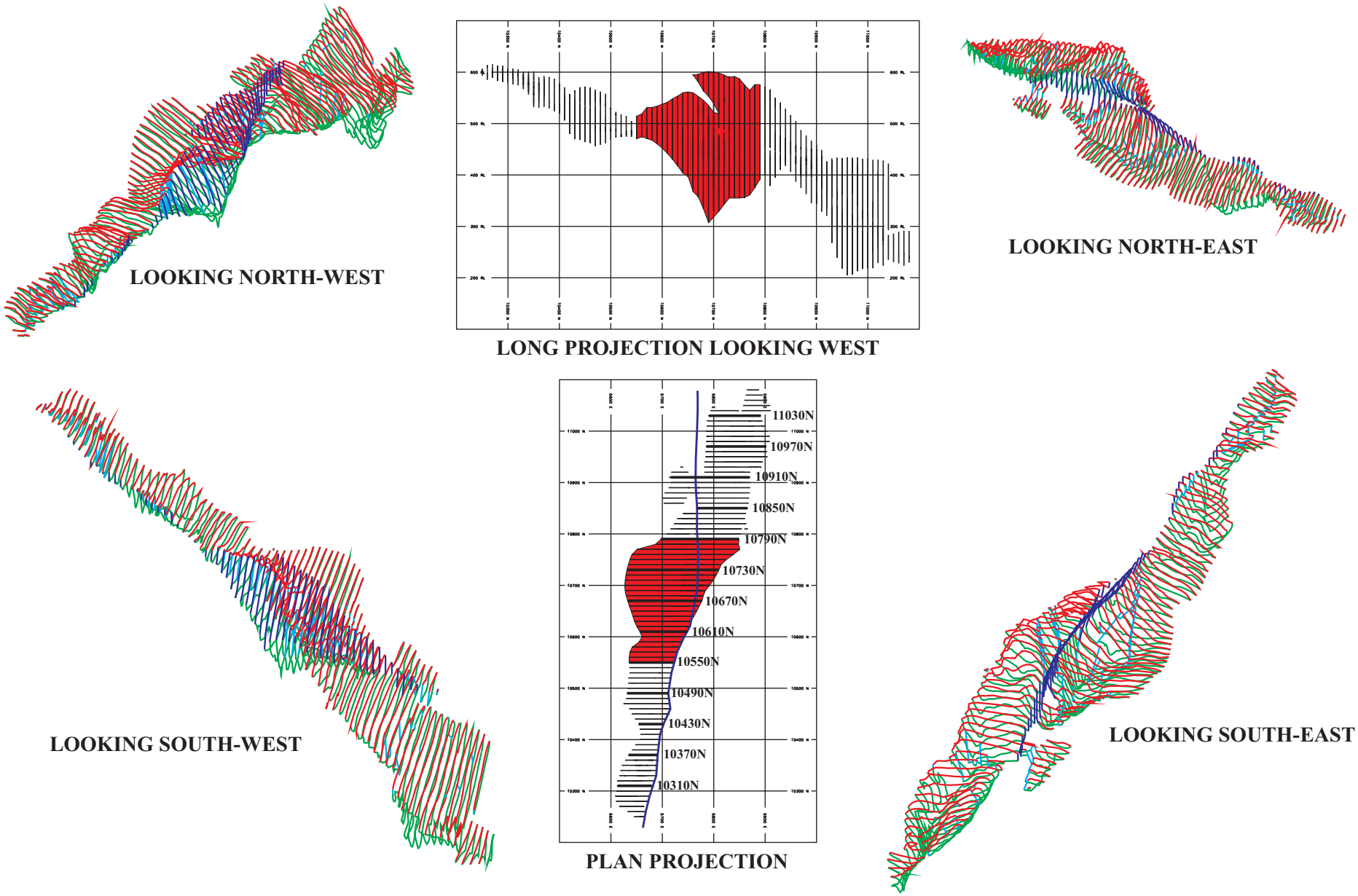

Figure 12 - Various views of the Hellyer deposit using 10m-spaced E-W profiles from the wireframe model.
(colours: red - hangingwall, green - footwall, dark blue - Jack Fault, light blue - other faults)
The shaded area on the projection views highlights the area covered by the microtextural study.
The bold annotated profiles on the plan projection refer to the sections selected for cross-section grade display.

east-west width of 200m and an average vertical thickness of 43m.

.

3.1.3 Resources

The Measured and Indicated Mineral Resources of the Hellyer deposit (excluding stringer mineralisation) as estimated by Aberfoyle Resources at a 5% (Pb+Zn) cutoff (Aberfoyle Resources, 1996) for the "virgin" deposit pre-mining are:

16.2 million tonnes at 0.38%Cu, 7.1%Pb, 13.9%Zn, 168 ppm Ag, 2.5 ppm Au, 2.2%Ba, 1.2%As, 24.8%Fe

This resource places Hellyer in the "world-class" category for Pb, Zn and Ag, according to the contained metal classification of Singer (1995). In terms of VHMS deposits worldwide, Hellyer can be ranked with Brunswick 12 and Rosebery in total contained metal.

3.2 Contact features

3.2.1 Footwall

The contact between massive sulphides and the altered andesitic footwall rocks is usually very sharp and non-lensy. Over the core of the alteration zone (Gemmell and Large, 1992) however, where the footwall is extremely pyritic and the overlying massive sulphide is strongly recrystallised, the contact can be gradational over a few metres. In these areas, the actual footwall can normally be accurately pinpointed by a subtle decrease in the background Ba assay (e.g. 0.15%Ba to 0.05%Ba) and a jump in rock density passing up into the massive sulphide (e.g. S.G. 4.0 to 4.5). Due to contrasting rock competency, the footwall contact is frequently sheared. Cross-cutting dextral faults show only minor displacements.

3.2.2 Hanging wall

The hanging wall contact of the deposit with the overlying HVS or PLS is also very sharp but can be highly irregular. Most often it is non-lensy apart from two areas where HVS bands are seen inside the massive sulphide (Keel Zone 10700-10740N and North End 10930-11070N). Cross-cutting dextral faults can have displacements up to 10m.

3.3 Gross mineralogy

Gross massive sulphide mineralogy (as identified in this research) has been quantitatively estimated by point counting (see below, section 5.3.2). This is summarised in Table 2.

Sulphides account for some 86% of the deposit, thus legitimising the term "massive sulphide". The high pyrite content contributes to the high average density of 4.56.

3.4 Recognised oretypes

Four major oretypes are recognised at Hellyer. Massive sulphide *senso stricto* is by far the most dominant and it has been conveniently subdivided (McArthur and Dronseika, 1990) according to marked Ag grade contrasts into:

(i) Footwall Depleted Zone (FWD), being that footwall portion with <100 ppm Ag
(ii) Hangingwall Enriched Zone (HWE), being the hangingwall portion with >100 ppm Ag.

Stratigraphically above the HWE, occur:
(iii) Baritic Cap (BAR), massive barite with minor massive sulphide "slugs"
(iv) Siliceous Cap (GSP), pyritic chert (Sharpe, 1992)

Table 3 shows how each recognised oretype has quite different grade tenor.

Table 2 - Gross mineralogical composition

Mineral Group	Mineral Species	Measured Volume %	Calculated Weight %
Simple sulphides	Pyrite	47.5	53.1
	Sphalerite	23.9	21.8
	Galena	5.1	8.7
	Arsenopyrite	1.0★	1.4
	Chalcopyrite	0.99	0.92
	Pyrrhotite	trace	trace
	Cubanite	trace	trace
	Argentite	trace	trace
	Marcasite	trace	trace
Sulphosalts	Tetrahedrite	0.21	0.20
	Bournonite	0.04	0.05
	Pyrargyrite	trace	trace
	Miargyrite	trace	trace
	Boulangerite	trace	trace
Metallic oxides	Magnetite	0.03	0.03
	Hematite	trace	trace
	Rutile	trace	trace
Native elements	Electrum	trace	trace
	Native antimony	trace	trace
Silicates	Quartz	6.8	4.0
	Sericite	2.4	1.5
	Chlorite	1.8	1.1
	Clays	trace	trace
	Hyalophane	trace	trace
Carbonates	Calcite, ankerite, siderite	3.9	2.4
Sulphates	Barite	4.7	4.7
Void space		1.6	0.0

★ Point counting not representative for arsenopyrite, see section 5.3.2.

Table 3 - Recognised oretype virgin resources (at 5% Pb+Zn cutoff)

Oretype	Tonnes X 10^6	SG	Cu %	Pb %	Zn %	Ag ppm	Au ppm	Ba %	As %	Fe %
GSP	0.1	3.80	0.28	4.4	7.2	140	3.3	4.0	0.77	18.2
BAR	0.5	4.25	0.27	3.5	5.7	117	2.0	30.3	0.26	10.0
HWE	10.0	4.49	0.34	8.2	15.5	220	3.0	1.3	1.59	23.6
FWD	5.5	4.52	0.48	5.6	11.7	78	1.7	1.1	0.52	28.4

3.5 Macroscopic textures

3.5.1 Types

Classification of massive sulphide texture in hand specimen was developed early in the feasibility drilling of Hellyer; initially as an aid to delineation of metallurgical oretypes. The textural classification system (McArthur, 1990 and Downs, 1990) described below remains in use today for both development mapping and core logging.

Six end-members are used in the textural classification system:

Massive (Ma) - fine-grained massive almost featureless pyrite±sphalerite±galena±arsenopyrite rock, occasionally shows colloform banding of pyrite (Plate 5a)

Banded (Bn) - alternating planar or contorted bands or layers <5mm width of pyrite and sphalerite±galena, pyritic bands are often boudinaged while sphalerite-galena often remobilises parallel to cleavage (Plate 5b)

"Boxwork veining" (Bx) - multigenerational cross-cutting boxworks and networks of symmetric crustiform veins with obvious colloform banding of pyrite/sphalerite (Plate 5c)

Fragmental (Fr) - reworked semi-angular to rounded fragments of variable composition and textured massive sulphide set in a fine-grained massive sulphide or gangue matrix (Plate 5d)

a. Massive (Ma)
HL331 172.5m

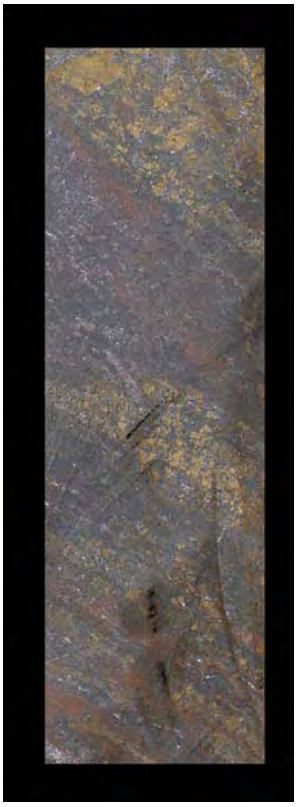

b. Banded (Bn)
HL200 105.6m

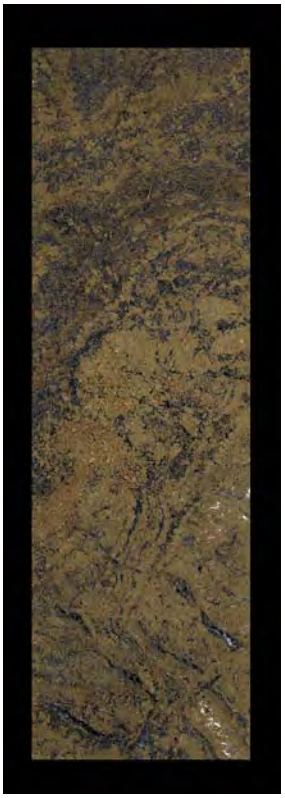

c. Boxwork veining (Bx)
HL381 89.5m

d. Fragmental (Fr)
HL385 52.0m

e. Recrystallised (Rx)
HL334 117.0m

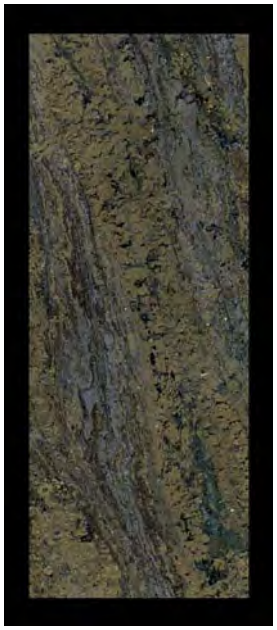

f. Shrinkage shadows (Ss)
HL231 16.3m
(restricted to pyritic band)

Plate 5 - Examples of the six end-members of the macroscopic texture classification system (natural size)

Recrystallised (Rx) - medium-grained, saccharoidal massive pyrite with only minor sphalerite±galena±chalcopyrite, often porous (Plate 5e)

"Shrinkage shadows" (Ss) - fine-grained arsenopyrite-rich massive sulphide with networks of regular pull-apart gashes <1mm width filled with mainly gangue minerals; gashes are perpendicular to any adjacent sulphide banding (Plate 5f)

As with any geological classification system, pure end-members are rare. The system allows further subdivisional classification by combination of textures in order of predominance, e.g. **BnMaSs** would describe a **predominantly banded** rock with **some massive** areas and **minor shrinkage shadows**.

Since this system has been used from drillhole HL020 onwards, the computer database[2] provides an excellent opportunity to spatially analyse occurrence of each textural type. Despite some problems with logging subjectivity, a method of calculating textural indices (McArthur, 1990) has been devised. The index for each texture is ascribed according to the number of textures and the predominance sequence logged by the geologist (Table 4). Some 14,072m of logged massive sulphide with indices calculated as such have been compared to sample assays. This process provides numerical confirmation of the texture/grade relationship as shown in Table 5.

Table 4 - Textural index coding - arbitrary index ascribed according to the code XX predominance position

Code position	Index
XX	10
XX--	9
XX----	8
--XX	6
--XX--	5
----XX	3

[2] The computer database used as the primary data source for this research is based on DATAMINE software. This has been used at the Hellyer Mine since 1988.

Table 5 - Grade variation with macroscopic texture

Texture Index	Freq %★	SG	Cu %	Pb %	Zn %	Ag ppm	Au ppm	Ba %	As %	Fe %
Ma=8-10	42.3	4.63	0.33	6.6	12.9	156	2.4	1.9	1.2	28.1
Bn=8-10	19.0	4.56	0.40	9.8	18.5	232	3.1	1.1	1.3	22.5
Bx=8-10	14.6	4.65	0.51	7.8	14.8	128	2.1	1.8	0.6	26.8
Fr=8-10	8.9	4.37	0.44	7.0	13.1	147	2.5	1.6	0.9	24.7
Rx=8-10	6.6	4.65	0.51	4.8	9.3	67	1.5	1.7	0.3	32.1
Ss=8-10	3.7	4.54	0.22	7.1	13.6	193	1.9	0.4	1.7	27.1
ALL	**100**	**4.57**	**0.38**	**7.2**	**13.9**	**161**	**2.4**	**1.6**	**1.0**	**26.7**

★ These 6 textures do not sum to 100 because of several other minor textural codes in use at times.

3.5.2 Spatial distribution

Attempts to manually correlate logged textures from drillhole to drillhole are somewhat frustrated by individual geologists' subjective logging style, e.g. the texture one geologist will code as "MaBn", another may code as "BnMa". This is overcome to some degree by numerical analysis of the arbitrary texture indices described above.

Firstly, the vertical or stratigraphic zonation pattern of macroscopic textures has been investigated by use of the "stratigraphic number" (SN), devised by McArthur (1988). This provides a 4th coordinate in stratigraphic space, arbitrarily set with SN=0 at the massive sulphide hangingwall and SN=99 at the footwall. The major oretype (as discussed above in section 3.4) boundaries are arbitrarily defined (Table 6) as to reflect the relative stratigraphic thickness of each zone.

Table 6 - Defined stratigraphic numbers for each oretype

Stratigraphic Number Range	Oretype
SN0-SN2	Siliceous cap
SN2-SN8	Baritic cap
SN8-SN60	Hangingwall enriched zone
SN60-SN99	Footwall depleted zone

SN numbers can be set for each logged texture interval according to relative position between the oretype boundaries (McArthur and Kuipers, 1990). This then provides an

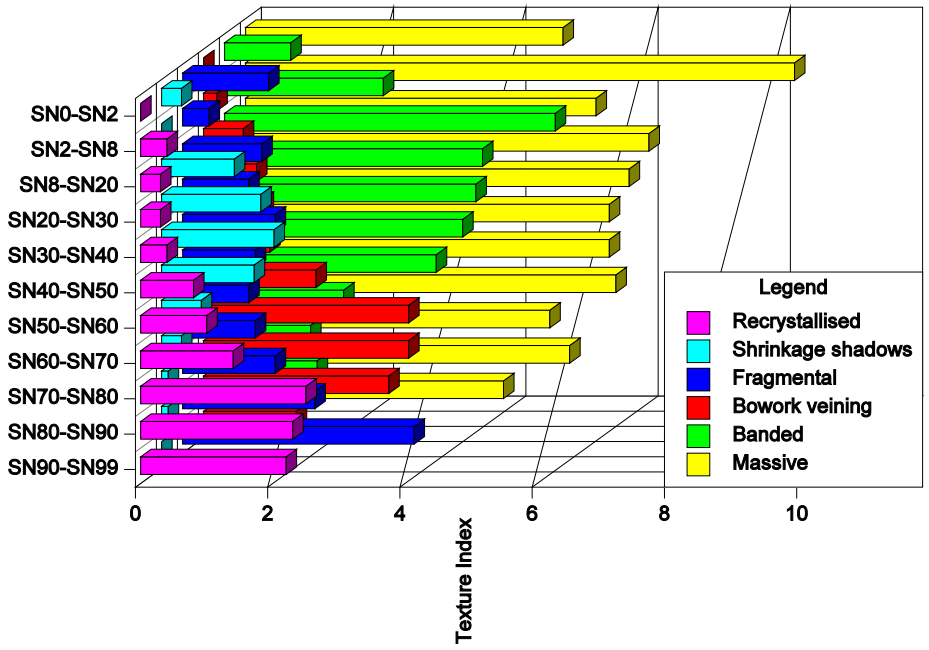

Figure 13 - Textural frequency according to stratigraphic position

elegant way to analyse textural occurrence according to stratigraphic position. This is summarised in Fig.13.

Important features and trends deserve mention:

- **massive** texture dominates throughout but steadily decreases towards the footwall
- **banded** texture occurs predominantly in the hangingwall enriched zone with a distinct maximum at the top of the massive sulphide; markedly less frequent in the footwall depleted zone where it steadily decreases towards the footwall
- **boxwork veining** occurs predominantly in the footwall depleted zone, particularly towards the top
- **fragmental** textures show little variation apart from a distinct maximum at the immediate footwall

- **recrystallised** texture is largely restricted to the footwall depleted zone but overall shows a steady increase towards the footwall
- **shrinkage shadows** closely follow the occurrence of banded texture, but have a maximum midway through the hangingwall enriched zone

Lateral zonation of macroscopic texture has similarly been analysed by interpolating texture indices into a 3D block model. The smoothing effect of the interpolation tends the minimise the subjective variability of the individually logged intervals and a meaningful zonation pattern results (Figs.14,15) - the "forest is seen through the trees".

Recrystallised textures concentrate proximally over the interpreted core of the footwall alteration zone (Gemmell and Large, 1992) whilst banded and shrinkage shadow textures occupy more distal positions. Fragmental ores concentrate at the footwall on the flanks of the seafloor high reconstructed by Downs (1993).

It is clear that macroscopic textures display a systematic zonation pattern that is reinforced by similar zonation discovered in metal content and microscopic textures (see sections 4.4 and 5.6 below).

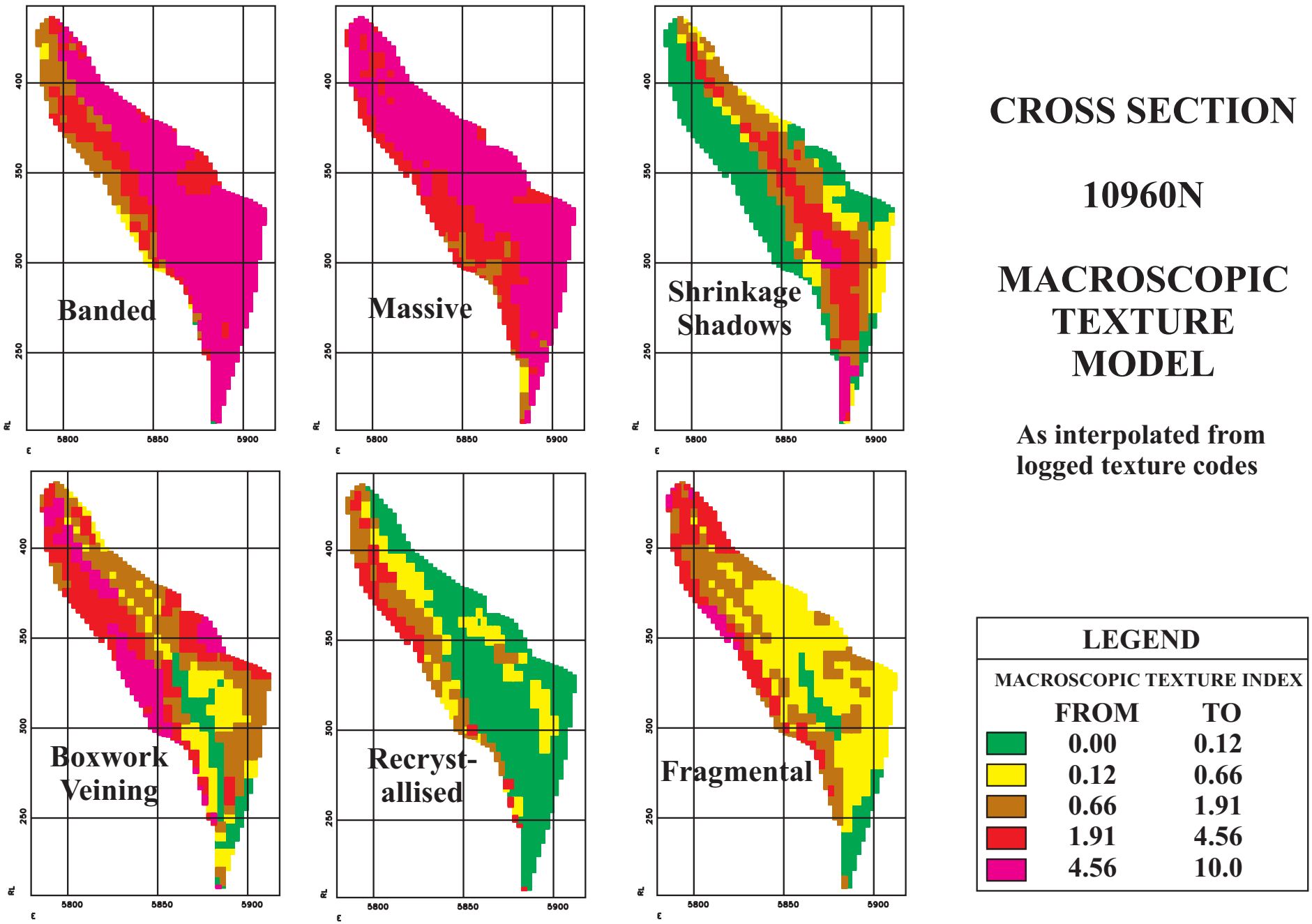

Figure 14 - Zonation of macroscopic texture as seen in cross-section 10960N

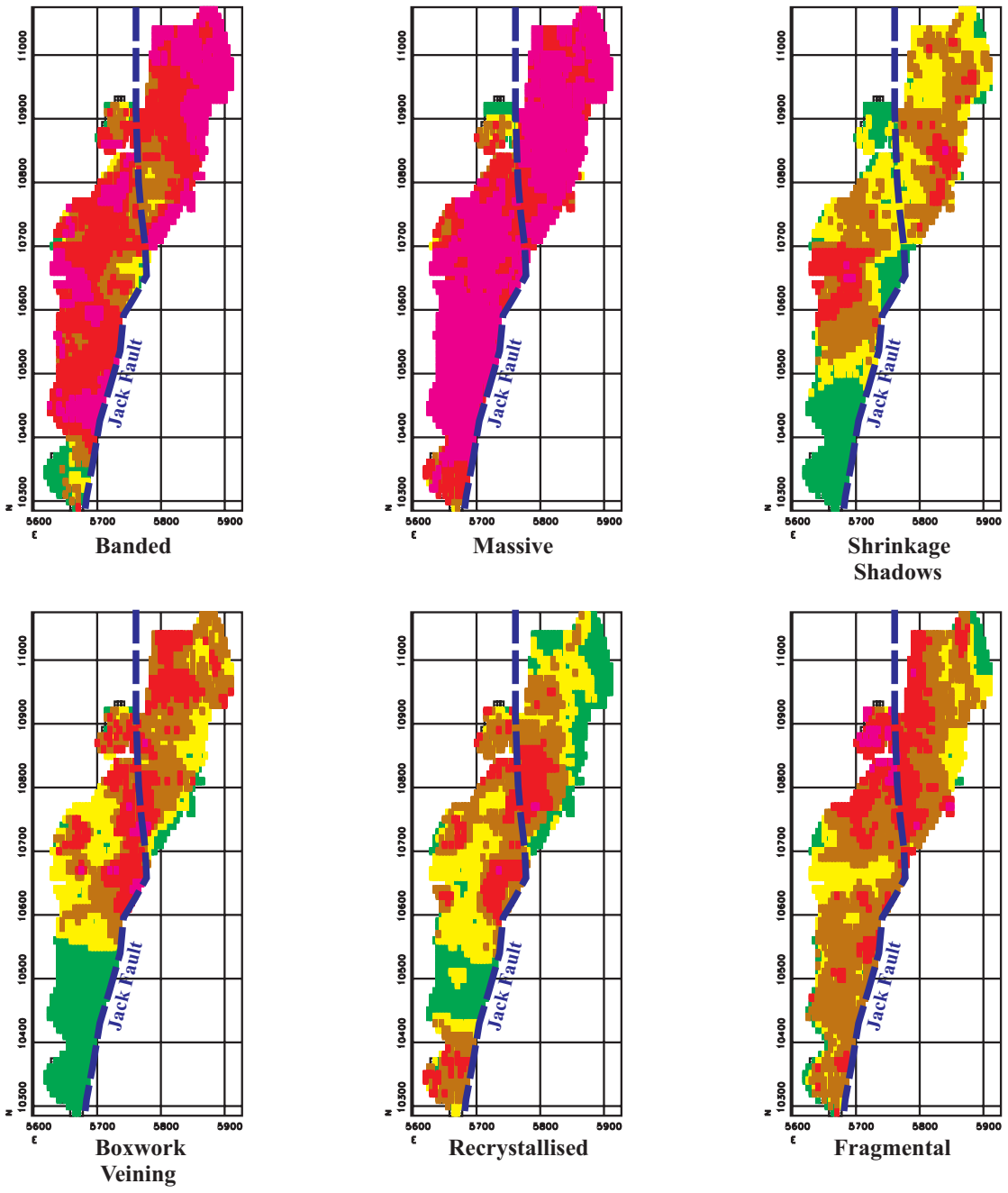

PLAN PROJECTION

Massive sulphide only

MACROSCOPIC TEXTURE MODEL

As interpolated from logged texture codes

LEGEND		
MACROSCOPIC TEXTURE INDEX		
	FROM	TO
	0.00	0.12
	0.12	0.66
	0.66	1.91
	1.91	4.56
	4.56	10.0

Figure 15 - Zonation of macroscopic texture as seen in plan projection

3.6 Structural features

3.6.1 Folding style

Middle Devonian folding of the deposit was strongly controlled by primary sulphide thickness variations and the competency of the enclosing rocks. Downs (1993) has reconstructed the depositional topography of the Cambrian sulphide mound (Fig.16) by removing fault displacements and unfolding the Devonian deformation. The

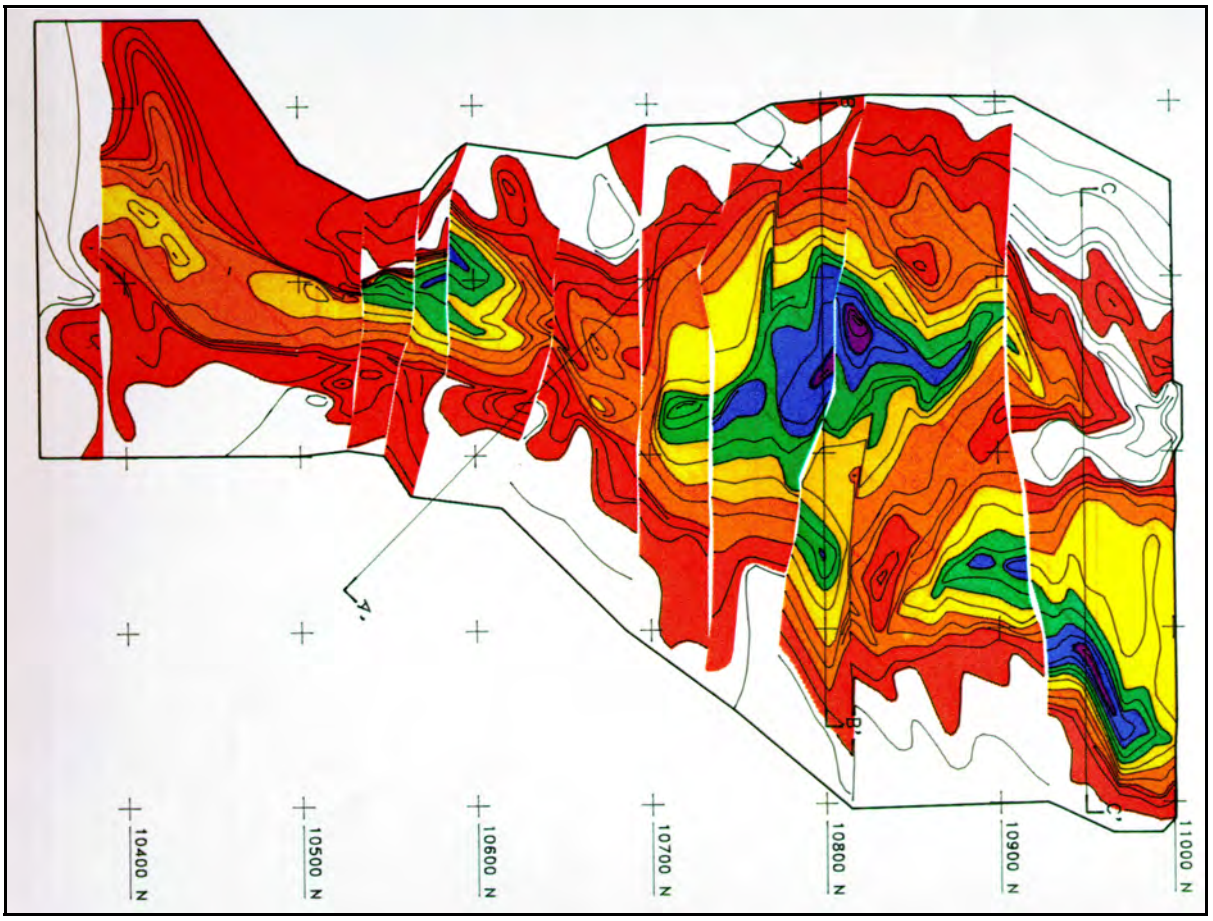

Figure 16 - Approximate Cambrian massive sulphide thickness with Jack Fault displacement removed (after Downs, 1993). Colours: white 0-5m, red 5-20m, orange 20-40m, yellow 40-60m, green 60-80m, blue 80-100m, purple >100m.

unfolding was achieved by taking the reasonable assumption that the HVS/PLS contact was a horizontal surface.

Strain partitioning as described by (Drown and Downs, 1990) led to syncline

development where primary thicknesses of sphalerite/galena-rich sulphide overlay phyllosilicate-rich altered footwall rocks (two areas east and west of the Jack Fault coinciding with the two half-grabens). In a similar manner, the anticline developed centrally over the more rigid pyrite-rich sulphide which overlay the siliceous core of the footwall alteration system. The relatively unaltered blocks of footwall andesite either side of the alteration system and the basalt in the hangingwall acted together as a rigid enclosing framework to effectively concentrate all the deformational strain within.

At two locations (10690N in the Keel Zone and 11010N in the North End) the synclines are locally almost isoclinal, bearing remarkable similarities to fold style at the more intensely deformed Que River deposit (McArthur and Dronseika, 1990). The anticlinal surfaces however, are all of broad, open form.

3.6.2 Cleavage

As documented by Downs (1993), macroscopic sulphide banding in the HWE tends to parallel cleavage. This banding will be shown later, to mainly be a realignment/extension of existing primary layering, with only minor remobilisation of galena. However, obvious zones of remobilised coarse-grained galena/tetrahedrite are often seen in the more intensely deformed areas, aligned parallel to cleavage. These remobilised zones are sub-parallel to, or cross-cut original primary layering.

3.6.3 Pull-aparts

Individual pyrite bands in the HWE are often extended parallel to cleavage and break in a brittle fashion into regular rectilinear blocks (here termed "pull-aparts") with remobilised galena±sphalerite filling the fractures. The surrounding sphalerite/galena bands deform in a ductile fashion around the pyrite. This is very similar to the shrinkage shadow texture described above in section 3.5.1.

In another form of pull-apart, short gashes up to 5cm wide are arranged perpendicular

to normal cleavage direction within the strongly recrystallised portions of the FWD; often filled with remobilised quartz, sphalerite, galena and chalcopyrite. Attractive crystal vughs are occasionally found inside these gashes (Plate 6).

Plate 6 - Spectacular octahedral galena crystal from a gash in the FWD (400 level)

3.6.4 Faulting

Faults seen within the massive sulphide (Fig.17) cluster into two main sets:

(i) steep east-dipping to vertical, striking NNE-SSW; moderate sinistral displacements; movement striations generally plunge shallowly to the south; predictable planar structures; sheared puggy clay gouge and cataclasis of adjacent massive sulphide; exemplified by the Jack Fault.

(ii) steep south-dipping to vertical, striking ESE-WNW to SE-NW; minor

dextral displacements; movement striations sub-horizontal; notoriously non-planar and

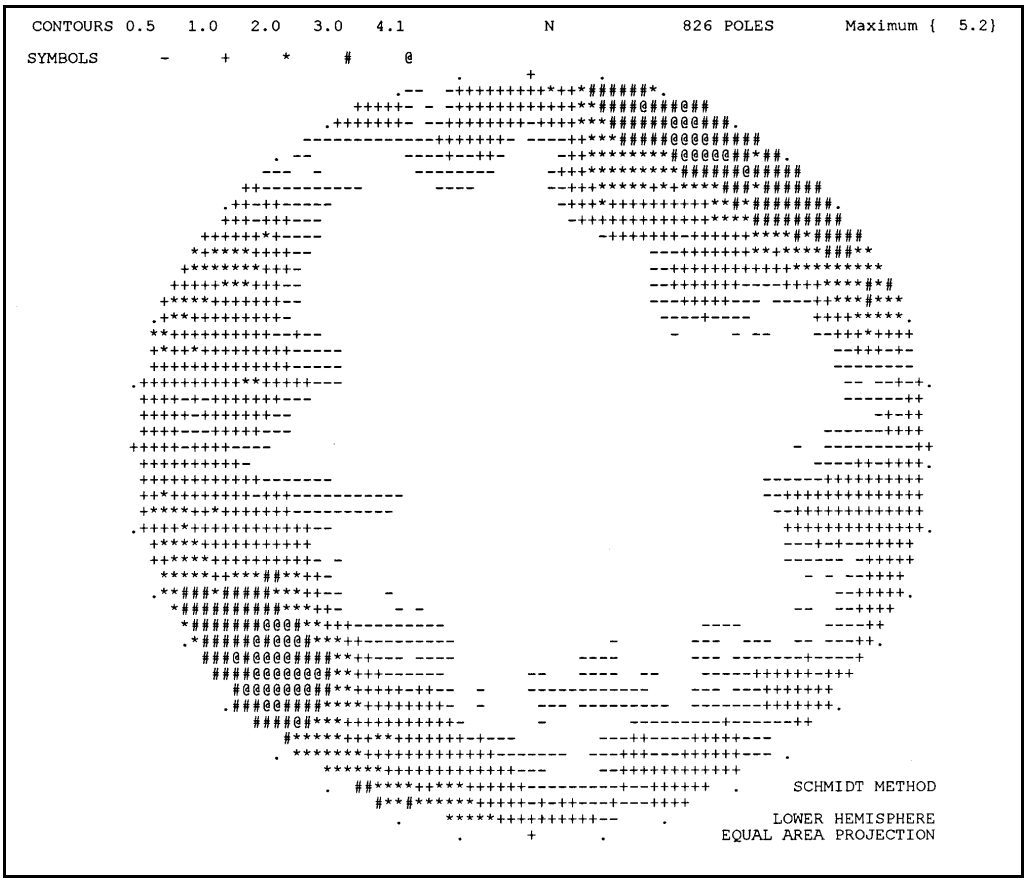

Figure 17 - Stereonet of all faults within the massive sulphide (from data collected by Aberfoyle geologists during routine development mapping)

feathering structures; open and cavernous, historically providing groundwater channelways; no significant cataclasis; very numerous.

3.6.5 Jointing

Jointing is most common in the massive and banded textured massive sulphide with several sets evident (Fig.18). The major set parallels the NE-SW fault set. Slickensided carbonate/chlorite coatings are common.

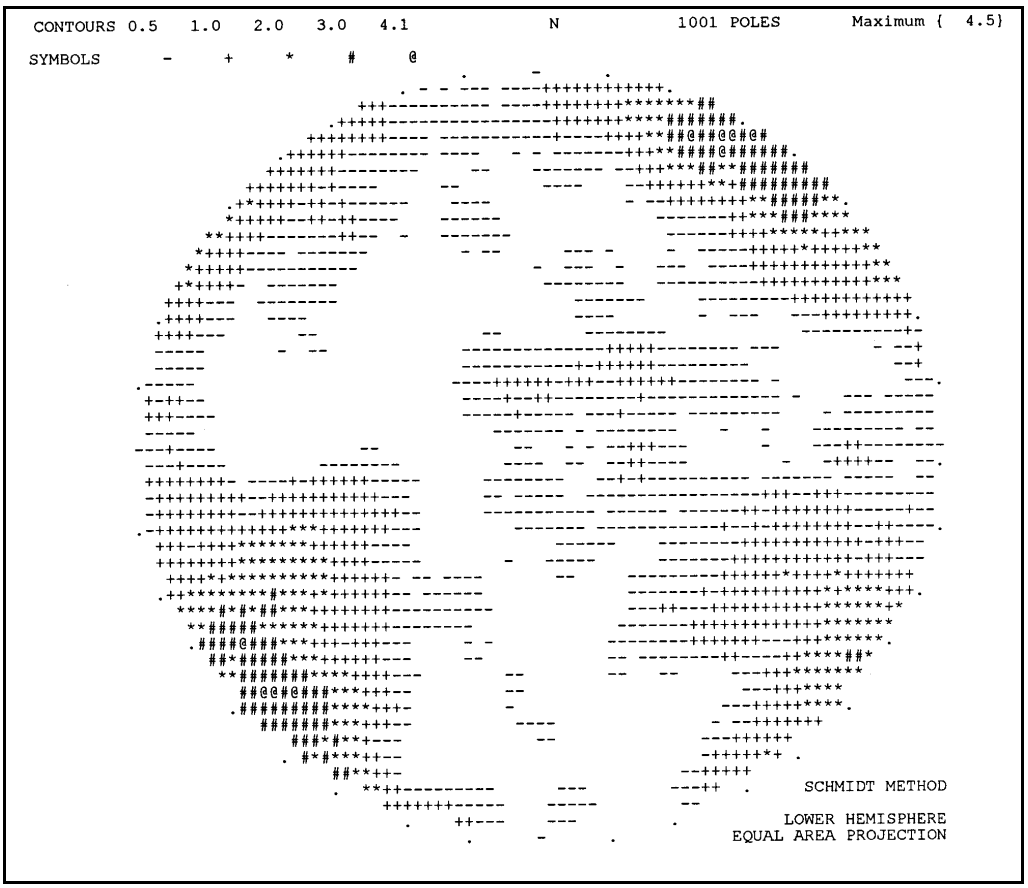

Figure 18 - Stereonet of all joints within the massive sulphide (Aberfoyle data)

3.7 The footwall alteration zone

The following summary is taken from the numerous detailed papers of Gemmell (1988, 1989, 1990, 1991), Gemmell and Large (1990a, 1990b, 1992) and Gemmell et al. (1990).

3.7.1 Morphology

Beneath the entire Hellyer massive sulphide and extending up- and down-plunge to the NNE-SSW occurs a well-preserved alteration zone and stringer vein system. This sub-vertical footwall alteration zone cuts across the gently dipping volcanostratigraphy of the feldspar-phyric andesites (FPS) and is known in exploration drillholes to at least 600m below the footwall. From available information it appears to narrow with depth. Conservatively, at least 250 million tonnes of altered rock lies vertically beneath the Hellyer deposit.

3.7.2 Mineralogical zonation

The footwall alteration has been subdivided by the mine geologists into:

(i) the inner strongly altered "Stringer Zone" (STZ) and
(ii) the outer less altered "Stringer Envelope Zone" (SEZ).

The STZ is further subdivided into approximate concentric zones (Fig. 19), each of characteristic mineralogy.

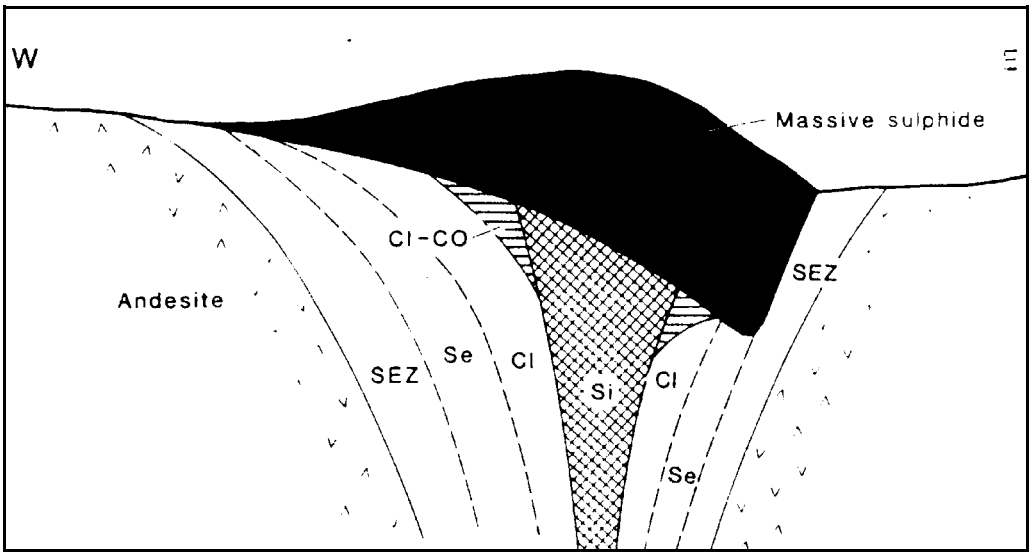

Figure 19 - Schematic cross-section pre-Jack Fault showing mineralogic zones of the footwall alteration (after Gemmell and Large, 1992). SEZ=Stringer Envelope Zone, Se=sericite, Cl=chlorite, Si=quartz, Cl-CO=chlorite-carbonate

The central ellipsoidal core of the alteration (Fig. 20), which is strongly siliceous and pyritic (±sphalerite/galena/chalcopyrite/barite stringers) is approximately 140m (N-S) X 70m (E-W) and occurs beneath the centre of the massive sulphide (10670N west of the Jack Fault, 10800N to the east). The alteration is so strong that all original, primary texture has been obliterated. However, a pseudofragmental texture can occur where later silica has flooded the earlier pervasive chlorite alteration. Sulphide content

decreases dramatically with increasing depth below the footwall. Subsidiary siliceous zones occur to the north and south of the main siliceous core.

Adjacent to the siliceous core occurs an irregular zone of strongly cleaved chlorite±pyrite alteration that also totally overprints any original volcanic texture. In the north-western portion of the footwall alteration zone, a chlorite-dolomite assemblage is common (Fig. 20). Base metal stringers are rare in the chlorite zone.

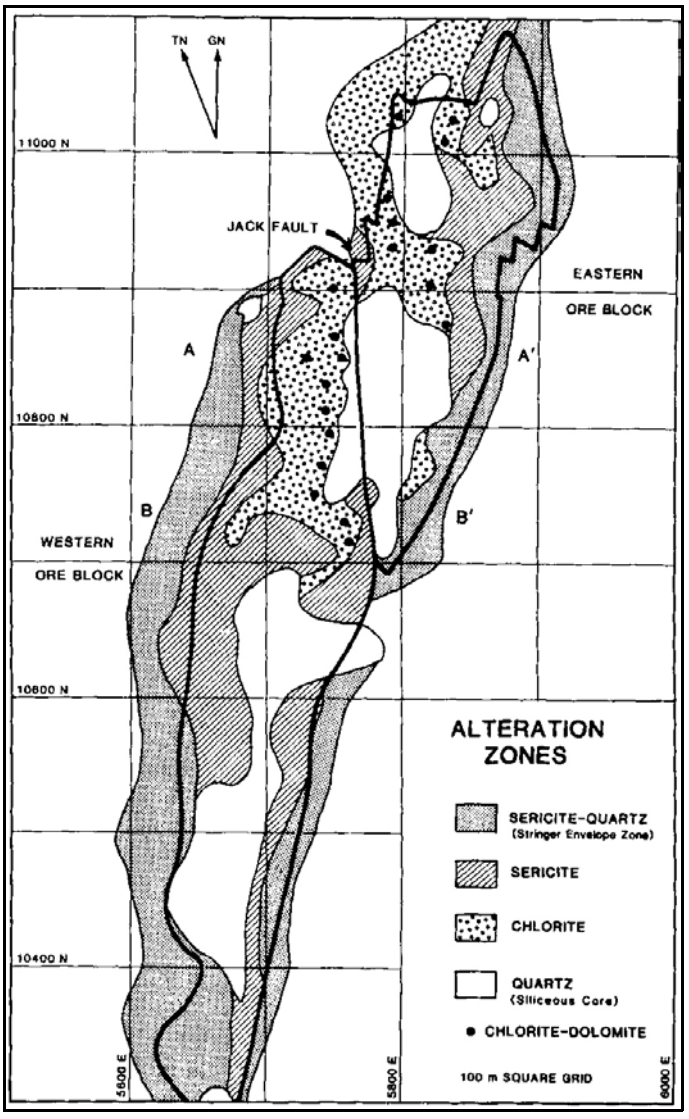

Figure 20 - Distribution of mineralogic zones immediately beneath the massive sulphide footwall (after Gemmell and Large, 1992).

The outermost zone of the STZ is a strongly cleaved sericite±pyrite dominant assemblage that grades into the chlorite zone. Base metal stringers are rare, but pyrite-rich stringers are common.

The outer SEZ is a characteristically altered andesite lava/volcaniclastic of pale, bleached appearance with comparatively sharp boundaries with the STZ inside and FPS outside. The alteration mineralogy is sericite/quartz with distinctive narrow pyrite veinlets giving the rock a "crackled" appearance. Base metal stringers are very rare, but pyrite stringers are very common.

Strain partitioning (elongation of original volcaniclastic fragments) is seen to steadily

decrease towards the SEZ/FPS contact (Drown and Downs, 1990).

3.7.3 Metal zonation

Gemmell and Large (1992) have described distinct zonation of metals surrounding their interpreted feeder zones (Fig.21). Fe and Cu are concentrated in the cores of the proximal feeders with other metals increasing outwards from the core. This pattern is also observed in the overlying massive sulphide (see section 4.4.2).

3.8 Alteration in the hangingwall basalt

The following summary is taken from Jack (1990) and Warren (1989).

3.8.1 Morphology

Calcite-"fuchsite"[3]±pyrite alteration in the hangingwall PLS basalt is concentrated in a plume-shaped region above the main footwall feeder described above. This alteration, although most intense immediately in contact with the massive sulphide hangingwall, extends completely up to the PLS/QRS contact. In fact, alteration tends to extend the furthest distance laterally just below the QRS contact, presumedly due to decreased hydrostatic loadings near the seafloor. Alteration is generally stronger in pillowed lavas due to enhanced permeability via interpillow areas (pillow margins are always most altered). Sheet lavas are more homogenous, less susceptible to transmission of fluids and therefore distinctly less altered.

3.8.2 Mineralogical zonation

The most intense alteration occurs immediately above the massive sulphide

[3]The Cr-rich hydromuscovite called "fuchsite" by all previous workers, may in fact be more accurately termed "mariposite" (J.B.Gemmell, pers.comm.) but for consistency, the historically accepted term "fuchsite" will be used throughout this thesis.

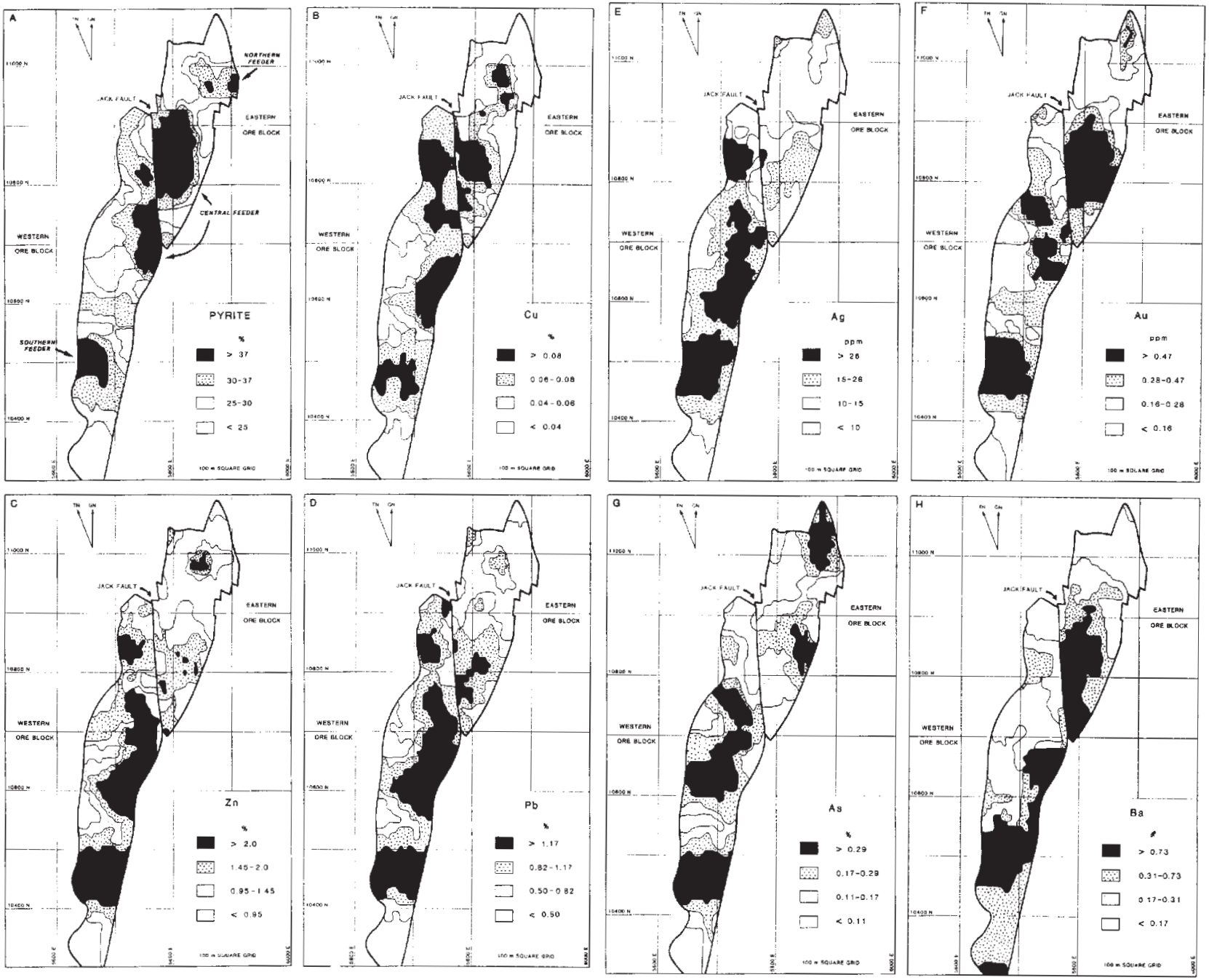

Figure 21 - Distribution of metals (and pyrite) in the uppermost 5m of the footwall alteration zone as interpolated by kriging (after Gemmell and Large, 1992).

hangingwall at 10800N where pervasive bright green fuchsite-calcite-pyrite has all but obliterated the original primary textures. Locally, the phyllosilicate content is so high that a strong cleavage has developed in the central anticlinal closure, severely effecting ground conditions for mining. Pyrite can occupy up to 20% of the rock, occurring as narrow stringer veinlets, contorted and extended by the deformation. Arsenopyrite rosettes are occasionally recorded. In a gross sense, Jack (1989) documents enrichment in CaO, K_2O, Al_2O_3 and Ba with depletion in Fe_2O_3, MgO and SiO_2.

Passing up into the less intense areas of the fuchsite plume, calcite occurs most commonly as a vein stockwork and pyrite content drops markedly to <5%. Here, most pyrite is located within the interpillow chert as colloform aggregates. Rhythmic pyrite layers in the lowermost beds of the QRS maybe related to the basalt alteration below.

An outer peripheral zone of pink albite-quartz±chlorite alteration occurs lateral to the calcite-fuchsite zone, again mainly concentrated in the pillowed lavas. Rarely intense, this alteration generally occurs as irregular patchy blotches; pyrite is very rare. In the albite altered zone, Jack (1989) records enrichment in Na_2O, CaO and SiO_2 with depletion in Fe_2O_3, MgO and Ba.

Narrow veinlets of calcite±barite+sphalerite+galena cut through the PLS and QRS above the deposit. These are interpreted as Devonian remobilisation, and therefore not part of the Cambrian mineralising episode.

4. METAL ZONATION IN THE MASSIVE SULPHIDE

Any zonation pattern that may exist in the metal content of an ore deposit can only be gleaned by interpreting available sample assays. It is important to fully appreciate:

(i) the quantity, quality and representativeness of the samples and their assays and

(ii) the geological suitability of any interpolation technique applied to these assays.

The bulk of this chapter will attempt to validate the data and the interpretive techniques applied.

4.1 The available raw data

4.1.1 Drill core samples

Since drilling began at Hellyer in 1983, all mineralised rock intersected has been sampled and assayed. Sample boundaries are placed at major lithology boundaries to avoid mixing of rock types in one sample. Up to drill hole HL262, all GSP, BAR and massive sulphide was sampled in nominal 1m intervals, with local adjustment near the contacts. From drill hole HL263 onwards, 2m intervals were used. Samples within the surrounding host rock or footwall alteration zone have always been at 2m intervals. Generally, at least two samples are taken in the "waste" preceding or following the massive sulphide intersection. Sample intervals are decided by each geologist when geological logging is complete (Downs, 1990). From drill hole HL085 onwards, all Hellyer drill core samples have the prefix 'HC', and all numbers come from the 200,000 series. The core is halved by diamond sawing, one half being retained for permanent archive. Where the sulphides are obviously banded, the core saw operator is instructed to ensure that wherever practicable, the cut subtends the maximum angle to this banding. Core recovery within the deposit averages 99.7%.

Virtually all samples have been prepared and assayed (apart from Analabs Au) by Aberfoyle's own laboratory at Luina (1983-1994) or Burnie (1994 onwards). The only

exception was drill holes HL240-HL273, when in early 1988, the Luina laboratory was temporarily understaffed. The samples from these holes were analysed by Analabs. A single sample preparation routine has been followed from the beginning (Fig.22). Coarse sample reject has been archived, with some totally consumed for metallurgical testing. Remaining pulverised material was kept for a short period in case repeat assaying was necessary, but rapid oxidation of the reactive pyrite in a moist atmosphere has rendered most pulps useless after 12 months.

Assaying method changed in 1989 when new instrument methods became available (Table 7).

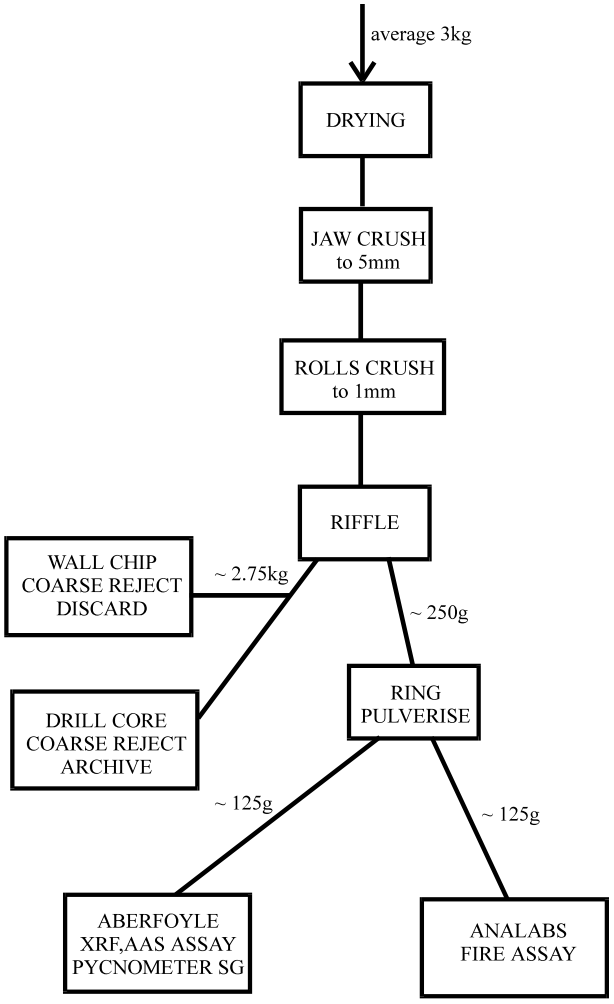

Figure 22 - Aberfoyle sample reduction flowsheet

Table 7 - Assaying methods used by Aberfoyle for Hellyer drill core

Element	Method up to HL435	Method from HL436	Detection limit	Reporting precision throughout
S.G.	air pycnometer	air pycnometer	-	0.01
Cu	AAS	XRF	0.01%	<1%Cu, 0.01%; >1%Cu, 0.05%
Pb	AAS	XRF	0.01%	<1%Pb, 0.01%; 1-10%Pb, 0.05%; >10%Pb, 0.1%
Zn	AAS	XRF	0.01%	<1%Zn, 0.01%; 1-10%Zn, 0.05%; >10%Zn, 0.1%
Ag	AAS	AAS	1 ppm	1 ppm
Ba	XRF	XRF	0.05%	<10%Ba, 0.05%; >10%Ba, 0.1%
As	XRF	XRF	0.01%	<1%As, 0.01%; >1%As, 0.05%
Au (Analabs)	Fire assay AAS finish	Fire assay AAS finish	0.01 ppm	0.01 ppm

Early "round robin" comparison with other laboratories and a strict regime of internal standards and duplicate determinations on every 10th sample ensured consistent assay quality and unbiasedness (J.Haggar, pers.comm.). Au assaying has all been done by Analabs by fire assaying a 50g sample with an AAS finish.

All assays have been entered manually into the DATAMINE database. The total number of drill core samples from within the deposit is 17,043 over 23,750m.

4.1.2 Development wall chip samples

Since the massive sulphide was first intersected by underground development in June 1986, wall chip samples have been taken from all mapped vertical surfaces. In the first few years, almost every ore face was sampled but this has now decreased to one wall of each mapped E-W crosscut and faces in N-S drives when mapped. The sample interval varies between 1-2m. The approximate 1-2kg sample is randomly chipped by geological pick (handheld pneumatic hammer used in early years) over an area within reach of the sampler (0.5-2m above the floor). The early use of a laid-out dropsheet has now been abandoned in favour of the sample bag held below the pick. Regrettably, the sample is biased by the fracturing of the wall surface. Joint plane surfaces parallel to the wall are virtually impossible to sample. All wall chip samples have the prefix 'HD', and all numbers come from the 400,000 series. The sample boundaries are measured by offset from the nearest survey peg and sample lines (pseudo-drill holes) constructed later after surveyed development outlines are available. The sample line is assumed to be 1m above the surveyed development floor RL. Samples are submitted to Aberfoyle's laboratory for rapid assay turnaround to assist grade control activities. Sample reduction procedure has been identical as for drill core (Fig.22) except coarse reject is discarded. Assay methods used are summarised in Table 8.

S.G. and Au are not determined on wall chip samples due to turnaround restrictions. All assays are manually entered into the DATAMINE database as pseudo-drill holes with the borehole ID prefix 'HD'. The total number of wall chip samples from within the deposit is 7,257 over 10,501m.

Table 8 - Assaying methods used by the Aberfoyle laboratory for Hellyer wall chip samples

Element	Method	Detection limit	Reporting precision up to Dec. 1989	Reporting precision from Dec. 1989
Cu	XRF	0.01%	0.01%	0.01%
Pb	XRF	0.01%	<1%Pb, 0.01%; 1-10%Pb, 0.05%; >10%Pb, 0.1%	0.01%
Zn	XRF	0.01%	<1%Zn, 0.01%; 1-10%Zn, 0.05%; >10%Zn, 0.1%	0.01%
Ag	XRF	1 ppm	1 ppm	1 ppm
Ba	XRF	0.05%	<10%Ba, 0.05%; >10%Ba, 0.1%	0.01%
As	XRF	0.01%	<1%As, 0.01%; >1%As, 0.05%	0.01%
Fe	XRF	0.05%	<1%Fe, 0.05%; >1%Fe, 0.1%	0.01%

4.1.3 Should all data be used?

During the feasibility study for Hellyer's development, considerable testing was undertaken to decide whether wall chip samples should be mixed with drill core samples for resource estimation purposes (Aberfoyle Resources Limited, 1987). After repetitive sampling by different samplers of the 10910N crosscut on the 400 level and comparison of wall sample assays with nearby drill holes, the decision was made to accept all wall chip samples as being of equal value to drill core samples. This was also accepted by the major resource consultant (A.G.Journel, pers.comm.). However, the number of drill core samples (17043) far exceeds that of wall chip samples (7257).

4.2 Sample statistics

4.2.1 Compositing

To permit valid statistical analysis it is necessary that the variable length samples are composited to a constant length. At Hellyer, compositing to nominal 5m lengths is performed within intervals of similar oretype (GSP, BAR and massive sulphide). There are three conventions that can be applied to compositing algorithms. By example, consider a massive sulphide intersection of 33.2m (say 8.6-41.8m depth).

Algorithm A - start compositing from zero depth in 5m intervals, discarding any composite less than 2.5m (arbitrary half). The 6 composites resulting would be:

10.0-15.0m	5.0m
15.0-20.0m	5.0m
20.0-25.0m	5.0m
25.0-30.0m	5.0m
30.0-35.0m	5.0m
35.0-40.0m	5.0m

Algorithm B - start compositing from the intersection start depth in 5m intervals, discarding any composite less than 2.5m. The 7 composites resulting would be:

8.6-13.6m	5.0m
13.6-18.6m	5.0m
18.6-23.6m	5.0m
23.6-28.6m	5.0m
28.6-33.6m	5.0m
33.6-38.6m	5.0m
38.6-41.8m	3.2m

Algorithm C - divide the intersection length into an integral number of composites of a constant length between 2.5-7.5m. The 7 composites resulting would be:

8.60-13.34m	4.74m
13.34-18.09m	4.75m
18.09-22.83m	4.74m
22.83-27.57m	4.74m
27.57-32.31m	4.74m
32.31-37.06m	4.75m
37.06-41.80m	4.74m

Aberfoyle have decided to accept Convention C, thus ensuring **all** of the sample length is used. Most intersections are large, meaning the resulting composite length is close to 5m. Bias is avoided, which would occur when discarding first or last sample in a zoned deposit like Hellyer, which often has the highest grades right at the hangingwall and the lowest grades right at the footwall. The statistical disadvantage of varying composite length is considered minor (Fig. 23).

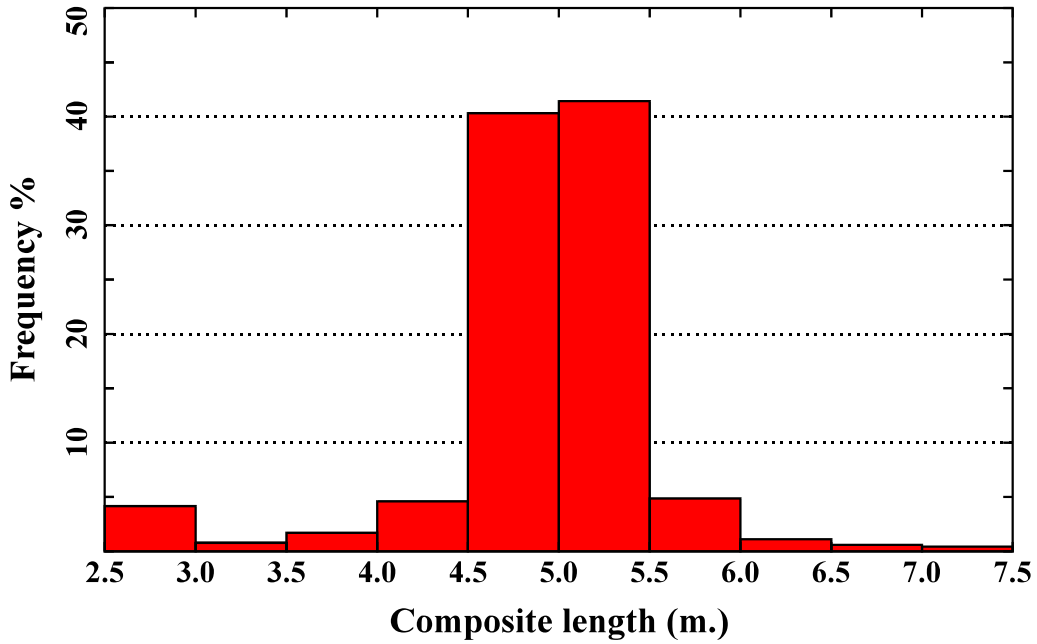

Figure 23 - Histogram of Hellyer composite lengths resulting from using algorithm C

4.2.2 Distributions

Distributions of all 5m composites for S.G. and all assayed elements are shown in Figs.24-32. Within the massive sulphide S.G., Pb, Zn and Fe approximate the normal distribution whilst Cu, Ag, Au and As approximate the log-normal distribution. Ba is normal in the BAR oretype and lognormal otherwise. There is no evidence of mixed populations (e.g. bimodal population) except possibly FWD Pb and Zn, where the normality fit is imperfect.

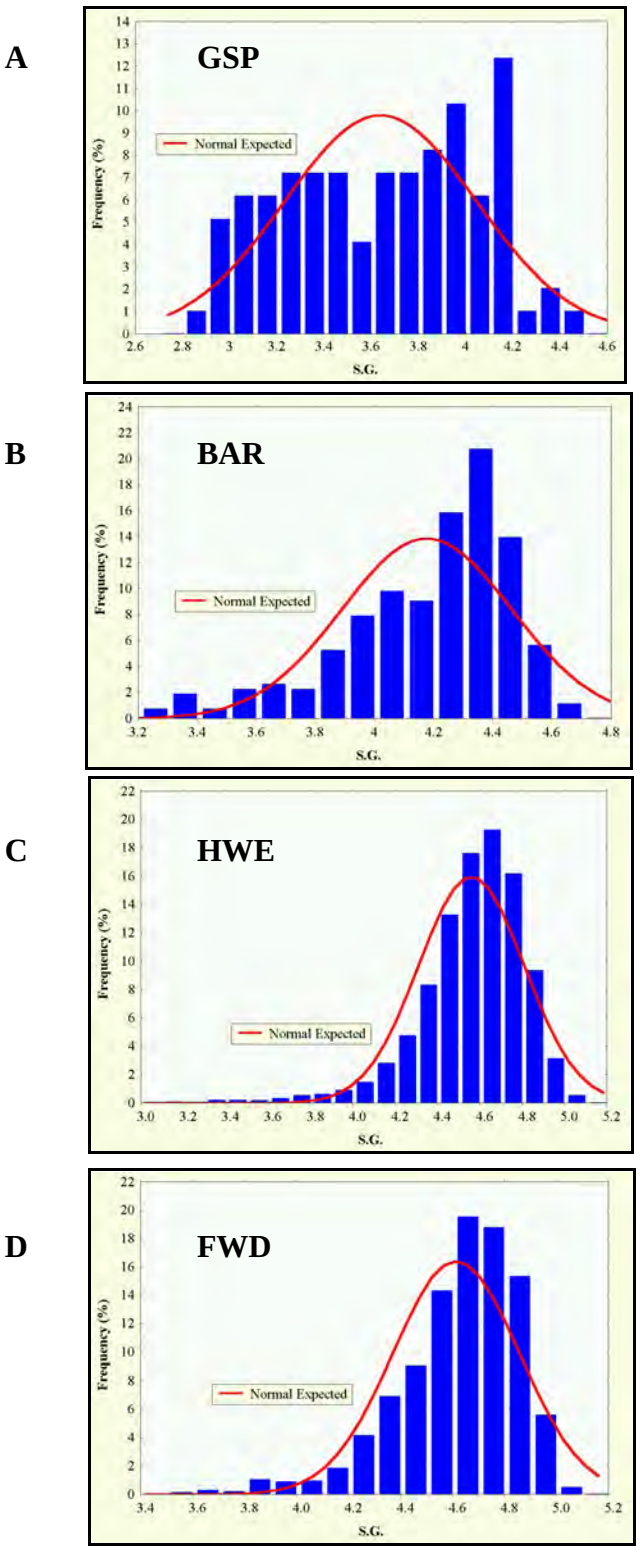

Figure 24 - S.G. histograms for (a) GSP, (b) BAR, (c) HWE and (d) FWD oretypes

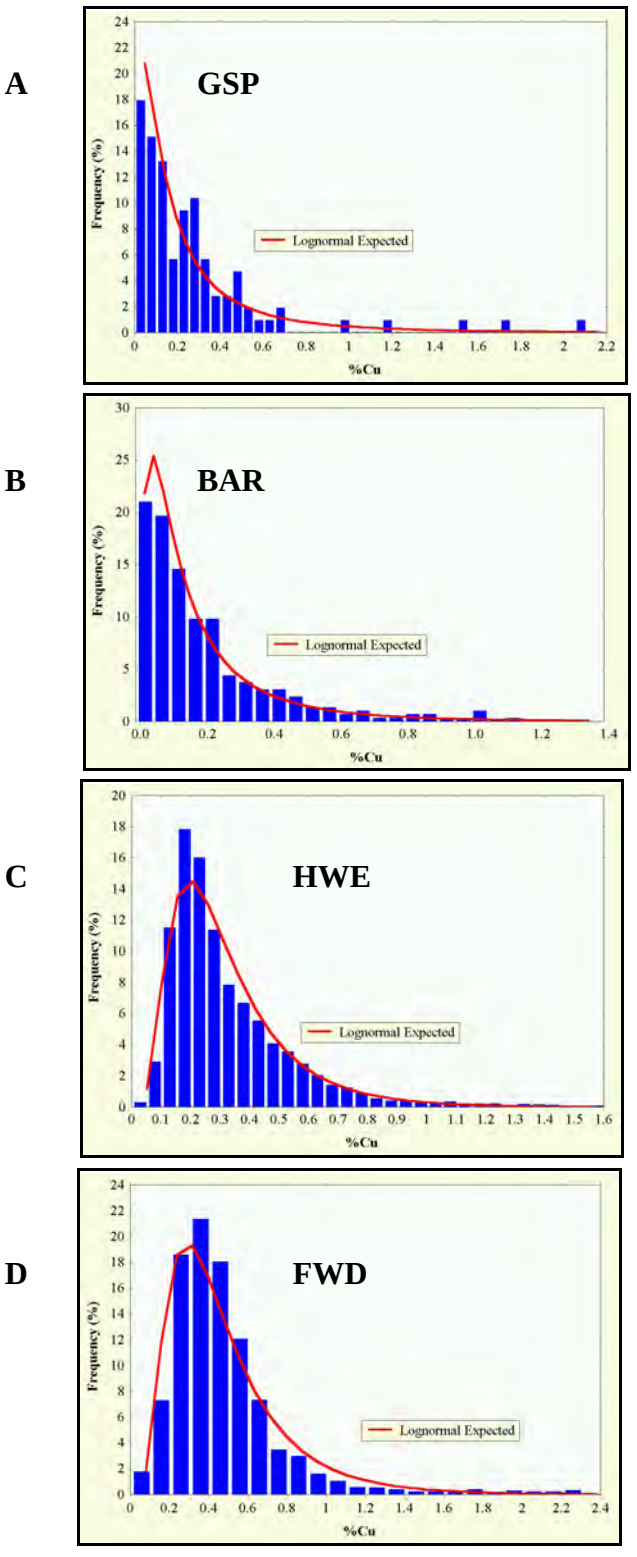

Figure 25 - %Cu histograms for (a) GSP, (b) BAR, (c) HWE and (d) FWD oretypes

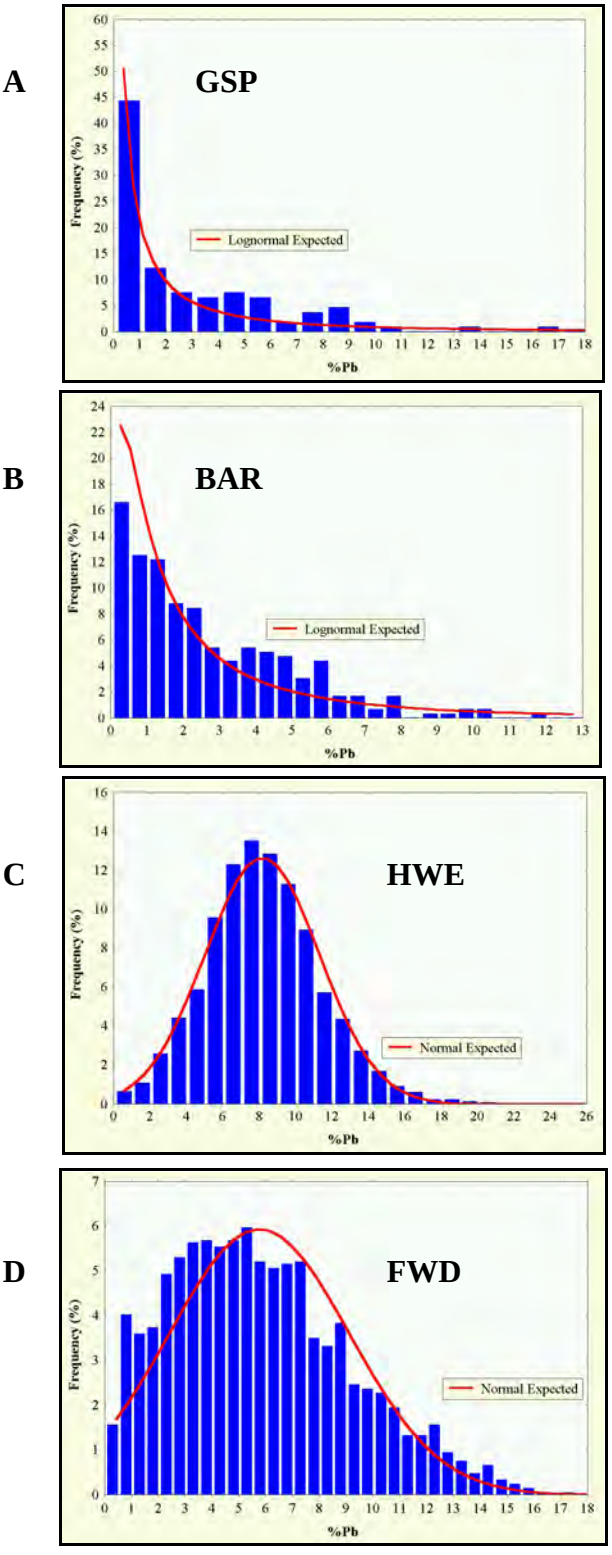

Figure 26 - %Pb histograms for (a) GSP, (b) BAR, (c) HWE and (d) FWD oretypes

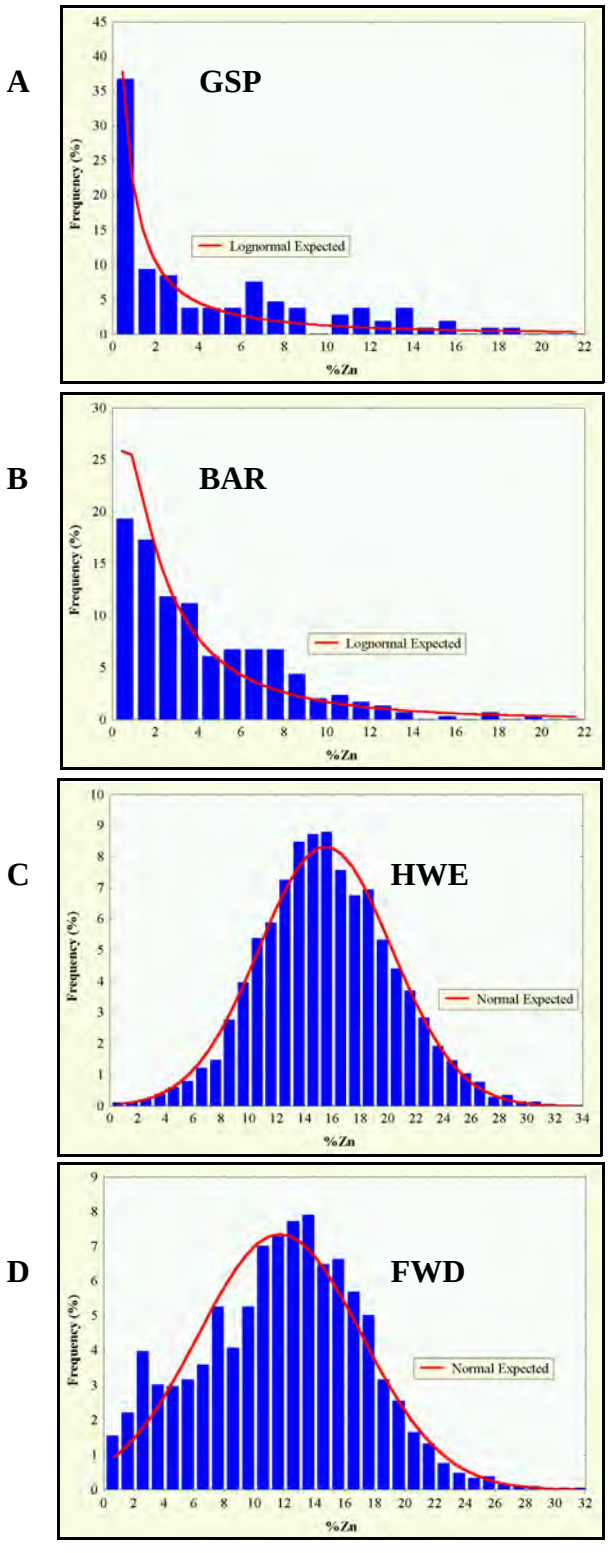

Figure 27 - %Zn histograms for (a) GSP, (b) BAR, (c) HWE and (d) FWD oretypes

A

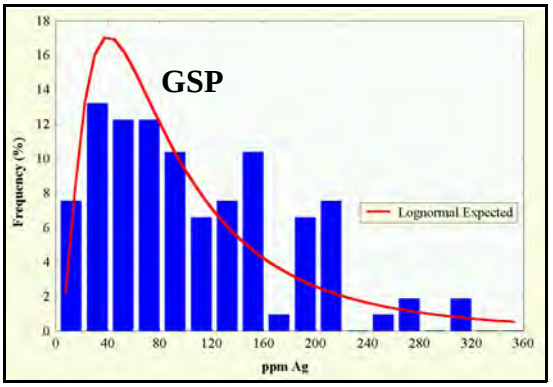

B

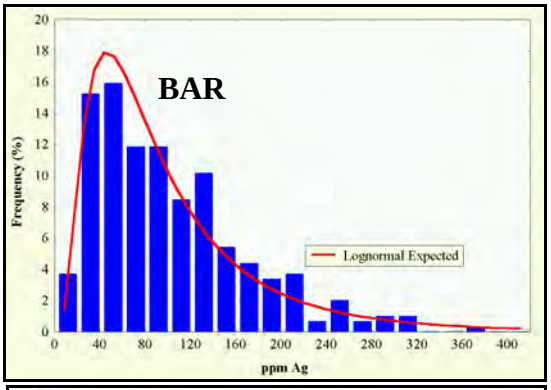

C

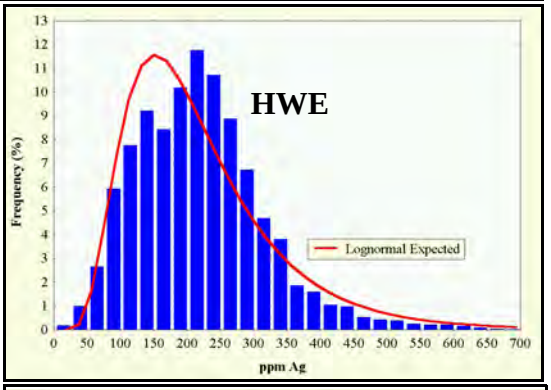

D

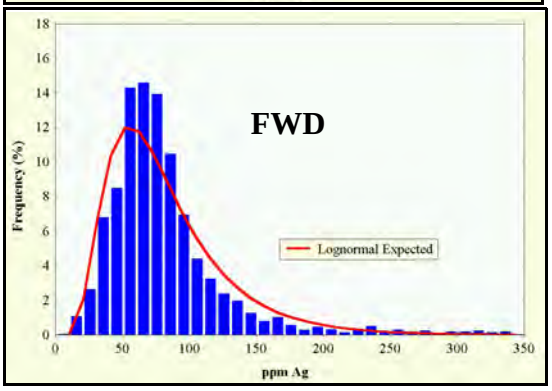

Figure 28 - ppm Ag histograms for (a) GSP, (b) BAR, (c) HWE and (d) FWD oretypes

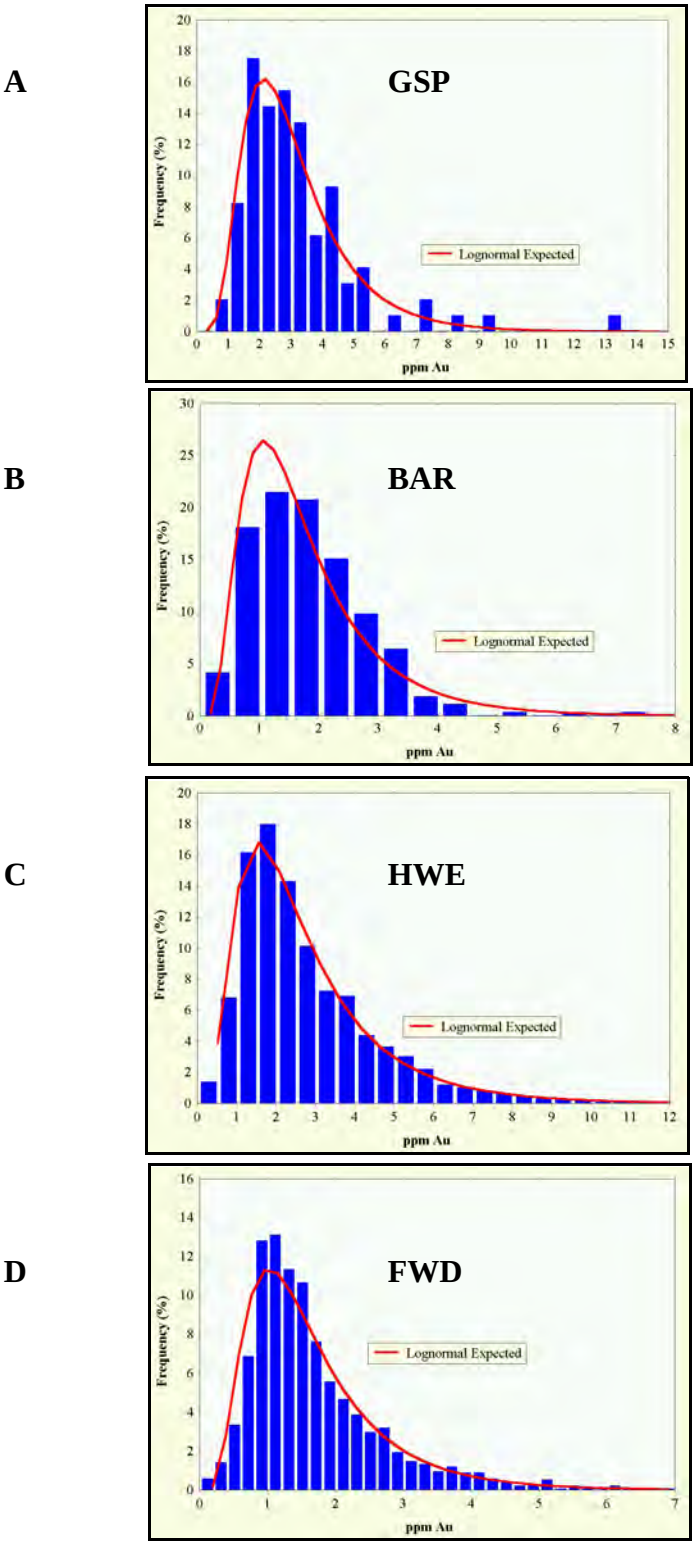

Figure 29 - ppm Au histograms for (a) GSP, (b) BAR, (c) HWE and (d) FWD oretypes

A

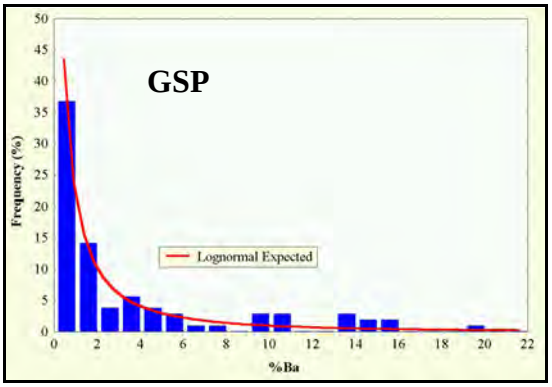

B

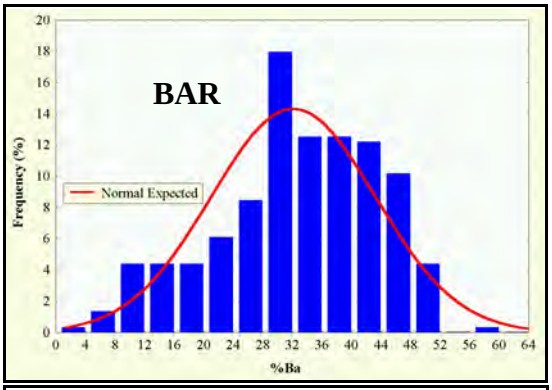

C

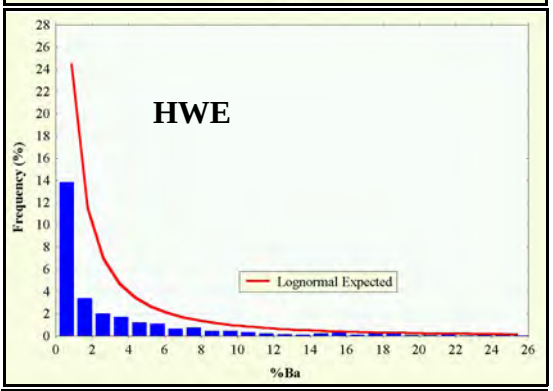

D

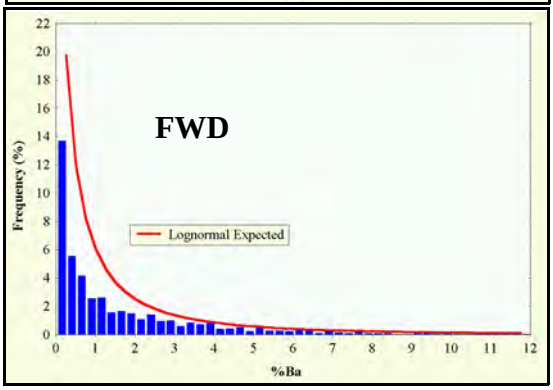

Figure 30 - %Ba histograms for (a) GSP, (b) BAR, (c) HWE and (d) FWD oretypes

A

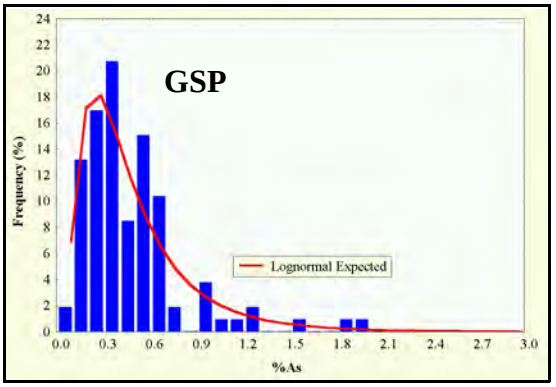

B

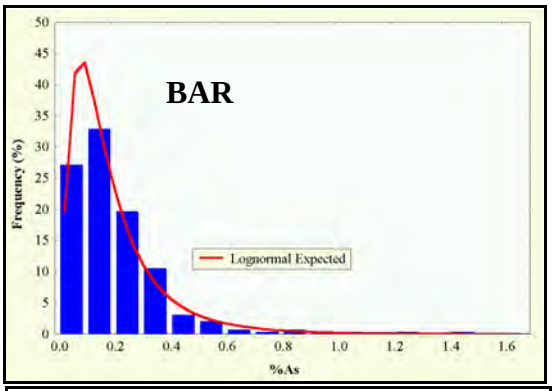

C

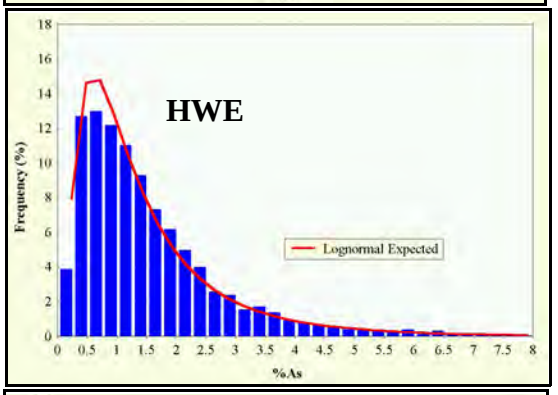

D

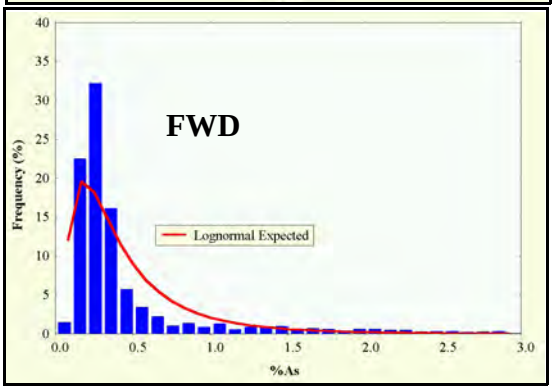

Figure 31 - %As histograms for (a) GSP, (b) BAR, (c) HWE and (d) FWD oretypes

A

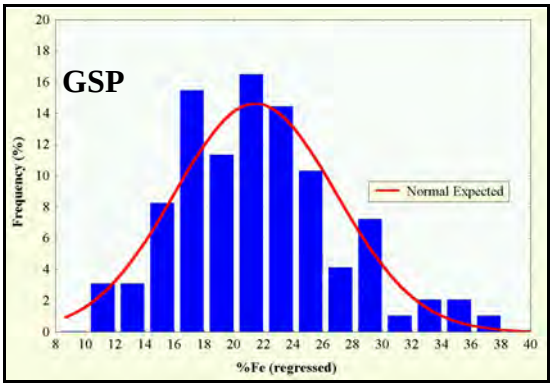

B

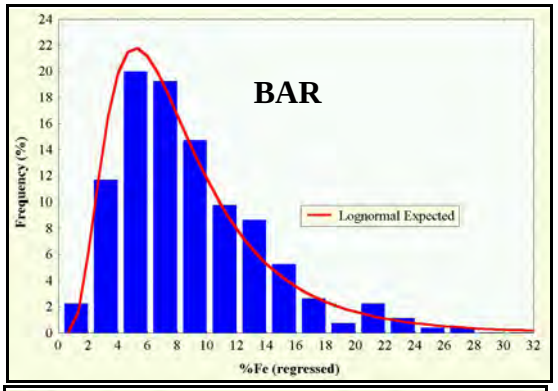

C

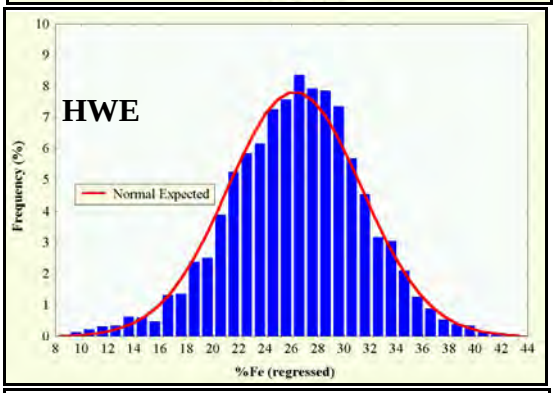

D

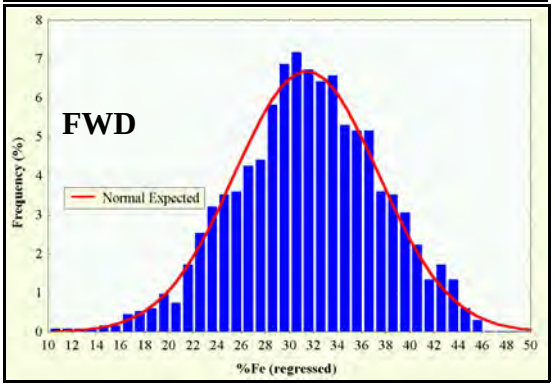

Figure 32 - %Fe (regressed) histograms for (a) GSP, (b) BAR, (c) HWE and (d) FWD oretypes

4.2.3 Statistics

Classical statistical parameters for all elements in each oretype are detailed in Table 9. This dataset of 7027 composites dates from the 1992 ore resource estimate. At the time of writing (mid-1996) this dataset had increased to 7842 composites due to minor additional 10m-spaced infill drilling and further wall chip sampling on newly established levels. Since all 20m-spaced drilling had been completed by 1992, the dataset used is considered representative. It is unfortunate that Fe has not been assayed routinely at Hellyer. The XRF Fe assay done on the wall chip samples is of dubious quality (M.T.Waters, pers.comm.) because of instrument calibration difficulties over such a large range of Fe content. For this reason, it has not been used in any serious analysis.

The mine geologists at Hellyer have used a back-calculation technique to estimate the total Fe assay from the measured S.G. and other available assays. This method assumes a constant Fe content and S.G. for each mineral, including gangue. The variability in Fe content of sphalerite and the gangue, and the variable gangue S.G. introduces error.

The author has recently found a more reliable method to estimate total Fe content from the other available assays. This involves using a 291 sample dataset from the polished section offcuts, all with quality assays, including Fe. A simple multiple linear regression (calculated using STATISTICA™ software) provides a reliable estimator (Fig.33). This formula has been applied to the 5m composite dataset (where S.G. is available, i.e. drill hole samples only).

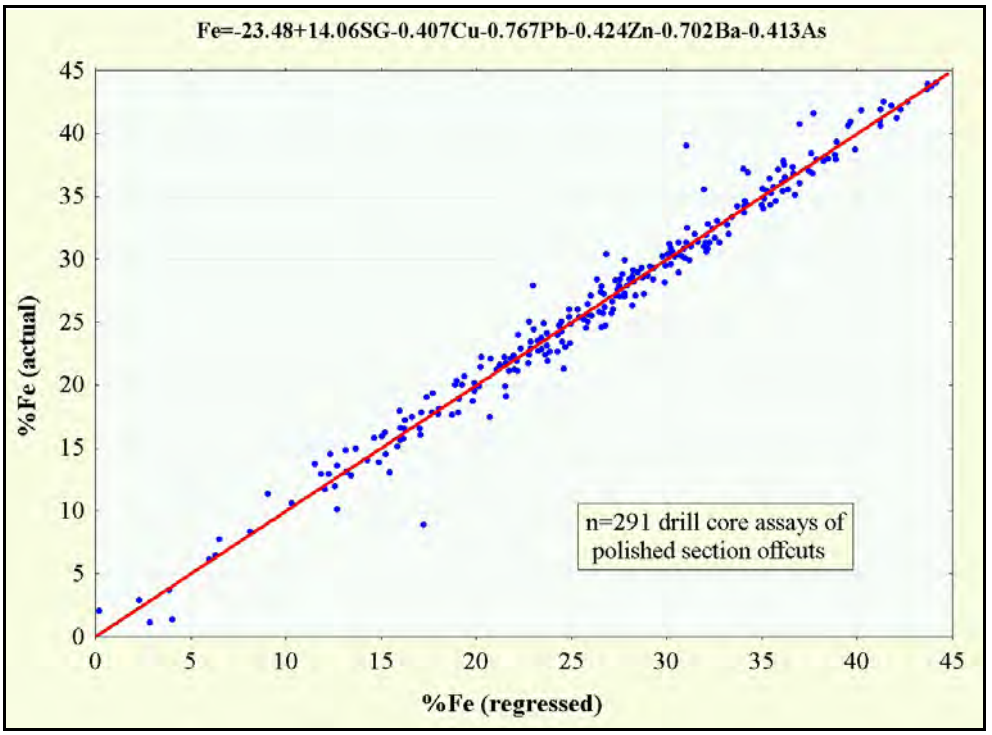

Figure 33 - %Fe regressed from (SG,Cu,Pb,Zn,Ba,As) versus actual %Fe assay

Clearly, there are significant differences in the statistical character of the four oretypes. The most marked differences between oretypes is reflected by the Ag and As assays where the FWD grade is 35-40% of the HWE grade.

Table 9 - Statistical parameters for 5m composites in GSP, BAR, HWE, FWD oretypes

(*COV coefficient of variation = standard deviation÷mean)

Element	Oretype	No.of 5m composites	Minimum	Maximum	Median	Mean	Standard deviation	C.O.V.*
S.G.	GSP	97	2.89	4.44	3.65	3.64	0.41	0.11
S.G.	BAR	265	3.25	4.65	4.25	4.18	0.29	0.07
S.G.	HWE	3182	3.11	5.08	4.60	4.56	0.25	0.05
S.G.	FWD	1341	3.29	5.05	4.66	4.61	0.24	0.05
%Cu	GSP	106	0.00	3.31	0.19	0.30	0.44	1.49
%Cu	BAR	295	0.01	1.15	0.13	0.20	0.21	1.03
%Cu	HWE	4515	0.01	2.27	0.26	0.33	0.23	0.70
%Cu	FWD	2111	0.01	3.45	0.41	0.49	0.37	0.75
%Pb	GSP	106	0.01	16.23	1.21	2.75	3.24	1.18
%Pb	BAR	295	0.00	11.67	1.95	2.62	2.29	0.87
%Pb	HWE	4515	0.12	23.90	8.00	8.17	3.15	0.39
%Pb	FWD	2111	0.11	19.09	5.36	5.76	3.36	0.58
%Zn	GSP	106	0.00	18.87	2.45	4.36	4.82	1.11
%Zn	BAR	295	0.01	19.97	3.15	4.15	3.59	0.87
%Zn	HWE	4515	0.20	34.14	15.28	15.50	4.79	0.31
%Zn	FWD	2111	0.15	31.20	12.10	11.71	5.42	0.46
ppm Ag	GSP	106	10	310	93	105	71	0.67
ppm Ag	BAR	295	4	380	85	101	68	0.67
ppm Ag	HWE	4515	0	1989	211	218	106	0.48
ppm Ag	FWD	2111	5	651	71	84	58	0.69
ppm Au	GSP	97	0.55	13.16	2.72	3.14	1.85	0.59
ppm Au	BAR	265	0.16	7.33	1.62	1.77	0.99	0.56
ppm Au	HWE	3182	0.20	28.12	2.26	2.79	1.93	0.69
ppm Au	FWD	1341	0.11	8.29	1.41	1.69	1.04	0.62
%Ba	GSP	106	0.00	19.37	0.50	2.77	4.41	1.59
%Ba	BAR	295	0.00	57.29	32.61	32.13	11.13	0.35
%Ba	HWE	4515	0.00	37.72	0.00	0.94	3.13	3.31
%Ba	FWD	2111	0.00	34.69	0.00	0.96	2.54	2.66
%As	GSP	106	0.06	3.65	0.39	0.51	0.45	0.89
%As	BAR	295	0.00	1.47	0.16	0.20	0.18	0.87
%As	HWE	4514	0.00	10.12	1.20	1.52	1.23	0.81
%As	FWD	2109	0.05	6.25	0.28	0.54	0.72	1.34
%Fe	GSP	97	11.27	36.18	21.17	21.45	5.45	0.25
%Fe	BAR	265	0.00	27.12	7.54	8.55	4.83	0.56
%Fe	HWE	3181	6.18	41.65	26.43	26.25	5.09	0.19
%Fe	FWD	1339	10.90	45.57	31.51	31.42	5.96	0.19

In terms of average variability, the following C.O.V. sequence applies:

Least variable	S.G.	0.05
	Fe	0.21
	Zn	0.39
	Pb	0.48
	Ag	0.55
	Au	0.66
	Cu	0.74
	As	0.97
Most variable	Ba	2.96

We would normally expect the most common mineral to have the lowest variability. The relatively low variability of the Ag assay (given the low tetrahedrite content) suggests a low-level background homogeneity included in another mineral (pyrite?). The same could be interpreted for Au. Conversely, the relatively high variability of the Ba assay (given the moderate barite content) suggests mixed populations producing a particular statistical sampling problem, possibly related to veining or clustering.

4.2.4 Correlation

Correlation matrices and cluster analysis are useful tools to investigate inter-relationships between elements (and therefore minerals). Tables 10-13 show the Pearson correlation coefficients for each deposit oretype with Table 14 showing by comparison the equivalent matrix for the footwall stringer zone. Correlation **coefficients shown in bold are significant at the 95% level.** Figures 34-38 show the corresponding cluster analysis "icicle" dendrograms.

Table 10 - Correlation matrix for the siliceous cap oretype (GSP), n=106

	Cu	Pb	Zn	Ag	Au	Ba	As	Fe
Cu	1.00							
Pb	0.16	1.00						
Zn	0.16	**0.92**	1.00					
Ag	0.07	**0.68**	**0.64**	1.00				
Au	0.09	-0.15	-0.08	0.10	1.00			
Ba	-0.11	0.13	0.08	0.06	-0.19	1.00		
As	-0.10	-0.04	0.02	0.07	0.16	**-0.21**	1.00	
Fe	0.01	**-0.34**	**-0.32**	-0.08	**0.39**	**-0.45**	**0.39**	1.00

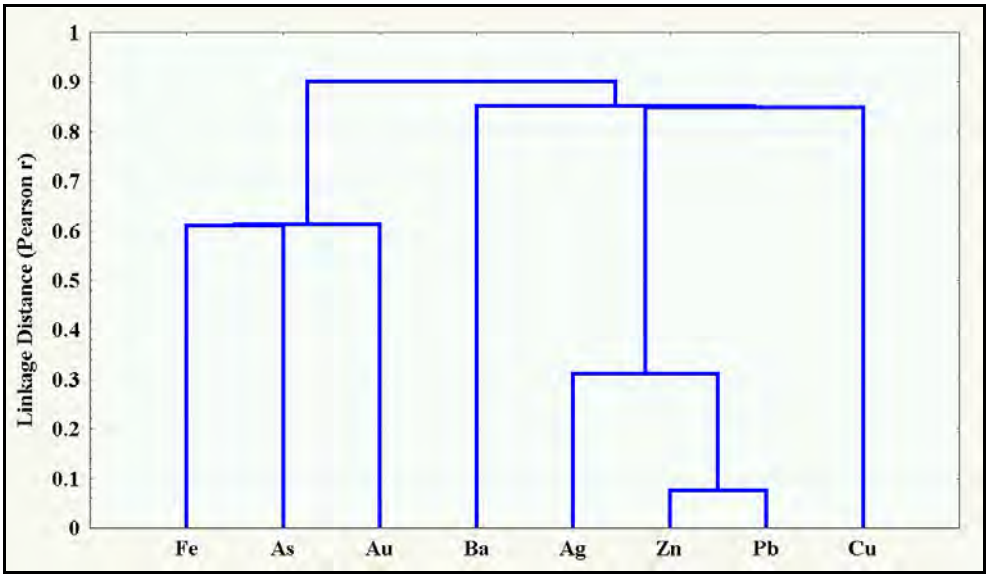

Figure 34 - Cluster analysis dendrogram for the siliceous cap oretype (GSP)

The GSP oretype (Table 10, Fig. 34) shows overall weak correlation between metals, apart from a very strong positive relationship for Pb-Zn-Ag. This may be an indication that these metals coprecipitated and have suffered very little remobilisation since. The moderate positive correlation between Fe-Au-As also suggests an association that is not apparent in the massive sulphide oretypes.

Table 11 - Correlation matrix for the baritic cap oretype (BAR), n=295

	Cu	Pb	Zn	Ag	Au	Ba	As	Fe
Cu	1.00							
Pb	**0.75**	1.00						
Zn	**0.79**	**0.95**	1.00					
Ag	**0.44**	**0.72**	**0.68**	1.00				
Au	**0.26**	**0.35**	**0.41**	**0.36**	1.00			
Ba	**-0.43**	**-0.55**	**-0.58**	**-0.43**	**-0.37**	1.00		
As	**0.14**	**0.28**	**0.32**	**0.23**	**0.46**	**-0.39**	1.00	
Fe	**0.32**	**0.44**	**0.46**	**0.39**	**0.43**	**-0.85**	**0.50**	1.00

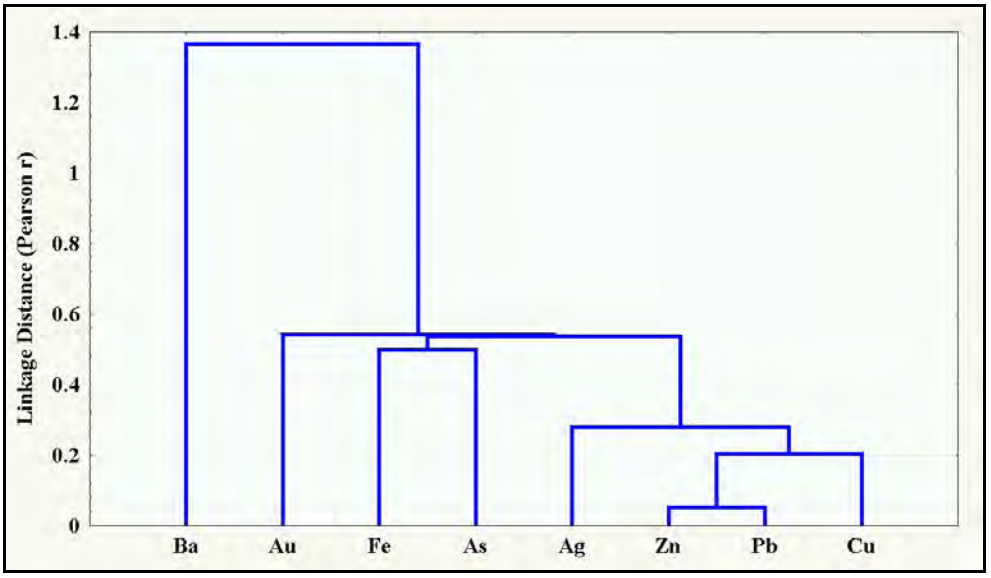

Figure 35 - Cluster analysis dendrogram for the baritic cap oretype (BAR)

The BAR oretype (Table 11, Fig. 35) matrix is strongly influenced by the "constant sum effect" because one mineral (barite) accounts for about 60% of the rock. Hence, all metals have a negative correlation with Ba. There is however, a strong positive correlation between Cu-Pb-Zn-Ag; similar to the GSP oretype, but including Cu. Fe shows a moderate positive correlation with all metals except Ba.

Table 12 - Correlation coefficients for the hangingwall enriched oretype (HWE), n=4515

	Cu	Pb	Zn	Ag	Au	Ba	As	Fe
Cu	1.00							
Pb	**0.33**	1.00						
Zn	**0.29**	**0.68**	1.00					
Ag	**0.08**	**0.56**	**0.44**	1.00				
Au	**0.26**	**0.21**	**0.06**	**0.27**	1.00			
Ba	**0.13**	**-0.07**	**-0.17**	**-0.14**	**0.09**	1.00		
As	**-0.21**	**-0.19**	**-0.08**	**0.11**	**0.10**	**-0.18**	1.00	
Fe	**-0.29**	**-0.53**	**-0.49**	**-0.32**	**-0.15**	**-0.41**	**0.20**	1.00

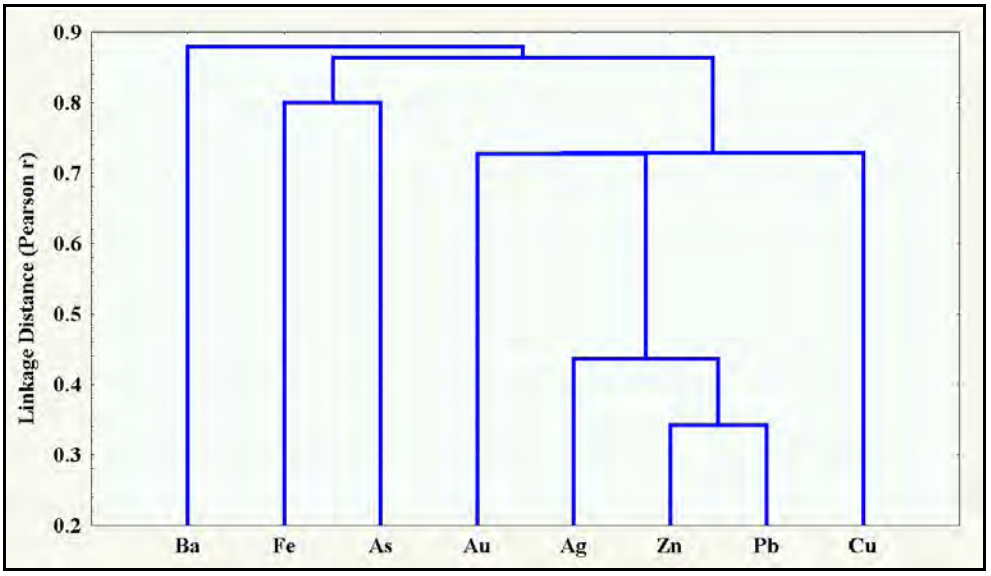

Figure 36 - Cluster analysis dendrogram for the hangingwall enriched oretype (HWE)

The HWE oretype (Table 12, Fig. 36) is also influenced by the "constant sum effect" because pyrite (and hence Fe) is such a dominant component of the massive sulphide. A moderate positive correlation is evident for Pb-Zn-Ag. Ag-Au-As also show a weak association. Ba is notably weakly negatively correlated with Pb-Zn-Ag suggesting quite separate deposition processes.

Table 13 - Correlation matrix for the footwall depleted oretype (FWD), n=2111

	Cu	Pb	Zn	Ag	Au	Ba	As	Fe
Cu	1.00							
Pb	0.03	1.00						
Zn	-0.01	**0.72**	1.00					
Ag	**0.08**	**0.44**	**0.37**	1.00				
Au	**-0.06**	**0.39**	**0.32**	**0.55**	1.00			
Ba	**-0.05**	-0.00	-0.03	0.03	**0.14**	1.00		
As	**-0.18**	**0.08**	**0.15**	**0.47**	**0.38**	-0.03	1.00	
Fe	0.00	**-0.70**	**-0.68**	**-0.35**	**-0.35**	**-0.34**	**-0.19**	1.00

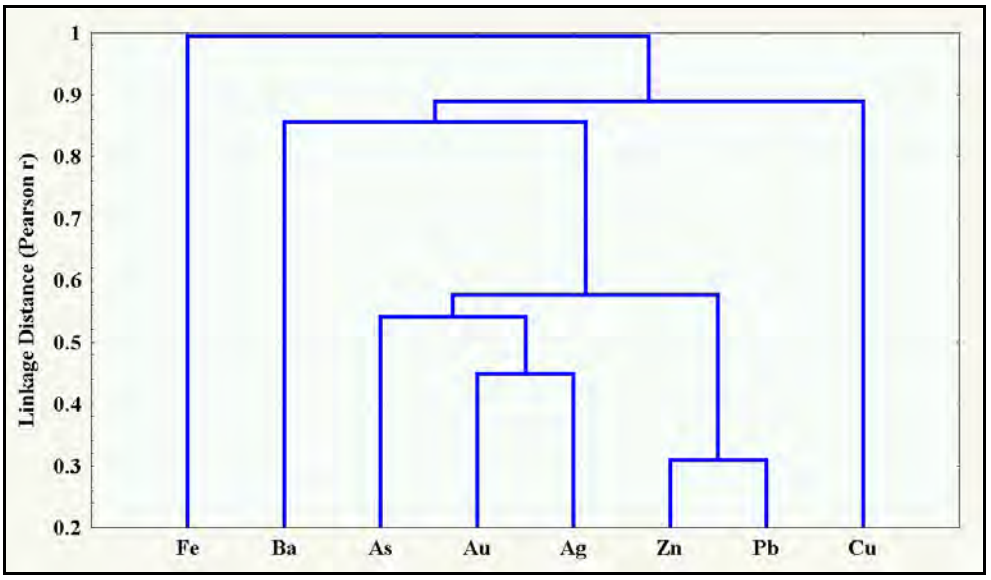

Figure 37 - Cluster analysis dendrogram for the footwall depleted oretype (FWD)

The FWD oretype (Table 13, Fig. 37) shows the weakest correlations of all the oretypes, suggesting the greatest superimposition of depositional processes. Pb-Zn however are obviously associated, as are Ag-Au-As. Again the "constant sum effect" gives consistent negative correlations between Fe and all other metals, apart from Cu.

Table 14 - Correlation matrix for the Hellyer footwall stringer zone, samples >=0.1%Zn only (STZ), n=2096

	Cu	Pb	Zn	Ag	Au	Ba	As	Fe
Cu	1.00							
Pb	**0.31**	1.00						
Zn	**0.19**	**0.78**	1.00					
Ag	**0.44**	**0.74**	**0.56**	1.00				
Au	**0.15**	**0.43**	**0.47**	**0.52**	1.00			
Ba	**0.14**	**0.21**	**0.15**	**0.19**	**0.31**	1.00		
As	0.02	**0.26**	**0.37**	**0.36**	**0.57**	-0.00	1.00	
Fe	**0.14**	**0.06**	**0.11**	**0.09**	**0.28**	**-0.05**	**0.06**	1.00

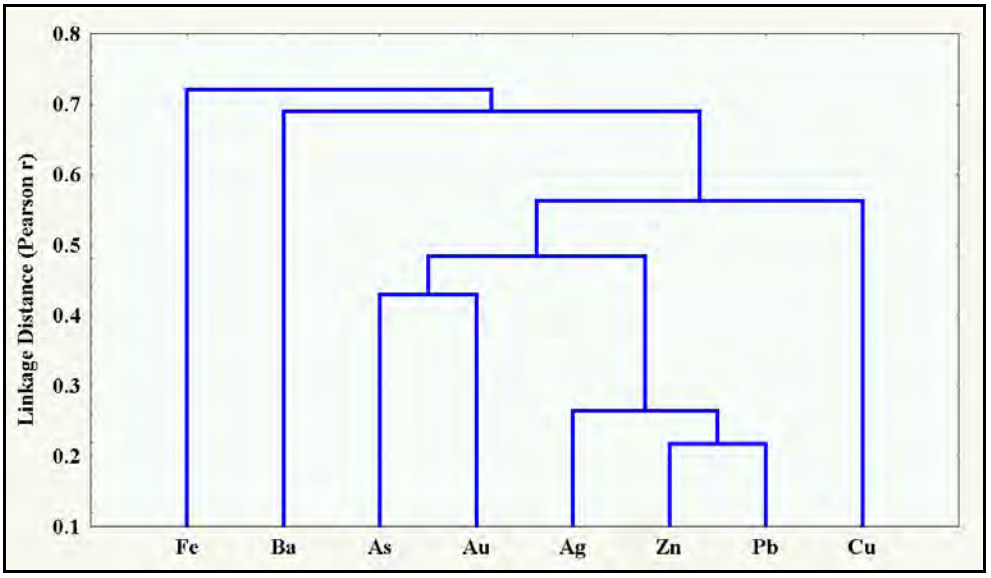

Figure 38 - Cluster analysis dendrogram for the Hellyer stringer zone (STZ)

In comparison, the stringer zone (STZ) (Table 14, Fig. 38) correlations are stronger than the massive sulphide above, and bear some similarity to the baritic cap associations. The Pb-Zn-Ag association is present, and there is a strong Ag-Au-As correlation.

Zonation in metal correlation can also be demonstrated by calculating correlation coefficients in stratigraphic (SN) layers (Fig. 39).

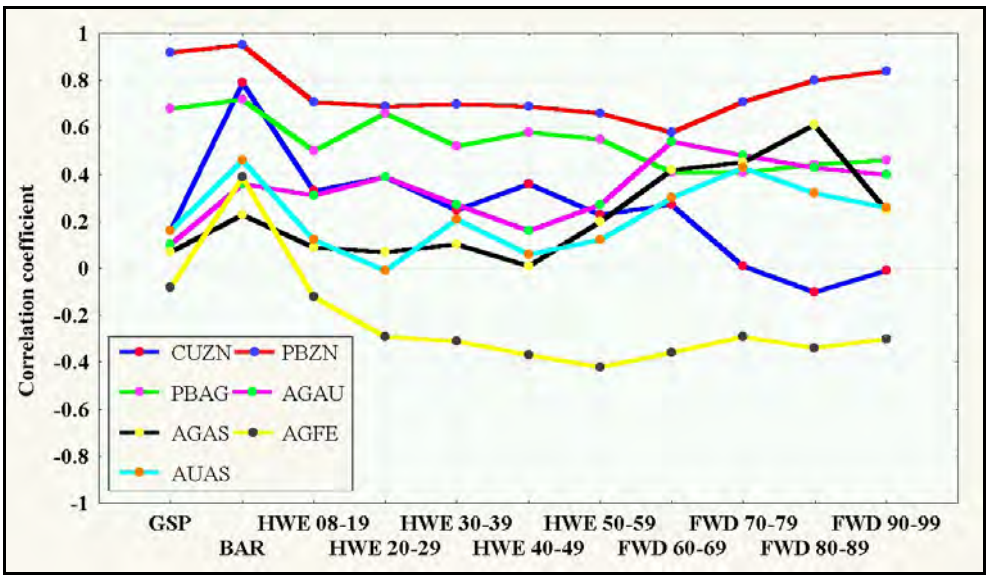

Figure 39 - Variation of correlation coefficient with stratigraphic position (SN)

The striking difference in correlations between the baritic cap and the other oretypes is highlighted in Figure 39. Note also that within the massive sulphide oretypes trends in correlation from layer to layer are gradual and not stepped. Nevertheless, most metal pair correlations show a real change in trend at approximately SN60. Remember (from section 3.5.2), the arbitrary SN60 boundary was originally defined as the 100ppm Ag contour; to conveniently divide the massive sulphide into two, macroscopically different oretypes. Figure 39 confirms that this boundary also separates two statistical populations.

Scattergrams of the 5m composite metal pairs depicted in Figure 39 are shown in Figures 40-46. Each oretype has been coloured individually to highlight some quite different relationships.

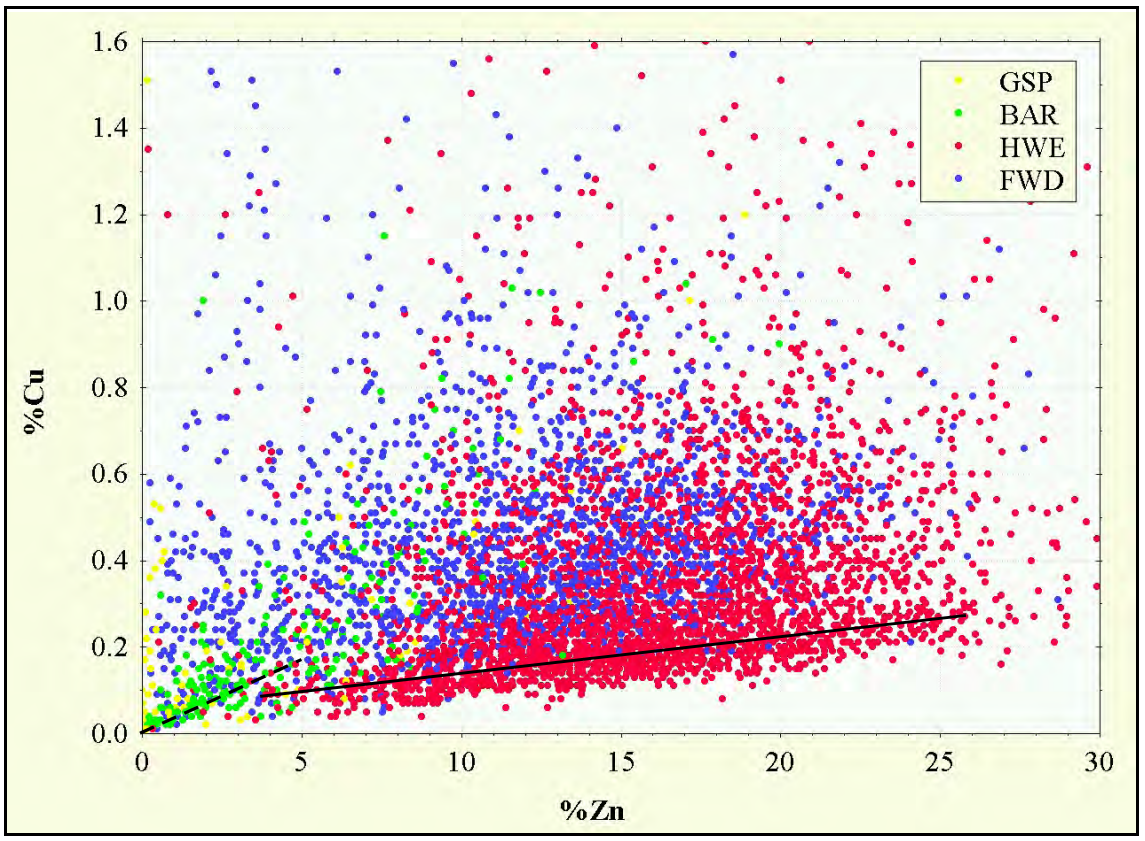

Figure 40 - Scattergram for Zn-Cu

Whilst GSP (Fig. 40) shows considerable scatter in Cu and Zn, a trend with a ratio of ~0.035%Cu per %Zn (Fig. 40 dashed line) is clear in the low grade portions of the BAR oretype. Within the HWE, a trend appears in the lower grade Cu with a ratio of ~0.01 (Fig. 40 solid line), roughly equivalent to ~0.6%Cu (or ~2% chalcopyrite) in sphalerite. This probably represents the "chalcopyrite disease" (see discussion in section 5.4.2) that is common throughout the HWE oretype. The FWD shows wide scatter with no trend.

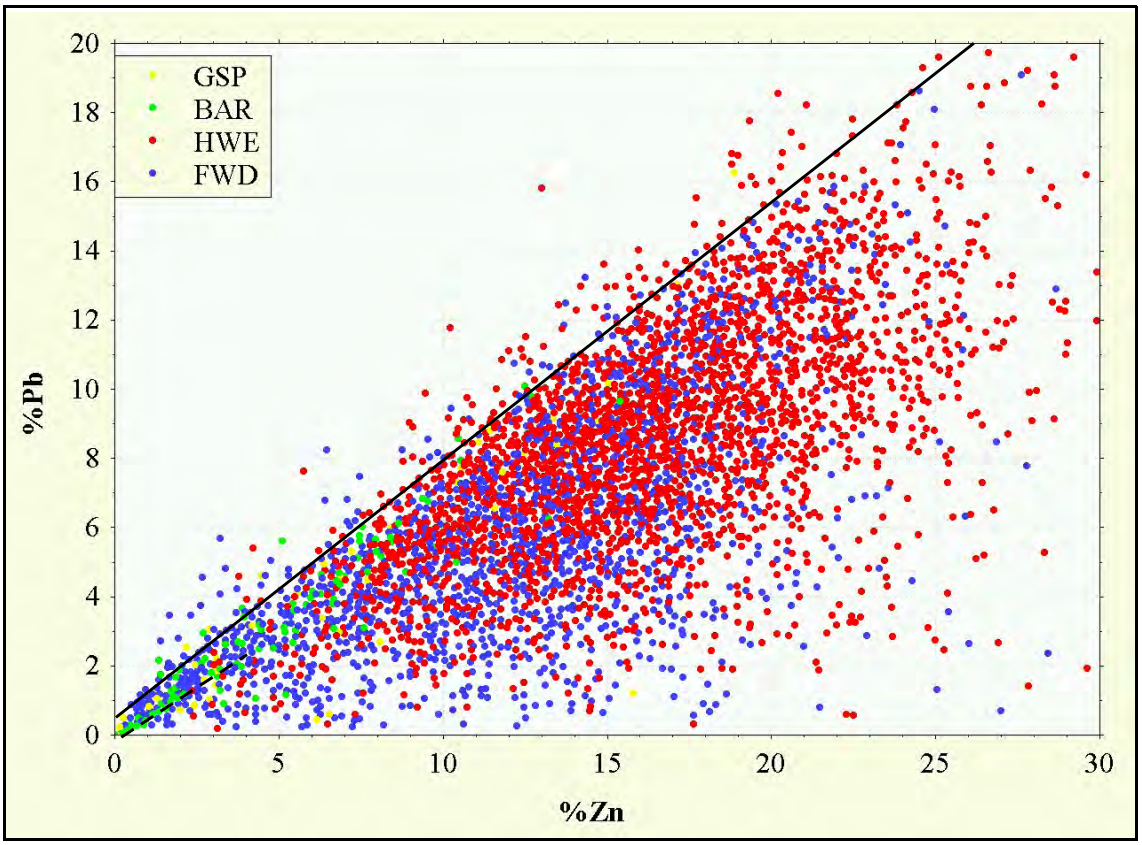

Figure 41 - Scattergram for Zn-Pb

All oretypes follow the same trend in Zn and Pb with a limiting ratio of ~0.8%Pb per 1%Zn (Fig.41 solid line). This suggests a systematic Pb saturation control. There are remarkably few samples above this "Pb saturation line" which indicates there was only very limited preferential Devonian remobilisation of galena. In the BAR oretype below 2.5%Zn, the trend is remarkably consistent (Fig. 41 dashed line). There is considerable scatter below this limiting ratio particularly in the massive sulphide oretypes.

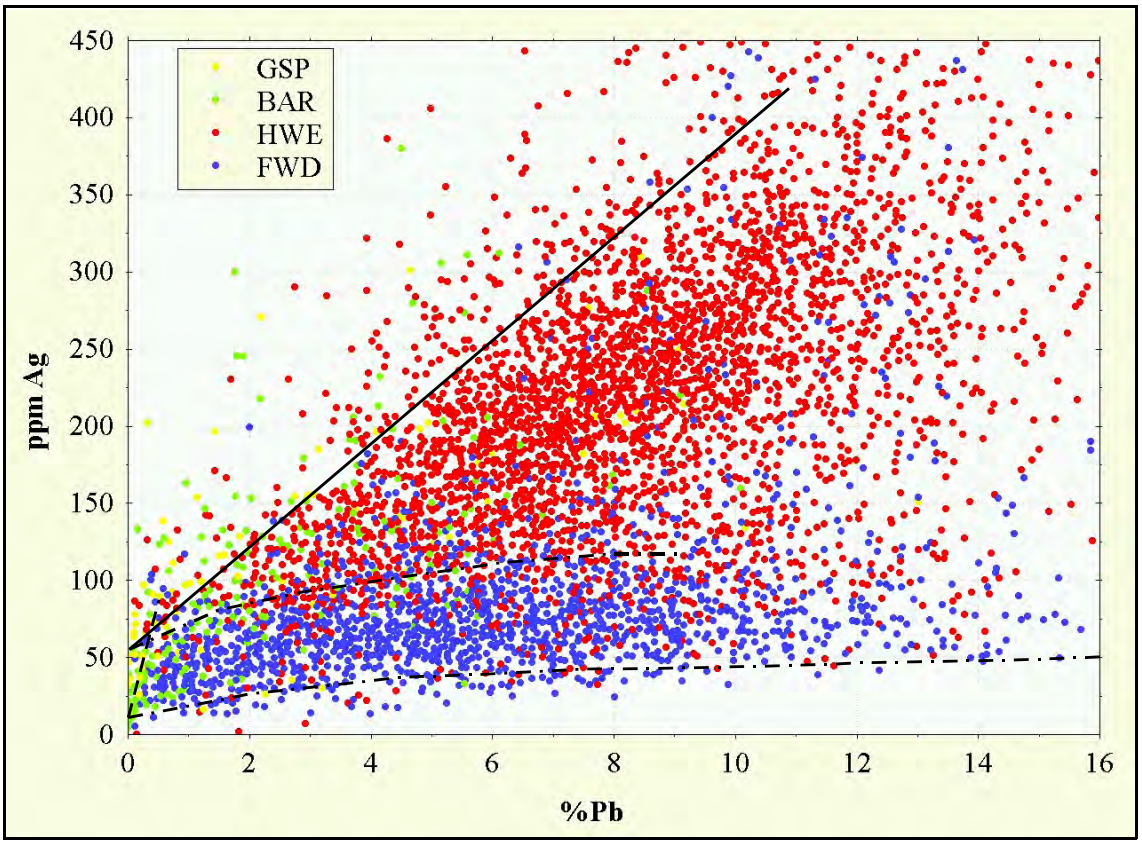

Figure 42 - Scattergram for Pb-Ag

Within the GSP and BAR oretypes for Pb and Ag, a small, tight trend (~200 ppm Ag per 1% Pb) exists in the area below ~0.5%Pb (Fig. 42, dashed line). Within the HWE, a limiting ratio of ~40 ppm Ag per 1% Pb (roughly equivalent to ~3500 ppm Ag in galena) trends back to an intercept of ~60 ppm on the y-axis (Fig. 42, solid line). This feature, together with a constant 50-100 ppm Ag in the FWD oretype (Fig.42, area between dash-dot lines), suggests a dominant mineral (pyrite?) consistently contains ~60 ppm Ag, and any excess Ag is closely related to Pb.

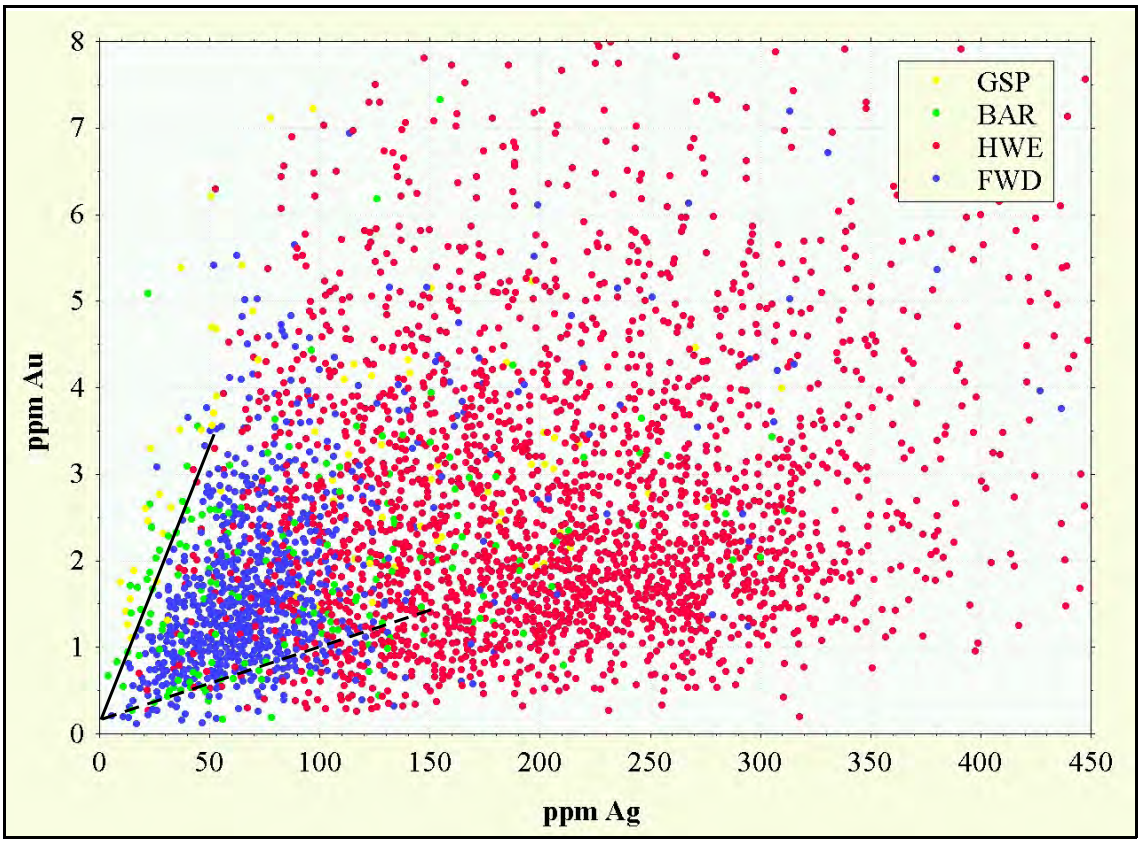

Figure 43 - Scattergram for Ag-Au

There is widespread scatter in the Ag-Au data apart from two indistinct trends in the BAR oretype: one steep gradient (~7.5 ppm Au per 100 ppm Ag; Fig. 43, solid line) and a much flatter gradient (~1 ppm Au per 100 ppm Ag; Fig. 43, dashed line). All samples lie scattered roughly between these two limiting ratios.

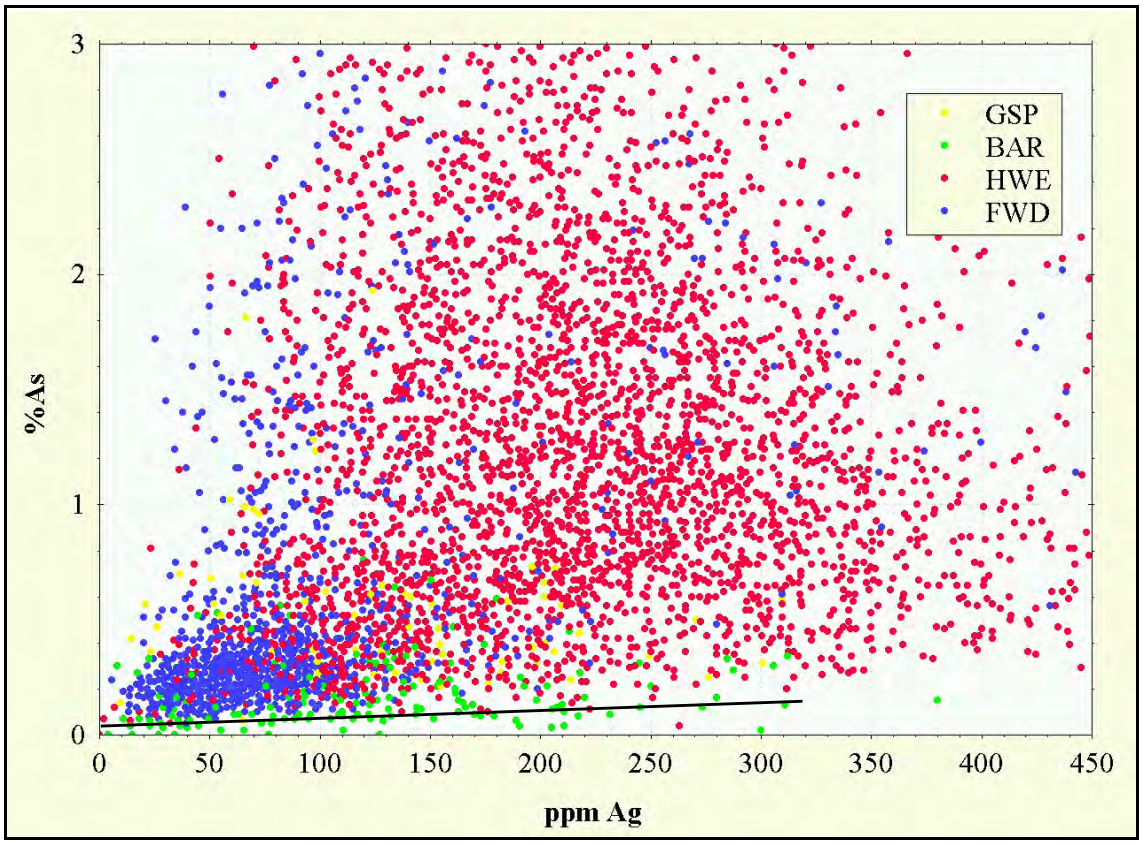

Figure 44 - Scattergram for Ag-As

Within the GSP oretype there is general scatter in Ag and As, but there is a distinct flat trend for the BAR (~0.1%As per 100 ppm Ag; Fig. 44, solid line). This trend forms a clear lower limiting ratio for all other samples. The HWE is total random scatter and the FWD oretype forms a tight cluster at low levels.

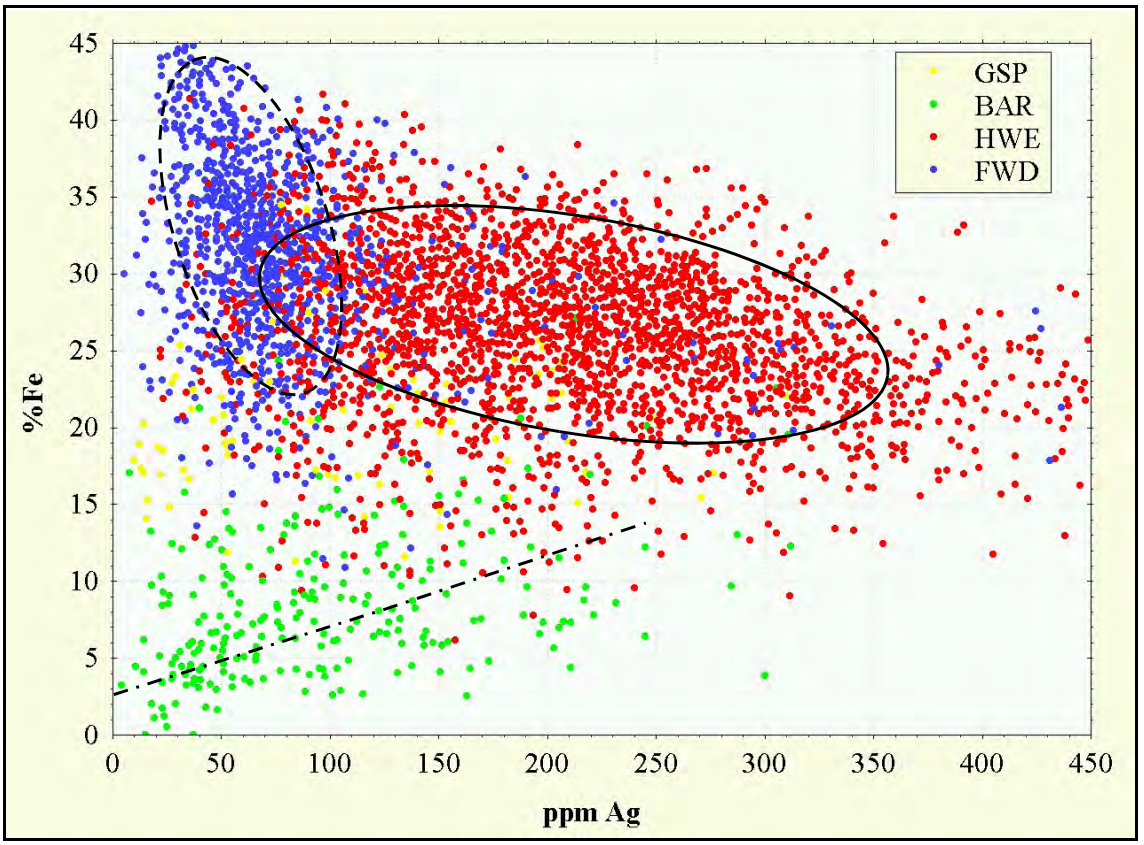

Figure 45 - Scattergram for Ag-Fe

The Ag-Fe data form an interesting plot (Fig. 45), despite the strong "constant sum effect" of dominant pyrite producing negative gradients in the massive sulphide. Apart from the GSP oretype which has random scatter in Ag and Fe, the other oretypes form obvious clusters (Fig. 45, ellipses) with only minimal overlap. Within the BAR, a broad positive gradient occurs (Fig. 45, dash-dot line), roughly equivalent to ~800ppm Ag in pure pyrite. The author is guarded about over-interpreting negative gradient trends in a system overshadowed by dominant pyrite.

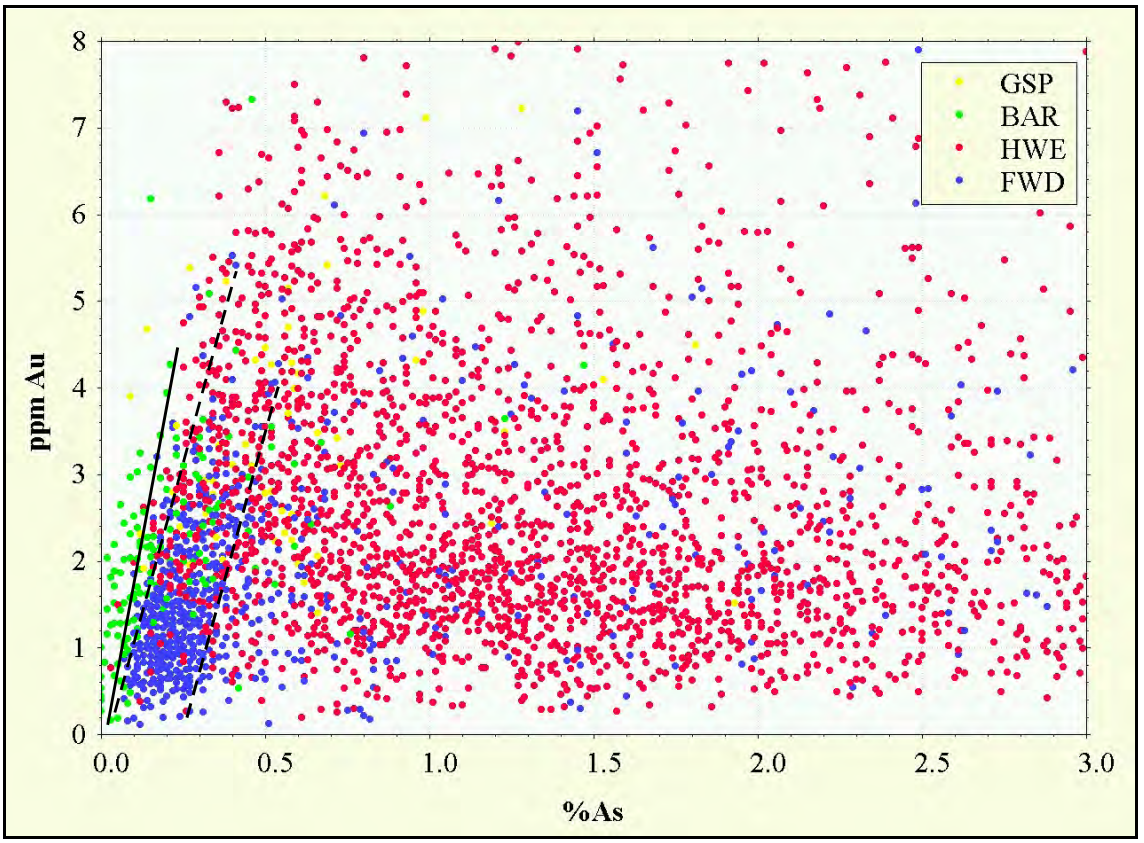

Figure 46 - Scattergram for As-Au

The GSP shows a broad steep gradient in As and Au (Fig. 46) whilst the BAR oretype forms a similar but tight, steep gradient (~15 ppm Au per 1% As, or ~650 ppm for arsenopyrite; Fig. 46, solid line). The HWE oretype shows only random scatter but has an upper limiting gradient coinciding with the BAR trend. FWD is tightly clustered at low levels (Fig. 46, between two dashed lines) and has a very sharp upper limiting ratio of ~13 ppm Au per 1% As.

4.3 3-D modelling technique

To enable an effective spatial analysis of the metal distribution at Hellyer, an interpolated 3D model has been used. The following description is an update of that provided by McArthur (1988) and McArthur and Kuipers (1990).

The modelling process at Hellyer has been designed specifically to cater for those deposit characteristics that are interpreted to control both metal content and continuity:

- sharp contacts, very little lensing
- folded and faulted contacts
- defined oretypes
- complex non-planar continuity
- stratigraphic zonation

The most important requirement was to spatially define the location of contacts. This was done by specifying for each drill hole, the precise downhole depths of the hangingwall and footwall contacts. 1:500 structure contour plans of both the hangingwall and footwall were then hand-drawn based on the computer-plotted hole intersection data plus those contacts mapped in development. Dipping faults were also structure contoured. After digitising, a triangular tessellated 3D wireframe was built using DATAMINE™ software[1]. This closed volume was then filled with blocks or cells, nominally 5m E-W, 10m N-S and 5m RL, with smaller subcells created near the contacts to more accurately reflect the local shape. Thus, the volume and 3D location of the defined deposit were established.

Oretype boundaries were interpreted on 10m-spaced cross sections from the available drill hole data and development mapping. These were digitised with their appropriate stratigraphic number (SN) attached. These lines of continuity provided the basis for mapping both the 5m assay composites and the model cells into the stratigraphic (SN)

[1] This process is now done quite differently using screen-based GUIDE™ software. The description provided in this thesis applies to the method used up to 1992 that generated the particular model used in this research for all spatial analysis.

space. Each composite or cell was ascribed an SN according to the distance from its midpoint to the nearest cross-section oretype boundaries above and below. For example, a drillhole composite halfway between the barite contact (SN8) and the base of the enriched zone (SN60) would have an SN={8+(60-8)*0.5}=34. Similarly, a model cell ¾ of the way between the base of the enriched zone (SN60) and the footwall (SN99) would have an SN={60+(99-60)*0.75}=89. Once this process was complete (some minor hand editing required in faulted areas), all samples and all model cells were known in a 4-dimensional space (X,Y,Z,SN).

The grade interpolation method used to estimate a grade for each model cell was ordinary kriging (David, 1977). Kriging is now widely accepted by the mining industry as the most optimal estimation technique available (provided the user makes proper use of geology). To estimate the grade for any given model cell, the kriging method selects a set of nearby samples and ascribes optimal weights to those samples. The weights calculated are optimal because the linear kriging equations are so designed to result in minimum estimation error. Inputs to the set of kriging equations come from the variogram, a function that shows how variance between two samples is dependent on their distance apart. Variogram functions (generally cubic equations) are modelled from experimental data measured in various directions from the actual samples. Various directions are used to account for continuity anisotropy, e.g. continuity is generally maximum along strike and minimum across dip.

At Hellyer, grade continuity is clearly parallel to the nearest oretype boundary (McArthur, 1988). Calculation of variograms within these folded and faulted continuity layers required special techniques. After much experimentation, it was concluded that the most practical method was to calculate isotropic (direction independent) variograms **within** stratigraphic layers as defined by the SN. The error made in substituting straight line distance for the actual fold-parallel curved stratigraphic distance is not considered significant because folds in continuity have open, low-amplitude geometry and long distance variances are not crucial in variogram construction.

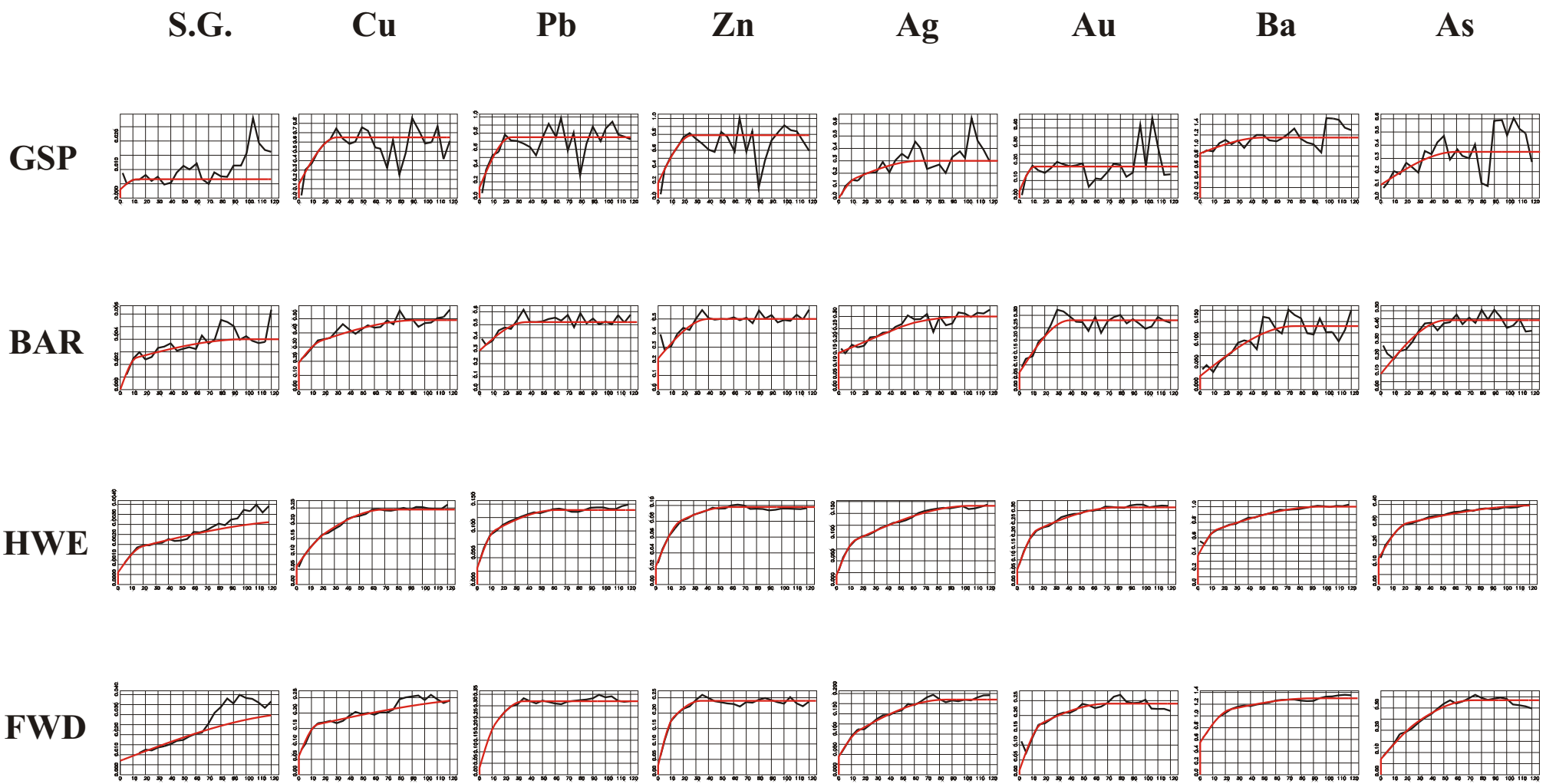

Figure 47

Variogram models (1992) for all assayed elements for each Hellyer oretype. Vertical axis is relative variogram value, horizontal axis is distance in metres between samples. Black solid line is experimental data measured from the 5m composites and red solid line is the cubic model. (experimental data for the GSP and BAR oretypes are erratic because of the reduced number of samples)

Eleven stratigraphic layers were chosen for variogram calculation (Table 15).

Table 15 - Stratigraphic layers for variogram calculation

ORETYPE	STRATIGRAPHY
GSP	SN00-SN01
BAR	SN02-SN07
HWE	SN08-SN19
HWE	SN20-SN29
HWE	SN30-SN39
HWE	SN40-SN49
HWE	SN50-SN59
FWD	SN60-SN69
FWD	SN70-SN79
FWD	SN80-SN89
FWD	SN90-SN99

After variogram calculation, it was found that all the HWE variograms were very similar, as were all the FWD variograms. These were then averaged, so that each oretype had one variogram for each element (Fig.47). The similarities and differences between metals as seen in the variograms, is inevitably connected to primary depositional relationships, i.e. metals coprecipitating in space and time should result in very similar variogram shape (*aside:* the author notes that this a subject that deserves research to input more geology into geostatistics). Take for example, the variograms for Cu in the HWE and FWD oretypes. The FWD model shows variability at short range (note inflexion at 13m), whilst the HWE model has very little evidence for any short range structure. Variability at short range suggests local "nuggetty" concentrations ~10m across; most probably due to remobilisation. The HWE Cu variogram suggests a more homogenous distribution. The opposite situation occurs with the As variograms. The HWE shows short range structure (inflexion at 20m), whilst the FWD is more homogenous.

Kriging of S.G., Cu, Pb, Zn, Ag, Au, Ba and As was performed within the 11 stratigraphic layers by using the nearest 20 samples from only within the layer or the closer halves of the adjacent layers (excepting the GSP and BAR oretypes which were treated individually). Some 38,652 cells were estimated using the 7027 sample composites. The kriged estimates were transformed in many different ways, (e.g. ratios, Zn number), to further investigate spatial relationships inside the deposit.

For display purposes, 60m-spaced cross-sectional profiles through the kriged model were infilled with smaller 1m square cells, to allow colouring between grade contours.

4.4 Zonation observed for metals and metal ratios

4.4.1 Stratigraphic across-dip zonation

Stratigraphic zonation (hangingwall to footwall) zonation is best investigated using the 5m composite dataset. Figs.48-56 plot average grade of each SN unitary layer.

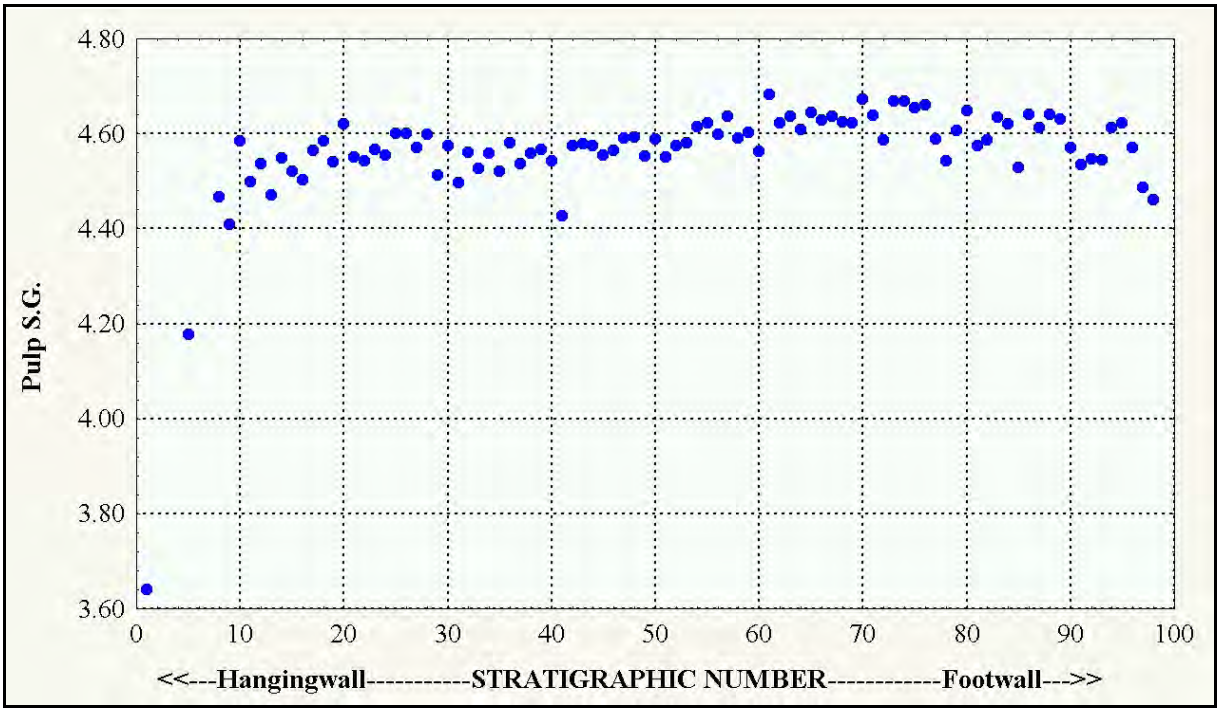

Figure 48 - Average 5m composite S.G. versus stratigraphic position (SN)

The trend for S.G. (Fig. 48) is obviously lowest in the hangingwall caps due to increased gangue and much lower pyrite content. Within the massive sulphide, the trend is very flat apart from:

a) a clear step up at SN55-60 (increase in pyrite)

b) decrease at SN8-16 (gangue increase)

c) decrease at SN90-99 (gangue increase)

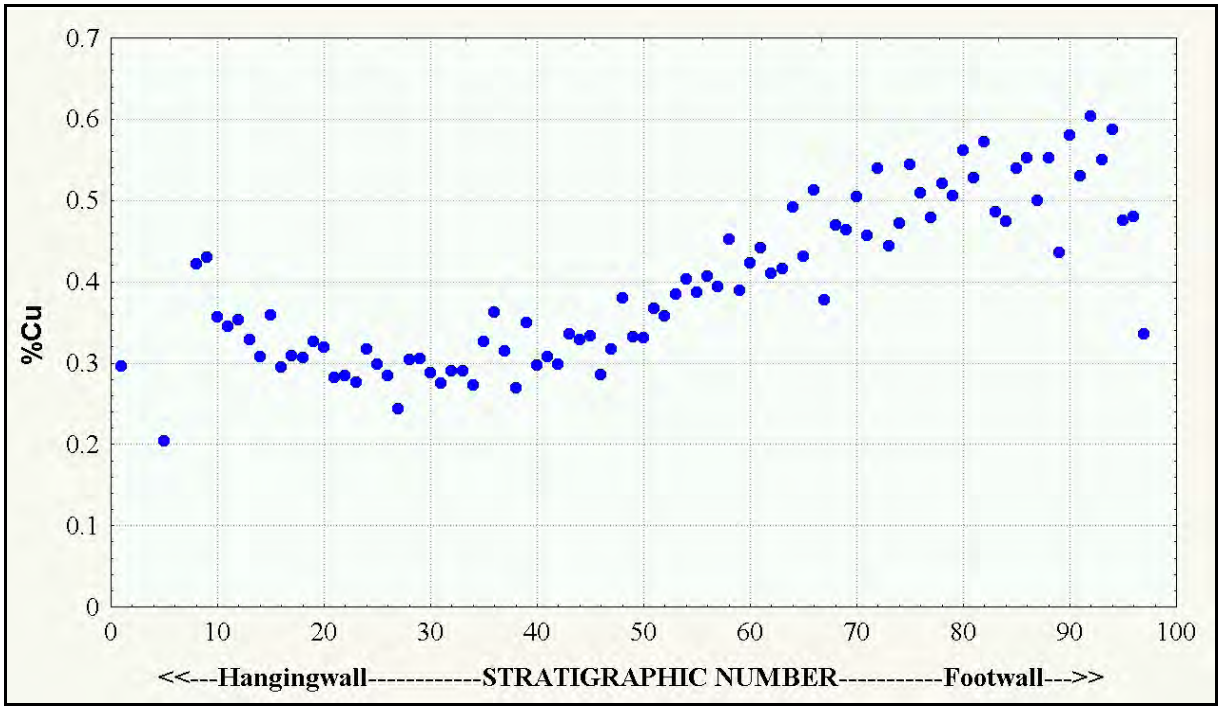

Figure 49 - Average 5m composite %Cu versus stratigraphic position (SN)

The Cu trend (Fig. 49) shows a smooth parabolic curve with a minimum at SN30. Maximum values are at SN93 just above the footwall with a secondary maximum right at the massive sulphide hangingwall. There is no apparent step at SN60 as seen for S.G. The baritic cap is exceptionally low in Cu grade.

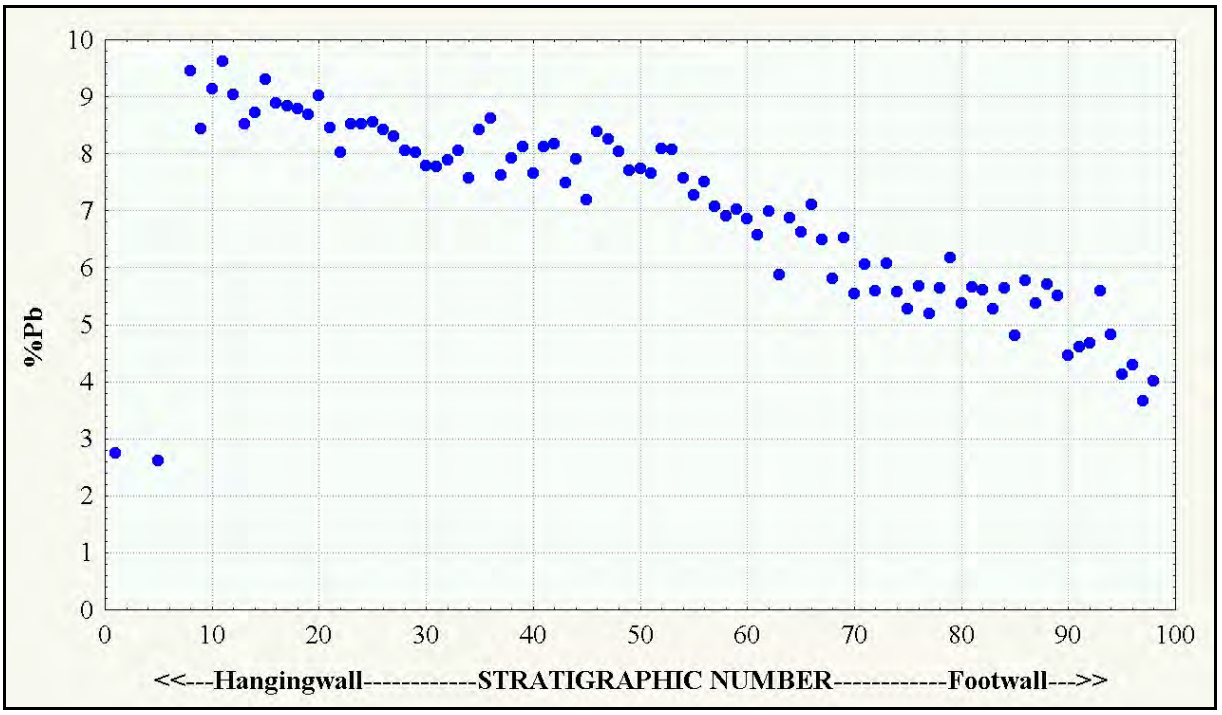

Figure 50 - Average 5m composite %Pb versus stratigraphic position (SN)

The Pb trend (Fig. 50) shows a regular decline from hangingwall to footwall, apart from a 0.5%Pb step up at SN35 and a slightly steeper gradient below SN55. The siliceous and baritic caps both have a low Pb grade, well below grades in the massive sulphide.

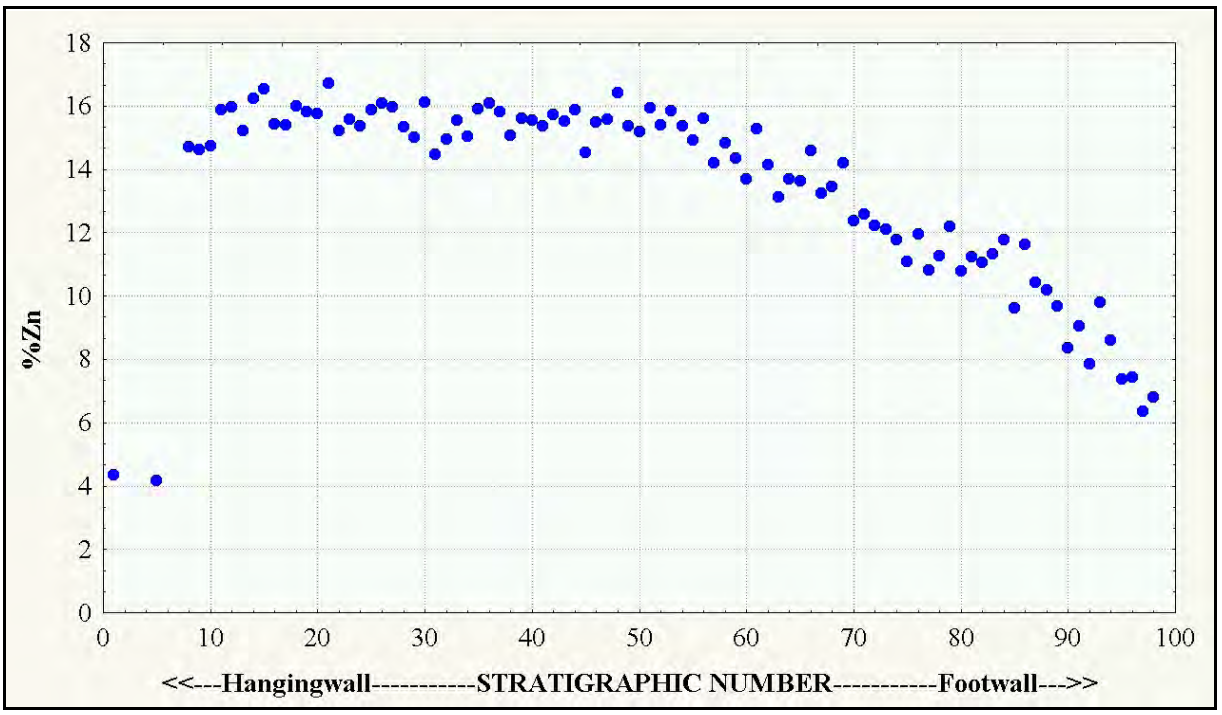

Figure 51 - Average 5m composite %Zn versus stratigraphic position (SN)

The Zn trend (Fig. 51) within the massive sulphide is extremely flat from SN11 to SN55 but declines steadily towards the footwall. There is a noticeable decrease in Zn grade right at the hangingwall which was not apparent for Pb. Similarly to Pb, the siliceous and baritic caps both have low Zn levels well below the grades for the massive sulphide.

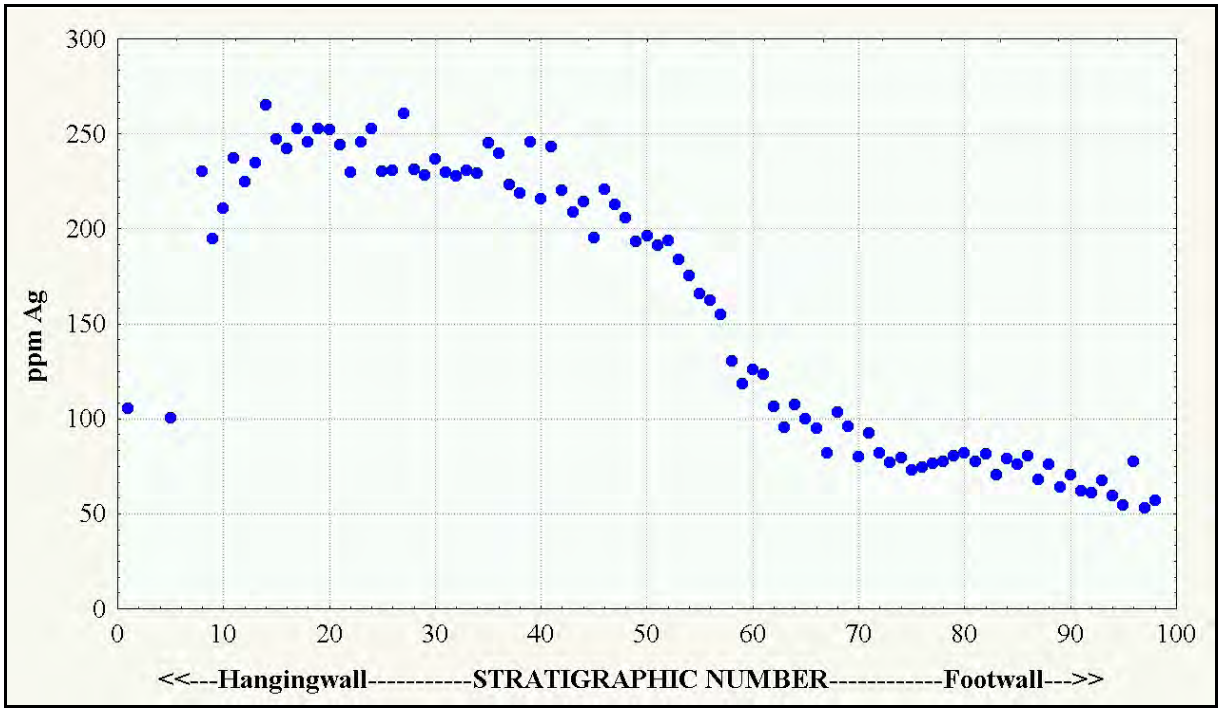

Figure 52 - Average 5m composite ppm Ag versus stratigraphic position (SN)

The Ag trend (Fig. 52), together with As (Fig. 55) shows the most zonation. This is to be expected since the stratigraphic number system is partially defined using the Ag grade (SN60 defined at the 100ppm Ag contour). The maximum occurs at SN20, with a small decrease above towards the hangingwall and below to SN45. There is a steep steady decline SN45-SN65 with a shallower decline below to the footwall. The average grade at the footwall contact is less than ¼ of the peak value just below the hangingwall. The siliceous and baritic caps both have low Ag grades, but in contrast to Pb and Zn (Figs. 50,51), the Ag grade exceeds that seen in the FWD.

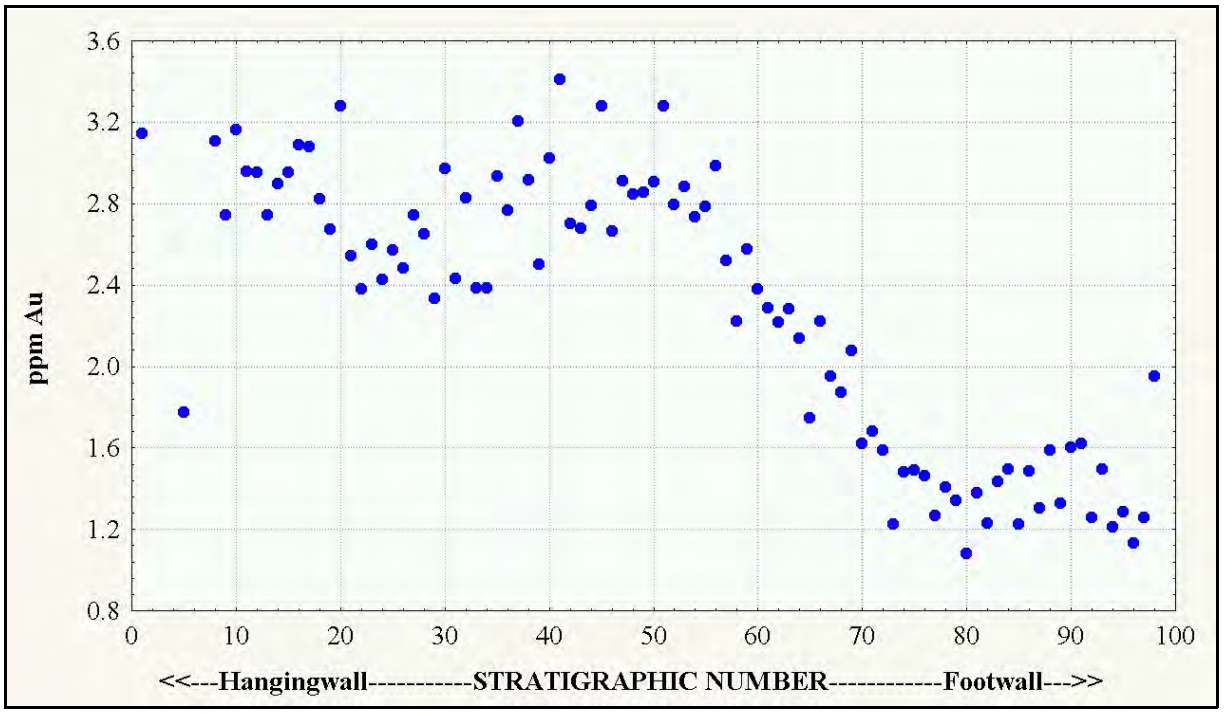

Figure 53 - Average 5m composite ppm Au versus stratigraphic position (SN)

The Au trend (Fig. 53) shows considerable variability from SN8 to SN50 with a maximum reached between SN40 and SN50. Below SN50 there is a steady decline to SN75 which then remains flat towards the footwall. In contrast to other metals, the siliceous cap has a similar Au grade to the HWE. The Au grade in the baritic cap is low, but similarly to Ag (Fig. 52) exceeds most grades in the FWD.

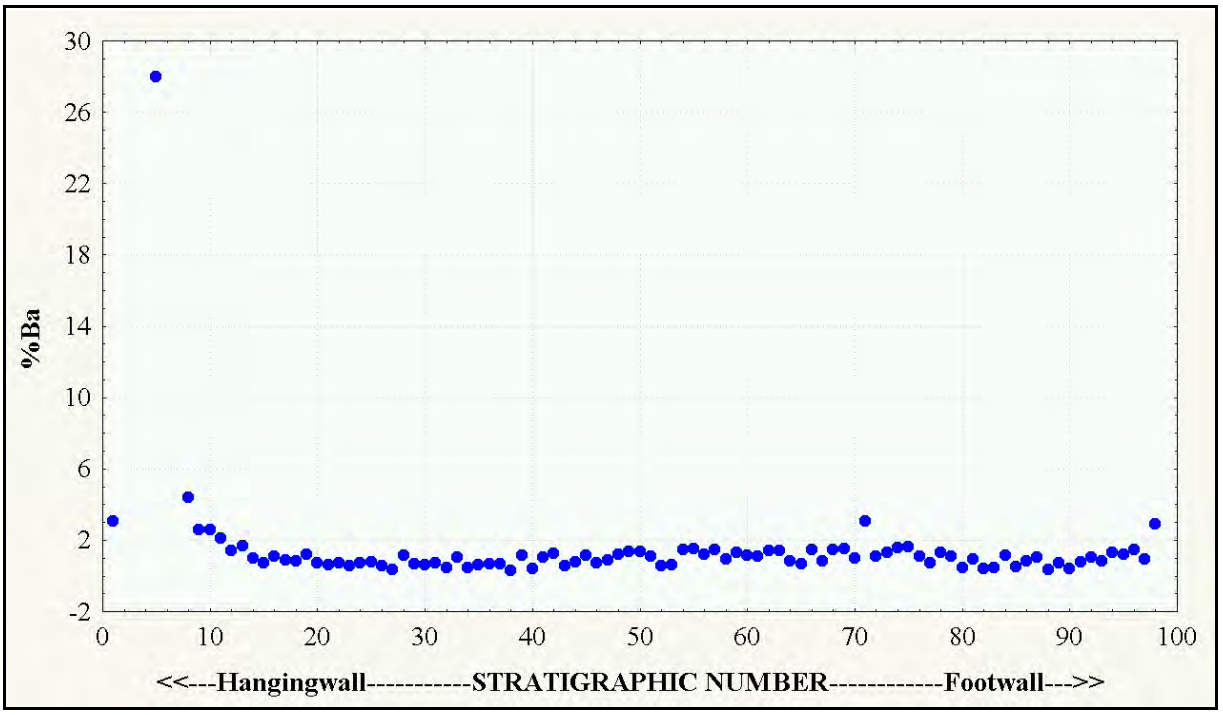

Figure 54 - Average 5m composite %Ba versus stratigraphic position (SN)

Apart from the obvious peak in the baritic cap, the overall Ba trend (Fig. 54) is particularly flat. There is a slight decrease below the barite from SN8 to SN15, but then the trend remains flat to the footwall.

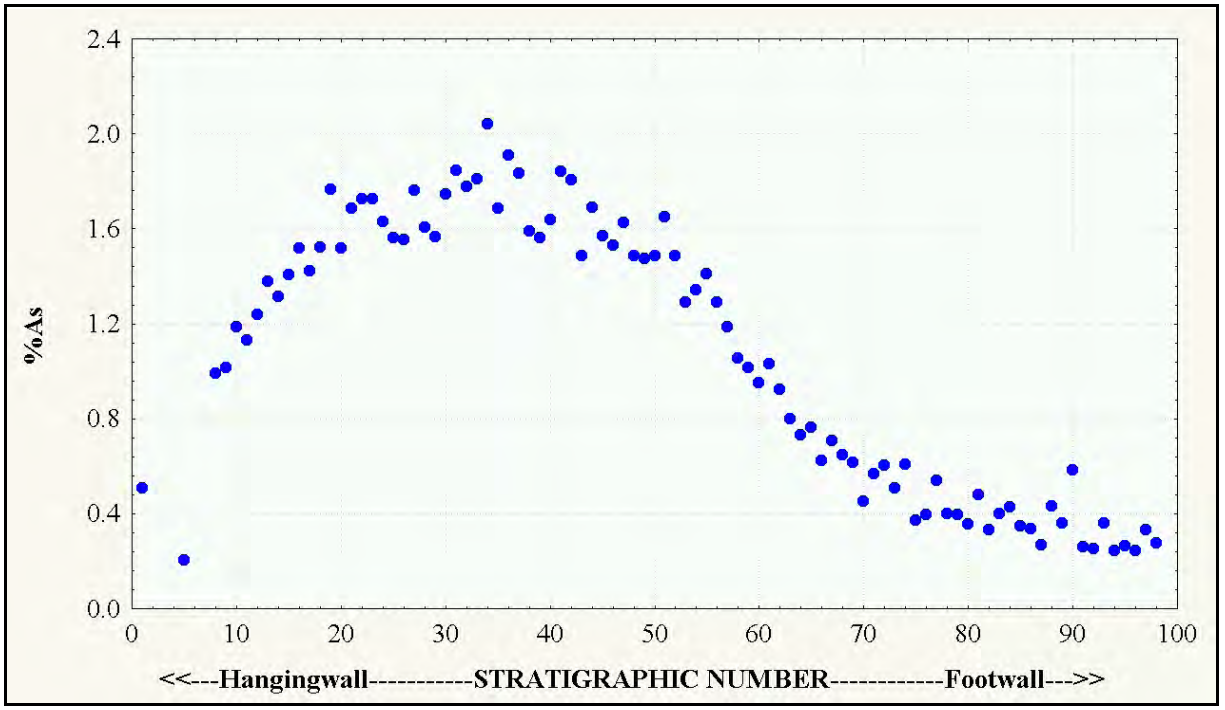

Figure 55 - Average 5m composite %As versus stratigraphic position (SN)

The As trend (Fig. 55) shows considerable regular zonation with a maximum between SN30 and SN40 approximately six times the minimum values at the extreme footwall. The HWE oretype shows an inverted parabolic trend with lowest values at the upper and lower boundaries. This is somewhat similar to the trend for Au (Fig. 53) and strikingly similar to that for the "shrinkage shadows" macroscopic textural zonation (Figs. 13,14). The As grade in the siliceous cap is above that for the FWD, but the baritic cap As grade is extremely low (this feature has been used by mine geologists to differentiate between true baritic cap material and remobilised barite veins in the massive sulphide that tend to have a much higher As tenor).

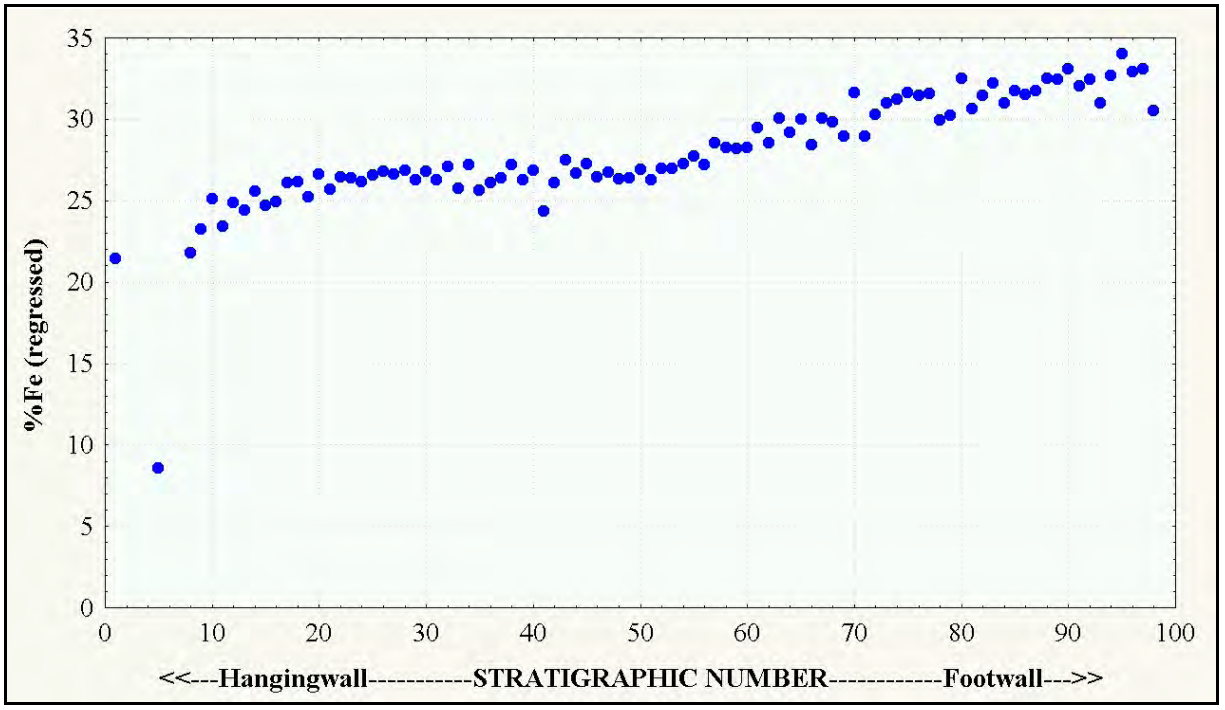

Figure 56 - Average 5m composite %Fe (regressed) versus stratigraphic position (SN)

The Fe trend (Fig. 56) is flat between SN20 and SN50 with a decrease above to the massive sulphide hangingwall. Below SN50 there is a steady increase up to a maximum right at the footwall. The pattern for the siliceous and baritic caps is similar to that for Au (Fig. 53) and As (Fig. 55) with grades in the BAR very low.

In summary, the stratigraphic across-dip zonation is well demonstrated from the raw 5m composite dataset. The original decision to use the 100 ppm Ag level to subdivide the massive sulphide into two oretypes (HWE, FWD) has proven to be correct (although ~0.9%As could have achieved the same result).

Pb, Zn, Ag, Au and As all have very similar trends with fairly consistent levels of enrichment in the HWE (by definition for Ag!) and then gradual decline in grade until the lowest values occur right at the footwall contact. Arsenic differs from the other metals in this group with a clear maximum in the centre of the HWE stratigraphy.

Cu and Fe have similar trends generally increasing to a maximum at the footwall but only Cu shows a slight increase at the massive sulphide hangingwall.

The GSP and BAR oretypes have very similar Pb, Zn and Ag levels. Within the GSP, the Cu, Au, As and Fe grades simply represent upward extrapolations of the massive sulphide trends. BAR shows negative anomalism for Cu, Au, Ba, As and Fe compared to the overall deposit trend.

4.4.2 Lateral zonation

The lateral zonation has been studied in both cross-section and plan projection views. Cross-sections spaced 60m apart were selected (Fig. 12). These coincided with major drill sections therefore minimising the amount of interpolation between drill hole samples. Cross-sections (2 x 60)=120m apart also approximate the Jack Fault measured displacement of 130m; e.g. the zonation pattern on the western side of the Jack Fault on section 10670N can be matched to the zonation pattern on the eastern side of the Jack Fault on section 10790N, thus allowing pre-Jack Fault reconstruction.

Each cross-section is colour-contoured according to global percentiles for each element or ratio, with the oretypes plotted to allow correlation with the metal distribution. Therefore over the complete set of sections there are equal areas of each colour to allow proper comparison between metals or ratios and between sections. Figures 57-69 display metal distribution for cross-sections 10310N-11030N at an approximate scale of 1:2500, whilst Figures 70-82 show distribution of selected metal ratios for the same sections. These ratios have been transformed to avoid very small or very large numbers - each ratio will lie between zero and 100. The Cu-Zn ratio (100Cu/(Cu+Zn)) and Zn-Pb ratio (100Zn/(Zn+Pb)) have been calculated in the same way as previous workers (Huston and Large, 1987) for direct comparison. All the remaining ratios have been normalised to overcome magnitude differences between the assays. The multiplier applied to the second element of the ratio pair was taken from the ratio of the global resource grades; e.g. for the Ag-Pb ratio,

the multiplier = [(global ppm Ag grade)/(global %Pb grade)] = 168/7.14 = 23.5.

Therefore a resulting ratio of 50 indicates a deposit average value. Similar multipliers

have been calculated for Au/Ag, Ag/As, Ag/Fe and Au/As.

The "chequerboard" pattern that appears on some plots (e.g. Fig. 63; 10670N, Ba) is an artefact of the colour contouring interpolation process and should be ignored.

Plan projections have been constructed by vertically integrating grades within each of the Jack Fault blocks and then shifting the east block south to approximate the pre-Jack Fault configuration. These projections are presented for the HWE and FWD oretypes. In a similar manner to the cross-sections, percentiles were set from the vertically averaged values. The plan projection percentile values do not coincide with the cross-section percentiles because the variance of the vertical averages is much less. Figures 83-84 display metal distribution for the HWE and FWD oretypes in plan projection at an approximate scale of 1:7000, whilst Figures 85-86 show distribution of selected metal ratios for each of the massive sulphide oretypes.

Cross-section zonation

Interpretation of the cross-sectional zonation patterns is not a simple exercise when confronted with Hellyer's extremely variable geometry. Nevertheless, by comparing the patterns from one section to another and from one element or ratio to another, gradually a summary arrangement falls into place. The comments below summarise the overall zonation geometry for each element and ratio.

Pb - general concentric zonation surrounding the footwall feeder zone with highest grades most distal, anomalously depleted in the South End, unusual enrichment on the footwall on 10910N section

Zn - general concentric zonation surrounding the footwall feeder zone with highest grades most distal (but definitely more proximal than Pb), less continuity than Pb, unusual enrichments in several footwall areas

Ag - general concentric zonation surrounding the footwall feeder zone with highest

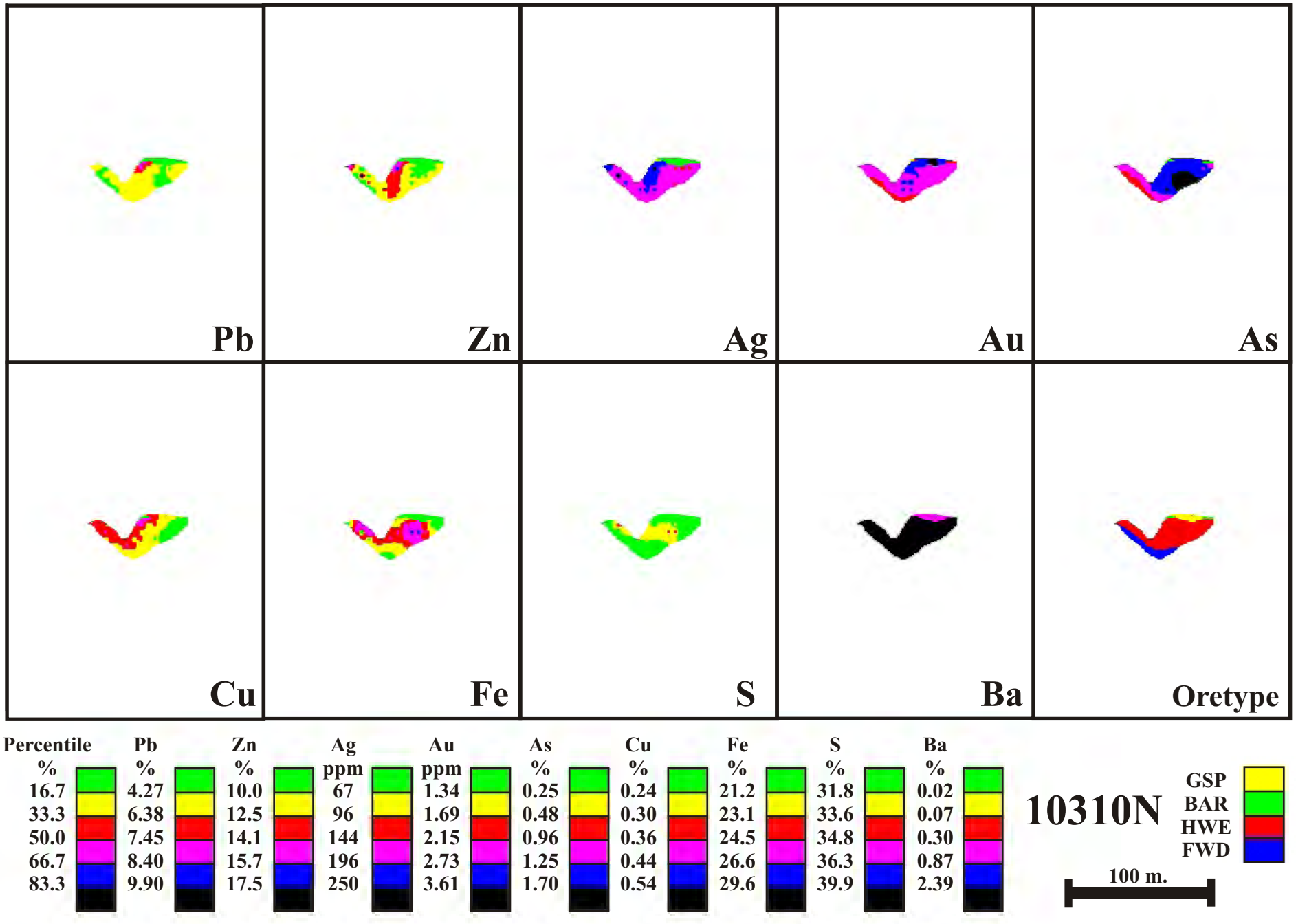

Figure 57 - Metal zonation pattern from the kriged 3D model for cross-section 10310N

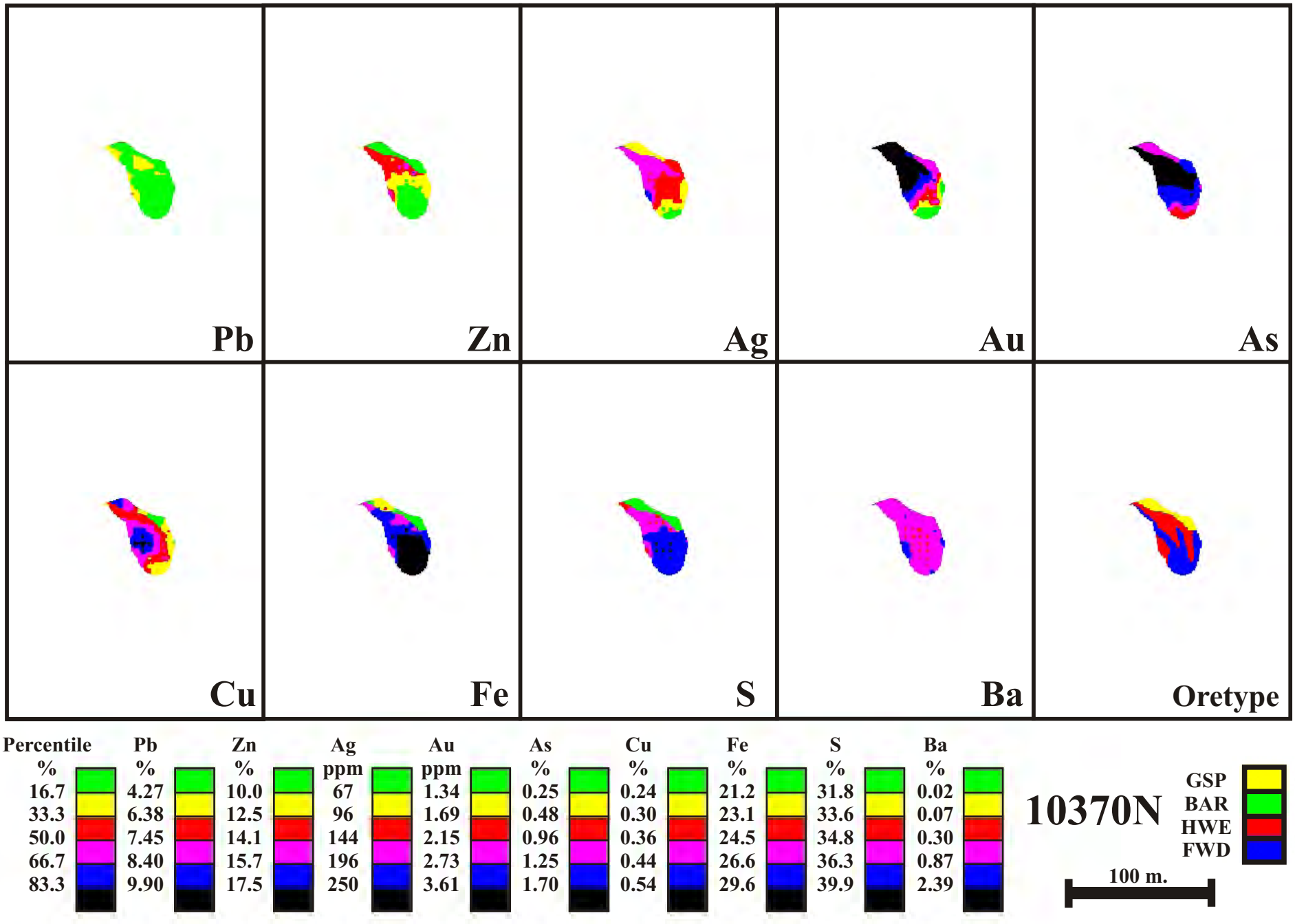

Figure 58 - Metal zonation pattern from the kriged 3D model for cross-section 10370N

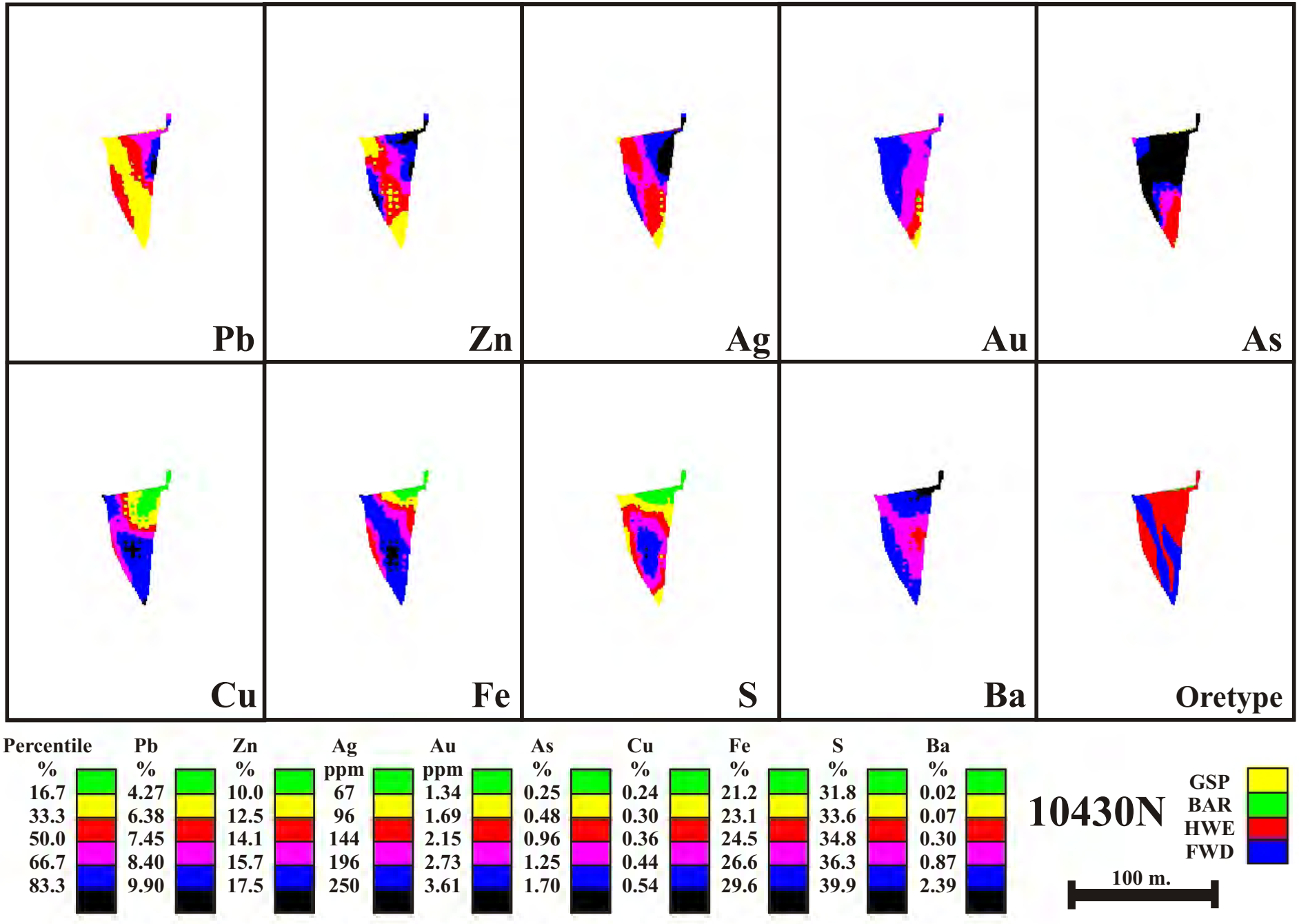

Figure 59 - Metal zonation pattern from the kriged 3D model for cross-section 10430N

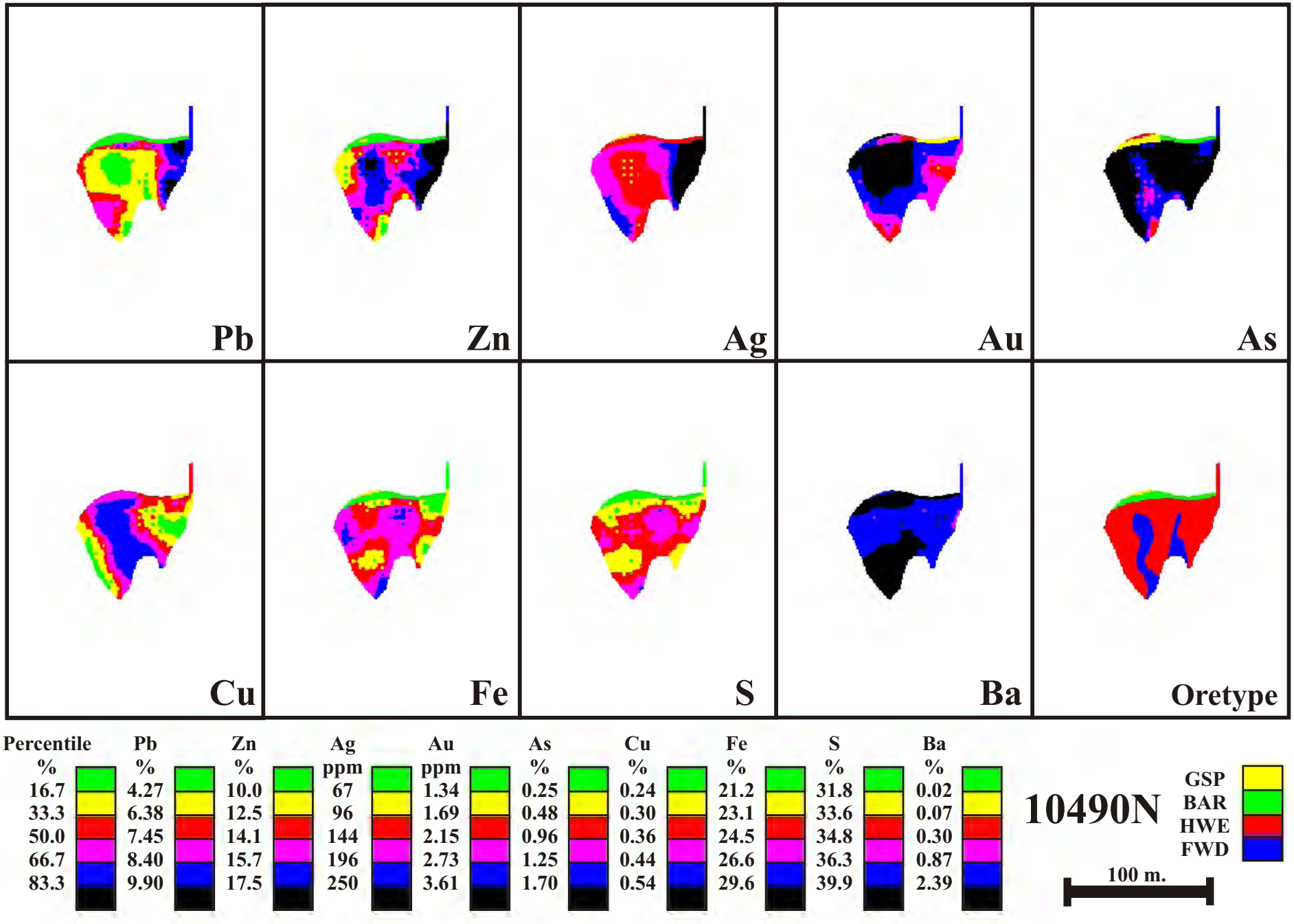

Figure 60 - Metal zonation pattern from the kriged 3D model for cross-section 10490N

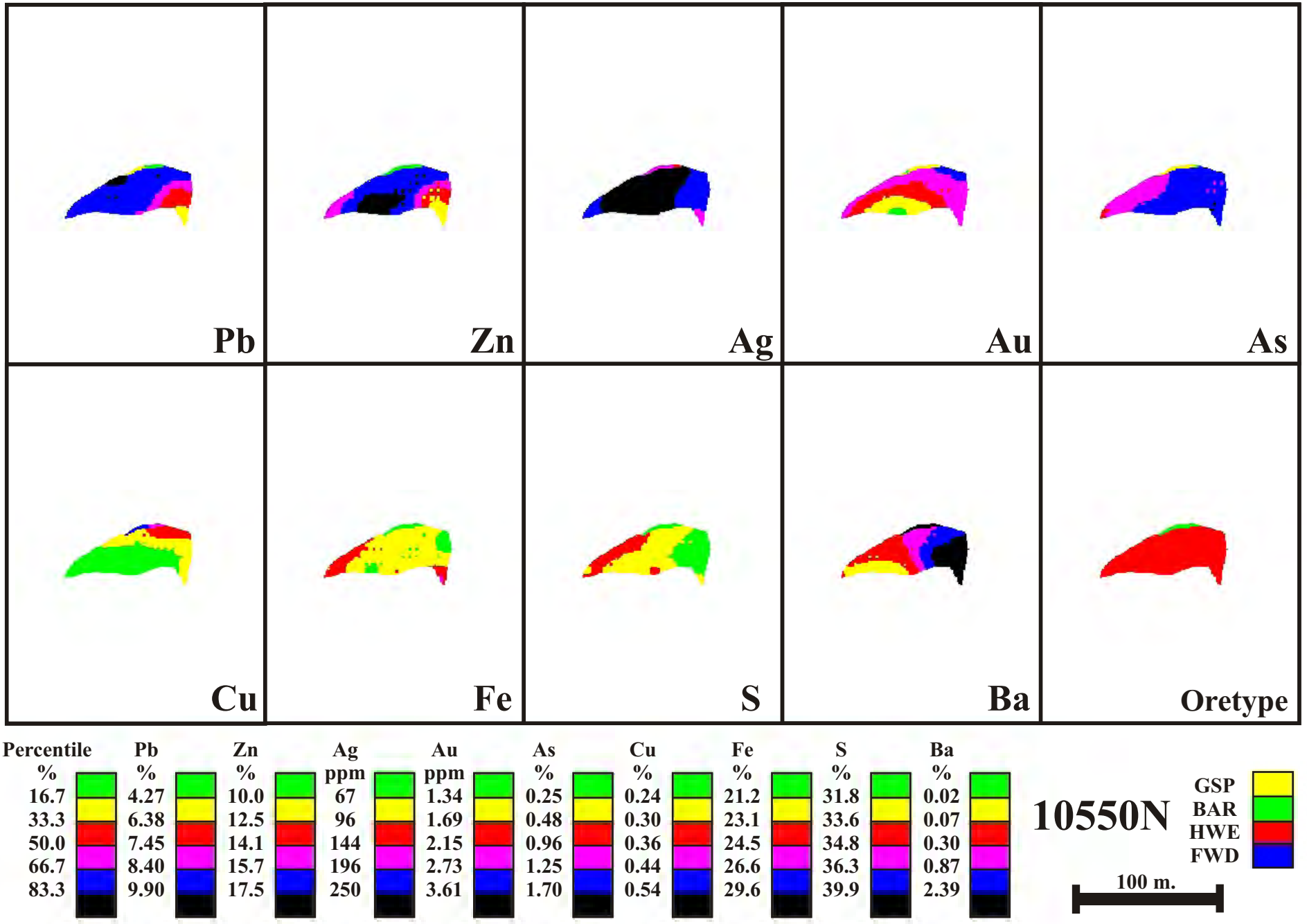

Figure 61 - Metal zonation pattern from the kriged 3D model for cross-section 10550N

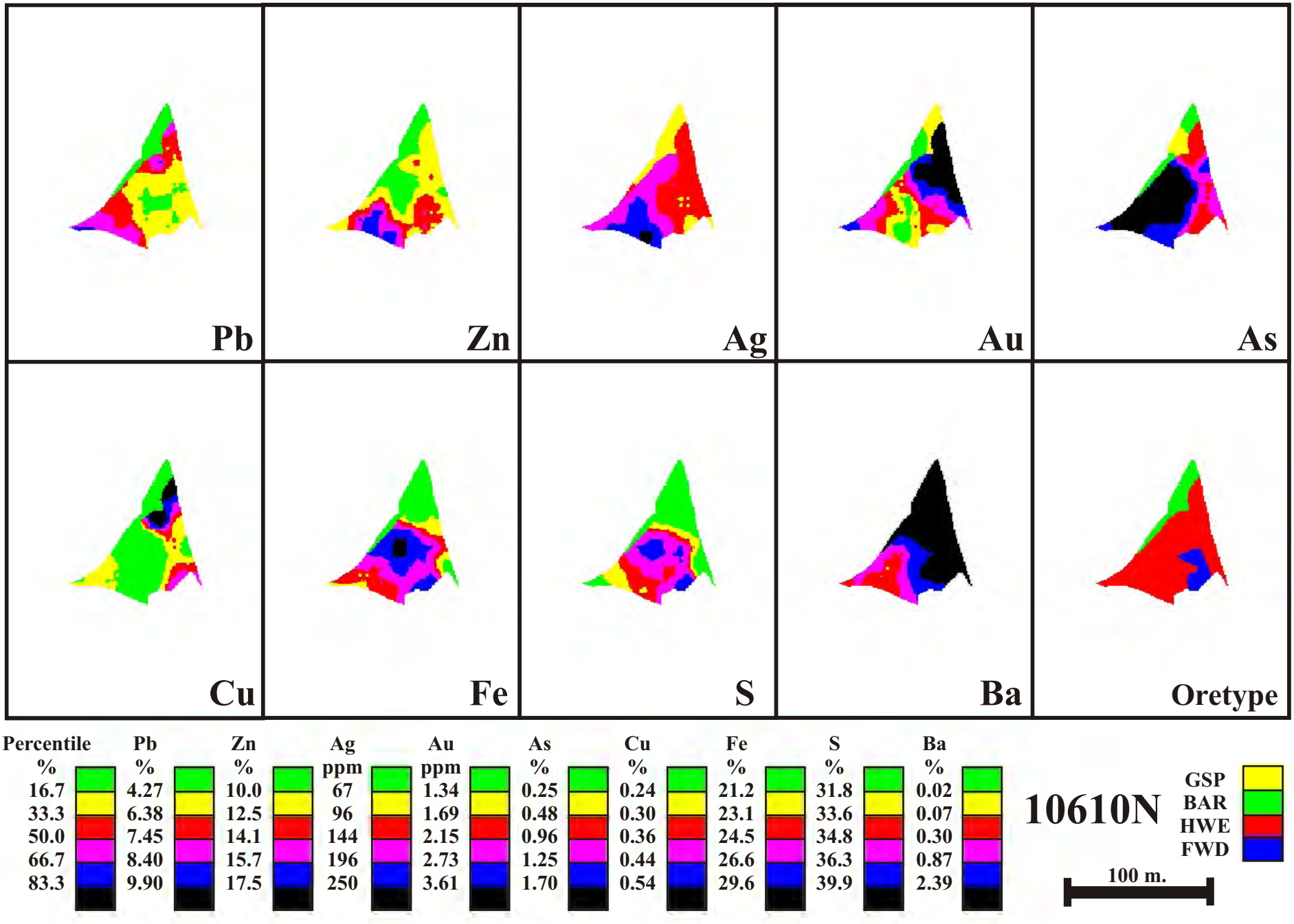

Figure 62 - Metal zonation pattern from the kriged 3D model for cross-section 10610N

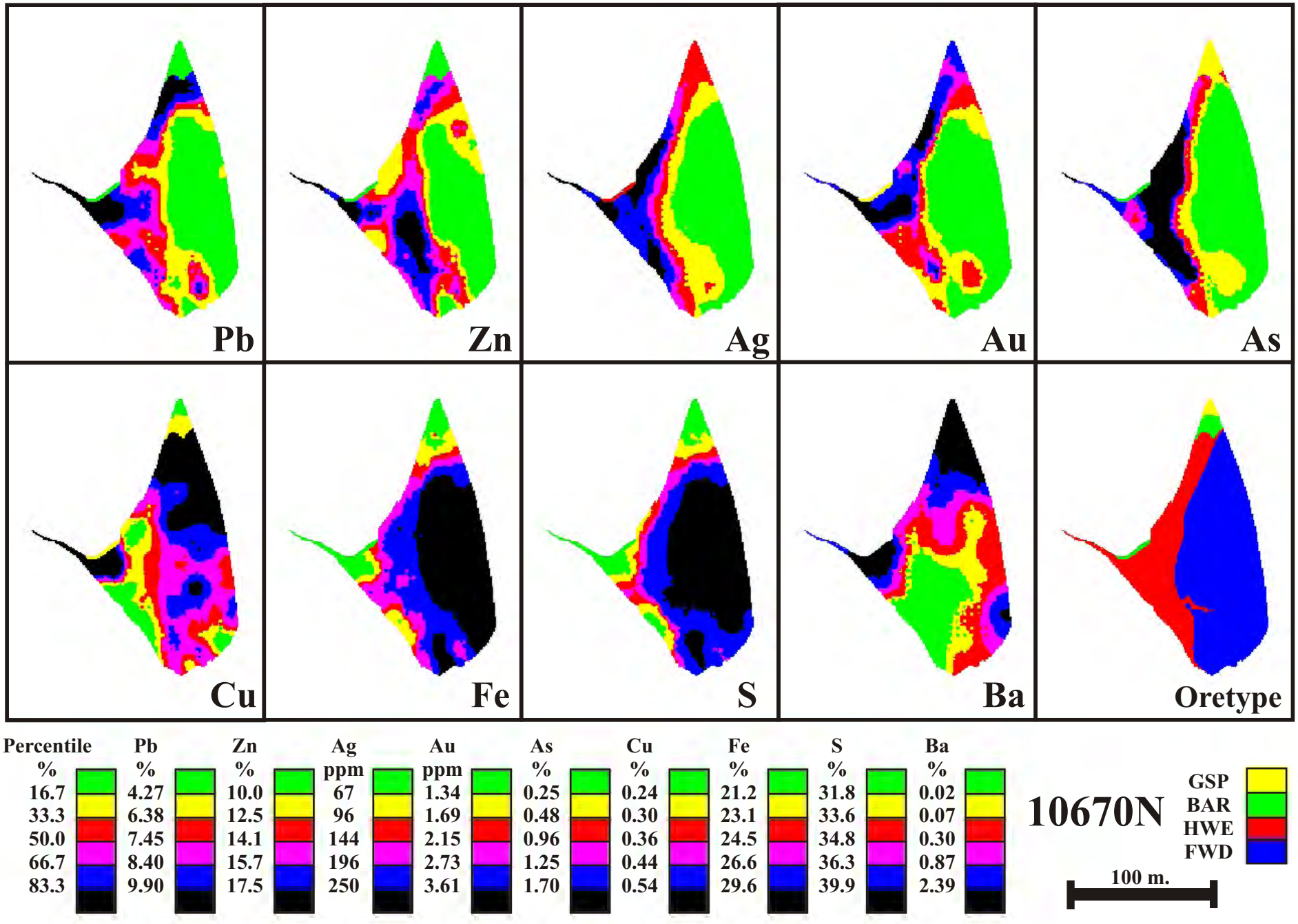

Figure 63 - Metal zonation pattern from the kriged 3D model for cross-section 10670N

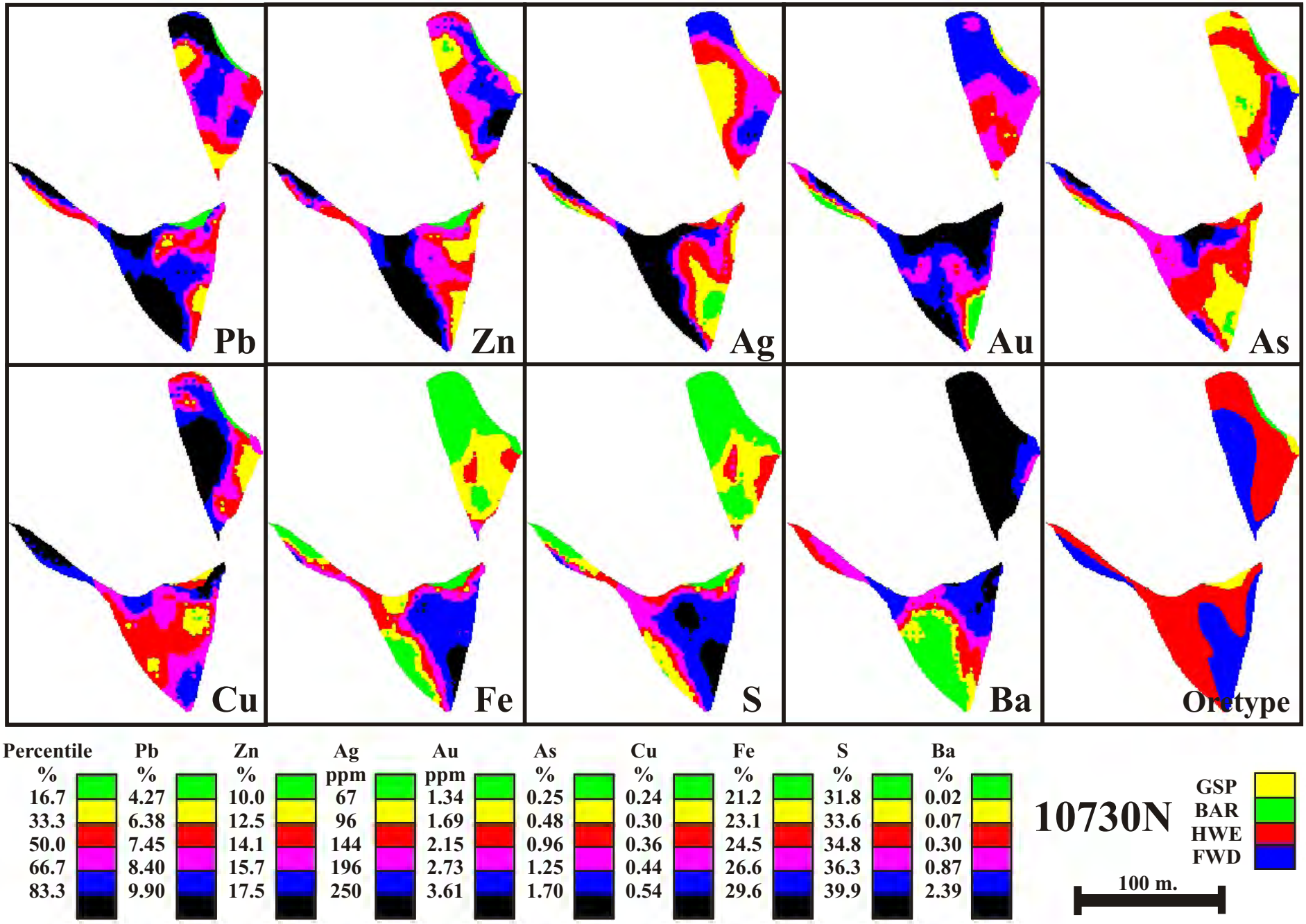

Figure 64 - Metal zonation pattern from the kriged 3D model for cross-section 10730N

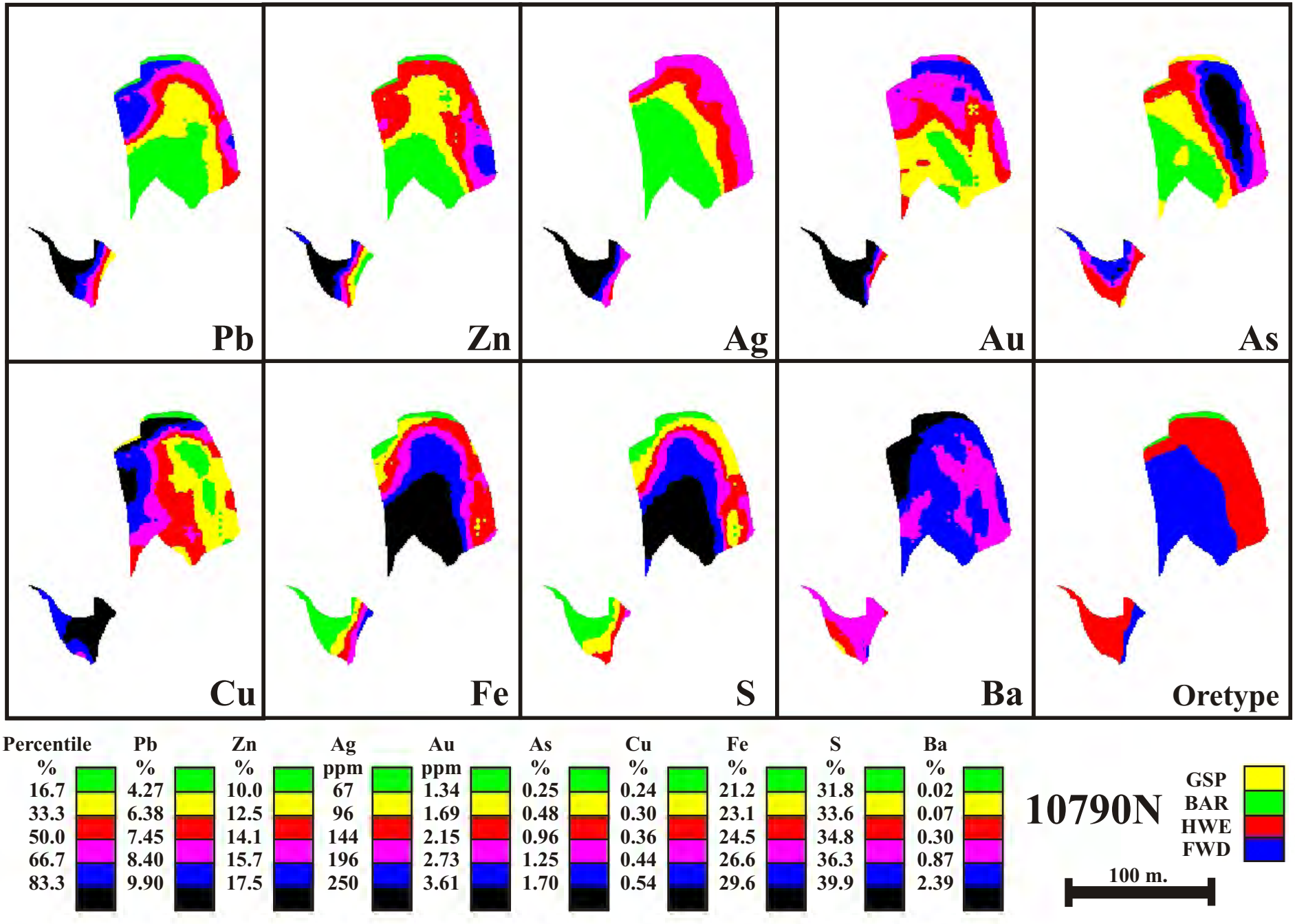

Figure 65 - Metal zonation pattern from the kriged 3D model for cross-section 10790N

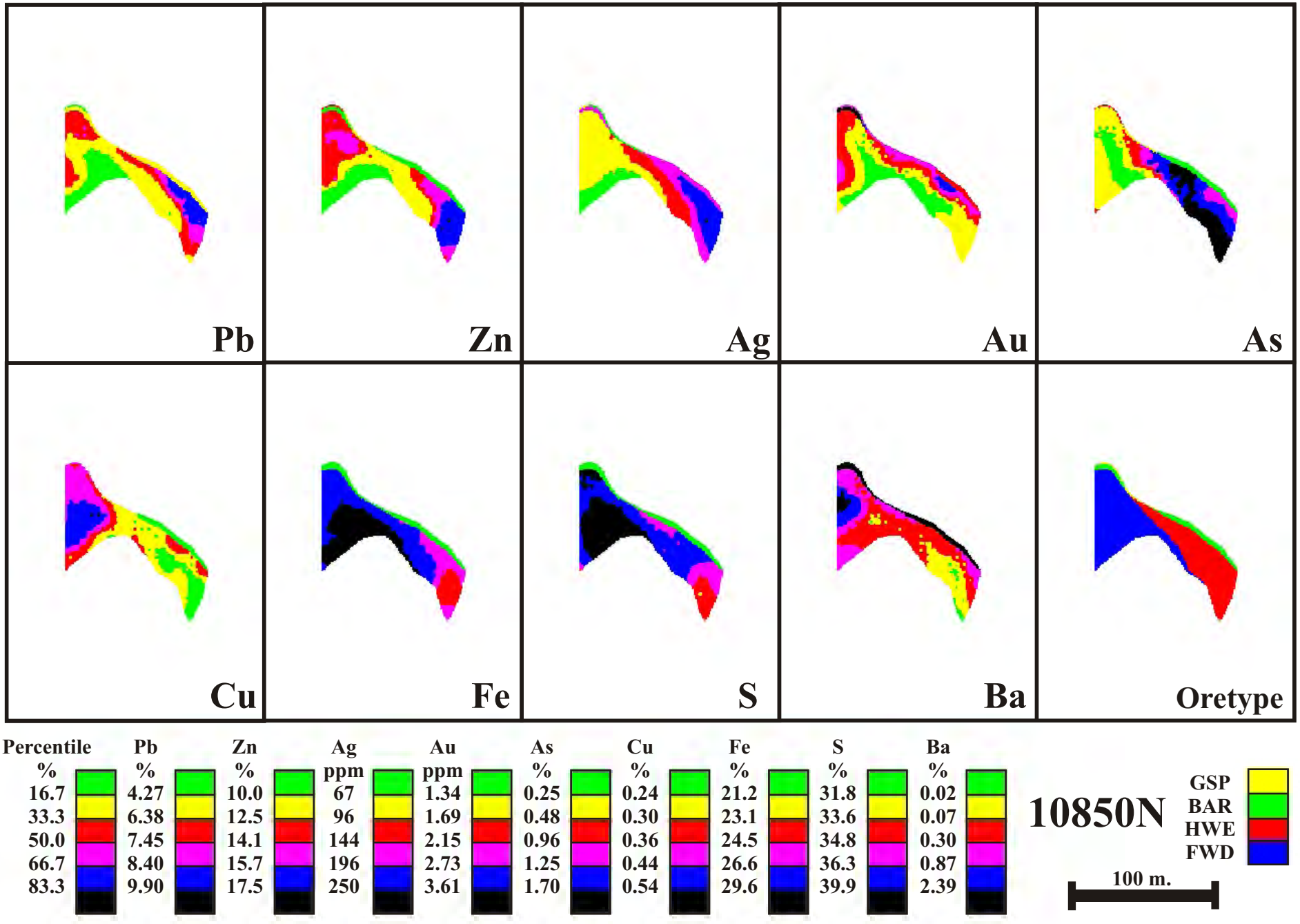

Figure 66 - Metal zonation pattern from the kriged 3D model for cross-section 10850N

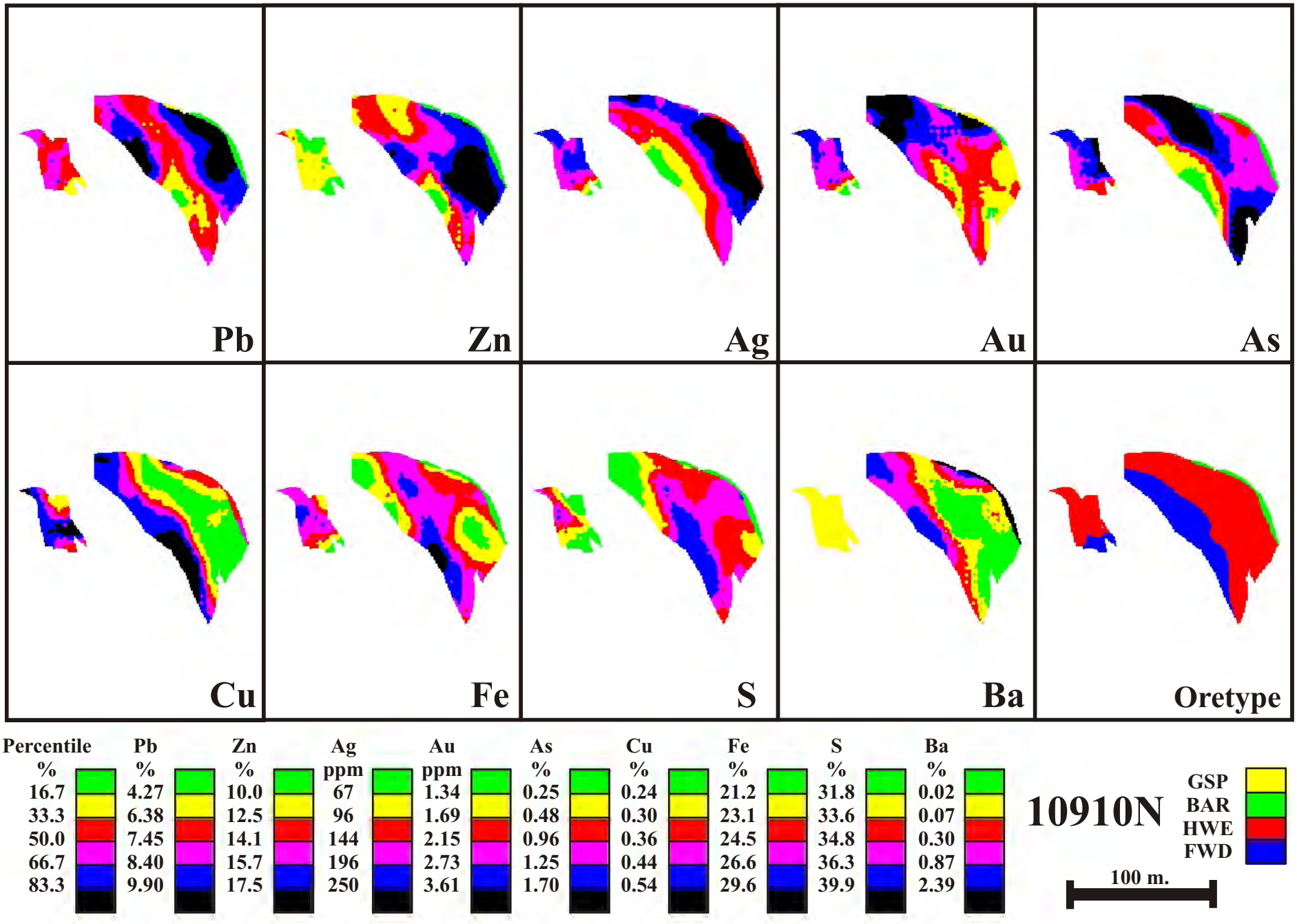

Figure 67 - Metal zonation pattern from the kriged 3D model for cross-section 10910N

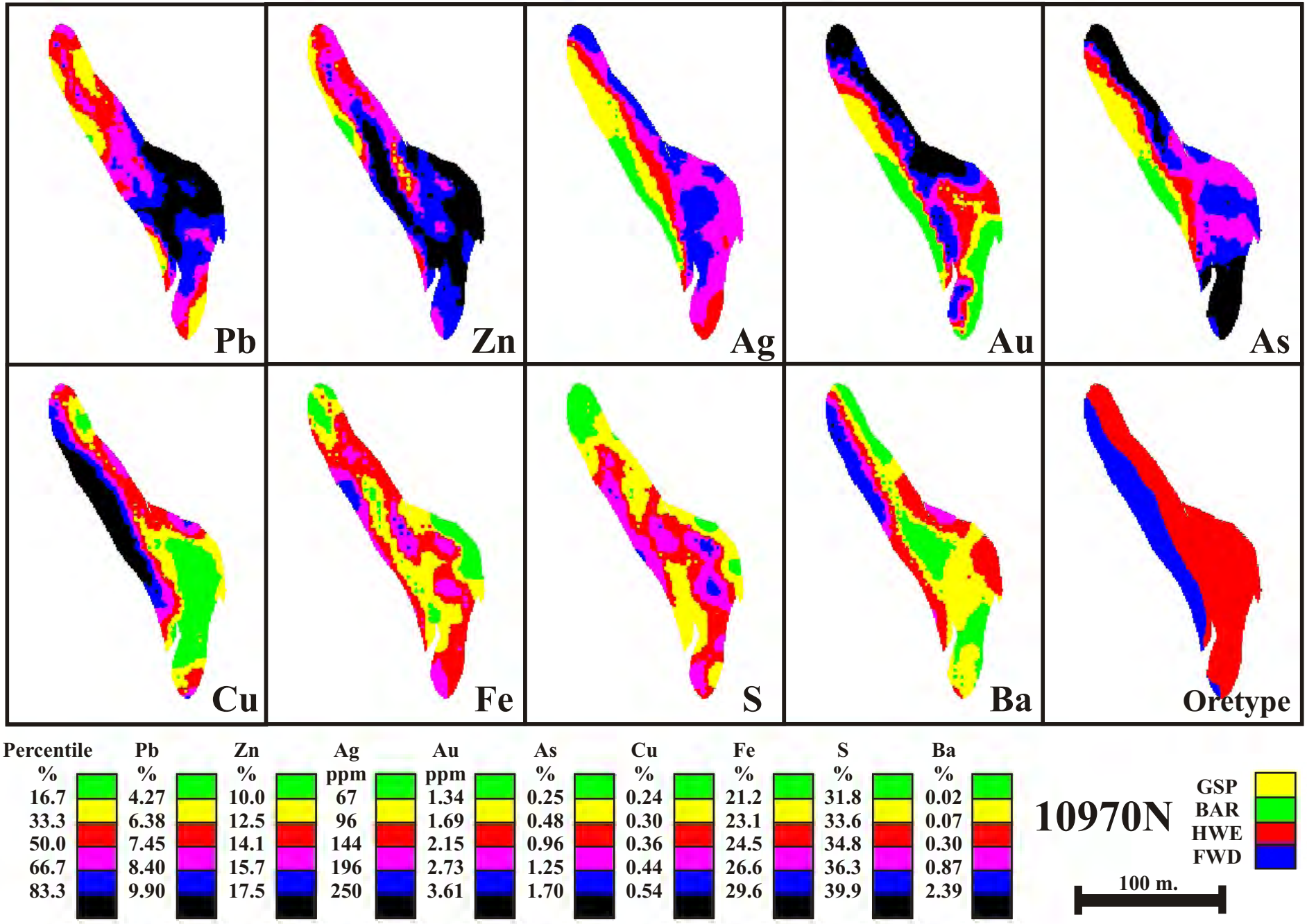

Figure 68 - Metal zonation pattern from the kriged 3D model for cross-section 10970N

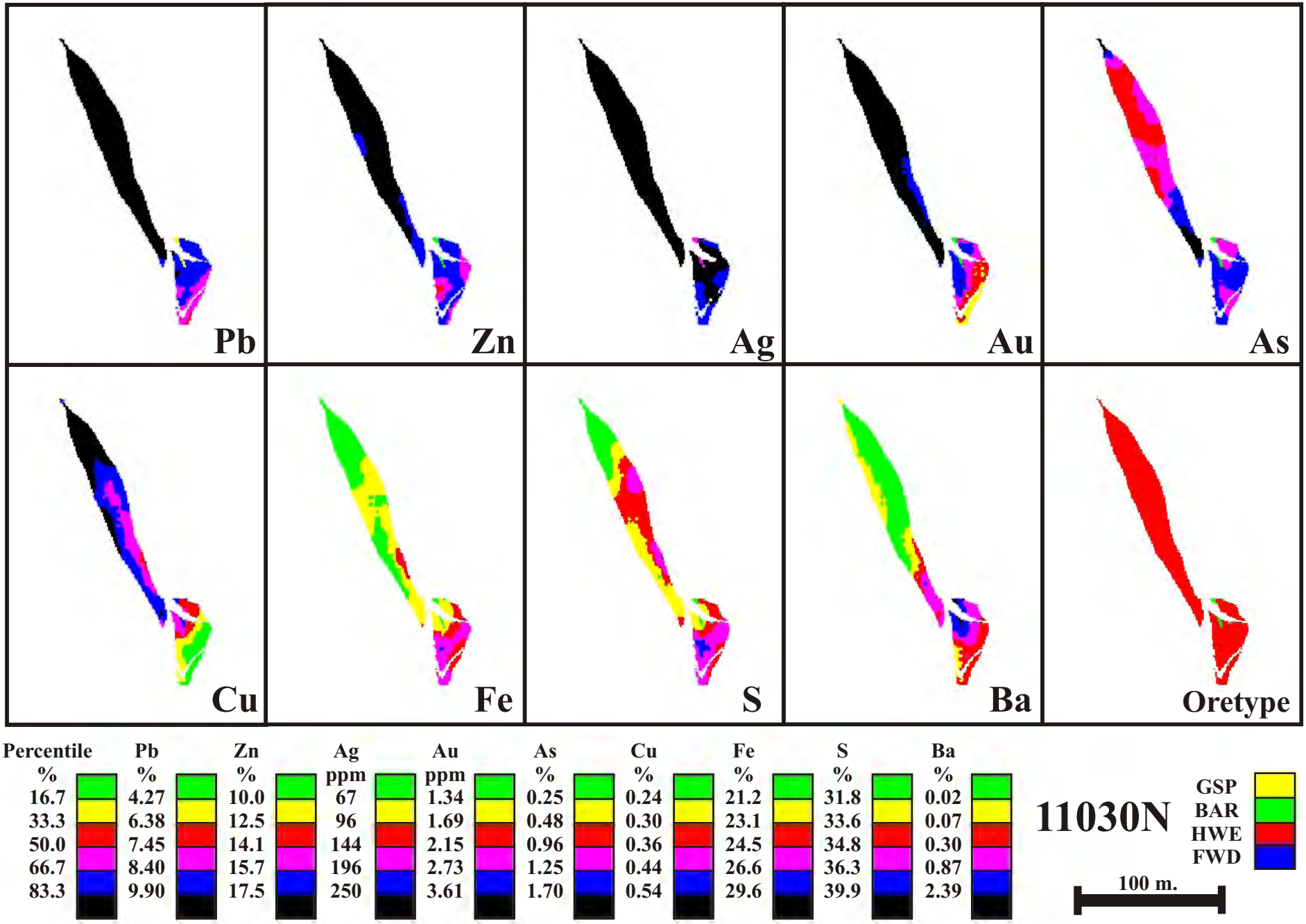

Figure 69 - Metal zonation pattern from the kriged 3D model for cross-section 11030N

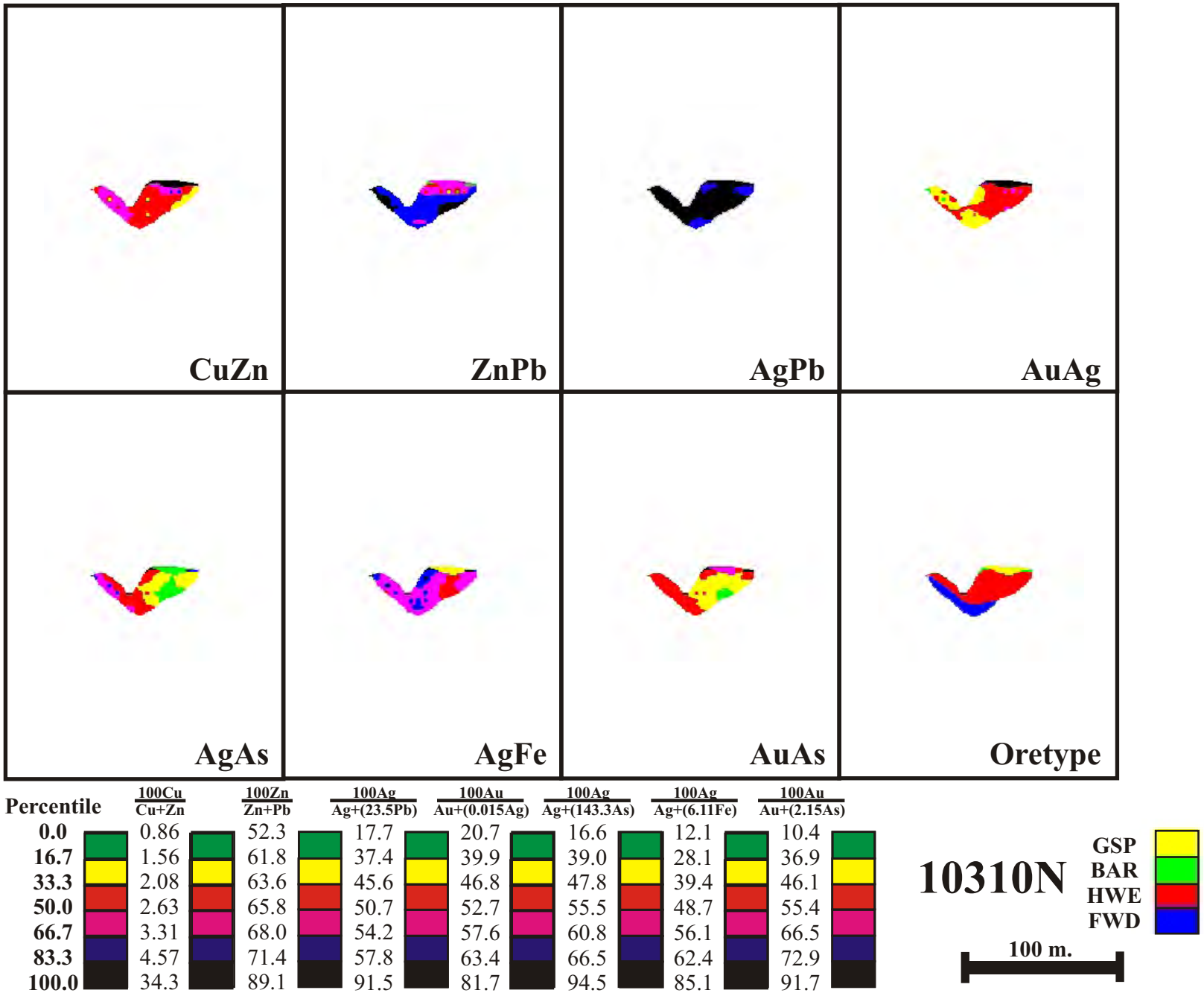

Figure 70 - Selected metal ratio zonation pattern from the kriged 3D model for cross-section 10310N
(Ag-Pb, Au-Ag, Ag-As, Ag-Fe, Au-As ratios have been normalised to overcome magnitude discrepancies)

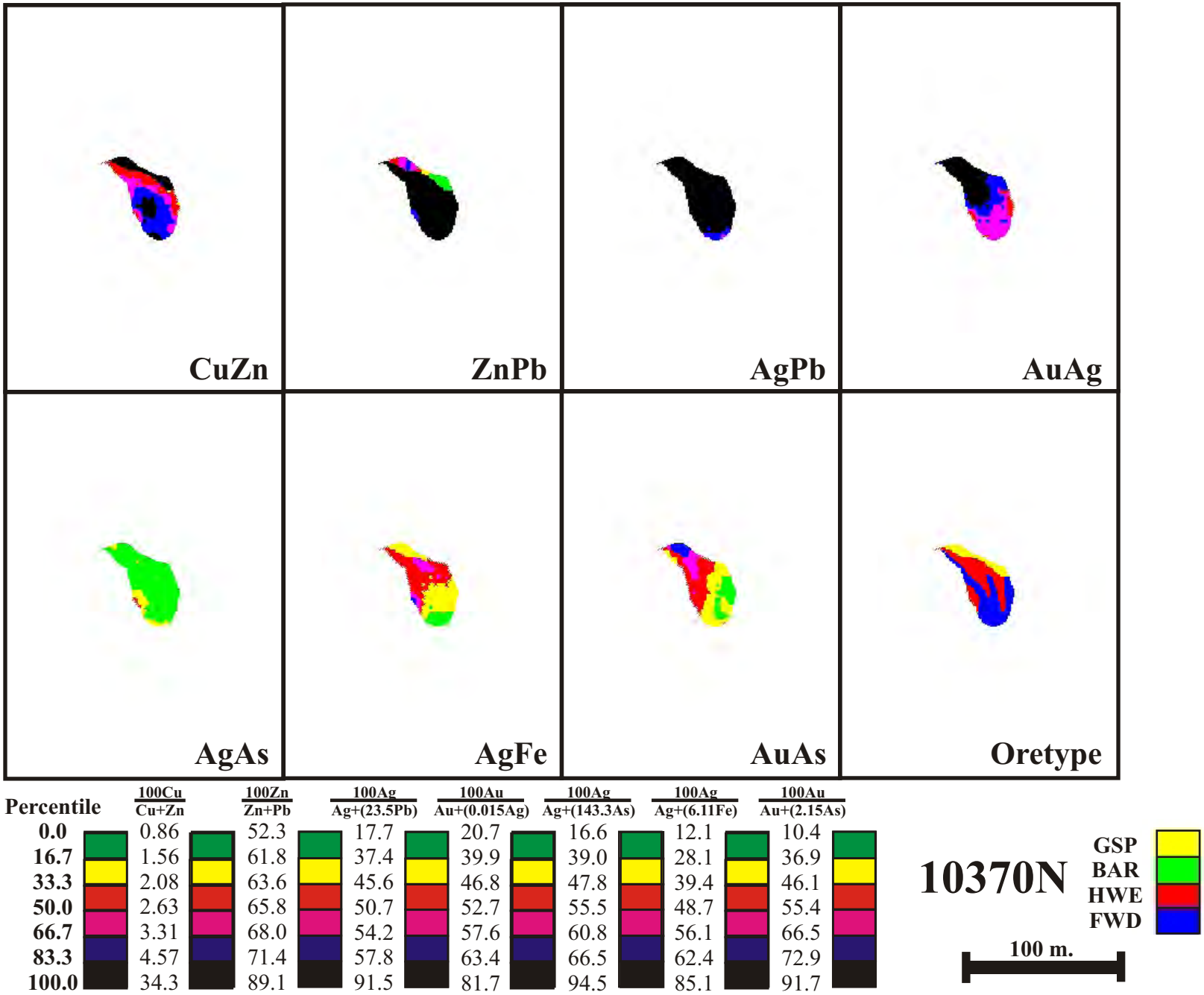

Figure 71 - Selected metal ratio zonation pattern from the kriged 3D model for cross-section 10370N
(Ag-Pb, Au-Ag, Ag-As, Ag-Fe, Au-As ratios have been normalised to overcome magnitude discrepancies)

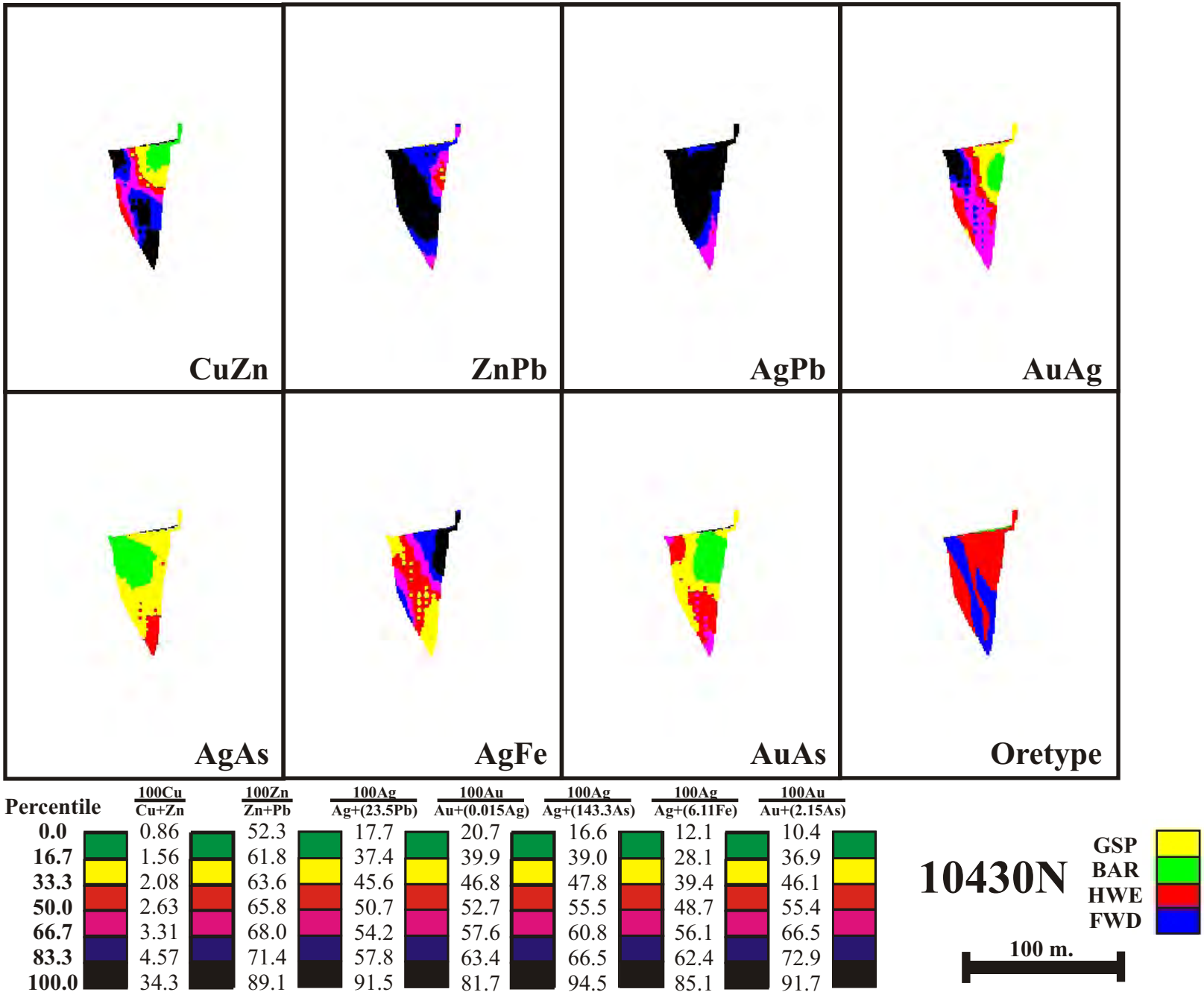

Figure 72 - Selected metal ratio zonation pattern from the kriged 3D model for cross-section 10430N
(Ag-Pb, Au-Ag, Ag-As, Ag-Fe, Au-As ratios have been normalised to overcome magnitude discrepancies)

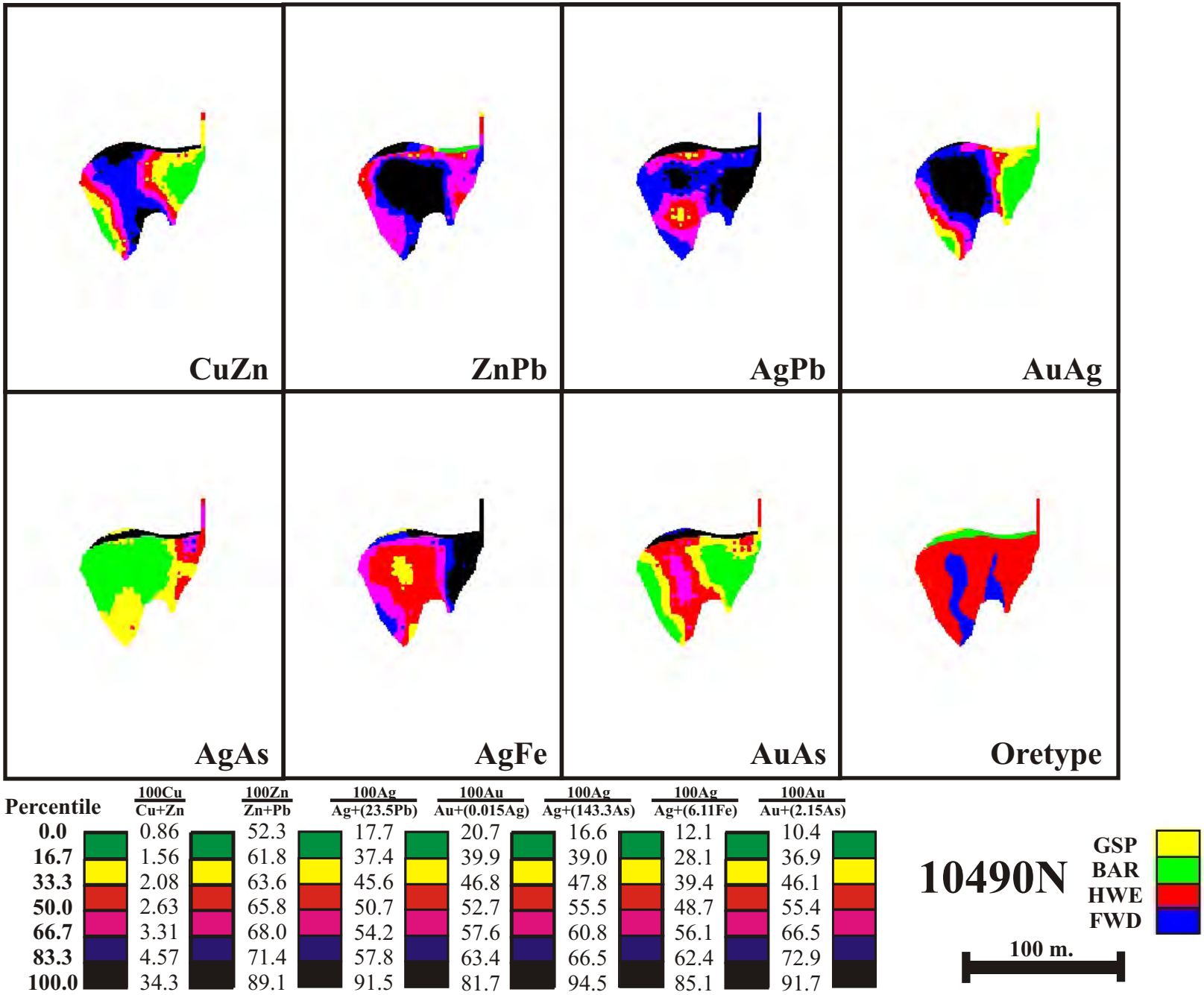

Figure 73 - Selected metal ratio zonation pattern from the kriged 3D model for cross-section 10490N
(Ag-Pb, Au-Ag, Ag-As, Ag-Fe, Au-As ratios have been normalised to overcome magnitude discrepancies)

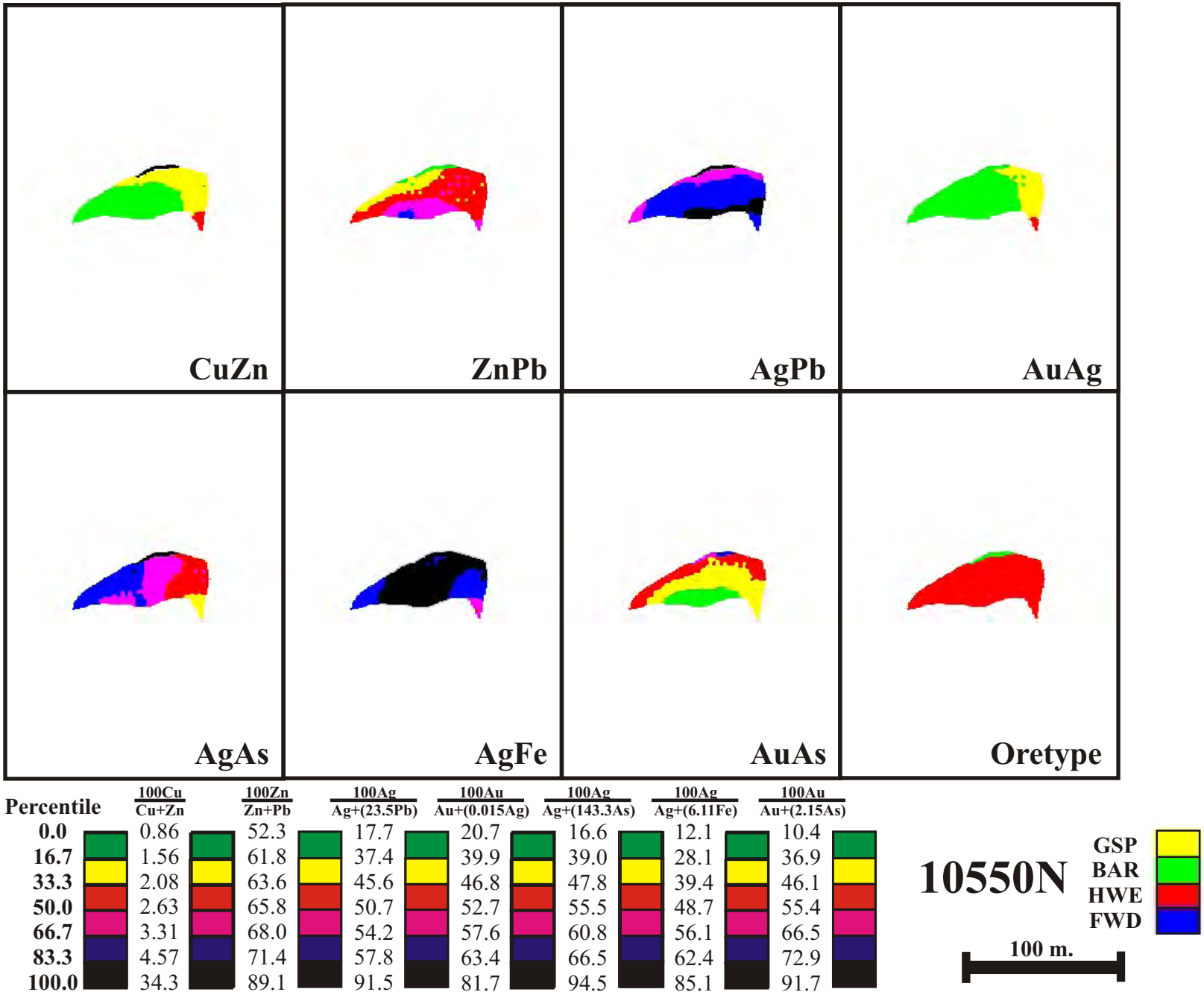

Figure 74 - Selected metal ratio zonation pattern from the kriged 3D model for cross-section 10550N
(Ag-Pb, Au-Ag, Ag-As, Ag-Fe, Au-As ratios have been normalised to overcome magnitude discrepancies)

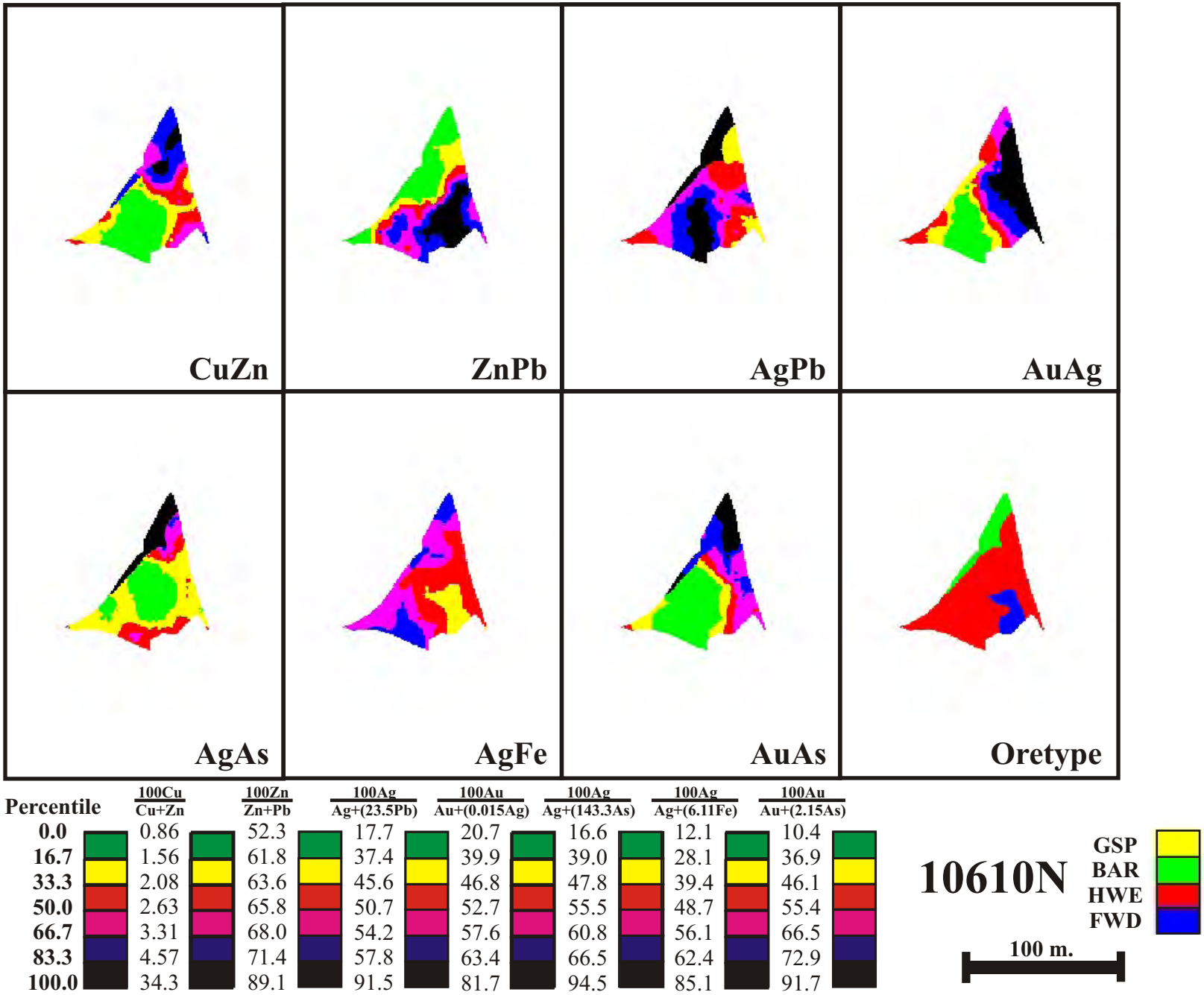

Figure 75 - Selected metal ratio zonation pattern from the kriged 3D model for cross-section 10610N
(Ag-Pb, Au-Ag, Ag-As, Ag-Fe, Au-As ratios have been normalised to overcome magnitude discrepancies)

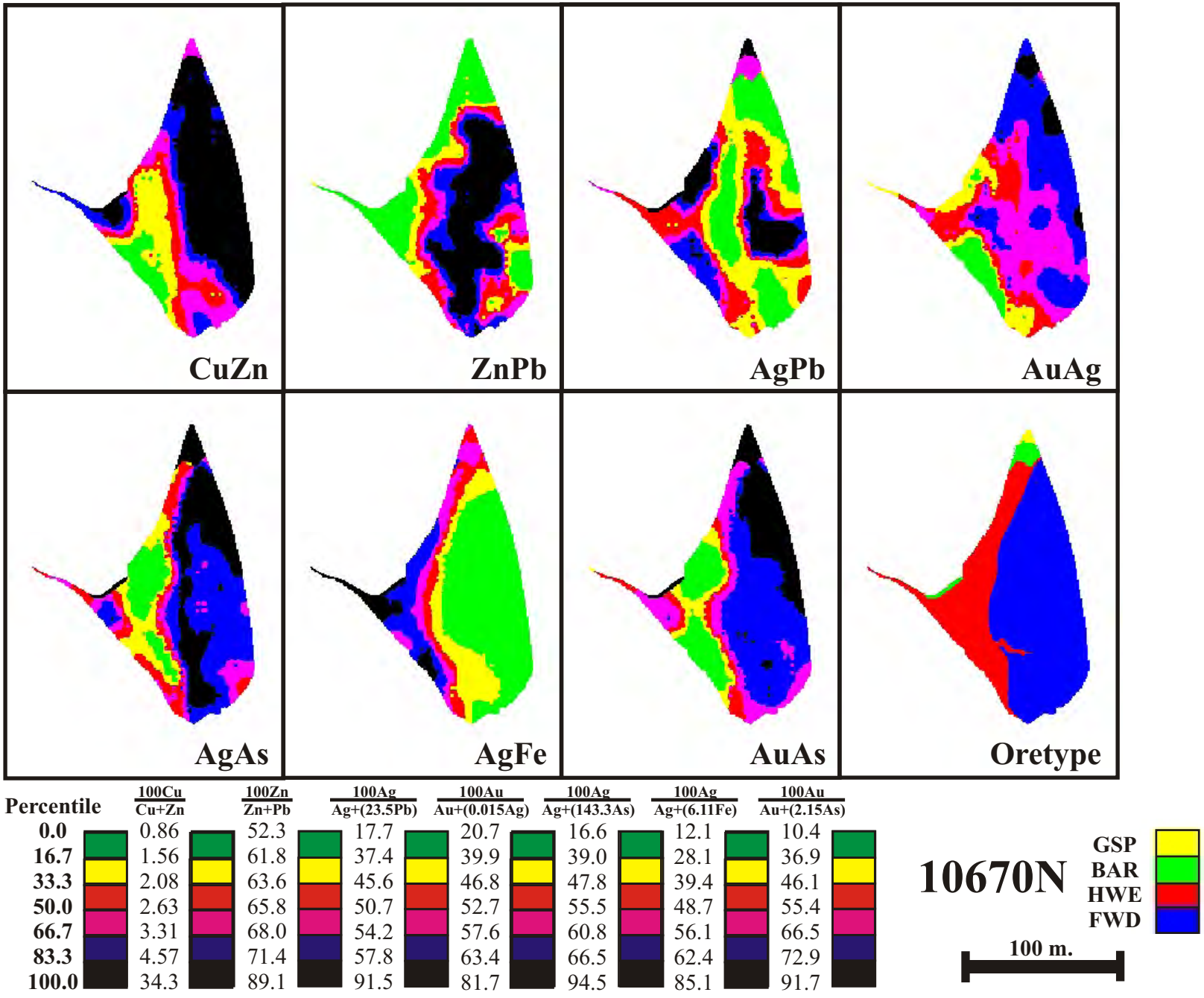

Figure 76 - Selected metal ratio zonation pattern from the kriged 3D model for cross-section 10670N
(Ag-Pb, Au-Ag, Ag-As, Ag-Fe, Au-As ratios have been normalised to overcome magnitude discrepancies)

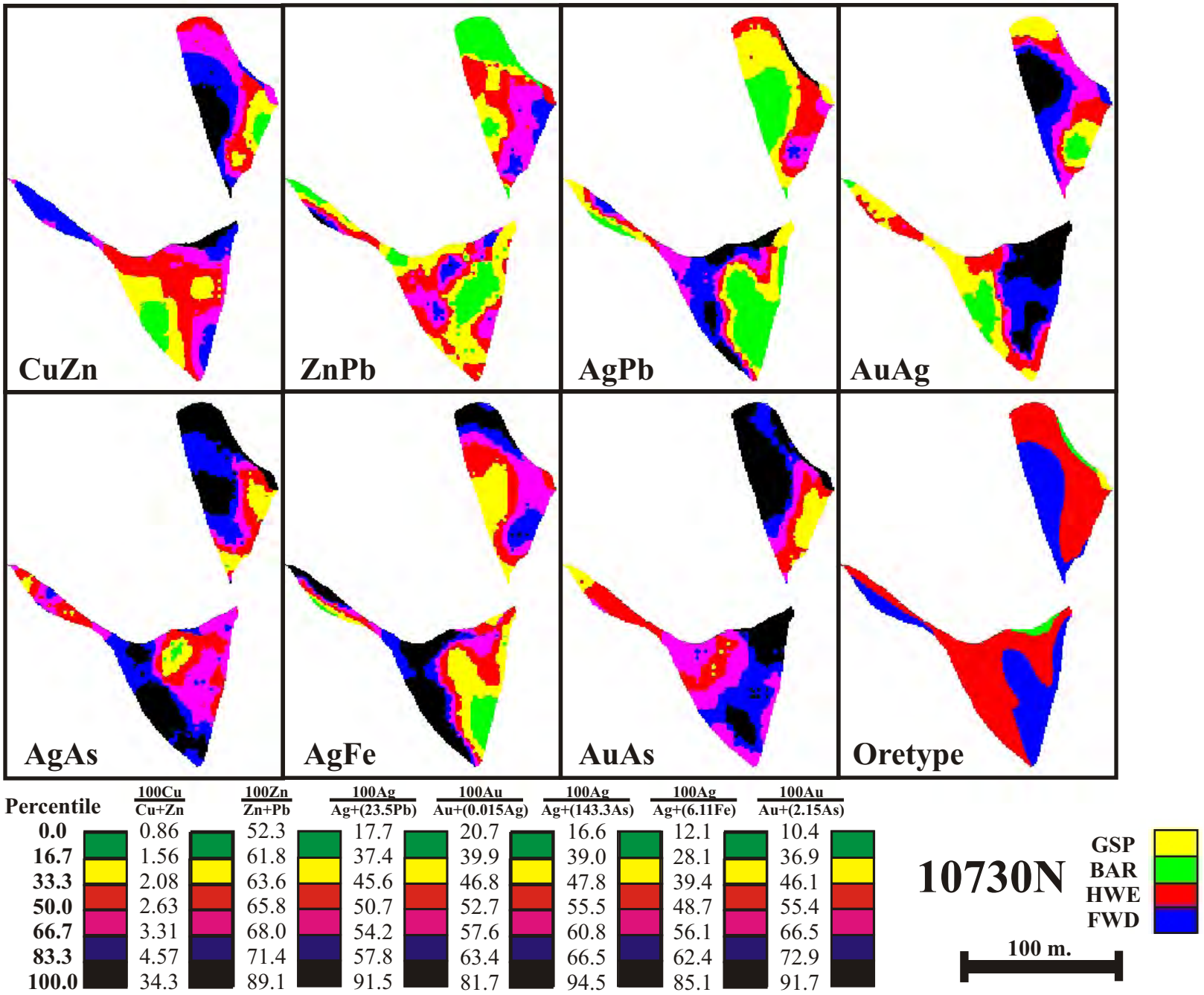

Figure 77 - Selected metal ratio zonation pattern from the kriged 3D model for cross-section 10730N
(Ag-Pb, Au-Ag, Ag-As, Ag-Fe, Au-As ratios have been normalised to overcome magnitude discrepancies)

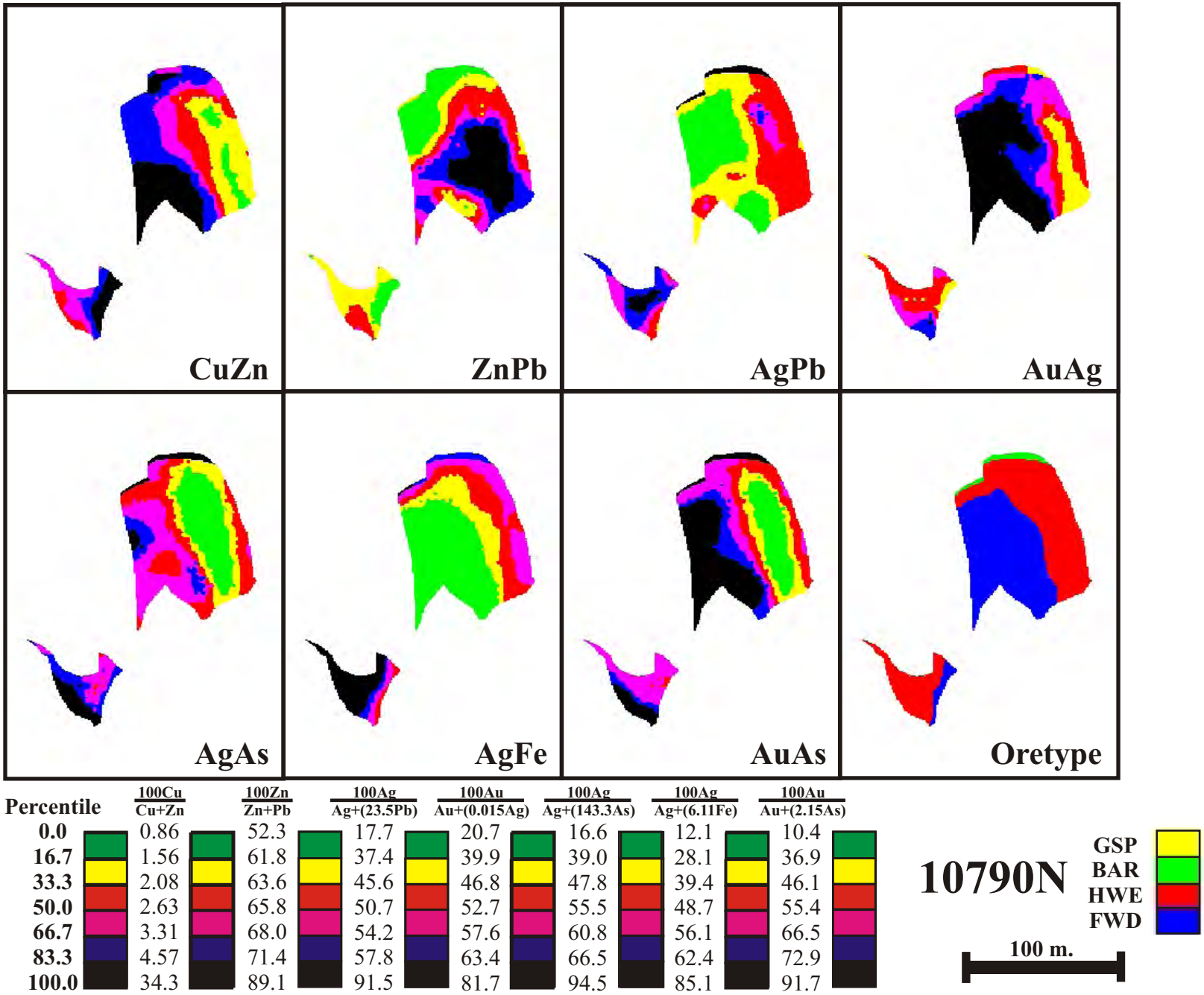

Figure 78 - Selected metal ratio zonation pattern from the kriged 3D model for cross-section 10790N
(Ag-Pb, Au-Ag, Ag-As, Ag-Fe, Au-As ratios have been normalised to overcome magnitude discrepancies)

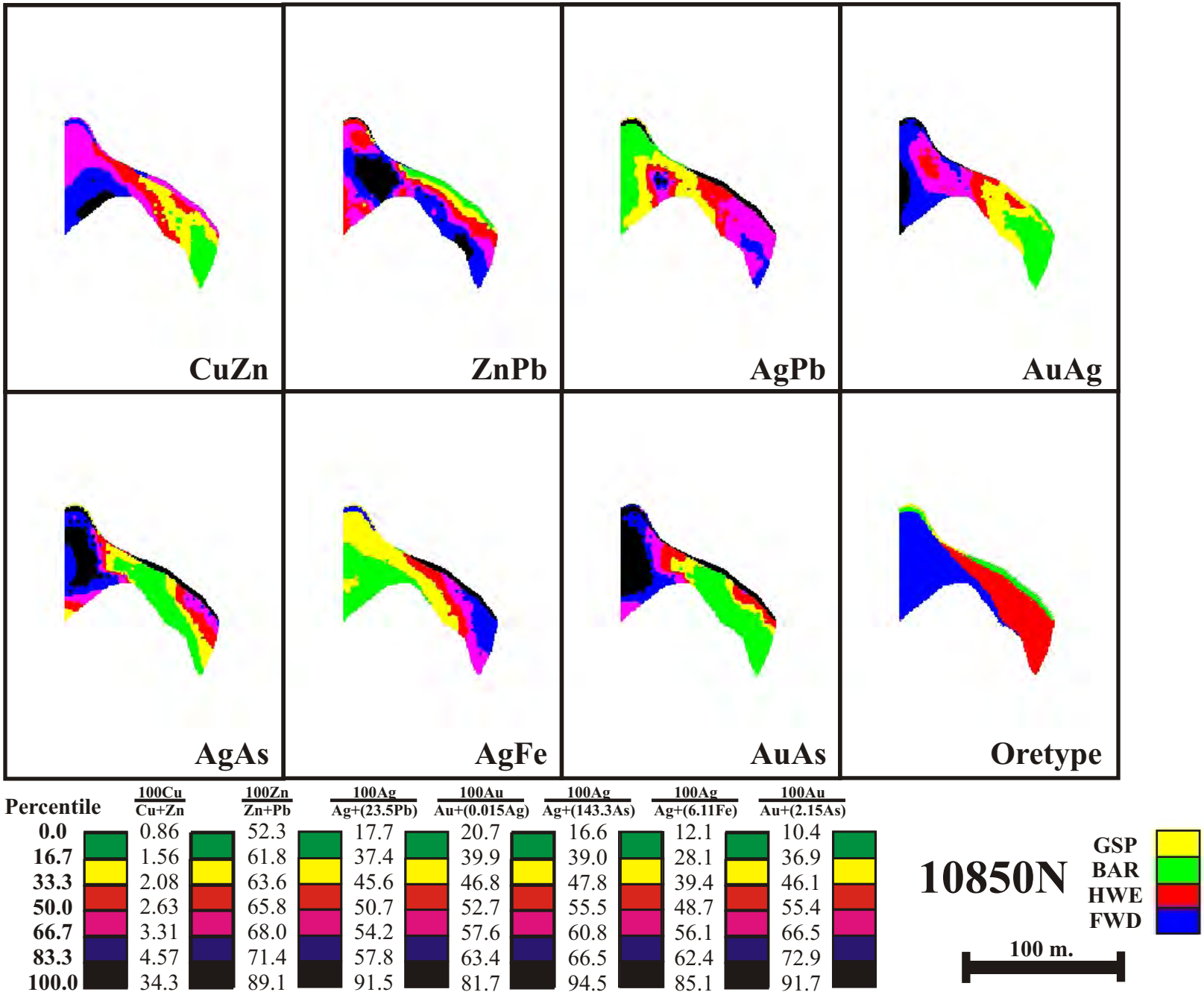

Figure 79 - Selected metal ratio zonation pattern from the kriged 3D model for cross-section 10850N
(Ag-Pb, Au-Ag, Ag-As, Ag-Fe, Au-As ratios have been normalised to overcome magnitude discrepancies)

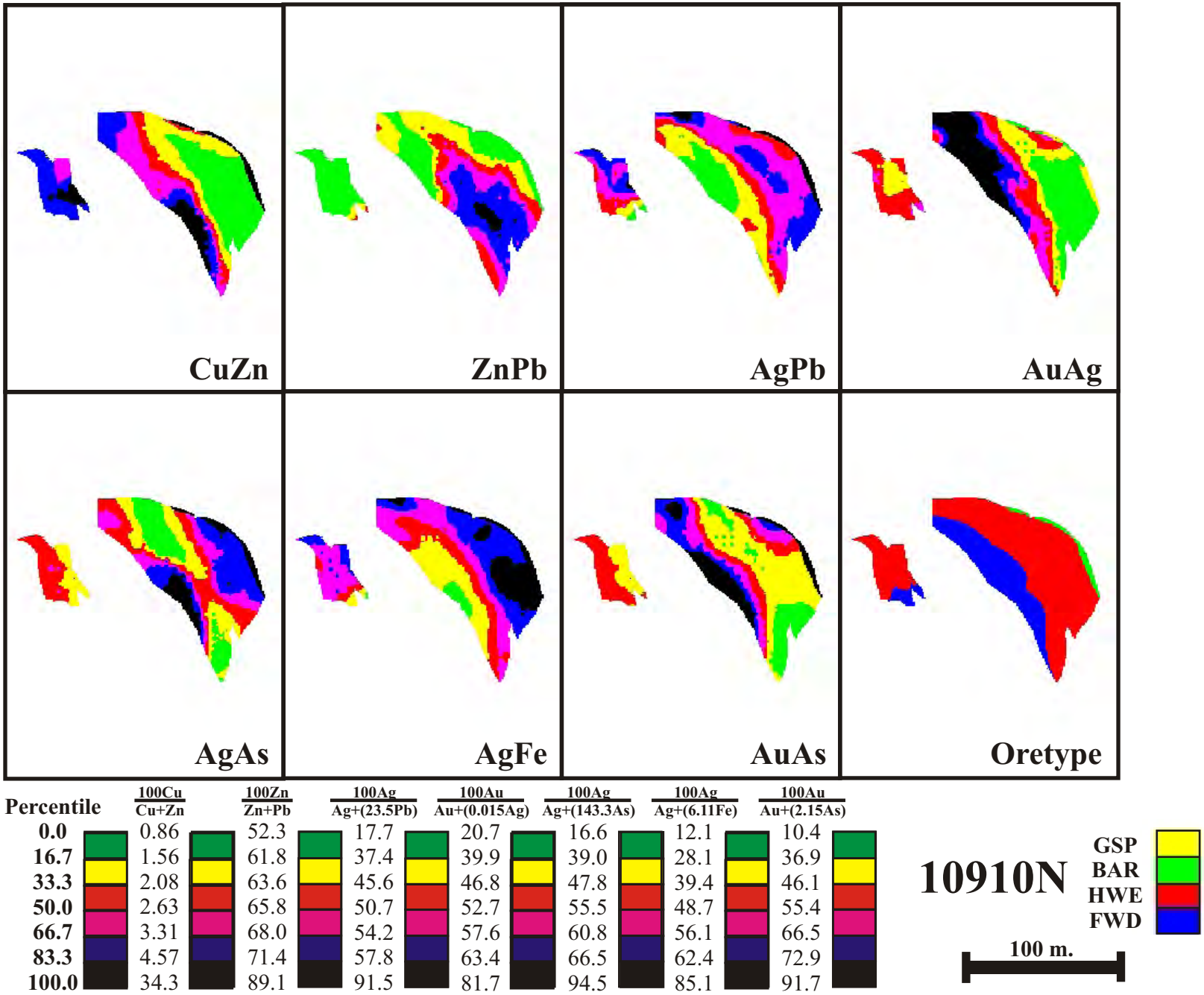

Figure 80 - Selected metal ratio zonation pattern from the kriged 3D model for cross-section 10910N
(Ag-Pb, Au-Ag, Ag-As, Ag-Fe, Au-As ratios have been normalised to overcome magnitude discrepancies)

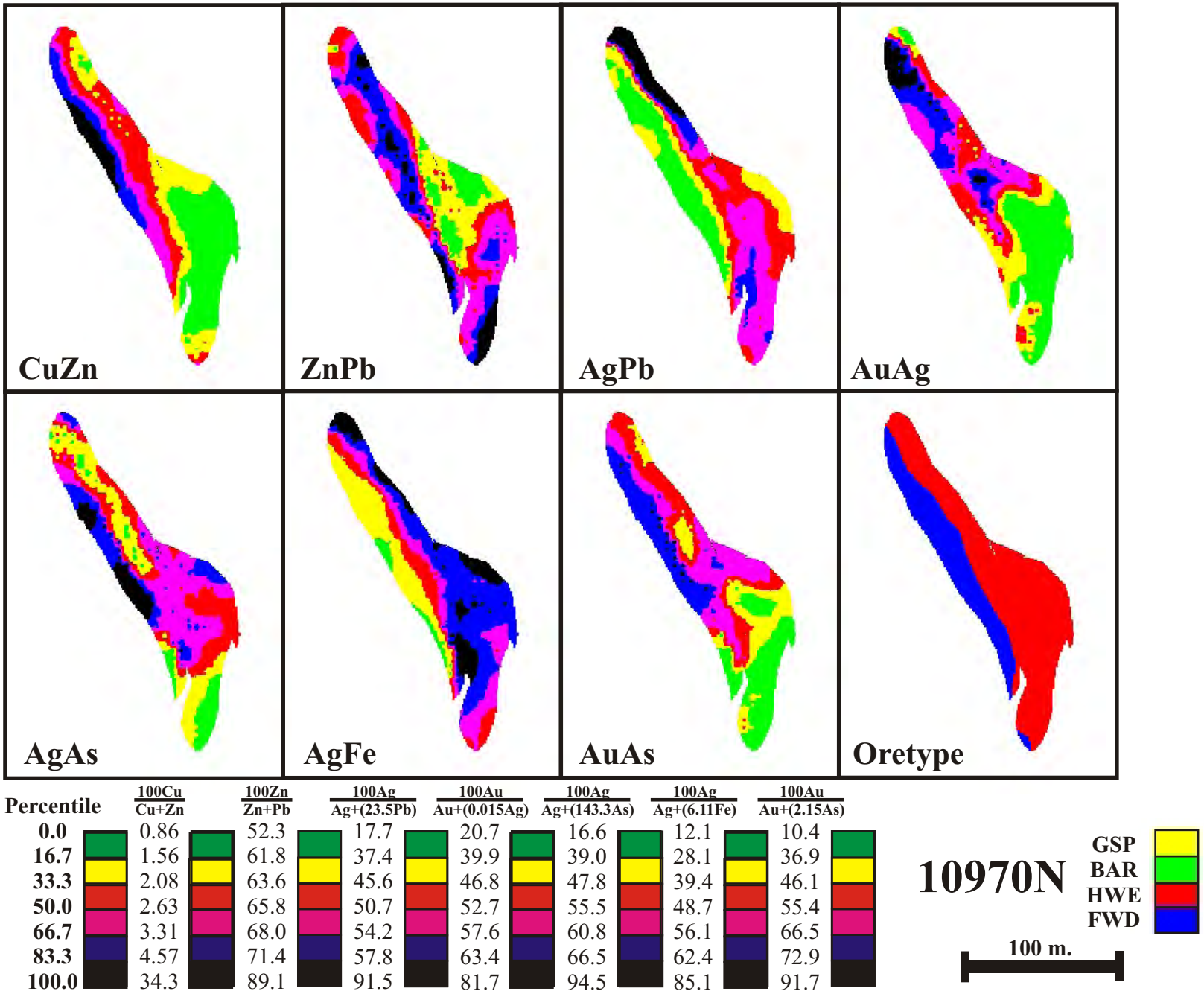

Figure 81 - Selected metal ratio zonation pattern from the kriged 3D model for cross-section 10970N
(Ag-Pb, Au-Ag, Ag-As, Ag-Fe, Au-As ratios have been normalised to overcome magnitude discrepancies)

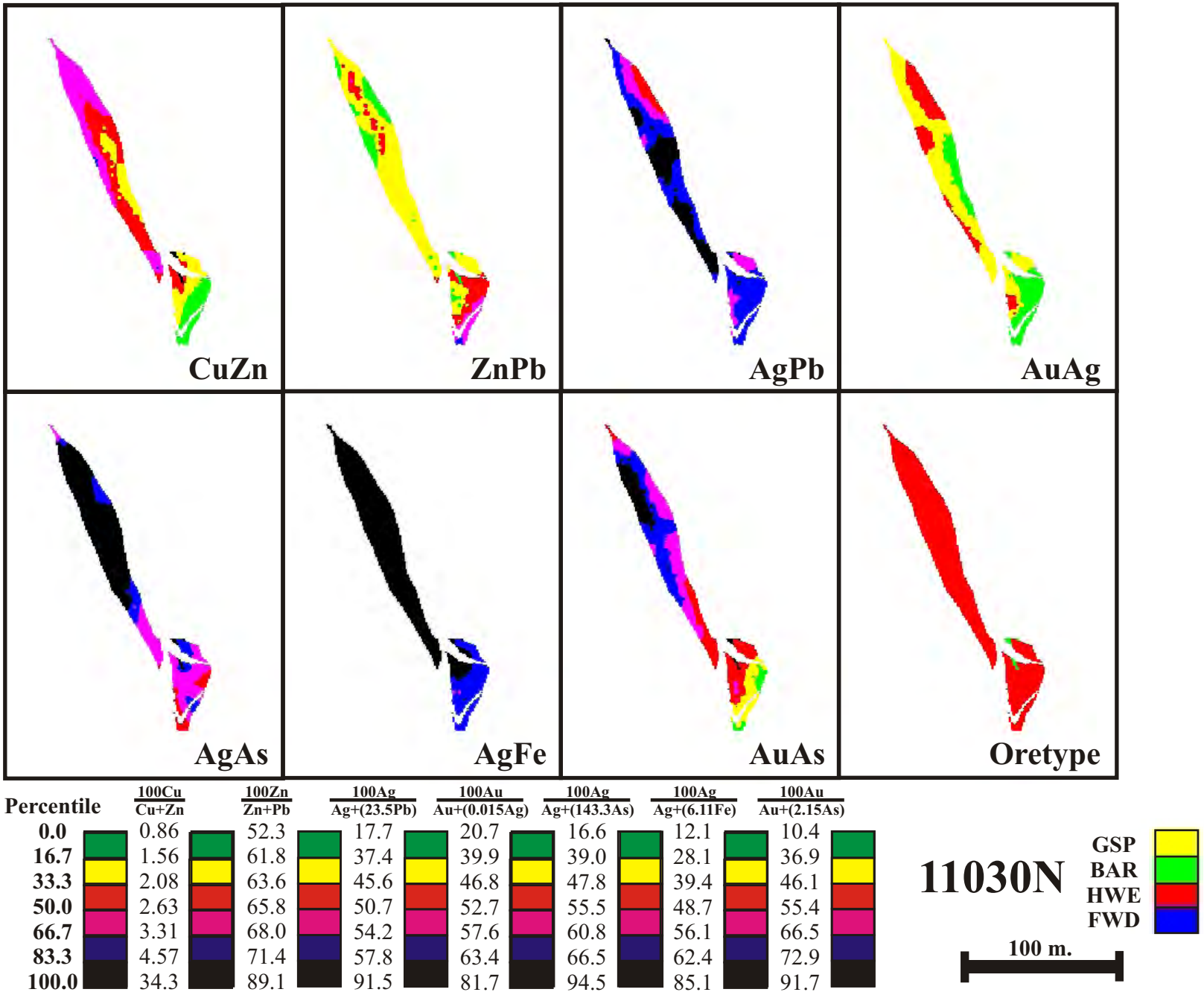

Figure 82 - Selected metal ratio zonation pattern from the kriged 3D model for cross-section 11030N (Ag-Pb, Au-Ag, Ag-As, Ag-Fe, Au-As ratios have been normalised to overcome magnitude discrepancies)

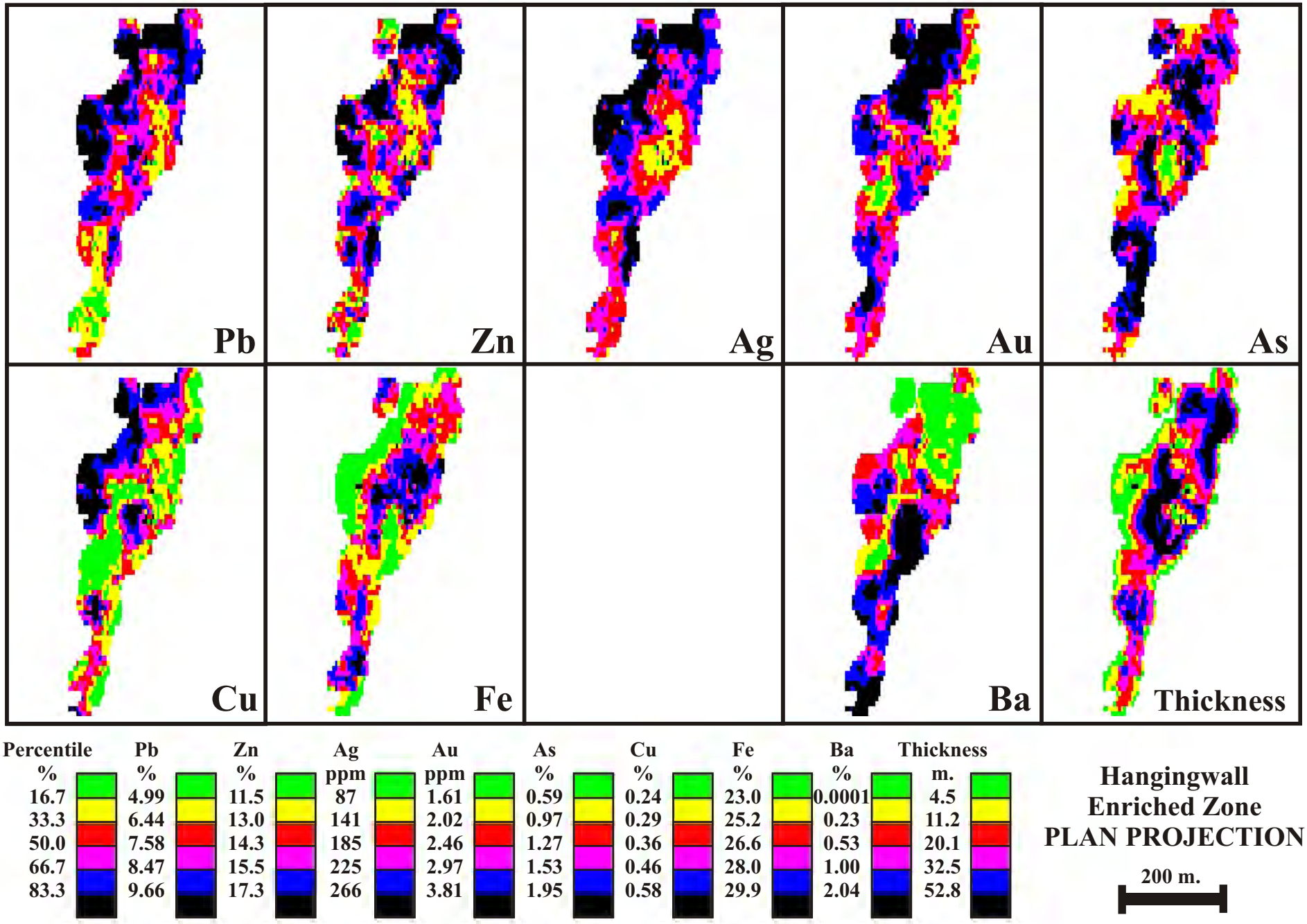

Figure 83 - Metal zonation pattern from the kriged 3D model for the hangingwall enriched zone (HWE) plan projection.
The Jack Fault displacement has been removed by shifting the eastern block 130m south.

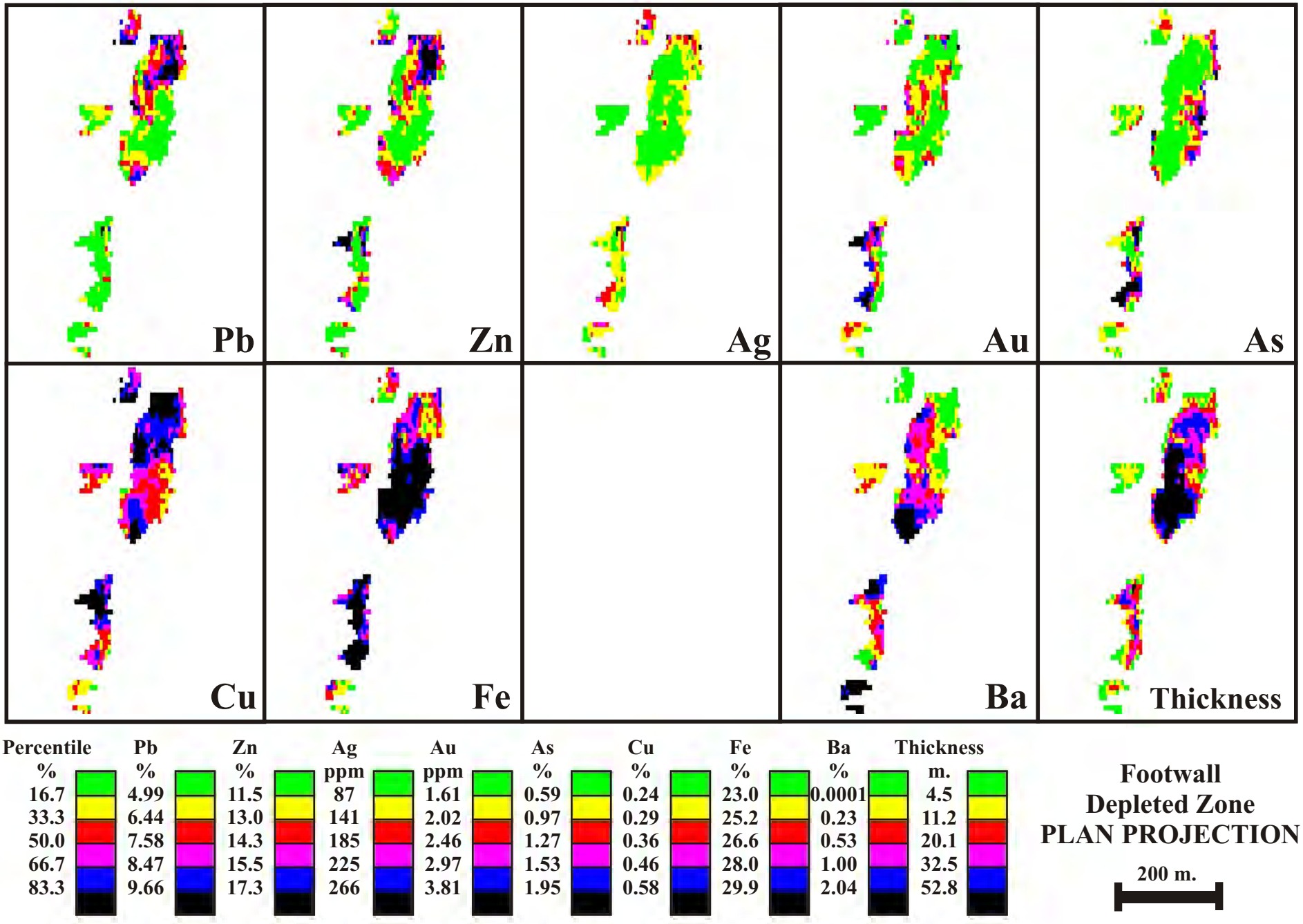

Figure 84 - Metal zonation pattern from the kriged 3D model for the footwall depleted zone (FWD) plan projection. The Jack Fault displacement has been removed by shifting the eastern block 130m south.

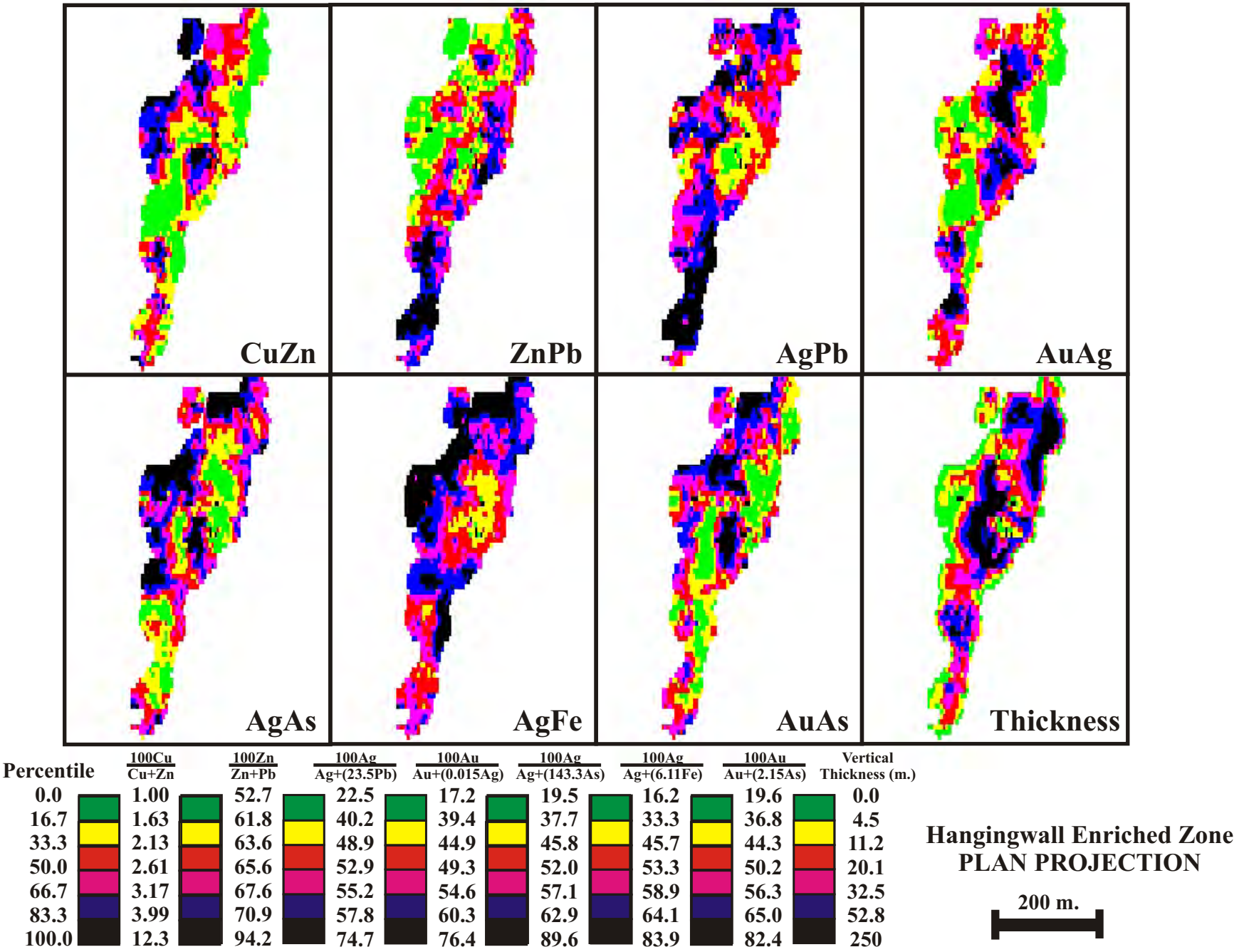

Figure 85 - Selected metal ratio zonation pattern from the kriged 3D model for the hangingwall enriched zone (HWE) plan projection.
The Jack Fault displacement has been removed by shifting the eastern block 130m south.
(Ag-Pb, Au-Ag, Ag-As, Ag-Fe, Au-As ratios have been normalised to overcome magnitude discrepancies)

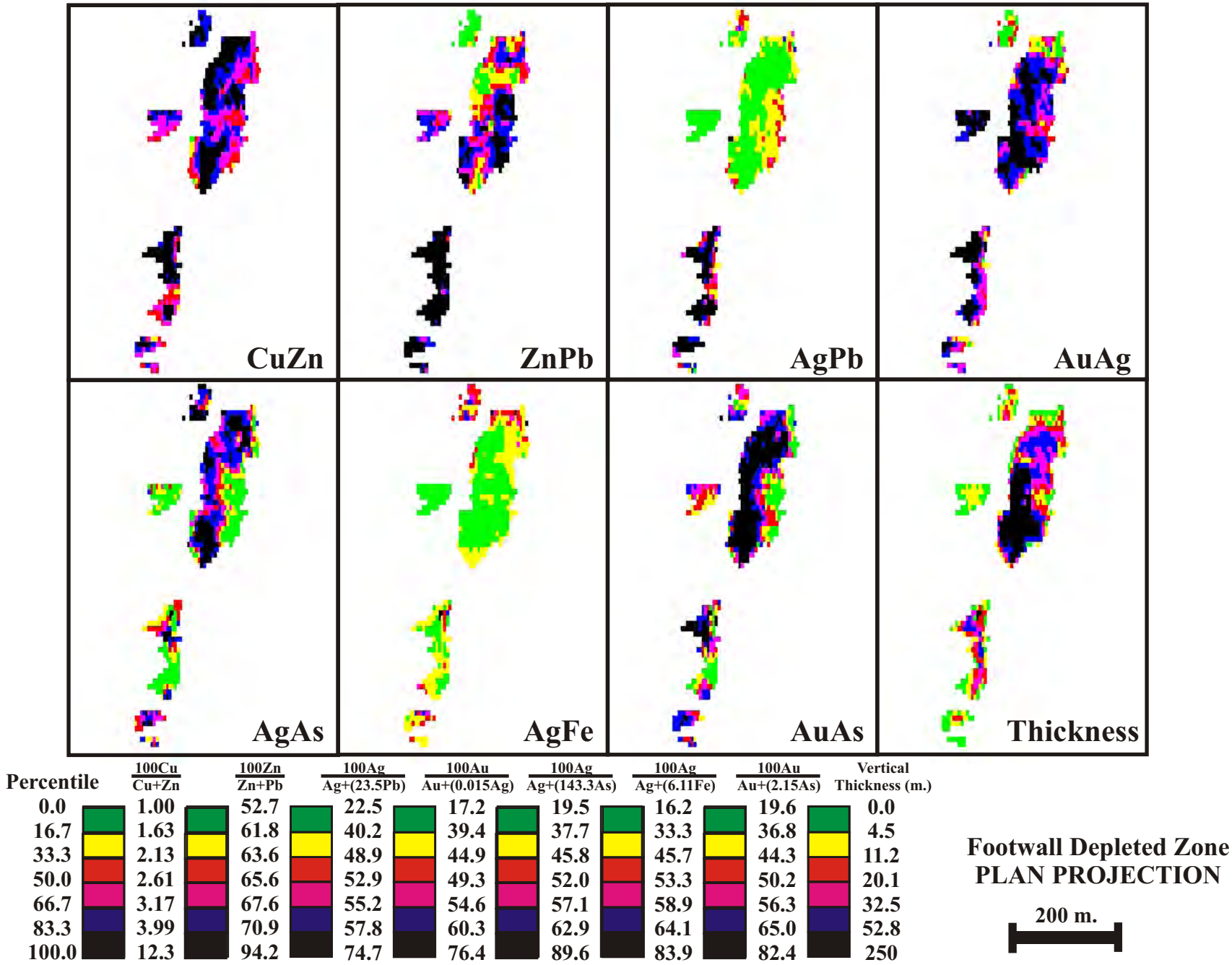

Figure 86 - Selected metal ratio zonation pattern from the kriged 3D model for the footwall depleted zone (FWD) plan projection.
The Jack Fault displacement has been removed by shifting the eastern block 130m south.
(Ag-Pb, Au-Ag, Ag-As, Ag-Fe, Au-As ratios have been normalised to overcome magnitude discrepancies)

grades distal (slightly beyond Pb), very regular "stratiform" arrangement

Au - general concentric zonation surrounding the footwall feeder zone with highest grades distal (approximating Ag), can be complex at intermediate lateral distances from the feeder, rich at both South End and North End

As - general concentric zonation surrounding the footwall feeder zone with highest grades distal (slightly distal of Ag, Au), very rich at South End

Cu - enrichment proximal to the footwall feeder zone often extending completely from footwall to hangingwall, "plumose" lateral enrichment on the massive sulphide hangingwall

Fe - enrichment proximal to the footwall feeder zone (more proximal than Cu), complex arrangements distally

Ba - apart from obvious enrichment in the BAR oretype and adjacent hangingwall massive sulphide, Ba is generally concentrated within the massive sulphide in a transgressive zone on both sides of the Jack Fault, anomalous stratiform footwall enrichment 10910-10970N, rich throughout the South End

Cu-Zn ratio - highest values proximal to the footwall feeder zone (more proximal than Cu), strong contrast over short distances, most definitive ratio of all

Zn-Pb ratio - highest values proximal but distal of Cu-Zn (e.g. 10670N/10790N), high values at South End, low values at North End

Ag-Pb ratio - general concentric zonation surrounding the footwall feeder zone, occasional anomalous high values in proximal areas (e.g. 10670N), not as stratiform and regular as Ag

Au-Ag ratio - highest values very proximal, slight increase at hangingwall (similar to

Cu), high values extend across BAR zone

Ag-As ratio - highest values proximal (distal of Au-Ag ratio) and distal e.g. 10910N, low values at South End, high values at North End

Ag-Fe ratio - identical to Ag zonation, except high values in BAR oretype

Au-As ratio - highest values proximal, similar to Ag-As but less concentration of high values on the distal hangingwall

Plan projection zonation

Analysis of the plan projections for both massive sulphide oretypes basically supports the observations made from the cross-sections. The vertical thickness plot (Fig. 84) clearly outlines a central, dominant, elliptical core of depleted oretype that is coincident with depleted Pb, Zn, Ag, Au and As and enriched Fe. This zone directly overlies the "central feeder" of Gemmell and Large (1992) as reproduced in Figure 21. Evidence for a "southern feeder" is shown by the elongate zone of FWD thickness and high Fe content also in Figure 84. This does not exactly match the position shown in Gemmell and Large (1992) but their analysis was based on much less drilling in the South End. There is only weak evidence to support the "northern feeder" of Gemmell and Large (1992): the northern extension of FWD thickness is not matched by a corresponding Fe enrichment, although there is some Cu concentration. On the other hand, the HWE thickness zones (Fig. 83) coincide with the two synclines, controlled largely by primary seafloor topography (Fig. 16, Downs, 1993).

The depletion observed for Pb, Zn, Ag, Au and As within the FWD over the central feeder is also reflected in a coincident (yet less marked) depletion in the overlying HWE oretype. Similarly the HWE is enriched in Fe in this area. This infers that the depletion process directly above the central feeder was active through the whole of the massive sulphide to the hangingwall.

The enrichment in Ba is generally concentrated in two zones. One, more or less spans the Jack Fault, while another is restricted to the HWE of the Keel Zone western "wing". The highest Ba content in the massive sulphide occurs just south of the central feeder where the Jack Fault suddenly changes strike from north-northeast to north. This suggests that the Mesozoic faulting suggested by Berry (1989) and Downs (1993) has provided openings parallel to the Jack Fault for remobilisation of barite at least within the massive sulphide.

The Cu-Zn, Au-Ag and Au-As ratios show high values, while the Zn-Pb, Ag-Pb and Ag-Fe ratios show low values over the central feeder. In fact, the Ag-Pb ratio pattern shows remarkable similarities to the As pattern, suggesting an important link between the depositional processes and the chemistry of these three metals.

4.5 Summary

To summarise, I present a concluding schematic diagram (Fig. 87) which shows interpreted areas of enrichment/depletion over stratigraphy-proximity space. Bear in mind this drawing must be deliberately diagrammatic, and is definitely not to scale! It merely represents an overall summary statement built from both the disciplined spatial analysis and other less scientific "impressions" gained by the author over the years.

The overall zonation trend at Hellyer is:

Fe→Cu→Zn→Pb→Ag→Au→As→Ba (from proximal→distal)

which closely follows those described by other workers for other volcanic-hosted massive sulphide deposits (well summarised by Large; 1977,1992, but also ably covered by Franklin et al., 1981 and Eldridge et al., 1983). The single anomaly in the whole zonation pattern is the Cu enrichment near the hangingwall contact.

The two most influential parameters controlling grade zonation at Hellyer have been

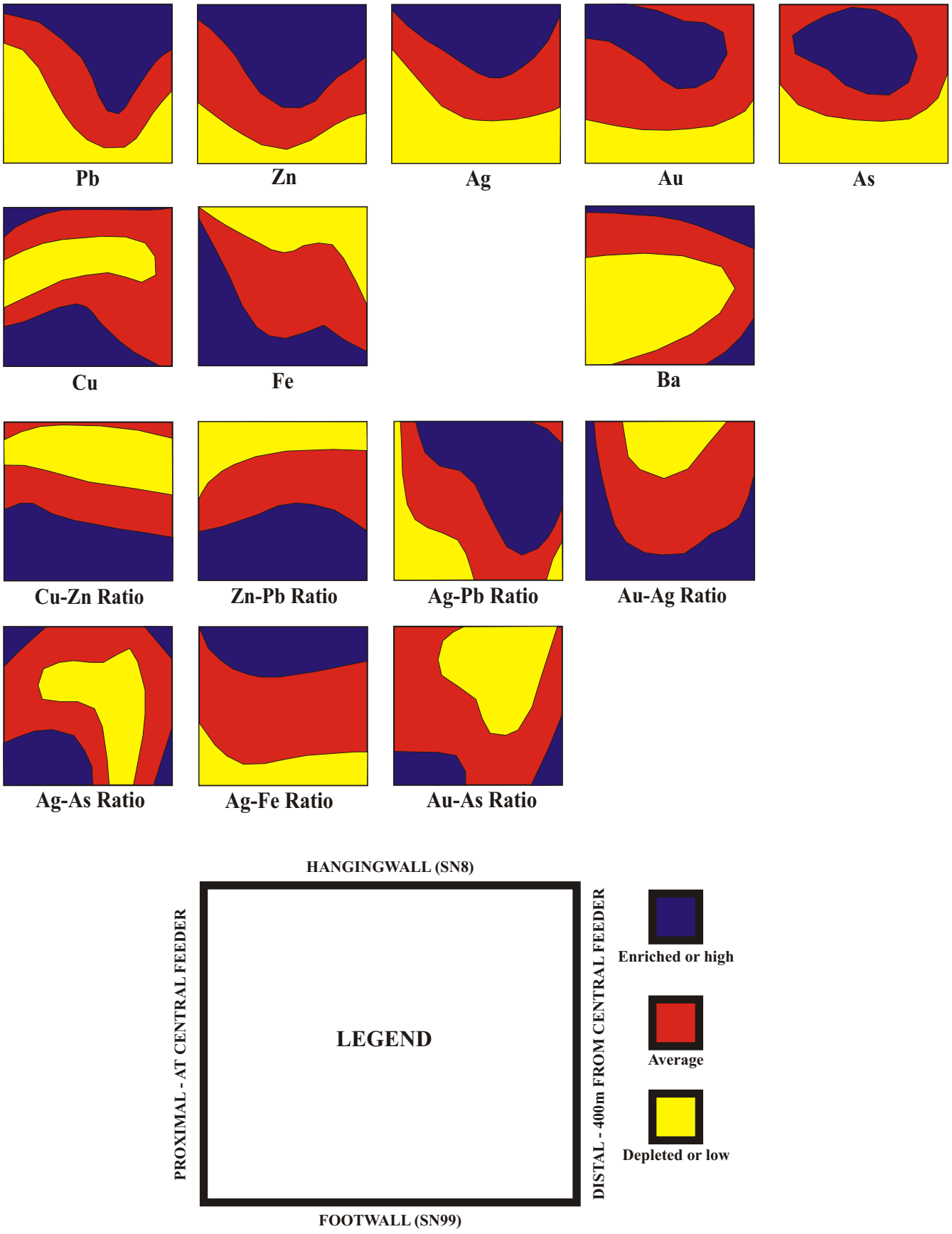

Figure 87 - Schematic summary of metal and metal ratio zonation patterns in the Hellyer massive sulphide

demonstrated to be stratigraphic position and distance from the central feeder. Theauthor's judgement is that perhaps two-thirds of the variability can be explained in terms of these two spatial locaters - the remainder are local, probably deformational and/or remobilisation features that defy modelling on a deposit scale.

Clearly, metal distribution at Hellyer is strongly related to thermal gradients within the evolving sulphide mound, that control metal solubility/deposition. The thermal gradients within the mound resulted from the opposing influences of a footwall feeder heat source and overlying cold seawater.

5. MASSIVE SULPHIDE MICROTEXTURES

5.1 Introduction

5.1.1 Overall objective

The aim of this microtextural study was to make a comprehensive, detailed assessment of the textural variety within the Hellyer deposit in a representative 3-dimensional context so as to permit an interpretation of the deposit's evolution.

5.1.2 Observational philosophy

The author made a deliberate decision to use disciplined scientific objectivity when making all microscopic observations. From the beginning, a considerable amount of detailed data were collected in a concise, systematic way so that there would be little need to go back to re-assess earlier observations. Some of the data collected, proved in the end, to be of no use in the concluding interpretation. Nevertheless, the data remain in readily accessible format for possible further study.

5.2 Sampling

5.2.1 Representivity

Representivity of samples is rarely addressed in most geological studies today. Due to time and budget constraints, or just plain ignorance, many workers (in the worst case) collect too few samples and then over-apply technological investigatory methods to arrive at an all-encompassing over-interpretation. In this study, sample selection was conducted carefully in an unbiased way to maximise representivity. Comparison of sample assays with global resource grades enabled direct measurement of the representativeness.

5.2.2 Core sample selection

In the beginning, when the research plan was being designed, the author envisaged a sample density of 300 polished sections over the deposit (i.e. the deposit as known in 1989 by 20m-spaced drilling, 10550N-11030N). As far as practicable, each sample should represent an equivalent volume. It was also decided that the drill core from every 3rd 20m-spaced cross-section would be sampled. In this way, the sampled ore on the western side of the Jack Fault could be reconstructed with the sampled ore on the eastern side; because (2 x 60m) = 120m would approximate the measured Jack Fault displacement of 130m. The area of defined orebody on each 60m-spaced cross-section was therefore measured (Table 16).

Table 16 - Orebody cross-sectional areas for the sampled sections

Section	Area m^2	Ideal no. of samples	Final no. of samples
10550N	2234	12	6
10610N	4049	22	19
10670N	11217	62	60
10730N	8803	49	50
10790N	7250	40	39
10850N	3799	21	20
10910N	6007	33	36
10970N	7947	44	45
11030N	2966	17	16
TOTAL	**54272**	**300**	**291**

From the table above, each ideal sample represented $181m^2$ of cross-sectional area. If a square grid on each cross-section is assumed, then samples were ideally required at the intersection points of a $\sqrt{181}$= 13.45m grid.

Available sample material (i.e. archived half drill core) obviously was not distributed over the cross-section to the required grid. A computer macro (i.e. programme) was written to search the entire length of all drilled orebody intersections within 10m of the nominated cross-section, and select a sample interval (1 or 2 metres) that was the shortest distance from each grid intersection point (Figure 88). On some sections, where drill density was locally sparse, the macro returned duplicate samples: these were deleted, so that the final total number of samples became 291.

Once the target sample locations were established, final sample selection was done in the core shed by taking the most representative 10cm piece of half-core from within the target interval. On some occasions the selection representivity was somewhat compromised by very broken core. Fortunately, this only tended to occur in homogeneous strongly recrystallised pyritic areas.

The sample was named using the following convention:

nn-hhh-ddd.d

where **nn** = truncated section northing, e.g. 67=10670N
hhh = hole number, e.g. 050=HL050
ddd.d = downhole depth to nearest 0.1m

5.2.3 Sample processing

Once all samples had been selected and bagged, they were individually examined for logging of macroscopic texture (using the coding system described in section 3.5.1) and marked for polished thin section preparation. A 50mm X 25mm area that was most representative of the total available flat surface was selected on the half drillcore. Where banded or layered textures were obvious, the area was selected to intersect the banding at the maximum possible angle. However, since most of the drillcore was TT46 size (36mm diameter), it was necessary to align the selected area more or less sub-parallel to the core axis.

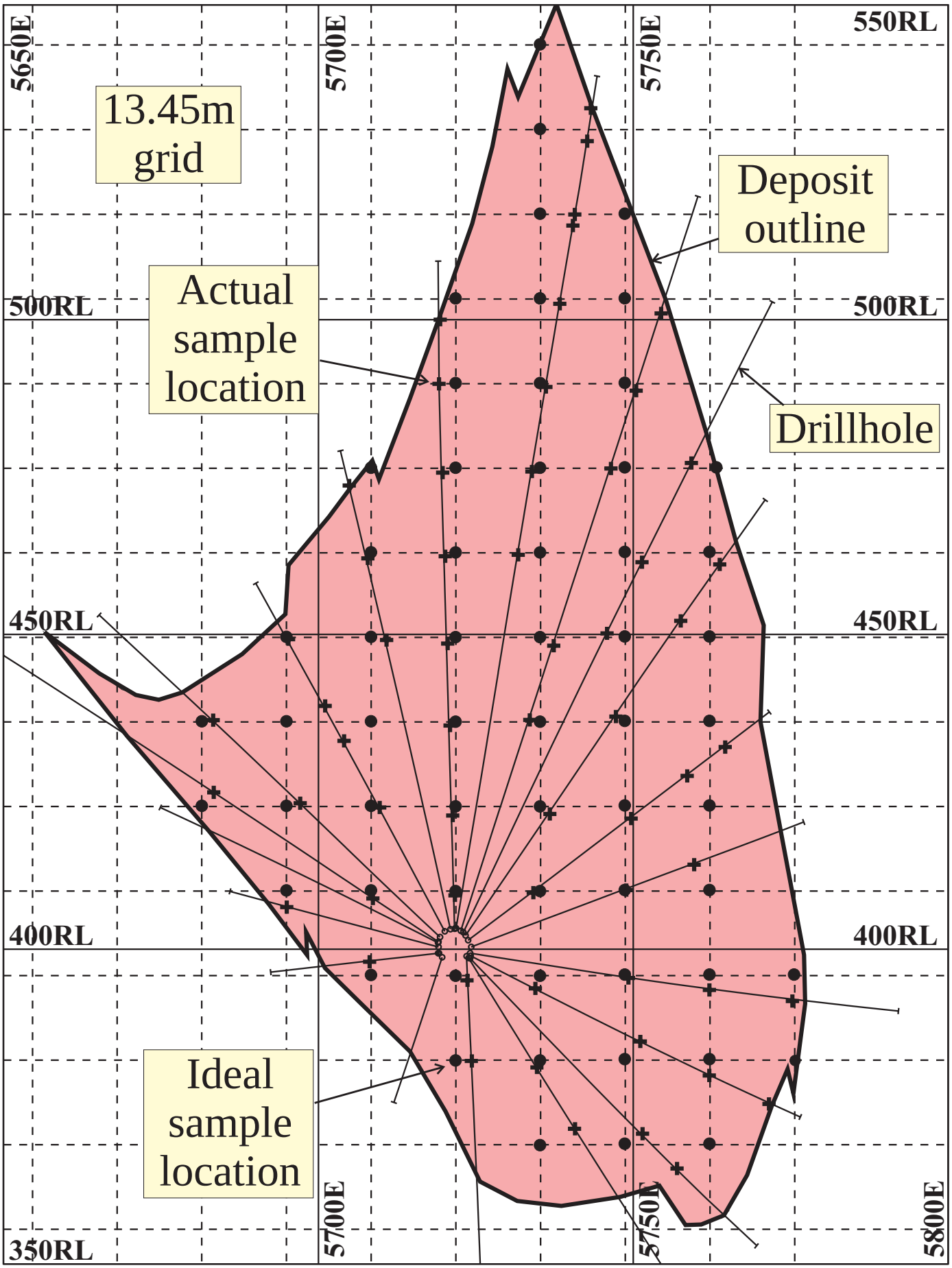

Figure 88 - Example of grid selection method as applied to available drillcore on cross-section 10670N

Standard polished thin sections were prepared by Ian Pontifex and Associates of Adelaide. The samples chosen on section 10850N were doubly polished, in expectation that sphalerite growth textures may be visually enhanced. Unfortunately cost constraints did not permit this to be extended to all samples. Pontifex was instructed to cut a ~5mm slice from the top of the sample (containing the area marked for sectioning) and to bag and return the remaining slab as a macroscopic reference archive. The 5mm slice was then cut to the 50mm X 25mm area as marked; the offcuts being separately bagged and returned for assay (Figure 89).

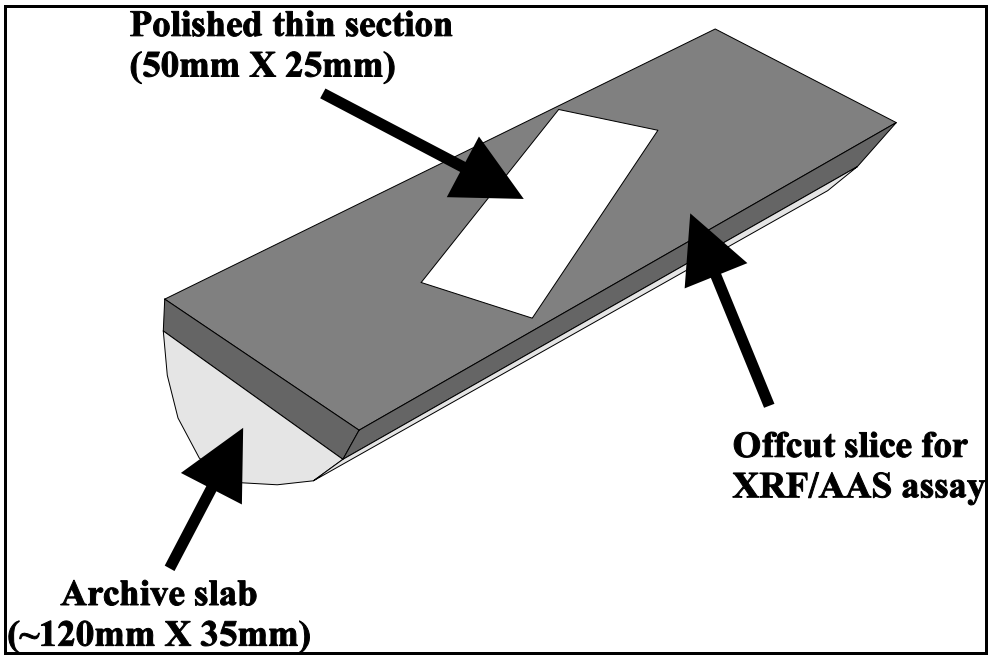

Figure 89 - Method for subdividing the half-core sample

The sample offcuts were submitted to Aberfoyle's laboratory for analysis. S.G. was measured on the pulp using an air pycnometer; Cu, Pb, Zn, Ba and As were determined using XRF; Ag, Bi and Sb by AAS, and Fe by a high quality titration method. Analabs provided a Au fire assay. A full listing of these assays is included in Appendix I(a). The representivity of the samples can be judged by their average assay, compared to the virgin resource grades for the same area (10520-11060N) (Table 17). All elements compare well, except Zn. This anomaly can only be explained by some unintentional bias towards sphalerite when the core pieces were selected.

Table 17 - Comparison of thin section sample assays to virgin resource

Element	Thin section samples	Virgin resource
S.G.	4.55	4.57
%Cu	0.38	0.38
%Pb	7.49	7.22
%Zn	14.50	13.54
ppm Ag	155	163
ppm Au	2.56	2.44
%Ba	2.18	2.53
%As	1.08	1.07
%Fe	26.5	27.3

5.3 Microscopic observations

5.3.1 Introduction

Microscopic observations were carried out using Aberfoyle's Nikon Labophot polarising microscope fitted with 5X, 10X, 20X, 40X and 100X(oil) objectives. An incremental stage was used for point counting and all photomicrography was done with a Nikon AFX-IIA attachment.

Work commenced with samples from 10550N and advanced northwards. **Unfortunately, examination of the full programme of 291 samples was not completed due to time constraints.** 174 thin sections were examined from sections 10550N, 10610N, 10670N, 10730N and 10790N. The last 29 samples (from 10790N) were documented in less detail but were point counted more comprehensively.

5.3.2 Point counting

Prior to commencement of point counting, an overall scan of the polished section was carried out and features worthy of further observation noted on a 6.5X scale map (Figure 90). At this stage all minerals were identified.

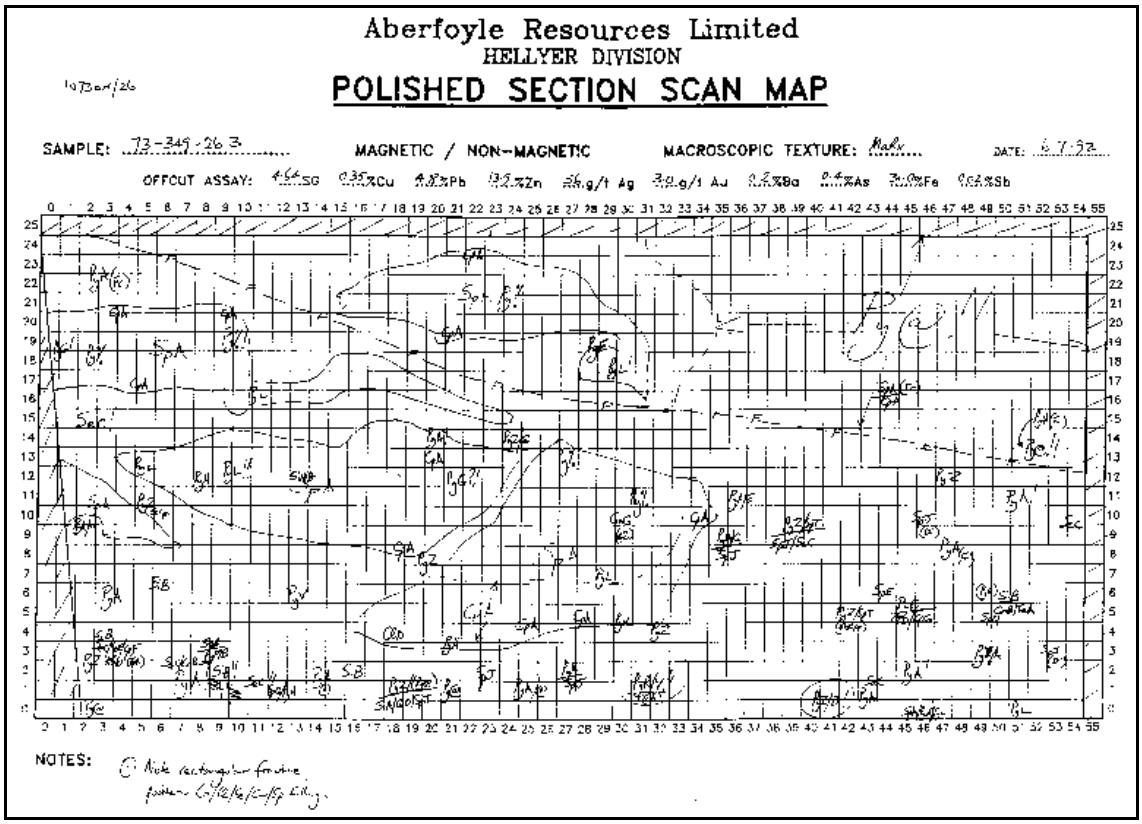

Figure 90 - Example polished section scan map drawn prior to point counting (39% of actual size)

Point counting was considered an essential part of the study to obtain quantitative estimates of gangue mineralogy which could not be determined from the available assays.

For the first 145 samples, grid point counting was done for approximately 430 points over the central 25mm X 25mm of each polished section. Five rows, aligned longitudinally 5mm apart, each included 86 points. This point count area was restricted because of mechanical limitations with the available incremental stage. Counting was made efficient by the use of a tape recorder with playback tallying (Figure 91). A spreadsheet program was then used to calculate a theoretical assay

from the mineralogical composition. This could then be compared to the offcut assay to check for any major anomalies.

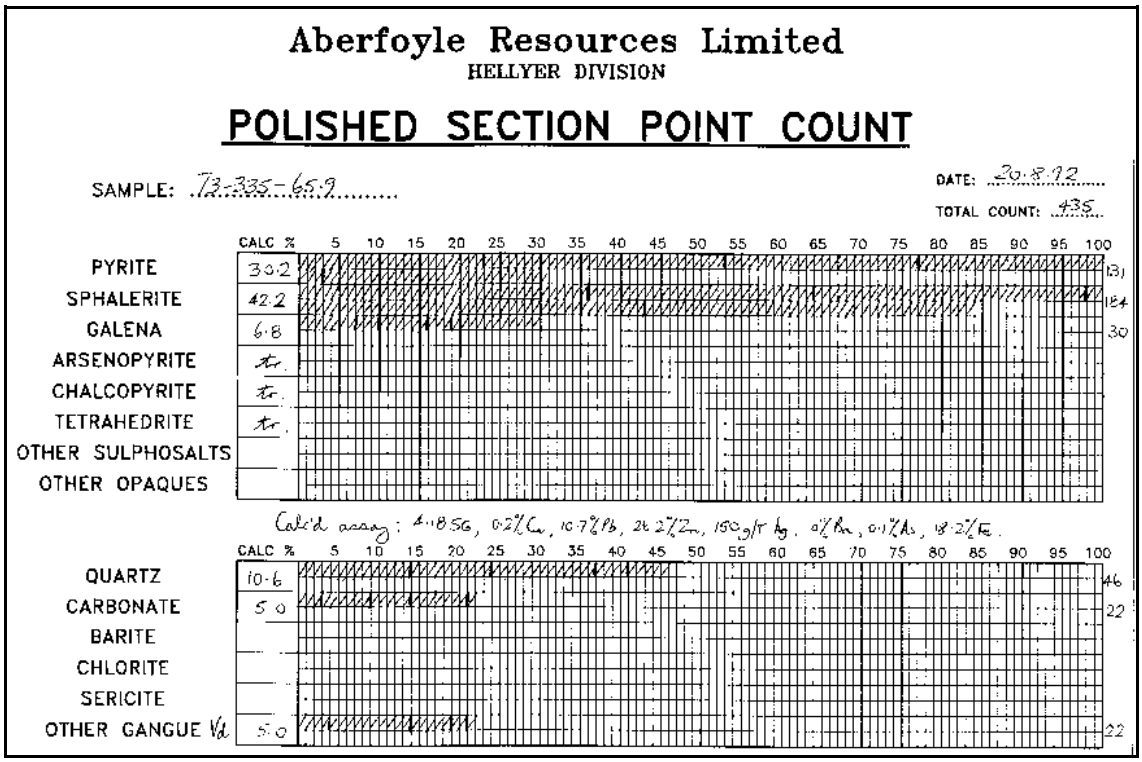

Figure 91 - Example tally sheet used for point counting (51% actual size)

The last 29 samples were point counted in a different way. Approximately 1000 points were counted on a 1.25mm X 1.0mm grid over the complete polished section. Each point was coded with a "mintex" code (see below) directly into a notebook computer. These 29 samples were not described otherwise.

All point count results are listed in Appendix I(a).

To judge the quality and representivity of the point counting, the overall average calculated assay for the 174 polished thin sections can be compared to the average of the offcut assays and the global virgin resource grades (Table 18).

Table 18 - Point count "assays" compared to offcut assays and deposit global grade

Element	Point count calculated assay	XRF/AAS offcut assay	Deposit global virgin grade
S.G. (bulk)	4.48	-	4.50
S.G. (pulp)	4.55	4.57	4.57
%Cu	0.41	0.37	0.39
%Pb	7.7	6.9	7.1
%Zn	13.8	13.7	13.9
ppm Ag	168	135	168
%Ba	2.8	3.3	2.0
%As	0.82	0.83	1.2
%Fe	26.7	26.7	27.5

All point count "assays" compare remarkably well with the offcut laboratory assays, except Pb and Ag. The author has no explanation for the Pb anomaly since galena is a readily identifiable mineral with a comparatively fixed composition. The Ag is within acceptable limits given: (a) the very poor count statistics for tetrahedrite and (b) the variable Ag content of tetrahedrite and galena. Compared to the overall deposit grade, all elements are representative except As. This is an unfortunate outcome from having to limit the study to 10550N-10790N, which is relatively depleted in As.

5.3.3 Texture classification

The author has developed for this study, a texture classification system that "pigeon-holes" individual mineral textures according to their habit and mineral associations. Each specific mineral-texture occurrence is termed a **"mintex"**. The three-character mintex codes are made up of a two-character mineral prefix, e.g. Py for pyrite, and a single-character suffix as the unique identifier (A-Z, a-z, etc.). Mintex codes were defined as they appeared during the ongoing microscopic observations. Therefore, the

originally ascribed code bore no relationship to depositional sequence; but was simply a convenient sequential label to classify textures as they became apparent. When the microscopic observations were completed towards the end of the project, textural sequence analysis of all the collected data enabled interpretation of the depositional history. Consequently, all the mintex codes have now been renamed so that they approximately reflect the interpreted crystallisation sequence (Appendix II). Some of the mintex are very similar, and in hindsight, should have been merged into one. The author has decided not to merge any codes, but to leave the classification in tact and to comment on any similarities. Table 19 shows the expanse of the mintex system, in decreasing order of abundance.

5.3.4 Textural database

With an expectation that vast amounts of observational data would be collected in the microtextural study, it was decided to attempt to use a rigorous database approach - one that would not only prompt the microscopist to look for certain features, but also to collate the data in a structured, yet easily retrievable format. To the author's knowledge, this method has not been applied before to textural analysis.

When microscopic observations commenced in 1991, Aberfoyle was using DOS-based Paradox™ database software at Hellyer. Assistance was provided by mine staff to set up a database using this software.

Several database tables were established:

- polished thin section offcut X,Y,Z locations and assays
- mineral volume % from point counting
- mintex codes and descriptions
- codes for textural description
- all microscopic observations
- photomicrograph locations, camera settings and descriptions

Table 19 - Minerals identified in decreasing order of volume abundance showing the number of mintex codes

Mineral	Code	Global volume %	No.of textural types
Pyrite	Py	47.5	40
Sphalerite	Sp	23.9	23
Quartz	Qz	6.84	19
Galena	Gn	5.10	22
Barite	Ba	4.72	7
Carbonate	Co	3.87	16
Sericite	Se	2.41	10
Chlorite	Cl	1.75	12
Arsenopyrite	As	1.03	16
Chalcopyrite	Cp	0.98	12
Tetrahedrite	Te	0.21	12
Clays	Cy	0.07	1
Bournonite	Bo	0.04	6
Magnetite	Mg	0.03	4
Hyalophane	Hy	0.02	1
Rutile	Ru	<0.01	2
Pyrrhotite	Po	<0.01	2
Cubanite	Cb	<0.01	2
Pyrargyrite	Pg	<0.01	2
Marcasite	Ma	<0.01	1
Boulangerite	Bg	<0.01	2
Hematite	He	<0.01	1
Miargyrite	Mi	<0.01	1
Argentite	Aa	<0.01	2
Native antimony	Sb	<0.01	1
Electrum	Au	<0.01	3
Void	Vd	1.6	2
TOTAL		100.00	222

The latter four tables were made always visible on the notebook computer screen beside the microscope, so that they could be easily edited or appended to, as new observations were made. All microscopic data was entered directly into the database, no other notes were taken. After all the data was collected, it was converted in 1995 to a modern Windows-based database, Microsoft Access™. Full text listings of the Access database as it now exists are provided in Appendix I(a).

5.3.5 Photomicrography

Photomicrography is clearly the most convenient way to document textural characteristics. It was essential to take an enormous number of photographs as microscopic observations progressed, to ensure adequate documentation of textures that may not have occurred in later samples. The first 363 photographs were taken on print film, but variability in processing resulted in unacceptable colour differences. All the remaining photographs were taken using Kodachrome 64 slide film (processed routinely by Kodak). Light intensity was set at the same setting throughout and manual override over the automatic exposure equipment was only necessary for crossed nicols illumination. Despite the care taken, variability of mineral colour in the returned slides was still apparent, presumedly due to varying film age and processing differences. All 2919 returned slides were checked, labelled, and then archived in clear plastic holders in mintex-photo number sequence.

When observations and photography were complete, all photomicrographs were examined in detail and up to eight (usually four or less) slides were selected as the best examples of each mintex. When some very minor mintex's were discovered to have no photograph, polished sections were retrieved and additional photographs taken. The set of **603 "best example" slides** were then digitally scanned by Kodak Australia into PhotoCD format. These digital files are stored on 7 compact discs and can be quickly retrieved, viewed, manipulated and re-saved using any bitmap image software such as Photoshop™ or Corel Photo-Paint™. Each digital image can be accessed in varying resolutions:

coarsest:	128 X 192 pixels	72K bytes
	256 X 384 pixels	288K bytes
	512 X 768 pixels	1.13M bytes
	1024 X 1536 pixels	4.50M bytes
finest:	2048 X 3072 pixels	18.0M bytes

After experimentation, it was found that the intermediate resolution of **512 X 768** pixels provided adequate sharpness for a postcard size image (each pixel = ~0.1mm on the print) printed with a 300 dpi ink-jet plotter. The effective pixel dimension for each microscope objective is shown in Table 20. These digital resolutions would probably exceed the optical acuity of the objectives.

Table 20 - Effective pixel dimension of digitally scanned photographs (512 X 768) for each microscope objective

Microscope objective used	Effective pixel dimension (μm)
5X	3.1
10X	1.5
20X	0.8
40X	0.4
100X	0.2

The digital images are readily imported into word processing or CAD software at any required magnification for addition of annotation, scale bars etc. Further notes on the manipulation of the digital images are included in Appendix II (page J).

5.3.6 Textural atlas (Appendix II)

A major objective of this study was to produce a large format detailed atlas of observed microtextures. This volume is basically a pictorial compilation of all the facts and interpreted paragenesis covering the wide diversity of Hellyer microtextures.

The author cannot overstate the importance that rigorous, systematic microscopy has been to this study. It formed a fundamental basis for all paragenetic interpretation and therefore deserved quality pictorial documentation - documentation which would effectively communicate the microscopic observations to the reader. Reference is made to page K at the front of Appendix II which provides an explanatory legend for each section of the atlas format. For each individual mintex (Fig. 92): cross-sectional oretype plots show spatial occurrence and volume% variability; frequency statistics highlight the texture's relative importance; annotated colour photomicrographs provide visual examples; average microprobe analyses are shown, if available; companion or associated mintex are listed; and finally, the author's interpreted paragenesis is depicted on a stylised timeline.

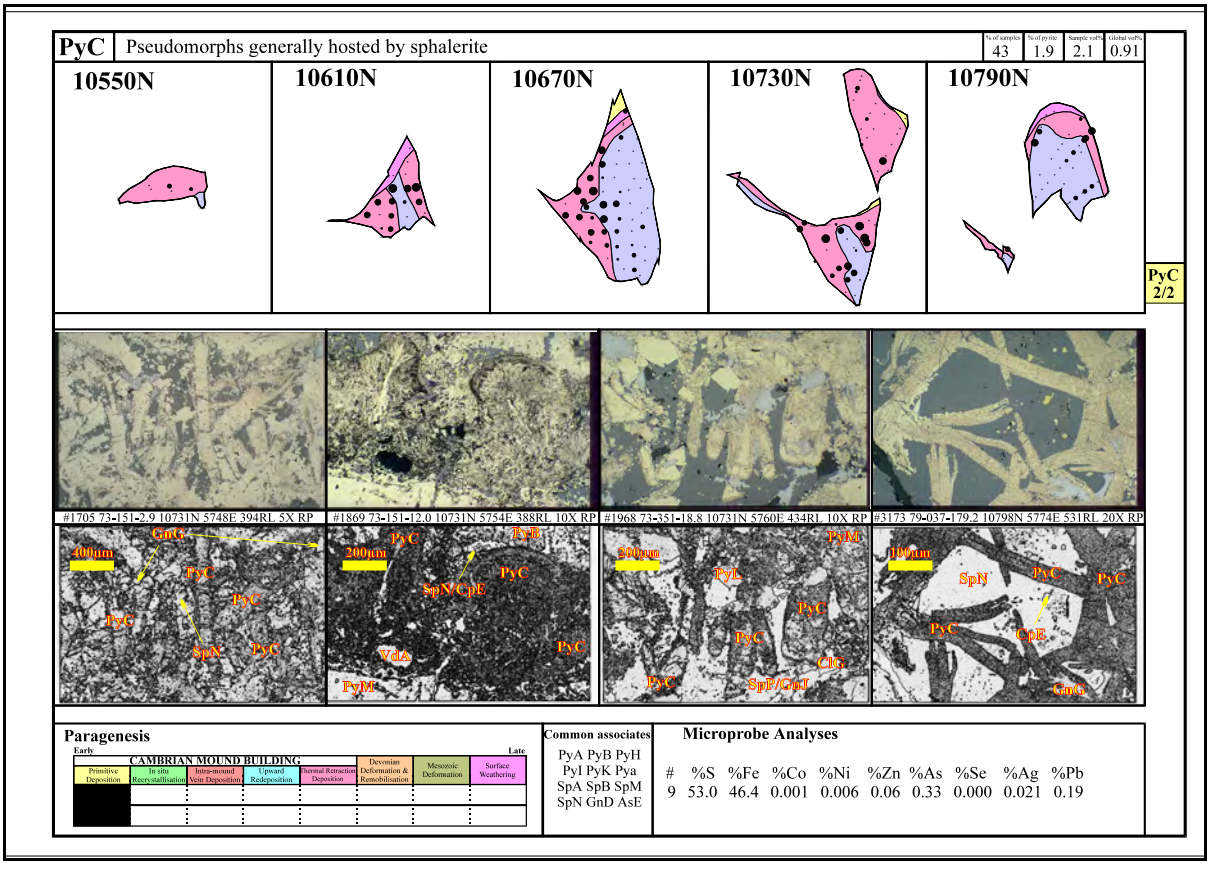

Figure 92 - Example page from the Appendix II textural atlas

5.4 Textural variation

5.4.1 Introduction

The amazing variety and complexity of observed textures at Hellyer presents a real interpretation challenge. The author's approach, has been to break down the complex textural systems into much smaller manageable units (i.e. mintex), study the spatial occurrence of these small units and then interpret the timing relationships between them. Attempts have been made to semi-quantify each mintex, by visually estimating area fractions (assumed to be equivalent to volume %) on each polished section. This ensures that the relative importance of each mintex is fully appreciated - a texture seen in only one or two samples may not be significant.

5.4.2 Textural features

Numerous early workers (e.g. Schneiderhöhn, 1952; Ramdohr, 1980; Craig and Vaughan, 1981) have presented ore texture classification schemes, but these tend to concentrate more on the high temperature textures. The textural features observable in Hellyer polished sections could be broadly categorised as follows (not in any particular order):

crystallinity	interstitial infilling
growth patterns	cross-cutting age relationships
pseudomorphs	intergrowths
deformation-induced	mineral associations
zonal inclusions	possible fossil structures
replacement	unusual characteristic features

The variation observed within these categories in discussed below, supported by example photomicrography (Plates 7-18).

The label shown below each image uses the following notation:

#ppp ss-hhh-ddd.d nnnnnN eeeeE rrrRL mmX RP/RX/TX

where **ppp** = photomicrograph number

ss-hhh-ddd.d = sample (as defined in section 5.2.2)

nnnnnN = sample northing

eeeeE = sample easting

rrrRL = sample RL

mmX = objective magnification used

RP = reflected light, nicols uncrossed

RX = reflected light, nicols crossed

TX = transmitted light, nicols crossed

Crystallinity

A crystallinity (i.e. crystal size) continuum is particularly well demonstrated in pyrite (Plate 7). Spongy, amorphous pyrite, often called *melnikovite*, is fairly common at Hellyer in areas where primitive remnants have been preserved. The range of crystallinity exhibited by pyrite is described below. ***Example A*** on the right, shows the typical brownish, poorly-polished appearance of PyA. Under high magnification, no crystallinity can be found. The brownish colouration appears to be due to uniformly distributed spherical voids or pores, <0.1µm across. An attempt to image these using SEM unfortuneately was unsuccessful. This type of pyrite typically tarnishes on the polished section very rapidly, presumedly due to the increased surface area created by the pore space. When probed, melnikovite is contaminated with Cu, Pb, Ag and As (see section 6.2.1). ***Example B*** (PyW) is only weakly crystalline with "bubbles" ~10µm across, either empty or filled with galena. ***Example C*** (PyM) is particularly common and comprises fine-grained crystalline pyrite with interstitial galena. This form contains much less Cu, Pb, Ag and As. ***Example D*** (PyT) is very crystalline, with highly polished annealed crystals up to 0.5mm. ***Example E*** (PyL) is also very crystalline, in the form of matrix supported cubes that can reach 1mm in size. Both PyL and PyT have very clean probe analyses (very low trace element contents).

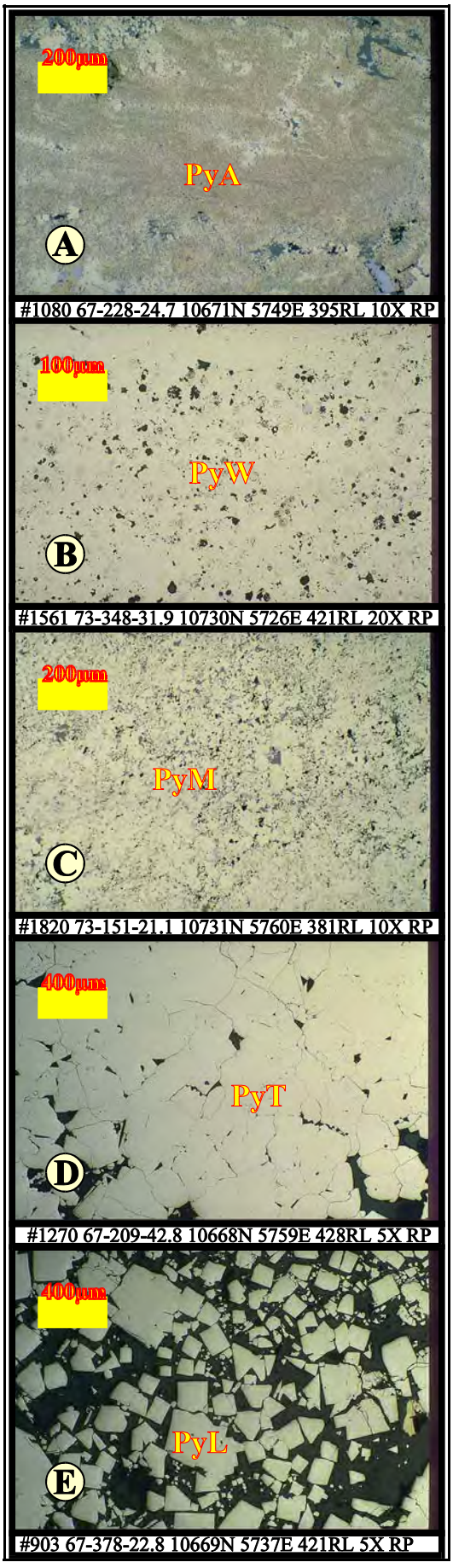

Plate 7 - Examples of crystallinity variation in pyrite➤

Growth patterns

Growth patterns can be seen at Hellyer as either colloform accumulation or as overgrowths (Plate 8). ***Example A*** on the right is a typical example of PyB/SpA colloform accretion, with the characteristic scalloped pattern indicating growth direction (in this case, upwards). In some samples, growth directions are consistent over the whole slide, and in others growth directions show an inwards symmetry, suggesting vein or crack infilling. Colloform pyrite can consist of melnikovite or very crystalline material. ***Example B*** shows a very common form of colloform pyrite (PyS) clearly growing inwards from the walls of a sphalerite crystal vugh (SpP). In this instance the pyrite itself was later infilled by galena and sphalerite (GnG/SpN). ***Example C*** shows spherical nucleii of concentrically grown melnikovite (PyB) that is further overgrown by inward colloform material. The inner voids are filled with chert (QzI). ***Example D*** typifies the euhedral overgrowths of crystalline pyrite (Pyc) over annealed pyrite aggregates (PyT). Probably this feature would be even further enhanced by etching. ***Example E*** is a fine example of chromatic growth bands visible with transmitted light, in annealed sphalerite (SpP). No doubt this feature would be more obvious in doubly-polished sections. Colour variation coincides with subtle changes in Fe content (see section 6.2.2).

Plate 8 - Examples of growth pattern variation➤

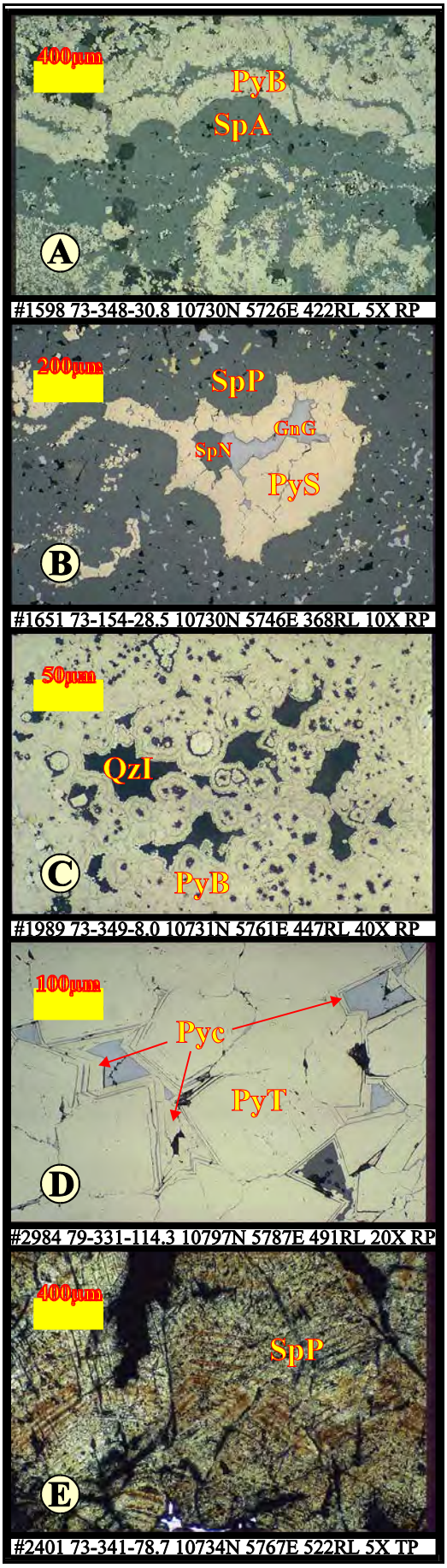

Pseudomorphs

Pseudomorphous replacement of pre-existing crystal forms is commonly seen in the preserved primitive areas of the deposit (Plate 9). In many instances the original mineral that was replaced can be identified by crystallographic shape, e.g. orthorhombic barite, platy pyrrhotite or hexagonal wurtzite, but mostly identification is difficult. Remnants of the former mineral are never seen. ***Example A*** is a typical example of melnikovite (PyI) pseudomorphing "sheafs" of a platy mineral, possibly a hydromuscovite (Alt and Wei-Teh Jiang, 1991), or "icefern" wurtzite (Ramdohr, 1980, p.579). ***Example B*** shows partly spongy pyrite pseudomorphs (PyC) of crystal clusters of sulphate(?) with late interstitial sphalerite (SpN). ***Example C*** shows inward growing crusts of melnikovite containing radiating groups of fine acicular sphalerite pseudomorphs (SpM). Galena (GnD), chalcopyrite (CpD), tetrahedrite (TeC) and rarely arsenopyrite (AsH) pseudomorphs can also take this form. ***Example D*** is a nice example of chert (QzI) pseudomorphing barite(?) crystals in a melnikovite matrix. ***Example E*** is not strictly pseudomorphous replacement but is a very common texture interpreted to demonstrate the transformation of wurtzite to sphalerite (SpG). Spongy pyrite (PyS) has filled the interstitial areas between the wurtzites, preserving the hexagonal form. Chalcopyrite blebs (CpA) occur as zonal "disease", also showing the original hexagonal form.

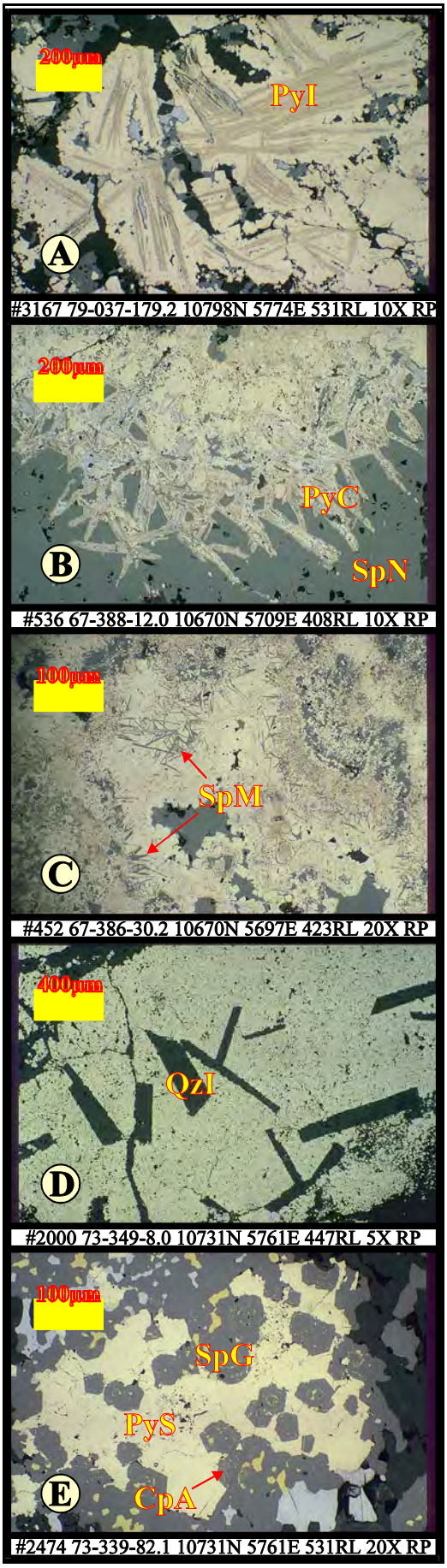

Plate 9 - Examples of pseudomorphous replacement➤

Deformation-induced

Textures produced as a result of an imposed deformational event are very common and generally strikingly obvious (Plate 10). Two deformational episodes are recognised: the major Devonian east-west compression and the shallow Mesozoic wrench faulting associated with the Henty Fault (Berry, 1989). ***Example A*** on the right is a common texture with annealed sphalerite (SpP) containing strung out galena (GnJ) remobilised parallel to Devonian-induced cleavage. General remobilisation of Gn, Sp, Cp, Te and Bo into deformation-prepared voids or interstitial areas is almost ubiquitous in the Hellyer deposit. ***Example B*** shows how general interstitial chert (QzI) is locally remobilised during the Devonian into low pressure "shadow beards" as fibres parallel to cleavage (QzL) around pyrite euhedra. ***Example C*** typifies Devonian "pull-apart" cracks in annealed pyrite (perpendicular to cleavage) that are filled with remobilised chalcopyrite (CpH) and galena (GnL). Sphalerite and tetrahedrite also occur in this form. ***Example D*** shows Mesozoic deformation with rounded fragments of Devonian-remobilised galena/sphalerite, surrounded by microfaults containing shattered pyrite (Pyl) and quartz (QzQ). ***Example E*** shows how Mesozoic deformation has shattered Cambrian annealed pyrite. Frequently this shattering tends to cataclasis, displaying well rounded fragments (Pyk)

.Plate 10 - Examples of deformation-induced textures➤

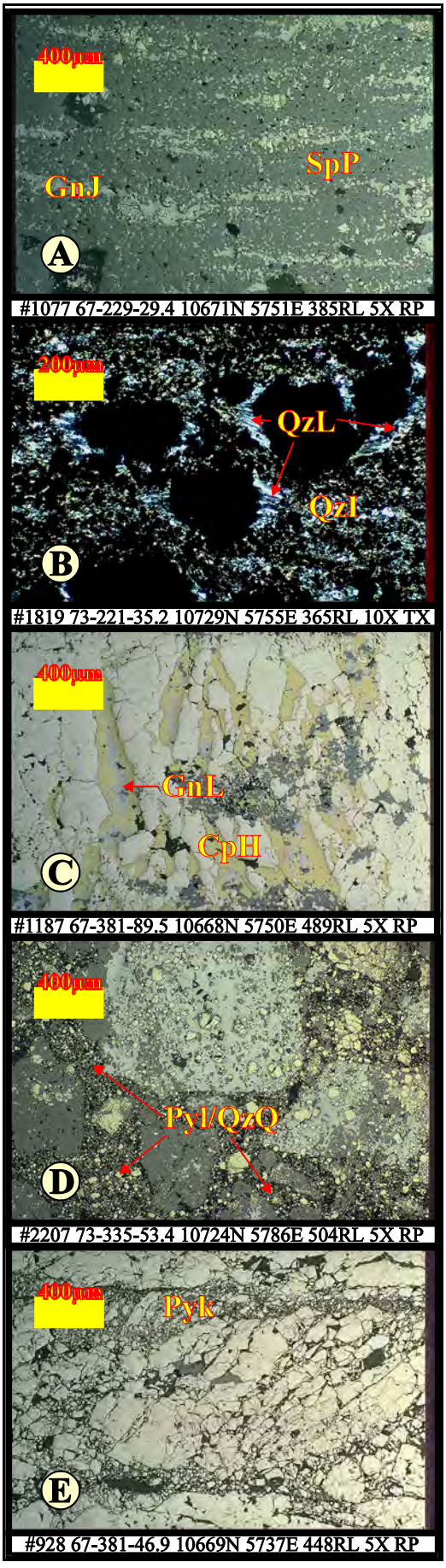

Zonal inclusions

Zonal inclusions are defined to be: mineral inclusions aligned according to the host mineral's crystallography (Plate 11). ***Example A*** on the right is a magnificent illustration of the so-called "chalcopyrite disease". Fine-grained blebs (CpA), generally <20µm across, are aligned on the hexagonal crystallographic planes of sphalerite (SpP, original wurtzite?). Local areas of remobilisation cut across the disease, coarsening both sphalerite and chalcopyrite. Later sections discuss chalcopyrite disease in detail. Pyrrhotite (PoA) also is seen in this form, but only rarely. ***Example B*** shows fine-grained blebs of sphalerite (SpF) aligned parallel to crystal boundaries of annealed pyrite (PyT). ***Example C*** is similar to example B, except galena (GnA) is coarser-grained and is less regularly arranged inside pyrite euhedra (PyL). ***Example D*** is also similar to ***B***, but here fine needles of an unidentified gangue mineral (UG, sericite?) cluster in annular zones inside each pyrite crystal. The last three examples are interpreted to be due to expulsion of contaminating material during Cambrian pyrite recrystallisation.

Plate 11 - Examples of zonal inclusions➤

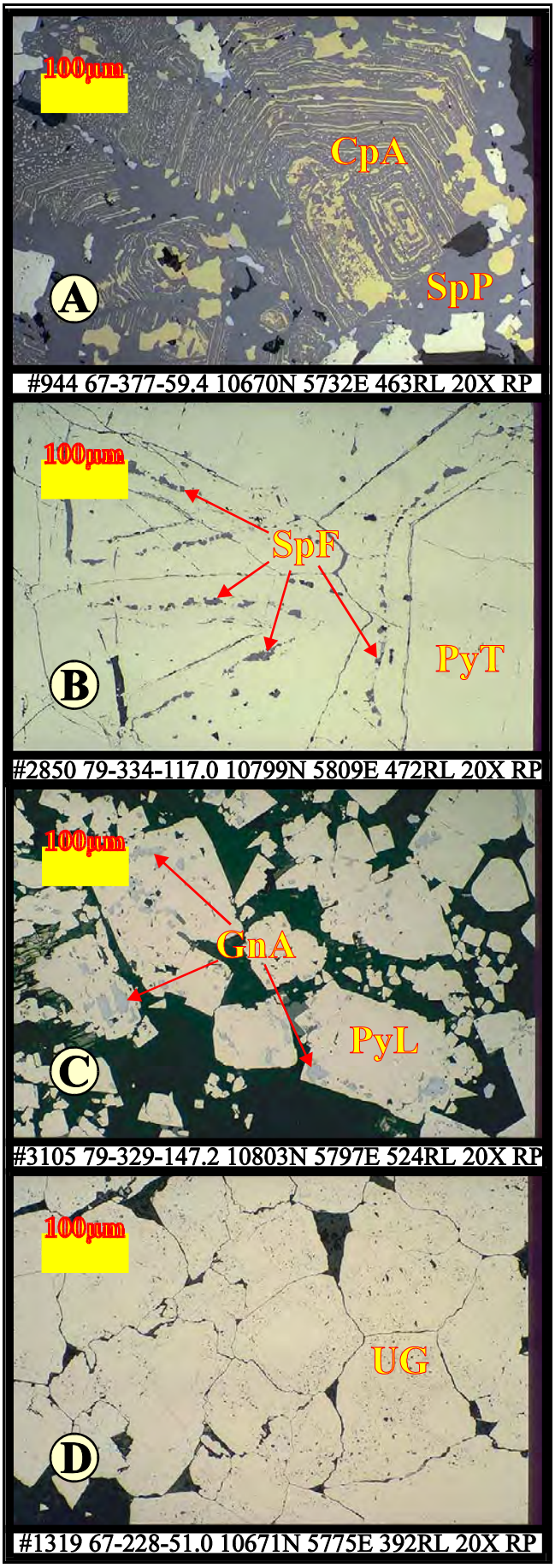

Replacement

In situ replacement of one or more minerals by another is frequently observed at Hellyer (Plate 12). Sphalerite and galena are most frequently replaced by quartz, carbonate or barite either late in the Devonian deformation or during the Mesozoic. ***Example A*** on the right shows a calcite/ankerite (CoM) replacement front that has all but consumed the interstitial sphalerite (SpN) to the left and part of the pull-apart Devonian sphalerite (SpR) in the centre. Pyrite remnants are untouched. ***Example B*** is very similar to example A, but here quartz (QzM) selectively replaces sphalerite (SpP) from the right. ***Example C*** shows patchy barite (BaF) partially replacing massive annealed sphalerite (SpP). ***Example D*** illustrates a common texture where Devonian remobilised galena (GnK) floods through a sphalerite (SpP) / pyrite (PyS) area totally consuming the sphalerite and even partially replacing the narrow pyrite rinds originally coating the sphalerite. Often galena pseudomorphs an original hexagonal wurtzite. Replacive chalcopyrite (CpG) occurs also. ***Example E*** shows coarse-grained arsenopyrite (AsD) replacing original semi-spongy pyrite (PyM). In some areas large masses of fine-grained arsenopyrite (AsI) / galena (GnC) form pervasive replacement fronts virtually eliminating all pyrite.

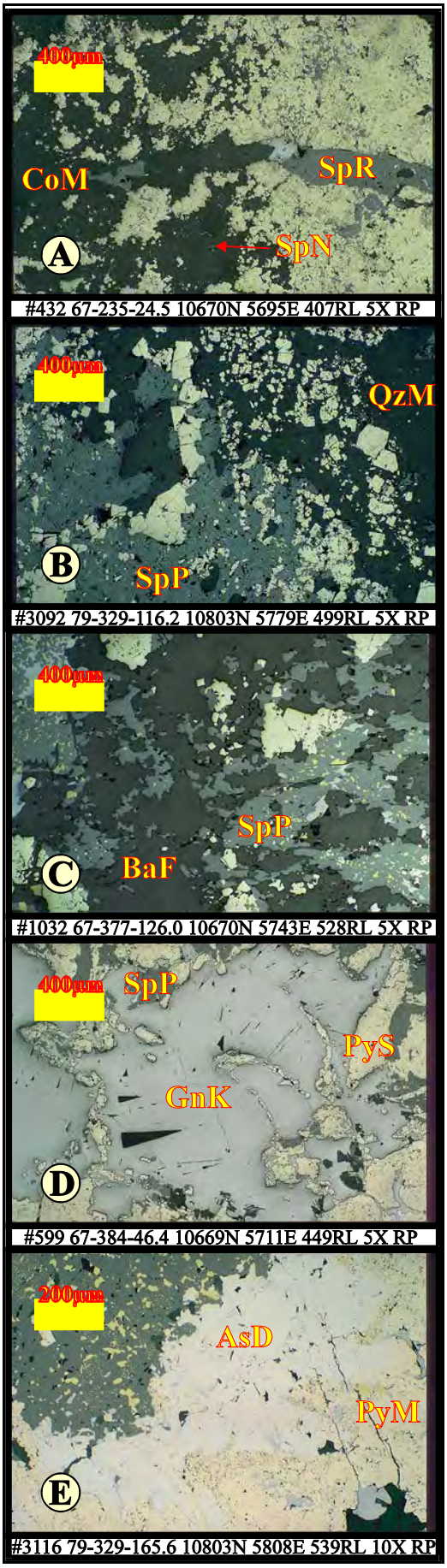

Plate 12 - Examples of replacement textures➤

Interstitial filling

Virtually all minerals (and empty void space) can occupy interstitial positions at Hellyer (Plate 13). While interstitial pyrite appears to be exclusively Cambrian, other minerals are later. The other sulphides are interpreted to have taken up interstitial positions either very late during the thermal retraction of the Cambrian mound, or during Devonian remobilisation. Gangue minerals occupied interstitial positions during both Devonian and Mesozoic deformations. ***Example A*** on the right typifies interstitial carbonate (CoE) with euhedral pyrite (PyL). Quartz (QzF, QzI, QzM); sericite (SeC, SeF); chlorite (ClB, ClE) and barite (BaF) can appear in identical positions. Interestingly, combinations of these minerals are not common. ***Example B*** shows Devonian-remobilised galena (GnG) and minor sphalerite (SpN) infilling spongy semi-colloform pyrite (PyB/PyK). The interstice may well have been empty up to Devonian time. This is the most common textural site for galena. ***Example C*** is typical of remobilised sphalerite (SpN) infilling pyrite cubes (PyL) with evidence of incipient replacement of pyrite. ***Example D*** shows Devonian remobilised chalcopyrite (CpF) filling interstices and cracks in massive recrystallised pyrite (PyT). ***Example E*** is similar to ***C*** and ***D*** with Devonian-remobilised tetrahedrite (TeG) infilling pyrite euhedra (PyL).

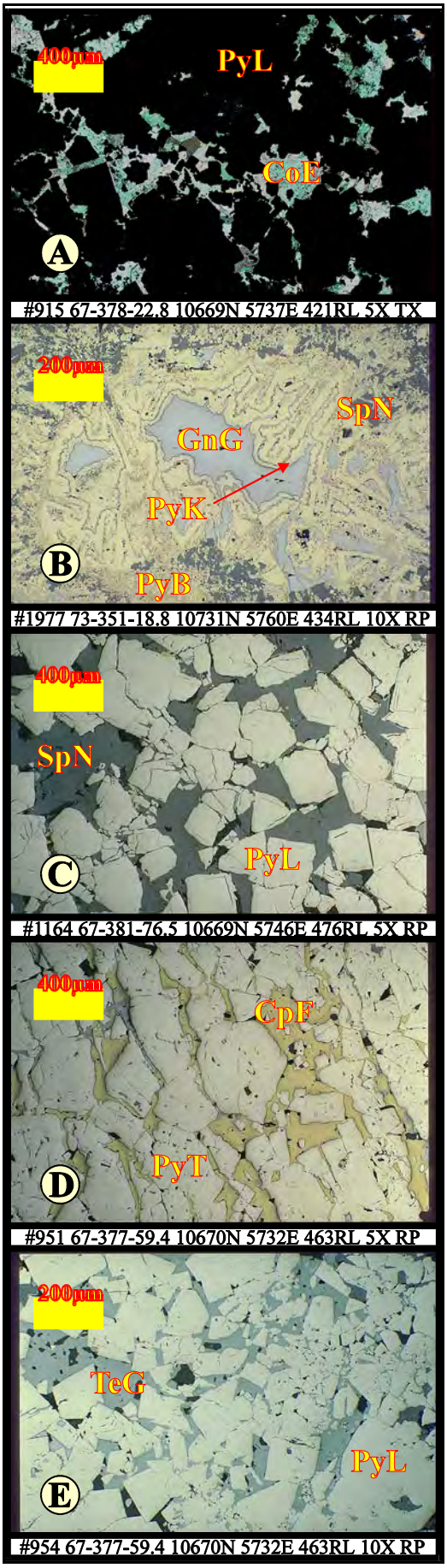

Plate 13 - Examples of interstitial infilling textures➤

Cross-cutting age relationships

Textures which clearly cut across a previously established texture are generally restricted to deformation-related events (Plate 14). The "pull-apart" infills discussed above (Plate 10C), can also be considered a cross-cutting feature. The most convincing examples of cross-cutting textures are part of the brittle Mesozoic deformation. ***Example A*** on the right shows a Mesozoic crack or microfault containing angular fragments of pyrite (Pyl) and sphalerite (SpW) in a siliceous matrix (QzQ), cutting through massive annealed sphalerite (SpP). Clearly, the pyrite fragments were mechanically transported to this site to infill the void space of the crack. ***Example B*** shows a discontinuous narrow (<10µm) vein of Mesozoic-remobilised chalcopyrite (CpK) cutting across Devonian-remobilised tetrahedrite (TeD), galena (GnL) and chlorite (ClF). ***Example C*** is similar, with a veinlet of Mesozoic tetrahedrite (TeJ) cutting across Cambrian sphalerite (SpP) and pyrite (PyT), as well as Devonian chalcopyrite (CpH). ***Example D*** shows strongly remobilised Devonian galena (GnK) partly replacing older sphalerite and a cross-cutting calcite vein network (CoK). Note the fine galena inclusions within the central calcite vein, which are absent on the far left. ***Example E*** shows a discontinuous Mesozoic barite (BaG) vein infilling a crack with transects strongly annealed Devonian sphalerite (SpP) and galena (GnJ)

.Plate 14 - Examples of cross-cutting textural features➤

Intergrowths

Intimate intergrowths between two or more minerals generally indicate either simultaneous deposition or some post-depositional unmixing process. At Hellyer, intergrowths can be observed across the entire paragenetic spectrum (Plate 15). ***Example A*** on the right is a beautiful, but rarely preserved example, of a primitive intricate intergrowth of melnikovite (PyI) and sphalerite (SpB). The fine-grained nature of the intergrowth would suggest deposition by rapid quenching of a hot solution. ***Example B*** shows a very common fine-grained replacive intergrowth of matrix galena (GnC) and arsenopyrite crystals (AsI). Sphalerite (SpL) can also occur intergrown with these arsenopyrite "felted mats". ***Example C*** shows a commonly seen intergrowth of sphalerite (SpO) with chlorite (ClE). Intergrowths of sphalerite with other gangue minerals are never seen. ***Example D*** is similar, but comprises a galena matrix (GnO) intergrown with an intricate sericite network (SeH). In a similar manner to the sphalerite/chlorite association of example C, galena only forms intergrowths with sericite. ***Example E*** is a rare example of what is interpreted to be unmixing of tetrahedrite (TeE) and galena (GnK) in a Devonian remobilised interstice. A somewhat similar texture also develops in Mesozoic-remobilised tetrahedrite (TeK) and cubanite (CbA).

Plate 15 - Examples of intergrowth textures➤

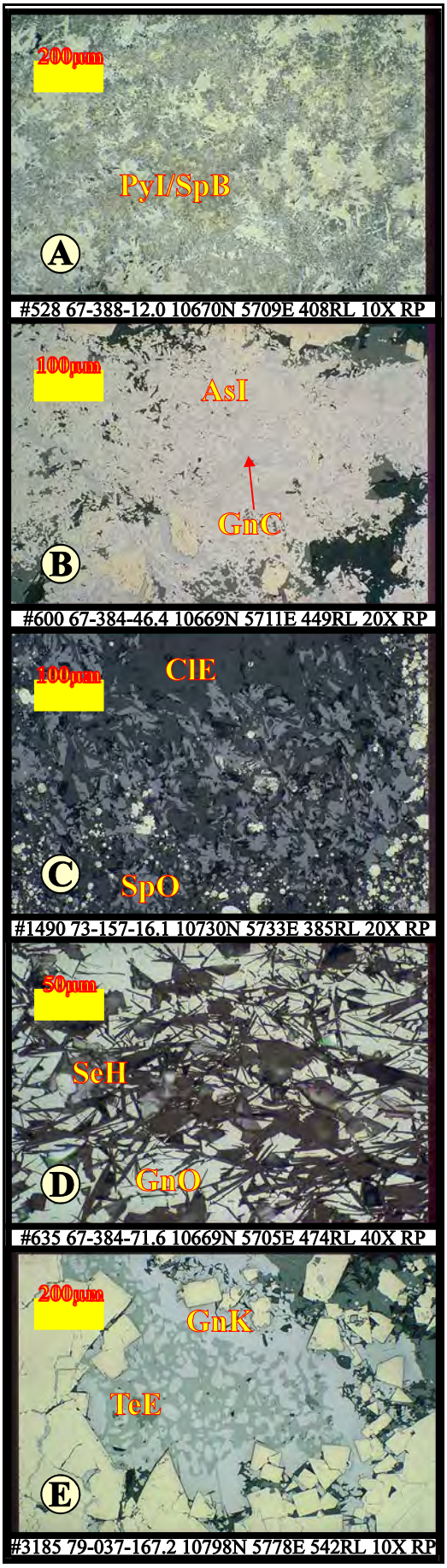

Mineral associations

A prevalent spatial relationship between minerals indicates probable co-deposition and therefore mutual preference for a certain combination of physico-chemical conditions. Such associations of two or more minerals in particular textural locations are notable features of the Hellyer mineralisation (Plate 16). ***Example A*** on the right depicts the very common association of pyrite framboids (Pyb) and their recrystallised partners (PyZ) contained in a chert (QzI) matrix. Arsenopyrite needles (AsJ) are also found commonly associated with chert. ***Example B*** is probably the most common and most economically important mineral association at Hellyer. Devonian-annealed sphalerite (SpP) contains irregular blebs of galena (GnJ), chalcopyrite (CpE) and rare tetrahedrite (TeF). Small corroded pyrite euhedra (Pye) complete the association. ***Example C*** shows the prevailing association of subhedral magnetite (MgA) hosted by massive annealed sphalerite (SpP). ***Example D*** typifies the very common association of Devonian-remobilised minerals occupying "shadow zones". Galena (GnL), sphalerite (SpR), tetrahedrite (TeE), bournonite (BoA) and chalcopyrite (CpH, absent here) frequently occur together. ***Example E*** shows the common association of electrum (AuB) with remobilised interstitial galena (GnG).

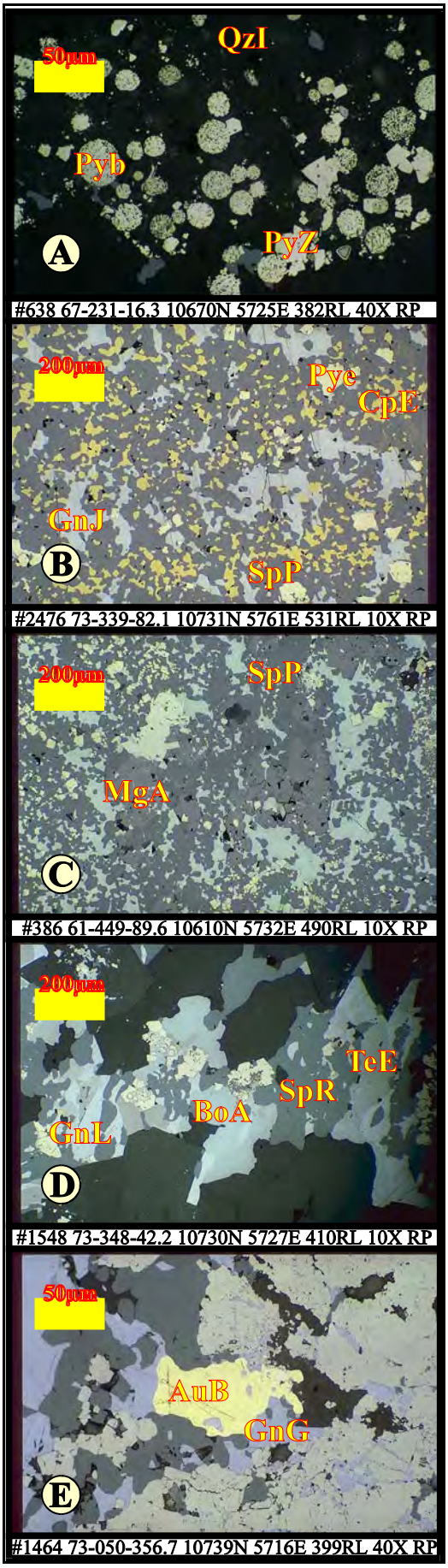

Plate 16 - Examples of common mineral associations➤

Possible fossil structures

Structures which bear some similarity to worm tubes found in modern seafloor chimney and mound mineralisation, have been observed at Hellyer (Plate 17). Unfortunately, the author has not yet sought the opinion of a palaeontologist. ***Example A*** and its magnified image in ***B*** show pyrite containing an elongate form approximately 800µm X 130µm with regular cross-segments, now shown by galena. The segments, in particular, are difficult to explain, if it were to be a crystal pseudomorph. ***Example C*** is a curved cylindrical? form 2.5mm X 300µm, with a clear wall structure. The interior pyrite is notably more spongy than the pyrite forming the "walls". ***Example D*** is an ovoid structure 100µm X 70µm containing galena and unidentified gangue. The surrounding pyrite also shows concentric structure out to a total diameter of about 250µm.

Plate 17 - Examples of possible fossil structures➤

Unusual characteristic features

Numerous unusual features were noted during the routine observations (Plate 18). Only a small selection of these is presented here. ***Example A*** on the right shows the distinctive "parquetry" twinning of bournonite (BoA) when viewed under crossed nicols. ***Example B*** shows a highly unusual (but common) crystallographic form for arsenopyrite (AsD). The author has no explanation for this so-called "nutcracker" or "crocodile" texture.

Example C shows the characteristic undulose extinction of barite at Hellyer, particularly in the baritic cap where large laths (BaA) have distorted under the effects of the Devonian deformation.

Example D also shows an undulose extinction, but in this instance in replacive calcite/ankerite (CoM). This feature is due to the plumose habit of this particular mintex.

Example E is a beautiful image of the commonly seen anomalous "Berlin blue" birefingence in the Devonian-recrystallised chlorite (ClE).

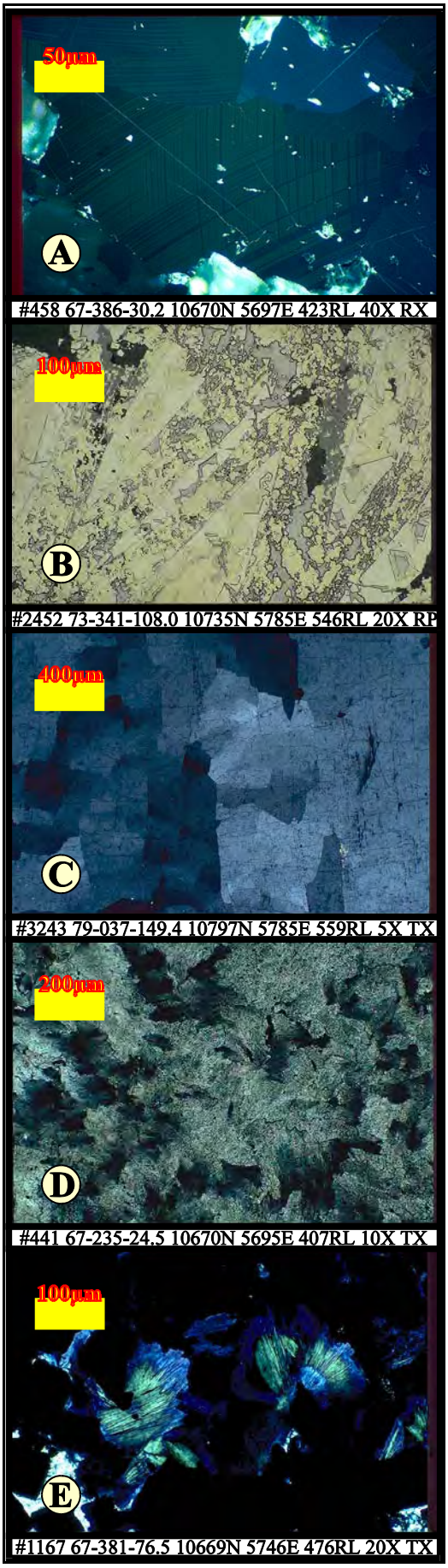

Plate 18 - Examples of unusual characteristics➤

5.4.3 Textural paragenetic groups

After detailed analysis of the textural variety at Hellyer, the following grouping according to interpreted time sequence of the latest crystallisation is proposed. Note that these groups are shown on the stylised timeline on each page of the Appendix II atlas.

Cambrian mound building

This major grouping applies to all processes involved with sulphide deposition on the Cambrian seafloor overlying the footwall alteration/stringer zone. In a temporal context, this grouping covers the total duration of the Hellyer hydrothermal system, up to its extinction, probably during deposition of the Que River Shale. This group is further divided into five subgroups. Although these are listed earliest to latest, all five processes are interpreted to be contemporaneous in various parts of the sulphide mound.

Primitive deposition

This sub-group includes those preserved primitive textures such as spongy, colloform ultrafine-grained intergrowths and pseudomorphs, that suggest rapid deposition at, or just beneath, the surface of the mound by the quenching action of cold, oxygenated seawater. The vast majority of these textures have been destroyed or recrystallised by later processes. Mintex that predominantly fall into this sub-group are:

Pyrite: PyA,B,C,D,E,F,H,I,J,K,U,W,Y
Sphalerite: SpA,B,C,D
Arsenopyrite: AsA,B
Chalcopyrite: CpA
Magnetite: MgA,B
Boulangerite: BgA,B

Pyrrhotite: PoA
Electrum: AuA
Quartz: QzI
Carbonate: CoA,B,C,D
Sericite: SeA

In situ recrystallisation

This sub-group covers recrystallisation in-place, without remobilisation. It generally covers examples of increasing crystallinity and those refined mineral products remaining after recrystallisation. These textures are inferred to be produced deeper in the mound where sustained higher temperatures exist (closer to heat source, distant from cold seawater), continually fluxed by upward-percolating hot solutions. Mintex that predominantly fall into this sub-group are:

Pyrite: PyL,M,N,O,P,Q,R,S,T,X,Z
Sphalerite: SpE,F,G
Galena: GnA
Arsenopyrite: AsC
Chalcopyrite: CpB
Quartz: QzF,G,H
Barite: BaA
Chlorite: ClA
Rutile: RuA

Intra-mound vein deposition

This sub-group includes a small set of symmetric crustiform textures that represent inward growth infilling of cracks in pre-existing sulphide. These cracks may have been created by "hydrothermal jacking" and/or local seismic activity. They represent upward

extensions of footwall stringer veins, providing "plumbing" for the rising solutions to reach the upper, cooler parts of the mound. Mintex that predominantly fall into this sub-group are:

Pyrite: PyV
Sphalerite: SpH,I,J
Galena: GnB
Quartz: QzJ
Barite: BaB

Upward redeposition

This sub-group covers those textures recognised to represent minerals that were redeposited above their original location after re-dissolution by rising warmer solutions. In actual fact, some textures categorised as "primitive" could also be considered as members of this sub-group. It is impossible to distinguish the fresh solutions that emanated from the seafloor from those that included metal redissolved from the lower parts of the mound. Mintex that predominantly fall into this sub-group are:

Pyrite: Pyc
Sphalerite: SpK,L,M
Galena: GnC,D,E,F
Arsenopyrite: AsD,E,F,G,H,I
Chalcopyrite: CpC,D
Tetrahedrite: TeB

Thermal retraction

This sub-group includes a variety of textures produced as a result of overall retreat of the hydrothermal system. As high temperatures in the

mound receded towards the footwall, primitively-textured minerals were deposited in available void space in lower parts of the mound. Mintex that predominantly fall into this sub-group are:

Pyrite: PyW,a,b,c,d
Sphalerite: SpN,O
Arsenopyrite: AsC,I,J
Quartz: QzK
Carbonate: CoD,E
Sericite: SeC
Chlorite: ClB
Hyalophane: HyA

Devonian deformation and remobilisation

This major group covers all the textures interpreted to be caused by the Devonian deformational event that were superimposed over the primary Cambrian textures. It includes annealing of sphalerite, alignment of sphalerite-galena to the local strain extension orientation and the remobilisation of galena, sphalerite, galena, chalcopyrite, sulphosalts and gangue minerals into tensional voids developed in pyrite. Mintex that predominantly fall into this sub-group are:

Pyrite: Pye,f,g,h,i,j
Sphalerite: SpP,Q,R,S,T,U
Galena: GnG,H,I,J,K,L,M,N,O,P,Q,R,S
Arsenopyrite: AsK,L,M,N
Chalcopyrite: CpE,F,G,H,I,J
Tetrahedrite: TeC,D,E,F,G,H,I
Bournonite: BoA,B,C,D,E,F
Pyrargyrite: PgA,B
Argentite: AaA,B

Pyrrhotite: PoB

Electrum: AuB,C

Native antimony: SbA

Magnetite: MgC

Quartz: QzL,M,N,O,P

Barite: BaC,D,E,F

Carbonate: CoF,G,H,I,J,K,L

Sericite: SeB,D,E,F,G,H,I

Chlorite: ClE,F,G,H,I,J

Rutile: RuB

Mesozoic Deformation

This group covers the Mesozoic brittle deformation event associated with the Henty Fault. Shattering and cataclasis of crystalline pyrite is the dominant texture but some remobilisation of barite, carbonate and quartz occurs in the fracture zones. Fine cross-cutting veinlets of tetrahedrite/chalcopyrite/cubanite also occur, but are comparatively rare. Mintex that predominantly fall into this sub-group are:

Pyrite: Pyk,l,m,n

Sphalerite: SpV,W

Galena: GnT,U,V

Arsenopyrite: AsO,P

Chalcopyrite: CpK,L

Tetrahedrite: TeJ,K,L

Cubanite: CbA,B

Marcasite: MaA,B

Magnetite: MgD

Quartz: QzQ,R,S

Barite: BaF,G

Carbonate: CoM,N,O,P

Sericite: SeJ
Chlorite: ClK,L

Surface weathering

Since the complete Hellyer orebody is below the base of surface oxidation, only rare instances of incipient weathering have been observed. Interstitial chlorite has been partially altered to clays. Mintex that predominantly fall into this sub-group are:

Pyrite: PyY
Hematite: HeA
Clays: CyA

5.5 Textural statistics

5.5.1 Global statistics

The frequency of occurrence for each individual mintex, as calculated from the point counting and visual estimates, are provided at the upper right-hand corner of each page of the texture atlas (Appendix II). The main purpose of showing these, is to remind the reader of the relative importance of each mintex. These figures are also provided in Table 21 arranged in decreasing order of occurrence. From perusal of the table, it is clear that most of the mintex are of insignificant volume. In fact, 95% of the deposit is accounted for by just 61 of the 222 mintex.

Table 21 - Frequency statistics for all mintex in decreasing order of occurrence

Rank	Mintex	% of samples	% of mineral	Sample volume%	Global volume%	Accum. volume%
1	**SpP**	82.8	64	32.00	15.22	15.22
2	**PyT**	79.9	26	27.18	12.48	27.70
3	**PyL**	71.3	15	17.89	7.33	35.03
4	**PyM**	80.5	14	14.17	6.55	41.58
5	**SpN**	94.3	14	6.02	3.26	44.84
6	**PyA**	73.0	6	6.75	2.83	47.67
7	**BaA**	9.8	55	45.94	2.58	50.25
8	**PyS**	50.0	5	8.90	2.56	52.80
9	**Pyk**	47.7	4	6.96	1.91	54.71
10	**PyV**	25.3	4	12.90	1.88	56.59
11	**PyW**	44.8	4	6.65	1.71	58.30
12	**SpR**	92.5	7	3.11	1.65	59.95
13	**GnK**	54.0	32	5.23	1.63	61.58
14	**VdA**	73.0	100	3.74	1.57	63.15
15	**SpG**	55.7	6	4.65	1.49	64.64
16	**QzL**	41.4	21	6.14	1.46	66.10
17	**PyB**	44.3	3	5.66	1.44	67.54
18	**QzI**	20.7	19	11.20	1.33	68.87
19	**GnG**	97.7	25	2.28	1.28	70.15
20	**PyH**	40.2	3	5.32	1.23	71.38
21	**CoE**	58.0	32	3.66	1.22	72.60
22	**QzM**	20.1	17	10.26	1.19	73.78
23	**SeC**	22.4	47	8.76	1.13	74.91
24	**QzF**	60.3	16	3.09	1.07	75.98
25	**CoK**	66.7	27	2.73	1.04	77.03
26	**GnJ**	81.6	20	2.14	1.00	78.03
27	**BaC**	8.6	19	18.36	0.91	78.94
28	**PyC**	42.5	2	3.70	0.90	79.84
29	**PyI**	46.6	2	3.38	0.90	80.75
30	**SeD**	23.6	34	6.11	0.83	81.58
31	**PyD**	25.3	2	5.41	0.79	82.36
32	**Pye**	74.1	2	1.83	0.78	83.14
33	**CoM**	14.4	20	9.40	0.78	83.92
34	**ClE**	51.7	43	2.53	0.75	84.67
35	**Pya**	21.8	2	5.70	0.72	85.39
36	**SpA**	29.3	3	3.95	0.67	86.05
37	**ClB**	21.8	35	4.83	0.61	86.66
38	**PyN**	11.5	1	8.64	0.57	87.23
39	**PyY**	53.4	1	1.80	0.55	87.78
40	**QzN**	43.1	8	2.12	0.52	88.30
41	**BaG**	20.7	11	4.27	0.51	88.81
42	**GnL**	59.8	9	1.34	0.46	89.27
43	**SpB**	24.7	2	3.22	0.46	89.73
44	**Pyd**	56.9	1	1.30	0.42	90.15
45	**PyO**	10.3	1	6.77	0.40	90.55

Table 21 - Frequency statistics for all mintex in decreasing order of occurrence

Rank	Mintex	% of samples	% of mineral	Sample volume%	Global volume%	Accum. volume%
46	**QzG**	5.7	6	11.53	0.38	90.94
47	**CoF**	14.9	9	4.12	0.35	91.29
48	**BaF**	17.8	7	3.30	0.34	91.63
49	**PyZ**	39.7	1	1.30	0.30	91.92
50	**AsI**	16.7	28	2.99	0.29	92.21
51	**GnM**	62.1	6	0.80	0.28	92.49
52	**CpF**	63.8	29	0.77	0.28	92.77
53	**AsC**	35.6	27	1.34	0.27	93.05
54	**Pyb**	46.0	1	1.00	0.27	93.31
55	**AsD**	12.6	25	3.54	0.26	93.57
56	**SpH**	12.1	1	3.63	0.25	93.82
57	**SpQ**	34.5	1	1.22	0.24	94.06
58	**ClF**	25.9	13	1.58	0.23	94.30
59	**PyE**	6.9	0	5.79	0.23	94.53
60	**QzQ**	14.4	3	2.70	0.22	94.75
61	**CpH**	62.1	22	0.61	0.22	94.97
62	**BaB**	5.7	5	6.51	0.21	95.18
63	**CpE**	78.7	21	0.46	0.21	95.39
64	**Pyc**	60.3	0	0.58	0.20	95.59
65	**CpG**	25.9	19	1.28	0.19	95.78
66	**CoA**	40.8	5	0.79	0.18	95.97
67	**QzO**	60.9	3	0.51	0.18	96.15
68	**SpI**	10.9	1	2.86	0.18	96.33
69	**CoL**	8.0	4	3.71	0.17	96.50
70	**BaD**	3.4	4	8.45	0.17	96.67
71	**GnD**	43.1	3	0.65	0.16	96.83
72	**QzK**	5.7	2	4.73	0.16	96.98
73	**Pyl**	20.7	0	1.23	0.15	97.13
74	**SeA**	0.6	6	43.26	0.14	97.27
75	**SeB**	23.6	6	1.03	0.14	97.41
76	**TeD**	29.3	56	0.68	0.12	97.53
77	**QzA**	1.1	2	16.44	0.11	97.63
78	**SpL**	10.3	0	1.83	0.11	97.74
79	**QzH**	8.0	1	2.11	0.10	97.84
80	**PyP**	37.9	0	0.44	0.10	97.94
81	**SpM**	28.2	0	0.55	0.088	98.02
82	**SeE**	6.9	4	2.13	0.085	98.11
83	**AsK**	19.5	8	0.71	0.080	98.19
84	**GnN**	6.3	2	2.17	0.079	98.27
85	**PyQ**	3.4	0	3.86	0.077	98.35
86	**ClG**	29.9	4	0.44	0.076	98.42
87	**CyA**	11.5	100	1.01	0.067	98.49
88	**GnH**	58.0	1	0.18	0.060	98.55
89	**TeE**	66.7	29	0.15	0.059	98.61
90	**SpE**	50.6	0	0.20	0.058	98.67

Table 21 - Frequency statistics for all mintex in decreasing order of occurrence

Rank	Mintex	% of samples	% of mineral	Sample volume%	Global volume%	Accum. volume%
91	**SpO**	9.2	0	1.04	0.055	98.72
92	**PyK**	18.4	0	0.51	0.054	98.77
93	**SpV**	10.3	0	0.83	0.050	98.82
94	**SpW**	8.0	0	1.04	0.048	98.87
95	**CpA**	85.1	5	0.10	0.048	98.92
96	**PyJ**	54.6	0	0.15	0.047	98.97
97	**QzR**	0.6	1	13.84	0.046	99.01
98	**PyU**	4.6	0	1.59	0.042	99.05
99	**AsF**	2.9	4	2.46	0.041	99.09
100	**SeF**	1.1	2	6.06	0.040	99.13
101	**ClK**	8.0	2	0.81	0.037	99.17
102	**AsE**	8.6	3	0.73	0.036	99.21
103	**GnS**	20.7	1	0.28	0.034	99.24
104	**CoG**	12.6	1	0.43	0.031	99.27
105	**CoH**	1.1	1	4.67	0.031	99.30
106	**SeJ**	1.1	1	4.24	0.028	99.33
107	**BoA**	8.0	72	0.56	0.026	99.36
108	**AsJ**	19.0	2	0.23	0.025	99.38
109	**QzP**	0.6	0	7.27	0.024	99.41
110	**SpS**	7.5	0	0.56	0.024	99.43
111	**PyR**	3.4	0	1.17	0.023	99.45
112	**GnC**	12.6	0	0.32	0.023	99.48
113	**SpC**	2.3	0	1.73	0.023	99.50
114	**GnI**	7.5	0	0.51	0.022	99.52
115	**MgA**	27.6	72	0.12	0.019	99.54
116	**HyA**	0.6	100	5.54	0.018	99.56
117	**Pyf**	5.2	0	0.62	0.018	99.58
118	**CoC**	1.1	0	2.60	0.017	99.59
119	**AsL**	21.8	2	0.13	0.017	99.61
120	**GnE**	3.4	0	0.84	0.017	99.63
121	**ClH**	3.4	1	0.83	0.016	99.64
122	**GnO**	6.9	0	0.42	0.016	99.66
123	**CpI**	25.3	2	0.11	0.016	99.68
124	**CoN**	0.6	0	4.15	0.014	99.69
125	**QzS**	0.6	0	4.15	0.014	99.70
126	**GnA**	32.2	0	0.07	0.013	99.72
127	**ClJ**	1.7	1	1.28	0.013	99.73
128	**SeG**	0.6	1	3.81	0.013	99.74
129	**QzB**	1.7	0	1.22	0.012	99.75
130	**PyF**	1.7	0	1.19	0.012	99.77
131	**SpJ**	0.6	0	3.46	0.011	99.78
132	**CoI**	1.7	0	1.08	0.011	99.79
133	**QzJ**	4.6	0	0.37	0.010	99.80
134	**ClL**	2.3	1	0.74	0.010	99.81
135	**TeF**	25.9	4	0.06	0.009	99.82

Table 21 - Frequency statistics for all mintex in decreasing order of occurrence

Rank	Mintex	% of samples	% of mineral	Sample volume%	Global volume%	Accum. volume%
136	**AsG**	4.6	1	0.32	0.008	99.83
137	**GnF**	8.0	0	0.18	0.008	99.83
138	**QzC**	3.4	0	0.41	0.008	99.84
139	**TeG**	12.6	4	0.11	0.008	99.85
140	**CpJ**	10.3	1	0.12	0.007	99.86
141	**CoJ**	0.6	0	2.08	0.007	99.86
142	**CpB**	31.0	1	0.04	0.007	99.87
143	**Pyg**	4.6	0	0.25	0.007	99.88
144	**BoB**	1.7	18	0.65	0.006	99.88
145	**GnU**	1.7	0	0.64	0.006	99.89
146	**MgD**	1.7	22	0.59	0.006	99.90
147	**PoB**	1.7	99	0.59	0.006	99.90
148	**BaE**	1.1	0	0.87	0.006	99.91
149	**SeH**	4.6	0	0.22	0.006	99.91
150	**CoO**	0.6	0	1.73	0.006	99.92
151	**TeA**	14.4	2	0.06	0.005	99.92
152	**QzD**	0.6	0	1.38	0.005	99.93
153	**GnP**	5.2	0	0.15	0.004	99.93
154	**AsH**	2.3	0	0.31	0.004	99.94
155	**QzE**	1.7	0	0.42	0.004	99.94
156	**TeJ**	10.9	2	0.06	0.004	99.94
157	**CpC**	4.0	0	0.14	0.003	99.95
158	**TeH**	4.0	1	0.11	0.003	99.95
159	**BoC**	5.2	7	0.08	0.002	99.95
160	**RuA**	2.9	63	0.15	0.002	99.96
161	**ClC**	0.6	0	0.69	0.002	99.96
162	**Pyh**	1.7	0	0.23	0.002	99.96
163	**CpK**	12.1	0	0.03	0.002	99.96
164	**CpD**	8.0	0	0.05	0.002	99.96
165	**PyX**	5.2	0	0.06	0.002	99.97
166	**Pyi**	2.3	0	0.13	0.002	99.97
167	**CpL**	0.6	0	0.52	0.002	99.97
168	**TeK**	1.1	1	0.26	0.002	99.97
169	**TeL**	5.2	1	0.06	0.002	99.97
170	**AsM**	9.8	0	0.03	0.002	99.97
171	**GnV**	6.9	0	0.04	0.002	99.98
172	**RuB**	3.4	37	0.07	0.001	99.98
173	**AsA**	1.1	0	0.17	0.001	99.98
174	**MgB**	4.0	4	0.05	0.001	99.98
175	**CbA**	0.6	86	0.31	0.001	99.98
176	**UG**	4.0		0.04	0.001	99.98
177	**CoD**	1.1	0	0.13	0.001	99.98
178	**SpT**	2.3	0	0.06	0.001	99.98
179	**GnQ**	1.7	0	0.07	0.001	99.98
180	**BoD**	1.7	2	0.07	0.001	99.99

Table 21 - Frequency statistics for all mintex in decreasing order of occurrence

Rank	Mintex	% of samples	% of mineral	Sample volume%	Global volume%	Accum. volume%
181	**GnT**	2.9	0	0.04	0.001	99.99
182	**SpD**	1.1	0	0.10	0.001	99.99
183	**ClD**	0.6	0	0.17	0.001	99.99
184	**CoP**	0.6	0	0.17	0.001	99.99
185	**GnB**	0.6	0	0.17	0.001	99.99
186	**MaA**	0.6	83	0.17	0.001	99.99
187	**SpK**	0.6	0	0.17	0.001	99.99
188	**BoE**	2.3	1	0.03	0.0005	99.99
189	**MgC**	0.6	1	0.10	0.0003	99.99
190	**AsN**	0.6	0	0.09	0.0003	99.99
191	**Pym**	2.9	0	0.02	0.0003	99.99
192	**AsB**	1.7	0	0.02	0.0002	99.99
193	**GnR**	2.3	0	0.02	0.0002	99.99
194	**TeC**	1.7	0	0.02	0.0002	99.99
195	**AaA**	0.6	60	0.05	0.0002	99.99
196	**CbB**	1.1	14	0.03	0.0002	99.99
197	**CoB**	1.1	0	0.03	0.0002	99.99
198	**PyG**	1.1	0	0.03	0.0002	99.99
199	**SpF**	0.6	0	0.05	0.0002	99.99
200	**TeB**	0.6	0	0.05	0.0002	99.99
201	**TeI**	1.7	0	0.02	0.0002	99.99
202	**AaB**	1.1	40	0.02	0.00011	99.99
203	**AsO**	1.1	0	0.02	0.00011	99.99
204	**AuB**	1.1	50	0.02	0.00011	99.99
205	**BgA**	1.1	67	0.02	0.00011	99.99
206	**ClI**	1.1	0	0.02	0.00011	99.99
207	**HeA**	0.6	100	0.03	0.00011	99.99
208	**PgA**	1.1	67	0.02	0.00011	99.99
209	**Pyj**	1.1	0	0.02	0.00011	99.99
210	**MaB**	1.1	17	0.01	0.00010	99.99
211	**AsP**	0.6	0	0.02	0.00006	99.99
212	**AuA**	0.6	25	0.02	0.00006	99.99
213	**AuC**	0.6	25	0.02	0.00006	99.99
214	**BgB**	0.6	33	0.02	0.00006	99.99
215	**BoF**	0.6	0	0.02	0.00006	99.99
216	**ClA**	0.6	0	0.02	0.00006	99.99
217	**PgB**	0.6	33	0.02	0.00006	99.99
218	**PoA**	0.6	1	0.02	0.00006	99.99
219	**Pyn**	0.6	0	0.02	0.00006	99.99
220	**SbA**	0.6	100	0.02	0.00006	99.99
221	**SeI**	0.6	0	0.02	0.00006	99.99
222	**SpU**	0.6	0	0.02	0.00006	100.00

An additional way to handle the mintex volume data is to ascribe proportions of each mintex volume % to each of the paragenetic groups (discussed above, section 5.4.3). These proportions are taken from the interpreted bars depicted on the paragenesis chart on the lower left-hand side of each atlas page.

Take for example the case of QzI (chert). This texture has been interpreted as:

DOMINANT - Primitive Deposition, score of 3, proportion of 0.50
MAJOR - Thermal Retraction, score of 2, proportion of 0.33
MINOR - Upward Redeposition, score of 1, proportion of 0.17

These estimated proportions can then be multiplied by the global volume % for the QzI mintex (i.e. 1.33%), so 0.67% can be ascribed to "Primitive Deposition", 0.44% to "Thermal Retraction" and the remainder 0.22% to "Upward Redeposition". When this process is repeated for all mintex for each mineral, an overall global estimate of proportions preserved in each paragenetic group is obtained (Table 22).

Table 22 - Percentage of volume of each mineral ascribed to each paragenetic group

Mineral	Prim. Depos.	In situ Recryst.	In mound Veins	Upward Redep.	Therm. Retr.	Dev.n Def.n	Mes.c Def.n	Surf. Weath.
Py	21	55	11	2	3	3	4	0
Sp	5	3	3	27	7	54	0	0
Gn	0	4	0	13	6	76	0	0
As	0	19	0	34	37	10	0	0
Cp	3	7	1	0	12	76	0	0
Te	0	0	0	0	1	94	3	0
Bo	0	0	0	0	0	100	0	0
Mg	77	0	0	0	0	1	22	0
Po	1	25	0	0	0	74	0	0
Cb	0	0	0	0	0	0	100	0
Pg	0	0	0	0	0	100	0	0
Ma	0	0	0	0	0	0	100	0
Bg	100	0	0	0	0	0	0	0
He	0	0	0	0	0	0	0	100
Aa	0	0	0	0	0	55	45	0
Sb	0	0	0	0	0	100	0	0
Au	25	0	0	0	0	75	0	0
Qz	12	23	0	3	9	49	4	0
Ba	0	41	5	0	0	44	11	0
Co	5	0	0	0	24	51	20	0
Se	15	1	0	0	30	43	11	0
Cl	9	0	0	0	26	62	3	0
Cy	0	0	0	0	0	0	0	100
Hy	0	0	0	0	100	0	0	0
Ru	0	63	0	0	0	37	0	0
Vd	14	43	0	0	0	0	29	14
TOTAL for HELLYER DEPOSIT	**13**	**32**	**6**	**9**	**7**	**29**	**4**	**0**

Therefore, approximately two-thirds of the textures observed are interpreted as preserved Cambrian mound-building features, and the remaining one-third is

interpreted as the result of a later deformation/remobilisation overprint.

5.5.2 Microtextural inter-relationships

As indicated in the "associated mintex" area of the atlas (Appendix II), certain mintex show close spatial relationships with others. Some are related by definition, e.g. PyH defined as "non-spongy colloform pyrite with galena rings" (GnH). Others are related, presumedly because of co-deposition. Statistical methods (e.g. cluster analysis) were used to analyse the spatial relationships, but this proved to be largely ineffective, due to the large number of variables (i.e. mintex) involved. An attempt to make use of the comprehensive point count data from the last 27 samples (X,Y coordinates and mintex recorded) by near neighbour analysis, was also ineffective due to the very common mintex "swamping" the statistics.

The following mintex sets (see Appendix II) were found (by simple observation) to be consistently spatially related:

Early primitive set - melnikovite forms, pseudomorphs with Devonian infills

> PyA, PyB, PyC, PyD, PyE, PyH, PyI, PyK, SpA, SpB, SpM, SpN, GnD, GnG, GnH, AsH, CpF, TeC, QzF, CoE, VdA (total ~19% by volume)

Cambrian in situ recrystallised set - recrystallised and annealed pyrite, rejected contaminant blebs, with later Devonian infills

> PyL, PyT, SpG, SpE, SpF, SpN, SpR, GnA, GnG, GnL, GnM, CpF, CpB, CpH, TeG, QzF, QzN, CoE, SeC, CyA, RuA, VdA (total ~34% by volume)

Late primitive set - bubbly melnikovite forms, framboids, overgrowths; arsenopyrite euhedra; chert and sericite

> PyB, PyH, PyW, PyZ, Pyb, Pyc, SpQ, GnH, AsJ, TeH, QzI, QzG, SeC (total

~8% by volume)

Arsenic replacement? set - mats of replacive fine-grained arsenopyrite with interstitial sphalerite and galena

SpL, GnC, GnI, AsI (total ~0.5% by volume)

Symmetric crustiform vein set - symmetric pyrite veins with hexagonal sphalerites; sphalerite, galena, quartz, barite, chlorite infills

PyV, SpG, SpH, SpI, GnN, QzJ, BaB, ClL (total ~4% by volume)

Massive Devonian annealed sphalerite-rich set - annealed sphalerite, cleavage-aligned galena; in situ remobilised blebs; corroded pyrite, magnetite, quartz and carbonate euhedra; pyrite infills and rinds

PyJ, PyP, PyS, Pye, SpG, SpP, GnJ, GnK, CpA, CpE, TeF, MgA, AuB, QzO, CoA (total ~23% by volume)

Devonian remobilised segregation set - remobilised sphalerite, galena, chalcopyrite and sulphosalts; as semi-replacive segregations and in tensional voids

Pyf, Pyg, SpR, GnK, GnL, GnM, AsM, CpF, CpG, CpH, TeD, TeE, BoA, BoC, BoD, PgA, PgB, AaA, AaB, SbA, QzL, QzN, CoF, CoK, SeD, ClE, ClF (total ~10% by volume)

Mesozoic cataclasis set - cataclasis of pyrite, sphalerite and galena healed by quartz and chlorite; veins of remobilised galena, chalcopyrite, tetrahedrite, cubanite, carbonate and barite

Pyk, Pym, SpV, SpW, GnU, GnV, CpK, TeJ, TeK, CbA, CbB, MaA, QzQ, QzR, CoK, BaG, VdA (total ~5% by volume)

5.6 Textural zonation

5.6.1 Spatial patterns observed for minerals

For this section, the reader is referred to the atlas (Appendix II). Pages A-E depict total mineral contents as measured by the point counting.

Pyrite (Py) (Appendix II, page A), being the most dominant mineral, shows a consistent pattern of enrichment within the boundaries of the footwall depleted zone (FWD). The highest pyrite content occurs near the footwall where the FWD is thickly developed on sections 10670N and 10790N. Not surprisingly, this matches the pattern for Fe in the 3D grade model (Figs. 63,65). The lowest pyrite content occurs on the hangingwall or distal footwall (e.g. 10670N).

Sphalerite (Sp) (Appendix II, page A) shows enrichment within the hangingwall enriched zone (HWE) and the upper parts of the FWD. The lowest sphalerite content occurs in the hangingwall caps and the most footwall areas of the FWD. Note the variability in content east of the Jack Fault on section 10730N, where late barite veins cut through the massive sulphide. The pattern generally mimics that for Zn in the 3D model.

Galena (Gn) (Appendix II, page A) closely follows the sphalerite distribution, but appears to reach maximum content closer to the hangingwall than does sphalerite (e.g. 10670N). The pattern follows that for Pb in the 3D model.

Arsenopyrite (As) (Appendix II, page B) is generally restricted to the HWE, apart from one area high in the FWD on section 10790N. Most of the FWD has only trace amounts of arsenopyrite. The pattern reflects the high variability of As in the 3D grade model.

Chalcopyrite (Cp) (Appendix II, page B) distribution is less well behaved than the previous metals, but there is overall enrichment within the central FWD. There also is

some enrichment on the hangingwall (e.g. 10670N, 10730N west) which matches the slight Cu enrichment reported on the hangingwall in the stratigraphic plot (Fig. 49). The lowest chalcopyrite content occurs in the distal footwall areas (e.g. 10670N). The overall pattern is close to that for Cu in the 3D grade model.

Tetrahedrite (Te) (Appendix II, page B) is clearly effected by the poor count statistics of a comparatively rare mineral. There is obvious enrichment within the bounds of the HWE (remember the HWE is defined to contain >100ppm Ag), but also significant amounts in some areas of the FWD (e.g. 10670N, 10790N). If these significant tetrahedrite contents in the FWD are not supported by the overall Ag assay (and the 3D model), then it must be assumed that this tetrahedrite is Ag-poor (see section 6.2.6 for tetrahedrite probe analyses).

Bournonite (Bo) (Appendix II, page C) is also effected by poor count statistics but nevertheless shows a distinct cluster within the HWE near the distal footwall on sections 10610N-10730N. This area shows evidence for the maximum Devonian extension (as seen by pull-apart textures). Bournonite always occupies Devonian tensional sites.

Magnetite (Mg) (Appendix II, page C) is effected by very poor count statistics but tends to occur close to the HWE/FWD boundary. The apparent anomalous concentration east of the Jack Fault on section 10730N can be explained since the HWE/FWD boundary occurs not far to the north.

Void (Vd) (Appendix II, page C) was not logged for samples on sections 10550N and 10610N. On the remaining sections, voids concentrate within the pyrite-rich FWD as well as near the Silic Fault forming the eastern footwall on 10730N.

Quartz (Qz) (Appendix II, page D) shows considerable variability over all sections but maximum content tends to occur where deformation in strongest (i.e. distal footwall regions on sections 10610N-10670N and near the major fault forming the eastern footwall on 10730N. Obviously, the siliceous cap samples are enriched in

chert.

Barite (Ba) (Appendix II, page D) shows obvious maximums in the baritic cap as well as in cross-cutting veins within the HWE of sections 10610N and 10730N east. Most samples are totally devoid of barite. There is a good match with the pattern for Ba in the 3D grade model.

Carbonate (Co) (Appendix II, page D) shows a lot of variability across all sections but is clearly enriched in the lower FWD. Parts of the HWE are totally devoid of carbonate.

Sericite (Se) (Appendix II, page E) shows concentrations at the hangingwall (e.g. 10610N-10670N), in the western wing of the Keel Zone on sections 10730N-10790N and in the FWD adjacent to the Jack Fault (10670N, 10790N east). There is a total lack of sericite in many samples. The overall distribution is more clustered than those for quartz and carbonate.

Chlorite (Cl) (Appendix II, page E) is quite variable across all sections but shows a somewhat antipathetic relationship to the sericite pattern. Significantly, only the samples near the Silic Fault forming the eastern footwall on section 10730N, are devoid of chlorite.

Clays (Cy) (Appendix II, page E) are effected by poor count statistics but tend to occur in areas of Mesozoic deformation where there is evidence of watercoursing well below the normal level of surface oxidation.

5.6.2 Spatial patterns observed for paragenetic groups

Atlas pages F-H depict summary maps of paragenetic group distribution constructed using the method described under section 5.5.1. It must be stressed that these maps reflect the distribution of the various paragenetic groups as preserved. Without the superimposition of the two deformation events, the distribution of Cambrian primary

features would be quite different.

Primitive Deposition (Appendix II, page F) is concentrated within the lower part of the HWE and the upper part of the FWD. The lowest values occur generally in the most proximal FWD.

In situ Recrystallisation (Appendix II, page F) is virtually ubiquitous but is clearly concentrated in the FWD.

Intra-mound Veining (Appendix II, page F) occurs mainly within the central FWD and the more proximal parts of the HWE.

Upward Redeposition (Appendix II, page G) concentrates within the HWE and the upper parts of the FWD.

Thermal Retraction (Appendix II, page G) is almost ubiquitous and shows considerable variability between adjacent samples. There is a slight tendency to concentrate in the upper parts of the FWD.

Devonian Deformation (Appendix II, page G) occurs in every sample but is concentrated within the HWE and the upper half of the FWD.

Mesozoic Deformation (Appendix II, page H) concentrates mostly adjacent to the Jack Fault and near the Silic Fault forming the eastern footwall on 10730N.

Surface Weathering (Appendix II, page H) is extremely rare but occurs mainly near Mesozoic faults.

Atlas page I clearly shows that only three paragenetic groups (Primitive, Recrystallised and Devonian Deformation) dominate the textural space.

5.7 Textural evolution

5.7.1 Introduction

The following discussion is based mainly on the microtextural observations. Tying in these interpretations with the observed metal zoning and microprobe analyses is covered later in Chapter 7. The reader is referred *(in italics)* to particular photographic examples in the atlas, that illustrate the features discussed.

5.7.2 Cambrian mound building

The primitive melnikovite pyrite and to a lesser extent, sphalerite, frequently occur as colloform crustiform growths with inbedded pseudomorphs *(PyB, #703).* These pseudomorphs *(PyC, PyI),* by their crystallographic form, probably were original anhydrite and barite (and/or possibly pyrrhotite and hydromuscovite). The unidirectional colloform growth structure of these original crusts suggests crystal growth of sulphates into empty space (or rather seawater) either at the surface of the growing mound, or within voids just below the surface. As these colloform accumulations grew upwards, older buried layers would find themselves further from the mound surface, and therefore further from the cooling effect of the seawater. As their depth below the mound surface increased, the surrounding temperature would rise; eventually to be replaced. As the sulphates were replaced, melnikovite pyrite was precipitated in the crystal casts to form the pseudomorphs seen preserved today. The melnikovite pseudomorphs were then overgrown by later melnikovite, partially filling the original inter-crystal voids *(PyK, #644, #3133).* But not all primitive pyrite shows evidence of pseudomorphing. Much occurs as weakly colloform or featureless melnikovite *(PyA, #1080, #1753, #2147),* occasionally forming intricately delicate intergrowths with chert *(PyU, #1988)* or ultrafine-grained intergrowths with sphalerite *(PyD, #527).* Perhaps this form is the result of replacement of massive, less drusy sulphate accumulations or even direct precipitation of melnikovite at the seawater interface.

Early hexagonal wurtzites formed open crystal groups that were overgrown by colloform melnikovite *(SpG, #2474)*. Closure of these pyrite overgrowths was often incomplete, leaving voids to be filled by later remobilisation *(PyS, #1651, #3061)*. Evidence exists of thin pyrite coatings on crystal faces that punctuated the wurtzite crystal growth *(SpG, #1681)*. During growth of these primitive wurtzites, epitaxial chalcopyrite coated the crystal faces episodically *(CpA, #944)*. Some primitive sphalerite is dominantly colloform showing unidirectional growth, again occasionally punctuated by pyrite coatings *(SpA, #2419)*. The dominant, massive, annealed sphalerite (SpP) seen throughout the HWE is interpreted to originally be primitive, colloform sphalerite and/or wurtzite crystal aggregates that alternated with coatings or infills of melnikovite. Euhedra of magnetite *(MgA, #777)* and siderite/ankerite *(CoA, #1611)* with boulangerite inclusions *(BgA, #1666)* were codeposited with the primary wurtzite/sphalerite, but were later corroded by Devonian remobilisation. There is no preservation of primary galena or tetrahedrite. However, the close association of these two minerals with sphalerite (where sphalerite is dominant), suggests they existed as bands or inclusions in the original primary colloform sphalerite.

The primitively deposited sulphides were increasingly overgrown and buried even further below the tempering effect of seawater. The temperature rose within the mound, due to direct contact with percolating hot fluids emanating from the footwall feeder, and the conduction of heat through the sulphides themselves. When a critical temperature was reached, melnikovite began to recrystallise, especially along fine cracks *(PyA, #1753)*. The unconnected ultrafine-grained spherical voids within the melnikovite were gradually converted to euhedral inter-crystal space, increasing fluid permeability. Some of the primary wurtzite and the colloform sphalerite/galena/tetrahedrite were dissolved back into solution and transferred to upper levels of the mound. Any voids created from the dissolution of sphalerite were rapidly filled by newly deposited pyrite. Some of the Cu, Pb, Zn and Ag contamination (presumedly occurring as sub-microscopic sulphide inclusions) was released from the melnikovite. These either coalesced into any newly created nearby interstices *(PyM, #1820, #1821)*, or were dissolved back into solution for transport to higher levels. Some of the arsenical melnikovite was converted to ultrafine-grained

crystals of arsenopyrite *(AsC, #2025)*, with additional interstitial void space created by the localised density change (pyrite ~5, arsenopyrite ~6). As temperatures increased further due to even deeper burial, pyrite was totally recrystallised into medium-grained euhedra *(PyL, #2841)* or annealed into massive aggregates *(PyT, #1270)*. At this stage all Pb, Zn, Ag, Au and As available to the percolating fluids were taken back into solution and transferred upwards to cooler parts of the mound. Some Pb *(GnA, #3105)*, Zn *(SpE, #971)*, Cu *(CpB, #1145)* and rare Ag *(TeI, #973)* was trapped inside the pyrite crystals. Chalcopyrite was only dissolved into solution in the hottest parts of the mound and transferred for redeposition in recrystallised pyrite intersticies in slightly cooler areas.

Irregular cracking of the upper part of the mound occurred coeval with the in situ recrystallisation processes described above. This could be due to local seismic activity and/or hydraulic "jacking", where less permeable parts of the mound succumb to increasing fluid pressures. Whilst these cracks clearly provided a pressure release and additional channelways for transfer of pregnant solution to higher levels, they also provided void space for new sulphide deposition (the "boxwork veining" discussed in section 3.5.1). Symmetric crustiform deposition of pyrite and/or wurtzite/sphalerite continued on the walls of the crack until it was sealed *(PyV, #1518; SpH, #770)*. Multiple generations of superimposed cracking with subsequent filling took place (see thesis frontispiece). In many cases, what appeared to be unidirectional primitive colloform growth of pyrite/sphalerite, could actually be just a portion of the crustiform banding deposited on one side of the crack (other symmetric side not visible in the sample). The author interprets that a high proportion of the sulphide banding seen at Hellyer was created in this way.

The buoyant hot solutions, percolated up through the recrystallised pyrite via connected intersticies and crack networks. As the temperature decreased, the solutions became depleted in Fe and Cu due to pyrite/chalcopyrite deposition and therefore enriched in Pb, Zn, Ag, Au, As and Ba. Arsenopyrite was probably deposited first mainly be replacing pre-existing pyrite *(AsD, #3116)* or as semi-replacive intergrowths with galena/sphalerite/sericite *(AsI)*. The author's interpretation is that

the vast bulk of the remaining contained metal in these rising solutions was deposited just below the mound surface crust, distal from the central feeder. Colloform accretion is envisaged with considerable lateral movement of solutions beneath the protective crust (to explain the occurrence of sphalerite-rich massive sulphide distal from the central feeder). Repeated injection of fresh solution over (and perhaps into) pre-existing colloform deposits would provide an explanation for the alternating bands of pyrite and sphalerite-galena-chalcopyrite seen in these areas (some evidence exists for subhorizontal symmetric banding). This zone, now recognised as the upper HWE, was strongly effected by ductile deformation in the Devonian deformation, and primary depositional features are not well preserved. Barite and silica were deposited at the seawater interface, in close proximity to the central feeder. They were deposited chaotically, as interdigitating layers of barite crystal aggregates ± sphalerite-rich massive sulphide (BAR zone), and chert-pyrite (GSP zone) (Sharpe, 1991).

Eventually, the mound reached its present volume and the heat source began to wane. The thermal retraction phase commenced. All the mineral deposition processes discussed above continued, but increasingly lower in the mound. Any interstitial voids remaining were gradually filled by precipitation from the cooling solutions. About 14% of the total deposit sphalerite and maybe 20% of the galena was deposited in any available void *(SpN, #812, #1024)*, *(GnG, #814, #1977)*. A bubbly form of melnikovite formed overgrowths and infills *(PyW, #807, #3183)*, whilst chert±pyrite framboids *(Pyb, #638)*, barite *(BaF, #2432)*, sericite *(SeC, #989)*, chlorite±pyrite framboids *(Pyb, #1804)* and carbonate *(CoE, #915)* took up the last remaining void space.

5.7.3 Devonian deformation and remobilisation

The Hellyer massive sulphide underwent east-west compression in the Middle Devonian with associated prehnite-pumpellyite facies metamorphism (Whitford et al., 1982). According to Spear (1993, p.17) this facies equates to a temperature range of 100-250°C which is sufficient to remobilise sphalerite, galena, chalcopyrite, all sulphosalts, electrum and all the gangue minerals. This is exactly what can be

observed texturally in all Hellyer samples. The strain partitioning concept put forward by Drown and Downs (1990) is well supported: massive pyrite areas underwent brittle deformation with extensive pull-apart tensile features while sphalerite-galena was deformed in an extensive, ductile manner.

The upper parts of the HWE are most deformed, with strong annealing of massive sphalerite and local coarsening remobilisation of galena and chalcopyrite *(SpP, #1412; GnJ, #2476); CpE, #2477)*. Inclusions of pyrite *(Pye, #681)*, arsenopyrite *(AsK, #1630)*, siderite/ankerite *(CoA, #579)* and magnetite *(MgA, #578)* were partially corroded during this annealing process. The massive sphalerite grains do not exhibit any significant elongation parallel to cleavage, but galena elongation is common *(GnJ, #1458)*. The galena remobilisation, on a macroscopic scale, sometimes parallels the regional steep east-dipping cleavage, but mostly parallels the overall pyrite/sphalerite banding (which in turn tends to parallel the orientation of the nearest orebody contact). Bands of fine-grained pyrite euhedra within the massive sphalerite frequently show small-scale folds and contortion *(PyP, #1929)*.

Chalcopyrite, galena, tetrahedrite, bournonite and quartz were all strongly remobilised into Devonian tensile voids; sphalerite and the other gangue minerals distinctly less so. Pull-apart cracks in crystalline pyrite, mostly <200µm across, were filled with galena *(GnM, #1742)*, chalcopyrite *(CpH, #1187)*, tetrahedrite *(TeE, #2661)*, bournonite *(BoA, #1608)* and sphalerite *(SpR, #1565)* or combinations (e.g. *SpT, #1679*) where chalcopyrite most commonly is located on the selvedge and galena in the centre. Rarely, arsenopyrite rhombs *(AsL, #1684)*, native antimony *(SbA, #1605)* and electrum *(AuB, #2735)* were deposited in the remobilised galena or tetrahedrite. The gangue minerals also filled pull-aparts in pyrite with well developed fibre growth parallel to cleavage. Over 20% of the total quartz occurs in this way *(QzL, #1316)*, but pull-apart infills of carbonate *(CoK, #2935)* and barite *(BaG, #3128)* are rare. Coarse-grained remobilisation into "pressure shadow" areas surrounding pyrite, quartz or carbonate euhedra also occurred, with galena *(GnL, #829)*, tetrahedrite *(TeD, #832)*, bournonite *(BoA, #459)* and sphalerite *(SpR, #625)* the most common. Rarely, pyrargyrite *(PgA, #509)* and argentite *(AaA, #544)* also were remobilised.

Chalcopyrite (CpG, #950) and galena (GnK, #2654) locally formed large remobilised segregations, that partially replaced sphalerite and even pyrite.

Much of the remobilised galena, chalcopyrite, tetrahedrite and to a lesser extent sphalerite, moved only small distances to take up generally available interstitial regions nearby *(GnG, #1852; CpF, #951; TeG, #954; TeA, #1643; SpN, #1718)* or to replace any available preserved melnikovite, particularly narrow colloform bands and pseudomorphs *(GnH, #598; GnD, #1570; SpM, #2961; TeC, #3134).*

In the hottest remobilised areas, rare late pyrite was redeposited on chalcopyrite surfaces *(CpF, #405; Pyg, #1112).*

Very late in the Devonian, quartz *(QzM, #548),* carbonate *(CoM, #432)* and barite *(BaF, #2485)* were remobilised partially replacing massive and interstitial sphalerite.

In the hangingwall caps, the Devonian deformation event strongly recrystallised the barite *(BaD, #2579)* into fibres and produced incipient recrystallisation of chert *(QzG, #2973)* in the GSP zone.

5.7.4 Mesozoic Deformation

During the Mesozoic deformation, shallow brittle faulting shattered the strongly pyritic areas of the FWD *(Pyk, #1272)*. In the most intensely fractured areas, shattering graded into cataclasis with mechanical rounding of fragments *(Pyk, #1202)* and interstitial voids. Where the Mesozoic faults cut through sphalerite-rich regions, they created unusual, but characteristic, irregular fracture networks *(Pyl, #1200),* infilled with angular pyrite *(Pyl, #2606)* and sphalerite *(SpW, #2166)* fragments set in a quartz *(QzQ, #2792)* and/or chlorite *(ClK, #3007)* matrix. Some Mesozoic fractures were completely filled with chlorite *(ClK, #2795)* or barite *(BaG, #2537)*; these clearly cut across Devonian remobilised minerals (e.g. *QzL, #2310, #2312*).

Rare narrow cracks that cut across all earlier features were filled with remobilised

galena *(GnV, #669),* chalcopyrite *(CpK, #502),* tetrahedrite *(TeJ, #1029),* cubanite *(CbB, #2201)* and very rare argentite *(AaB, #563).*

5.8 Summary and concluding remarks

The microtextural study has clearly established a vast array of diverse textures that comprise the Hellyer massive sulphide as preserved today. Two-thirds of the deposit has original Cambrian mound-building textures preserved, whilst the remainder reflects overprints from the Devonian and Mesozoic deformations. Careful analysis of these textures, mapped in 3-dimensional space, has allowed classification of textural suites into paragenetic groupings that reflect contemporaneous deposition and refining processes. These processes were strongly controlled by temporal and spatial variation of temperature within a growing sulphide mound that overlay a well focussed central feeder zone in the footwall. While deformation in the Devonian, recrystallised and/or remobilised all minerals except pyrite, there was only minor displacement of minerals from their original, Cambrian depositional locations. Mesozoic deformation was restricted to fault-related pyrite cataclasis and very minor low-temperature remobilisation.

6. MINERAL CHEMISTRY

6.1 Introduction

The aim of the microprobe programme was to investigate how mineral composition varied according to spatial location and textural style. It was hoped that this could then be tied to the interpreted paragenetic sequence to assess how mineral composition changed with time during the massive sulphide deposition.

Previous microprobe analyses of massive sulphide samples from three early exploration holes were undertaken by Ramsden et al. (1990); for a specially commissioned gold study by Gemmell (1990a); and of baritic and siliceous cap material by Sharpe (1991).

6.2 Method

6.2.1 Sample selection

Samples were selected for microprobing in two stages. The initial stage involved selecting every sample on section 10610N, and the second stage involved selecting 1 in 5 samples from sections 10670N and 10730N (west) (Fig. 93). An additional 7 samples were probed for identification and special analyses (Table 23). Unfortunately, time constraints did not permit a full coverage over all the samples examined in the microtextural study.

Some analyses were discarded due to contamination from other mineral(s) or very low totals.

Table 23 - Samples used for microprobe work showing the number of analyses performed for each mineral (Py=pyrite, Sp=sphalerite, Gn=galena, As=arsenopyrite, Cp=tetrahedrite, Bo=bournonite, Ba=barite, Co=carbonate, Cl=chlorite).

Sample	Rings	Total	Py	Sp	Gn	As	Cp	Te	Bo	Ba	Co	Cl	Other
61-442-69.0	4	42	8	18	9			1		2	4		
61-443-76.7	6	55	17	15	12		2	3		6			
61-449-59.0	4	41	8	14	6	2	4	5				2	
61-449-89.6	4	42	12	14	7		2	3		2	2		
61-450-72.2	5	66	12	35	10	4					2		3
61-450-85.9	3	30	4	14	10		1				1		
61-451-112.3	4	57	19	16	13		3			5	1		
61-451-125.9	3	15	6	3	3		1	1		1			
61-451-99.7	5	51	9	15	13		7	2		4			1
61-452-44.1	4	42	8	9	6	1		4	6		8		
61-452-57.3	4	34	10	11	3	2		2			6		
61-452-71.8	4	30	6	6	4	4			5		5		
61-452-84.6	4	22	4	7	1	7					3		
61-452-97.6	3	14	3	4	2			3		2			
61-454-45.0	2	29	6	10	2			5	4		2		
61-454-58.9	6	58	15	22	14	3	2				2		
61-454-71.3	2	12	2	4	3		1	2					
61-454-82.3	4	18	3	6				4			2		3
61-455-61.6	5	51	15	21	7	2	5						1
67-208-37.0	1	2										2	
67-209-42.8	3	34	16	10	4		4						
67-229-41.6	4	39	17	15	5						2		
67-231-16.3	4	49	13	10	10	5	6	5					
67-234-10.7	1	4											4
67-377-126.0	4	52	18	15	11		2	3		3			
67-377-59.4	4	53	15	20	6		9	3					
67-378-70.8	4	29	11	11	3		2				2		
67-381-102.4	4	20	10	5						3	2		
67-381-76.5	1	7										6	1
67-382-17.3	4	49	16	19	12		2						
67-382-96.1	4	57	12	21	10	1	1	8			4		
67-384-59.7	4	39	24	8	5			2					

Sample	Rings	Total	Py	Sp	Gn	As	Cp	Te	Bo	Ba	Co	Cl	Other
67-385-21.6	1	3						2					1
67-385-39.9	2	47	13	20	8	4	2						
67-388-42.4	2	22	6	9	5						2		
73-050-356.7	6	90	18	29	16		1	6	2		12		6
73-151-21.1	5	65	26	20	12		7						
73-157-6.3	5	65	13	26	16	2					8		
73-221-17.9	2	14										14	
73-341-78.7	2	9									4		5
73-342-127.6	1	4										1	3
73-347-20.4	7	81	13	18	12	11	7	20					
73-347-49.5	5	71	23	25	16						7		
73-348-30.8	6	80	27	30	5		2	3			10		3
73-349-8.0	5	51	45		2			1			3		
73-351-36.7	5	68	22	16	14			6			10		
73-355-30.6	5	61	17	29	10			3			2		
73-357-77.4	6	72	16	32	12	1	6	5					
10610N Total	76	709	167	244	125	25	28	35	15	22	38	2	8
10670N Total	47	506	171	163	79	10	28	23	0	6	12	8	6
10730N Total	60	731	220	225	115	14	23	44	2	0	56	15	17
TOTAL	183	1946	558	632	319	49	79	102	17	28	106	25	31
Total Valid	**183**	**1872**	**543**	**621**	**319**	**45**	**76**	**102**	**8**	**28**	**105**	**25**	**31**

6.2.2 Locational technique

The standard technique was used to accurately identify the beam position for each analysis. Areas of representative mineralogy and texture (or, minerals requiring identification) were selected and marked with drawing ink "rings" 3-4mm in diameter. While ensuring the polished section was always aligned "east-west" across the microscope stage, each ring was photographed with print film. The author has found through experience, that unless each photograph is taken with the same orientation, locating the beam position in fine-grained textures can be difficult. The processed postcard-size colour prints were then labelled with sample and ring number, before probe sessions began. Once the polished section was placed in the

probe, location of the beam was achieved by visually comparing the video display on the probe with the colour photograph taken through the microscope. Analysis points were labelled with drawing ink using a sequential numbering system unique for each ring (Py1,Py2, Py3,Sp1,Sp2 etc). All available locational photomicrographs are included in Appendix I(b).

6.2.3 Instrumentation

All analyses were carried out between May 1991 and November 1993 by the author (assisted by W. Jablonski) using the Camebax SX50 microprobe installed in the Central Science Laboratory at the University of Tasmania. Operating parameters used for each analysis label and calculated detection limits are provided in Appendix I(b).

6.2.4 Data handling

All raw analyses, together with locational data, were entered into a database (full listing provided in Appendix I(a)). These data were then transferred to spreadsheet software for validation (rejecting any examples of contamination or very low totals), normalising (see below), grouping according to location and textural type and finally, averaging.

Because microprobe analysis was undertaken in 8 two-day sessions over a 2½-year period (with inevitable instrument and calibration drift), there was considerable variation in analysis totals between the sessions (Table 24). In hindsight, the correct method would have been to use one polished section (with all minerals represented) as a standard. This could have been analysed at the beginning and conclusion of each probe session, with subsequent corrections for drift. Given that this drift correction method was not used, it was decided to normalise all analyses to sum to 100%. This was necessary to enable valid comparison of analyses between samples at different 3D locations. The author felt that investigation of mineral compositional zonation could not proceed without some correction for the totals drift.

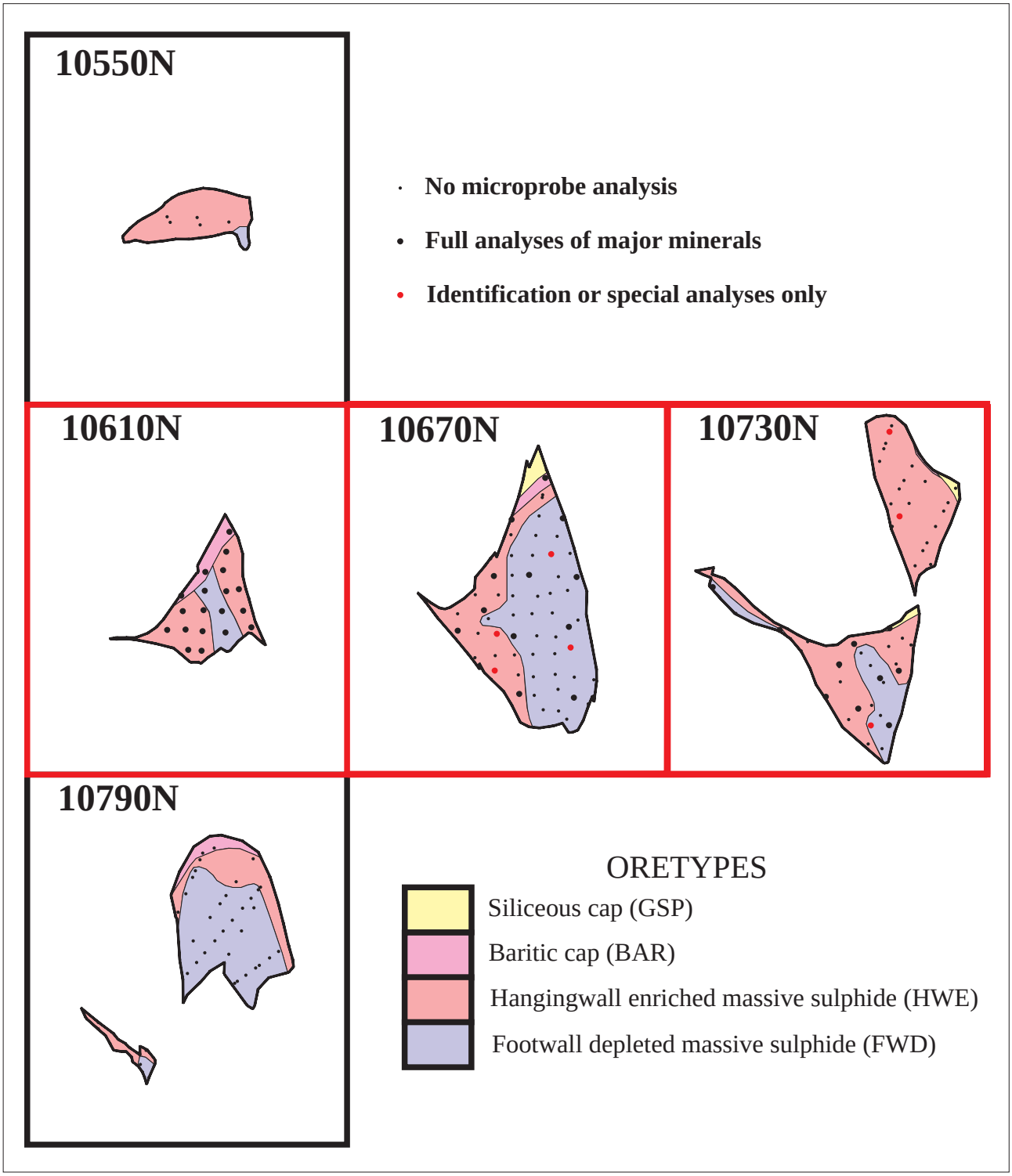

Figure 93 - Location of samples used for microprobe analyses

Table 24 - Variability of analysis totals according to probe label used

PROBE LABEL	LOWEST TOTAL	HIGHEST TOTAL	MEAN TOTAL
AGAUHG	98.80	100.57	99.65
BARIUM	97.50	103.10	101.24
GALENA	95.51	103.27	98.68
PBSALT	91.66	100.79	97.33
PYASGOLD	91.70	102.12	98.39
PYRITE	94.52	103.01	99.33
PYTRACE	99.32	99.54	99.43
SPHALER	92.03	101.20	98.77
TETRA	92.05	101.96	98.95

6.3 Results and interpretation

6.3.1 Pyrite

Pyrite analyses are summarised in Table 25. The most striking compositional variation is between the spongy melnikovite and the crystalline pyrite. This is particularly evident for Cu ([crystalline Cu content : melnikovite Cu content] ratio of 0.18), As (0.23), Pb (0.32) and Ag (0.55). Au also appears to be concentrated in melnikovite, but there were insufficient analyses performed using the high quality PYTRACE or PYASGOLD labels to be confident of the result. Significantly, Zn does not follow the pattern of the other metals, and has a higher content in the crystalline pyrite. A further illustration of the "compositional refining" that relates to increased crystallinity, is shown (Fig. 94) by comparing PyA (very primitive featureless melnikovite) with PyM (intermediate crystallinity) and PyL/PyT (euhedral and annealed pyrite).

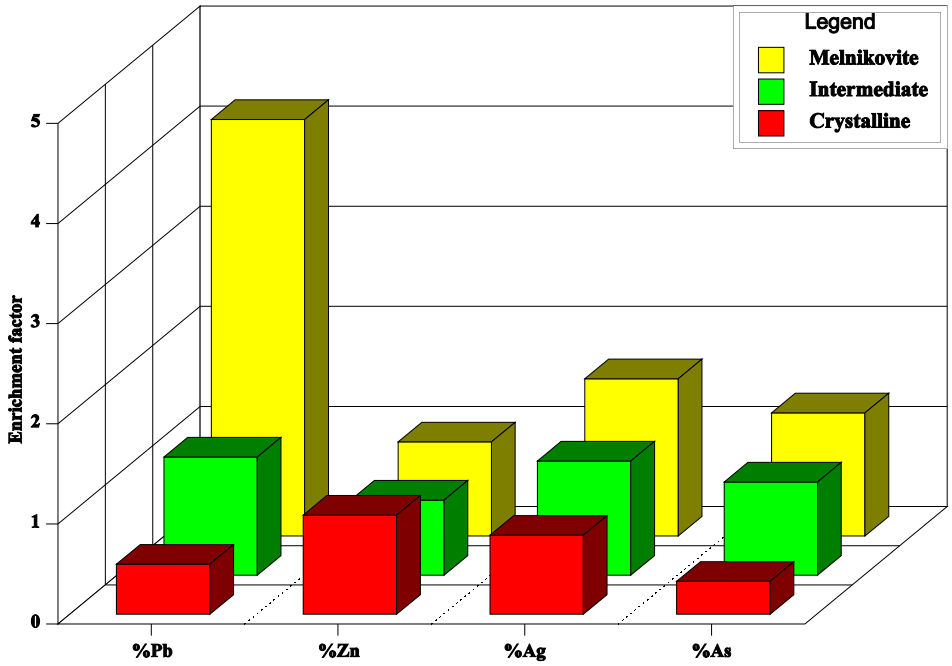

Figure 94 - Relationship between pyrite crystallinity and base metal composition. Metal contents have been normalised by calculating an "enrichment factor", which is the ratio between an individual content and the volume weighted global average pyrite composition.

The author interprets that a continual refining (i.e. rejection of base metal impurities) process took place as the pyrite was recrystallised in situ during the Cambrian mound building event. This rejected base metal was taken back into solution (augmenting its existing base metal content) and was transferred higher in the mound. An attempt has been made to construct a semi-quantitative metal balance of pyrite contaminants. If it is assumed, that all existing crystalline pyrite, was originally melnikovite with base metal impurities similar to that analysed for the now-existing preserved melnikovite, the following estimates apply.

- from Table 3; the total mass of massive sulphide is 16.2 Mt
- from Table 2; the pyrite accounts for 53.1% by weight
- from above, the total mass of pyrite is (0.531 X 16.2) = 8.6 Mt
- from Table 21; of all pyrite, 23% (1.98 Mt) is melnikovite and 77% (6.62 Mt) is crystalline

- from Table 25; preserved melnikovite has average contaminant levels of 0.062%Cu, 0.678%Pb, 0.022%Ag, 1.077%As - this is assumed to be the grade of all pre-existing melnikovite
- from Table 25; crystalline pyrite has average contaminant levels of 0.011%Cu, 0.219%Pb, 0.012%Ag, 0.248%As - this is assumed to be the minimum grade attainable after recrystallisation
- the 6.62Mt of crystalline pyrite was recrystallised from original melnikovite, therefore releasing (0.062-0.011)=0.051%Cu, (0.678-0.219)=0.459%Pb, (0.022-0.012)=0.010%Ag, (1.077-0.248)=0.829%As
- the contaminant metal released amounts to:

  (6.62 Mt X 0.051%) = 3376t Cu

  (6.62 Mt X 0.459%) = 30386t Pb

  (6.62 Mt X 0.010%) = 662t Ag

  (6.62 Mt X 0.829%) = 54880t As
- the present metal content of the deposit (less that held within all pyrite, from Table 25) is:

  (16.2 Mt X 0.38%) - (8.60 Mt X 0.043%) = 57862t Cu

  (16.2 Mt X 7.1%) - (8.60 Mt X 0.328%) = 1121992t Pb

  (16.2 Mt X 168ppm) - (8.60 Mt X 0.014%) = 15184t Ag

  (16.2 Mt X 1.2%) - (8.60 Mt X 0.445%) = 156130t As
- the proportion of metal that was released by the pyrite refining process is therefore estimated to be:

  3376/57862 = **6% of the Cu**

  30386/1121992 = **3% of the Pb**

  662/15184 = **4% of the Ag**

  54880/156130 = **35% of the As**

The author therefore concludes that whilst this refining process appears insignificant for Cu, Pb and Ag; a substantial proportion of the semi-replacive arsenopyrite (AsI, AsK) observed in the HWE (Fig. 55) was sourced from As released by pyrite refining, through in situ recrystallisation of the FWD below.

Table 25 - Summary of microprobe analyses for pyrite (blank=not analysed)

Mintex	No.of analyses	Volume fraction	Normalised composition											
			%S	%Fe	%Co	%Ni	%Cu	%Zn	%As	%Se	%Ag	%Au	%Pb	%Total
PyA	48	0.076	52.4	46.0	0.01	0.01	0.02	0.09	0.55	0.01	0.02	0.02	1.36	100
PyB	24	0.039	52.6	46.0	0.00	0.01		0.08	0.95	0.01	0.02		0.33	100
PyC	9	0.025	53.0	46.4	0.00	0.01	0.00	0.06	0.33	0.00	0.02	0.01	0.19	100
PyD	3	0.000	52.3	46.8			0.03		0.84	0.00	0.06	0.05		100
PyH	10	0.028	52.0	45.2	0.00	0.00		0.04	2.48	0.01	0.03		0.23	100
PyI	6	0.022	52.7	46.4	0.01	0.01	0.03	0.06	0.53	0.03	0.01	0.00	0.31	100
PyL	54	0.168	52.8	46.6	0.01	0.01		0.12	0.21	0.01	0.01		0.15	100
PyM	67	0.137	52.8	46.3	0.00	0.01	0.02	0.07	0.42	0.01	0.02	0.00	0.39	100
PyS	75	0.054	52.5	46.7	0.01	0.01	0.04	0.18	0.24	0.01	0.01	0.00	0.45	100
PyT	34	0.259	52.6	47.0	0.01	0.01		0.08	0.11	0.01	0.01		0.17	100
PyU	4	0.001	51.1	45.2	0.01	0.14	0.20	0.03	1.91	0.02	0.05	0.00	2.11	100
PyV	17	0.047	52.5	46.7	0.00	0.01		0.08	0.61	0.01	0.01		0.16	100
PyW	77	0.042	51.6	45.9	0.00	0.01	0.18	0.03	1.96	0.01	0.03	0.02	0.45	100
PyZ	4	0.006	52.6	46.0	0.00	0.03	0.01	0.23	0.92	0.01	0.04	0.00	0.19	100
Pya	9	0.020	52.6	46.8	0.00	0.00		0.20	0.30	0.00	0.01		0.05	100
Pyb	22	0.005	52.3	45.5	0.01	0.05		0.24	0.85	0.01	0.02		1.02	100
Pyc	7	0.005	52.4	46.2	0.00	0.01	0.10	0.10	1.12	0.01	0.01	0.06	0.15	100
Pyd	12	0.010	52.5	46.6	0.01	0.01	0.05	0.30	0.44	0.02	0.02	0.03	0.24	100
Pye	44	0.014	52.8	46.4	0.01	0.00		0.39	0.22	0.01	0.02		0.17	100
Pyk	6	0.041	52.3	47.5	0.00	0.02		0.04	0.05	0.01	0.00		0.10	100
All analyses weighted by global volume%		**1.000**	**52.54**	**46.55**	**0.006**	**0.010**	**0.043**	**0.095**	**0.445**	**0.008**	**0.014**	**0.009**	**0.328**	**100**
Melnikovite weighted by global volume%		**0.238**	**52.32**	**45.98**	**0.005**	**0.011**	**0.062**	**0.068**	**1.077**	**0.009**	**0.022**	**0.017**	**0.678**	**100**
Non-melnikovite weighted by global volume%		**0.762**	**52.65**	**46.75**	**0.006**	**0.009**	**0.011**	**0.104**	**0.248**	**0.007**	**0.012**	**0.001**	**0.219**	**100**

Correlation coefficients between metals are generally low, apart from: Ag/Au 0.40, Ag/Cu 0.28, Ag/As 0.25 and Ag/Ni 0.23.

Spatial plots of pyrite composition are not provided, since composition is clearly controlled by crystallinity (and therefore individual mintex types). The reader is referred to the spatial mintex plots of the atlas in Appendix II.

6.3.2 Sphalerite

Sphalerite analyses are summarised in Tables 26-28. The raw analyses suffered from unavoidable chalcopyrite contamination within the beam area, due to ultrafine-grained blebs ("chalcopyrite disease"). This has been corrected by assuming all Cu is contained within chalcopyrite and then subtracting proportional amounts of S, Fe, Ag, Se (from average probe composition). The final dataset shows considerable variation in %Fe, and lesser, but significant variation in Hg. Correlation coefficients are all very close to zero, apart from Mn/Se 0.14.

The lower part of Table 26 shows a tendency for sphalerite %Fe to decrease slightly, passing from early to late through the paragenetic sequence. The remobilised sphalerites (optically paler in colour) have lower than average %Fe (interstitial infills SpN 2.7%Fe, pull-apart infills SpR 2.2%Fe). On the other hand, the primitive sphalerites (optically quite dark in colour) have higher than average %Fe (colloform SpA 4.4%Fe). Figure 95 shows average sphalerite %Fe plotted at the sample locations on each cross-section. Maximum Fe content occurs within the HWE, particularly adjacent to the western termination. Minimum Fe content occurs in the baritic cap and in the more proximal parts of the FWD.

The occurrence of "chalcopyrite disease" appears to have no relationship to composition. Averages (normalised, less chalcopyrite) are: diseased sphalerite, 2.9%Fe and non-diseased sphalerite, 3.1%Fe. Several scans across obviously zoned sphalerite crystals found only very small differences from centre to edge. However, in most cases, the core of the crystal assayed 0.1-0.2%Fe higher than the crystal margin.

No trend for sphalerite Hg content against paragenetic position is observed and similarly no zonation is apparent from the spatial plots (Fig. 96). However, significant maximum values occur in the baritic cap on section 10610N.

Table 26 - Summary of microprobe analyses of sphalerite by mintex and paragenetic group

Mintex	No.of analyses	Volume fraction	Normalised composition								
			%S	%Mn	%Fe	%Cu	%Zn	%Se	%Ag	%Hg	%Total
SpA	9	0.032	33.4	0.02	4.49	0.11	61.9	0.01	0.00	0.03	100
SpG	32	0.073	33.2	0.03	5.31	2.94	58.4	0.01	0.02	0.02	100
SpH	19	0.013	33.1	0.01	3.21	0.03	63.6	0.01	0.01	0.03	100
SpI	3	0.007	33.8	0.01	6.87	0.36	58.9	0.00	0.01	0.05	100
SpN	132	0.098	33.2	0.01	2.82	0.13	63.8	0.01	0.01	0.04	100
SpO	3	0.002	32.9	0.01	1.00	0.13	65.9	0.00	0.01	0.03	100
SpP	326	0.686	33.3	0.02	3.60	0.32	62.7	0.01	0.01	0.03	100
SpQ	25	0.009	33.6	0.02	2.27	0.45	63.6	0.00	0.01	0.06	100
SpR	57	0.076	33.1	0.02	2.35	0.17	64.3	0.01	0.01	0.04	100
SpS	6	0.001	33.3	0.03	2.01	0.21	64.4	0.00	0.01	0.05	100
SpW	3	0.002	33.3	0.01	4.15	0.09	62.4	0.01	0.00	0.02	100
All analyses weighted by global volume%		**1.000**	**33.26**	**0.022**	**3.581**	**0.471**	**62.60**	**0.007**	**0.012**	**0.034**	**100**

Primitive Deposition	0.05	33.45	0.02	4.49	0.11	61.89	0.01	0.00	0.03	100
In situ recrystallisation	0.03	33.23	0.03	5.31	2.94	58.45	0.01	0.02	0.02	100
Intra-mound veining	0.03	33.31	0.02	5.00	1.45	60.16	0.01	0.01	0.03	100
Upward redeposition	0.27	33.27	0.02	3.60	0.45	62.60	0.01	0.01	0.03	100
Thermal retraction	0.07	33.24	0.01	2.75	0.14	63.80	0.01	0.01	0.04	100
Devonian remobilisation	0.54	33.25	0.02	3.37	0.29	63.01	0.01	0.01	0.03	100

Mintex	No.of analyses	Volume fraction	Normalised composition (less chalcopyrite)								
			%S	%Mn	%Fe	%Cu	%Zn	%Se	%Ag	%Hg	%Total
SpA	9	0.032	33.4	0.02	4.40		62.1	0.01	0.00	0.03	100
SpG	32	0.073	33.1	0.03	2.90		63.9	0.01	0.02	0.03	100
SpH	19	0.013	33.1	0.01	3.18		63.7	0.01	0.01	0.03	100
SpI	3	0.007	33.8	0.01	6.61		59.5	0.00	0.01	0.05	100
SpN	132	0.098	33.2	0.01	2.71		64.0	0.01	0.01	0.04	100
SpO	3	0.002	32.9	0.01	0.89		66.2	0.00	0.01	0.03	100
SpP	326	0.686	33.3	0.02	3.34		63.3	0.01	0.01	0.03	100
SpQ	25	0.009	33.6	0.02	1.91		64.4	0.00	0.01	0.06	100
SpR	57	0.076	33.1	0.02	2.22		64.7	0.01	0.01	0.04	100
SpS	6	0.001	33.3	0.03	1.84		64.8	0.00	0.01	0.05	100
SpW	3	0.002	33.3	0.01	4.09		62.5	0.01	0.00	0.02	100
All analyses weighted by global volume%		**1.000**	**33.24**	**0.022**	**3.197**		**63.48**	**0.007**	**0.012**	**0.034**	**100**

Primitive Deposition	0.05	33.44	0.02	4.40		62.09	0.01	0.00	0.03	100
In situ recrystallisation	0.03	33.09	0.03	2.90		63.93	0.01	0.02	0.03	100
Intra-mound veining	0.03	33.24	0.02	3.82		62.86	0.01	0.01	0.03	100
Upward redeposition	0.27	33.25	0.02	3.23		63.44	0.01	0.01	0.03	100
Thermal retraction	0.07	33.23	0.01	2.64		64.06	0.01	0.01	0.04	100
Devonian remobilisation	0.54	33.24	0.02	3.13		63.55	0.01	0.01	0.04	100

Table 27 - Summary of microprobe analyses of sphalerite by sample

Sample	No.of analyses	Sphalerite Volume%	Normalised composition								
			%S	%Mn	%Fe	%Cu	%Zn	%Se	%Ag	%Hg	%Total
61-442-69.0	18	42.6	33.0	0.01	1.25	0.07	65.7	0.00	0.01	0.04	100
61-443-76.7	12	39.6	33.2	0.01	2.15	0.09	64.5	0.01	0.01	0.02	100
61-449-59.0	14	24.2	33.3	0.01	1.69	0.06	64.9	0.00	0.00	0.05	100
61-449-89.6	14	30.0	33.2	0.02	1.44	0.12	65.2	0.01	0.02	0.03	100
61-450-72.2	35	64.0	33.8	0.02	7.07	0.19	58.9	0.00	0.01	0.05	100
61-450-85.9	14	48.0	33.5	0.03	4.18	1.12	60.9	0.01	0.01	0.03	100
61-451-99.7	15	25.4	33.3	0.01	1.18	0.07	65.4	0.00	0.01	0.06	100
61-451-112.3	16	39.6	32.6	0.01	1.36	0.15	65.8	0.01	0.01	0.02	100
61-451-125.9	3	3.8	33.2	0.02	1.47	0.20	65.1	0.01	0.01	0.03	100
61-452-44.1	9	23.4	33.7	0.03	2.88	0.13	63.1	0.01	0.02	0.07	100
61-452-57.3	11	12.0	33.6	0.01	2.63	0.06	63.6	0.01	0.01	0.06	100
61-452-71.8	6	7.4	33.1	0.01	3.54	0.01	63.3	0.00	0.02	0.06	100
61-452-84.6	7	18.2	32.9	0.01	2.79	0.01	64.2	0.00	0.03	0.05	100
61-452-97.6	4	0.1	34.4	0.01	0.69	0.05	64.6	0.01	0.01	0.14	100
61-454-45.0	10	39.6	33.3	0.01	5.09	0.59	61.0	0.01	0.02	0.05	100
61-454-58.9	20	44.6	33.5	0.02	4.65	0.09	61.7	0.00	0.01	0.03	100
61-454-71.3	4	17.0	33.9	0.02	4.38	0.04	61.6	0.01	0.00	0.03	100
61-454-82.3	5	0.4	32.7	0.01	1.63	1.06	64.4	0.00	0.00	0.16	100
61-455-61.6	21	45.4	32.9	0.01	4.92	0.11	62.0	0.01	0.01	0.03	100
67-209-42.8	8	0.1	32.2	0.01	1.28	0.05	66.4	0.01	0.00	0.04	100
67-229-41.6	15	5.8	33.0	0.01	1.03	0.08	65.8	0.01	0.01	0.06	100
67-231-16.3	10	19.0	33.2	0.02	5.31	0.62	60.7	0.01	0.01	0.07	100
67-377-59.4	20	19.4	33.8	0.02	3.05	2.40	60.7	0.01	0.00	0.01	100
67-377-126.0	15	26.0	33.5	0.01	1.12	0.08	65.2	0.01	0.01	0.03	100
67-378-70.8	11	8.4	34.3	0.01	2.13	0.25	63.3	0.01	0.01	0.04	100
67-381-102.4	5	17.6	34.3	0.00	1.12	0.23	64.3	0.01	0.02	0.01	100
67-382-17.3	19	31.4	32.4	0.03	4.12	0.10	63.3	0.00	0.01	0.03	100
67-382-96.1	21	23.4	33.1	0.01	1.35	0.08	65.4	0.01	0.01	0.04	100
67-384-59.7	8	9.8	33.4	0.02	3.38	0.10	63.0	0.01	0.01	0.03	100
67-385-39.9	20	34.6	32.3	0.02	4.80	0.38	62.5	0.00	0.01	0.04	100
67-388-42.4	9	30.0	32.7	0.01	5.59	0.04	61.6	0.00	0.01	0.05	100
73-050-356.7	28	61.0	33.3	0.01	5.63	0.27	60.8	0.01	0.01	0.01	100
73-151-21.1	19	10.6	33.2	0.01	1.57	0.09	65.1	0.01	0.01	0.03	100
73-157-6.3	26	56.6	33.1	0.02	5.33	0.10	61.4	0.01	0.02	0.03	100
73-347-20.4	17	19.6	32.9	0.01	2.29	0.20	64.5	0.01	0.02	0.06	100
73-347-49.5	25	60.2	33.1	0.01	2.44	0.09	64.3	0.01	0.01	0.04	100
73-348-30.8	30	32.6	33.3	0.01	4.56	0.08	62.0	0.01	0.01	0.01	100
73-351-36.7	16	19.4	33.2	0.01	2.11	0.06	64.5	0.01	0.01	0.05	100
73-355-30.6	29	17.2	33.4	0.08	1.67	0.23	64.6	0.02	0.01	0.01	100
73-357-77.4	32	19.6	33.4	0.05	3.46	0.80	62.2	0.01	0.01	0.02	100
All analyses weighted by Sp volume% per sample			**33.22**	**0.017**	**3.579**	**0.254**	**62.86**	**0.007**	**0.012**	**0.035**	**100**

Table 28 - Summary of microprobe analyses of sphalerite by sample (less chalcopyrite)

Sample	No.of analyses	Sphalerite Volume%	Normalised composition (less chalcopyrite)								
			%S	%Mn	%Fe	%Cu	%Zn	%Se	%Ag	%Hg	%Total
61-442-69.0	18	42.6	33.0	0.01	1.19		65.8	0.00	0.01	0.04	100
61-443-76.7	12	39.6	33.2	0.01	2.08		64.7	0.01	0.01	0.02	100
61-449-59.0	14	24.2	33.3	0.01	1.64		65.0	0.00	0.00	0.05	100
61-449-89.6	14	30.0	33.2	0.02	1.34		65.4	0.01	0.02	0.03	100
61-450-72.2	35	64.0	33.8	0.02	6.94		59.2	0.00	0.01	0.05	100
61-450-85.9	14	48.0	33.5	0.03	3.30		63.1	0.01	0.01	0.03	100
61-451-99.7	15	25.4	33.3	0.01	1.12		65.5	0.00	0.01	0.06	100
61-451-112.3	16	39.6	32.6	0.01	1.23		66.1	0.01	0.01	0.02	100
61-451-125.9	3	3.8	33.2	0.02	1.30		65.5	0.01	0.01	0.03	100
61-452-44.1	9	23.4	33.7	0.03	2.78		63.4	0.01	0.02	0.07	100
61-452-57.3	11	12.0	33.6	0.01	2.58		63.7	0.01	0.01	0.06	100
61-452-71.8	6	7.4	33.1	0.01	3.54		63.3	0.00	0.02	0.06	100
61-452-84.6	7	18.2	32.9	0.01	2.78		64.2	0.00	0.03	0.05	100
61-452-97.6	4	0.1	34.4	0.01	0.65		64.7	0.01	0.01	0.14	100
61-454-45.0	10	39.6	33.2	0.01	4.66		62.0	0.01	0.02	0.05	100
61-454-58.9	20	44.6	33.5	0.02	4.59		61.8	0.00	0.01	0.03	100
61-454-71.3	4	17.0	33.9	0.02	4.35		61.7	0.01	0.00	0.03	100
61-454-82.3	5	0.4	32.7	0.01	0.74		66.4	0.00	0.00	0.16	100
61-455-61.6	21	45.4	32.9	0.01	4.84		62.2	0.01	0.01	0.03	100
67-209-42.8	8	0.1	32.2	0.01	1.23		66.5	0.01	0.00	0.04	100
67-229-41.6	15	5.8	33.0	0.01	0.96		65.9	0.01	0.01	0.06	100
67-231-16.3	10	19.0	33.2	0.02	4.82		61.9	0.01	0.01	0.07	100
67-377-59.4	20	19.4	33.7	0.02	1.01		65.2	0.01	0.01	0.01	100
67-377-126.0	15	26.0	33.5	0.01	1.04		65.4	0.01	0.01	0.03	100
67-378-70.8	11	8.4	34.2	0.01	1.92		63.8	0.01	0.01	0.04	100
67-381-102.4	5	17.6	34.3	0.00	0.93		64.7	0.01	0.02	0.01	100
67-382-17.3	19	31.4	32.4	0.03	4.04		63.5	0.00	0.01	0.03	100
67-382-96.1	21	23.4	33.1	0.01	1.28		65.6	0.01	0.01	0.04	100
67-384-59.7	8	9.8	33.4	0.02	3.30		63.2	0.01	0.01	0.03	100
67-385-39.9	20	34.6	32.3	0.02	4.51		63.2	0.00	0.01	0.05	100
67-388-42.4	9	30.0	32.7	0.01	5.56		61.7	0.00	0.01	0.05	100
73-050-356.7	28	61.0	33.3	0.01	5.43		61.3	0.01	0.01	0.01	100
73-151-21.1	19	10.6	33.2	0.01	1.50		65.2	0.01	0.01	0.03	100
73-157-6.3	26	56.6	33.1	0.02	5.26		61.6	0.01	0.02	0.03	100
73-347-20.4	17	19.6	32.9	0.01	2.13		64.9	0.01	0.02	0.06	100
73-347-49.5	25	60.2	33.1	0.01	2.38		64.5	0.01	0.01	0.04	100
73-348-30.8	30	32.6	33.3	0.01	4.50		62.1	0.01	0.01	0.01	100
73-351-36.7	16	19.4	33.2	0.01	2.06		64.6	0.01	0.01	0.05	100
73-355-30.6	29	17.2	33.4	0.08	1.47		65.0	0.02	0.01	0.01	100
73-357-77.4	32	19.6	33.4	0.05	2.82		63.7	0.01	0.01	0.03	100
All analyses weighted by Sp volume% per sample			**33.21**	**0.017**	**3.378**		**63.34**	**0.007**	**0.012**	**0.035**	**100**

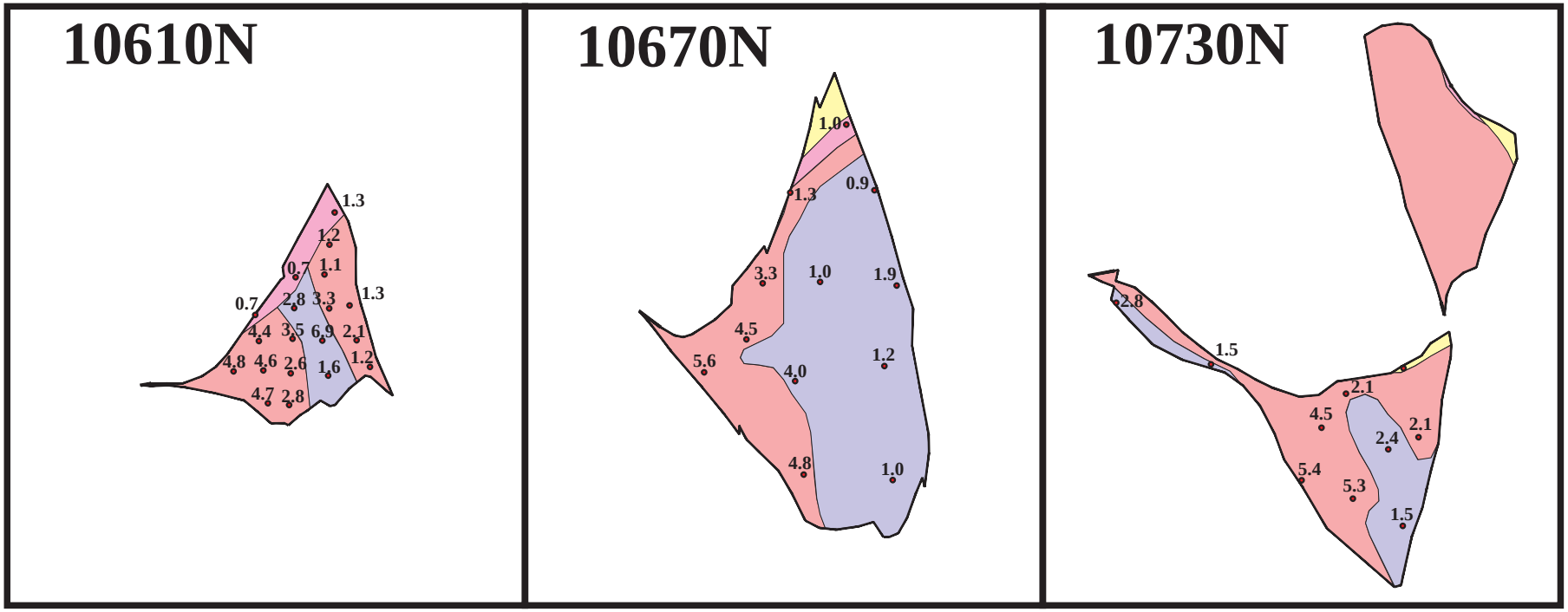

Fig. 95 - Sphalerite %Fe analyses (normalised, less chalcopyrite)

ORETYPES

- Siliceous cap (GSP)
- Baritic cap (BAR)
- Hangingwall enriched massive sulphide (HWE)
- Footwall depleted massive sulphide (FWD)

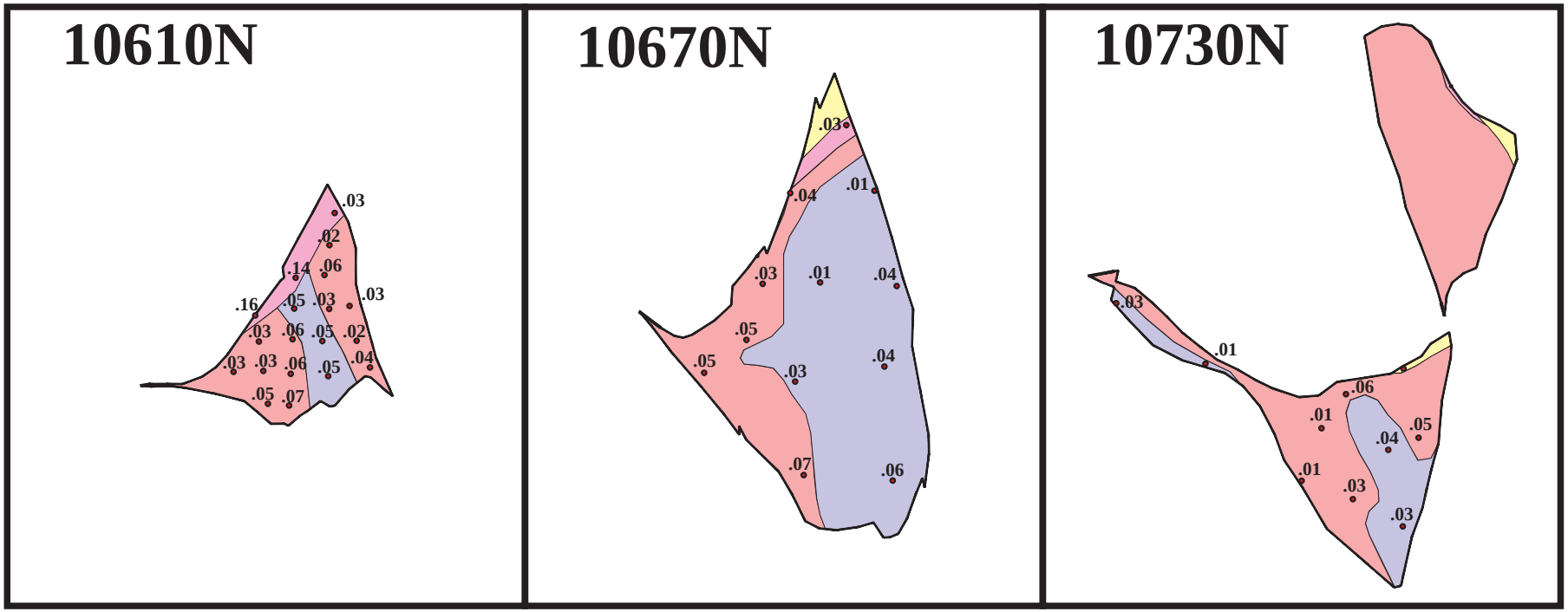

Fig. 96 - Sphalerite %Hg analyses (normalised)

6.3.3 Galena

Galena analyses are summarised in Tables 29-30. There is appreciable compositional variation of the trace elements Ag, Bi and Se. Ag in particular shows wide variability between zero and 0.8% by weight (Fig. 97) and has a high correlation coefficient of 0.66 with Bi.

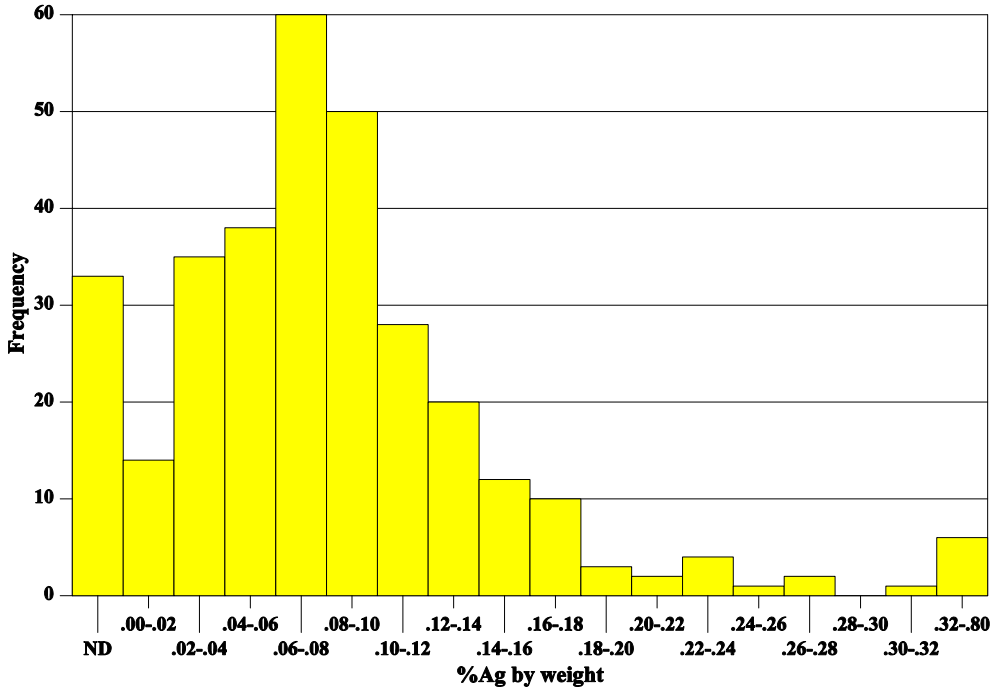

Figure 97 - Distribution of galena Ag analyses (ND=not detected)

The trend of Ag content against paragenetic position is flat and inconclusive. However, the highest Ag contents tend to occur within the FWD and the lowest values in the baritic cap (Fig. 98). One anomalous sample near the western termination on 10610N had two analyses averaging 0.76%Ag, but this coincided with 1.84%Bi content, suggesting submicroscopic inclusions of an unidentified Bi-Ag species (e.g. schapbachite-matildite $AgBiS_2$). Ramdohr (1980, p.657) refers to coupled Ag-Bi in galena as a high temperature indicator, since $AgBiS_2$ has increased solubility in PbS above 215°C due to $AgBiS_2$ lattice similarities with galena. Unfortunately, Sb content was not determined. Sb analyses may have suggested submicroscopic tetrahedrites or bournonite (Ramdohr, 1980, p.655).

Bismuth content appears to decrease passing from early textural galena to later remobilised varieties. Spatial variation of Bi is identical to Ag (Fig. 99), with highest levels in the FWD. Selenium distribution also appears to concentrate in the FWD (Fig. 100), although it shows no correlation with other determined elements. One anomalous sample in the western wing of the Keel Zone had three analyses exceeding 0.5%Se.

Table 29 - Summary of microprobe analyses of galena by mintex

Mintex	No.of analyses	Volume fraction	Normalised composition					
			%S	%Se	%Ag	%Pb	%Bi	%Total
GnF	6	0.001	13.3	0.01	0.04	86.5	0.22	100
GnG	90	0.239	13.5	0.02	0.09	86.2	0.25	100
GnJ	91	0.205	13.4	0.05	0.08	86.3	0.26	100
GnK	64	0.377	13.2	0.01	0.08	86.5	0.19	100
GnL	21	0.104	13.3	0.02	0.11	86.3	0.23	100
GnM	28	0.067	13.5	0.01	0.07	86.3	0.22	100
GnS	7	0.008	13.5	0.02	0.07	86.2	0.12	100
All analyses weighted by global volume%		**1.000**	**13.36**	**0.025**	**0.084**	**86.36**	**0.224**	**100**

Table 30 - Summary of microprobe analyses of galena by sample (blank=not analysed)

Sample	No.of analyses	Galena Volume%	Normalised composition					
			%S	%Se	%Ag	%Pb	%Bi	%Total
61-442-69.0	9	12.0	13.6	0.01	0.06	86.2	0.15	100
61-443-76.7	12	7.2	13.5	0.01	0.07	86.3	0.16	100
61-449-59.0	6	2.0	13.6	0.03	0.12	86.2		100
61-449-89.6	7	7.4	13.3	0.01	0.04	86.5	0.12	100
61-450-72.2	10	3.0	13.7	0.03	0.06	86.2		100
61-450-85.9	10	11.2	13.5	0.03	0.06	86.5		100
61-451-99.7	13	7.2	13.3	0.01	0.02	86.7		100
61-451-112.3	13	10.0	13.2	0.00	0.06	86.6	0.14	100
61-451-125.9	3	1.2	13.4	0.01	0.03	86.5		100
61-452-44.1	6	6.6	13.2	0.01	0.08	86.7		100
61-452-57.3	3	2.4	13.2	0.01	0.09	86.7		100
61-452-71.8	4	0.4	13.0	0.00	0.19	86.8		100
61-452-84.6	1	0.8	13.0	0.01	0.03	86.9		100
61-452-97.6	2	0.1	13.1	0.01	0.02	86.9		100
61-454-45.0	2	7.2	12.3	0.00	0.07	87.6		100
61-454-58.9	14	13.8	12.9	0.00	0.07	87.0		100
61-454-71.3	3	4.6	13.2	0.00	0.04	86.8		100
61-455-61.6	7	3.2	13.4	0.03	0.37	85.4	0.83	100
67-209-42.8	4	0.4	12.8	0.06	0.34	86.0	0.77	100
67-229-41.6	5	0.8	13.4	0.05	0.08	86.2	0.29	100
67-231-16.3	10	0.1	13.4	0.01	0.13	86.3	0.16	100
67-377-59.4	6	3.8	13.6	0.03	0.22	85.4	0.72	100
67-377-126.0	11	11.4	13.4	0.00	0.02	86.4	0.16	100
67-378-70.8	3	1.2	13.6	0.04	0.21	85.7	0.48	100
67-382-17.3	12	8.0	13.5	0.01	0.07	86.2	0.21	100
67-382-96.1	10	6.8	13.5	0.02	0.03	86.2	0.18	100
67-384-59.7	5	4.2	13.8	0.00	0.09	86.0	0.12	100
67-385-39.9	8	10.6	12.9	0.01	0.08	86.8	0.16	100
67-388-42.4	5	8.8	13.7	0.00	0.08	86.1	0.13	100
73-050-356.7	16	16.2	13.8	0.00	0.07	86.0	0.14	100
73-151-21.1	12	1.4	13.5	0.04	0.09	86.2	0.23	100
73-157-6.3	16	11.8	13.0	0.01	0.10	86.6	0.21	100
73-347-20.4	12	6.6	13.1	0.01	0.08	86.6	0.24	100
73-347-49.5	16	11.6	13.8	0.00	0.04	86.0	0.18	100
73-348-30.8	5	1.2	13.9	0.05	0.14	85.5	0.35	100
73-349-8.0	2	0.2	13.7	0.06	0.08	86.0	0.24	100
73-351-36.7	14	5.6	13.5	0.00	0.08	86.2	0.20	100
73-355-30.6	10	3.0	13.2	0.46	0.05	86.1	0.22	100
73-357-77.4	12	7.0	13.5	0.04	0.07	86.3	0.12	100
All analyses weighted by Gn volume% per sample			**13.36**	**0.016**	**0.072**	**86.41**	**0.143**	**100**

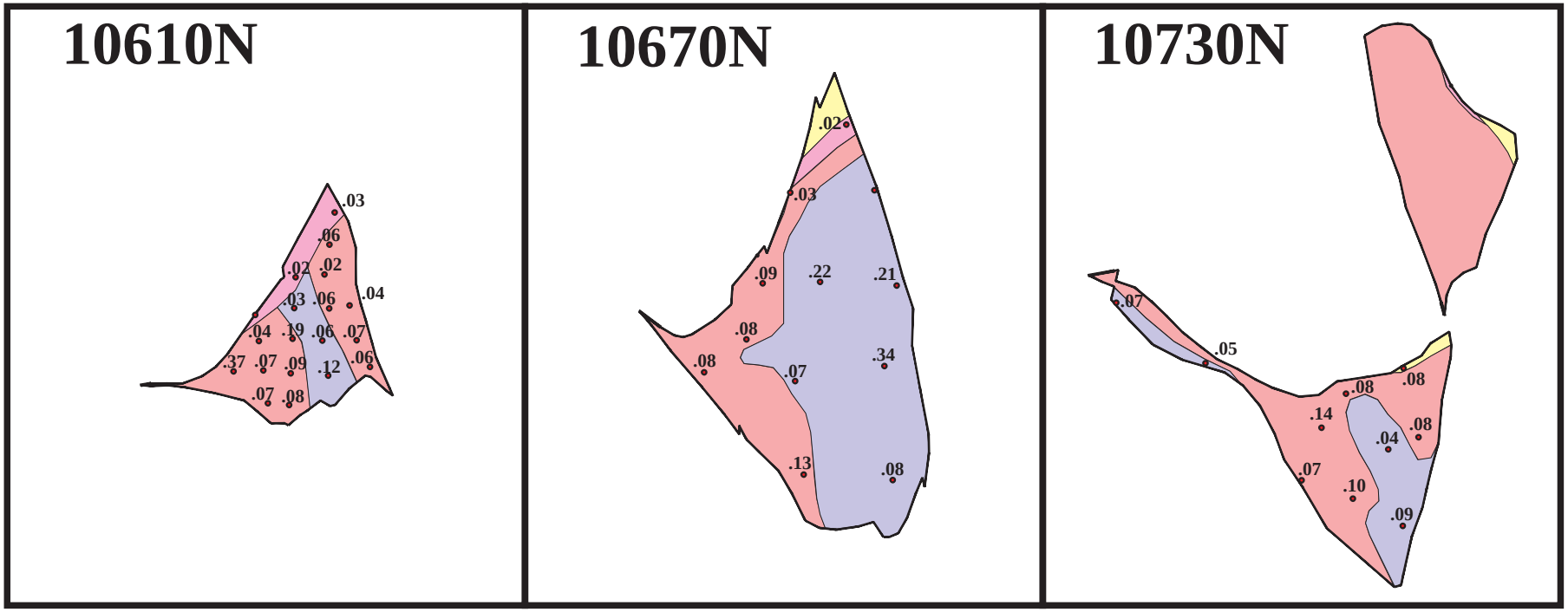

Fig. 98 - Galena %Ag analyses (normalised)

ORETYPES

- Siliceous cap (GSP)
- Baritic cap (BAR)
- Hangingwall enriched massive sulphide (HWE)
- Footwall depleted massive sulphide (FWD)

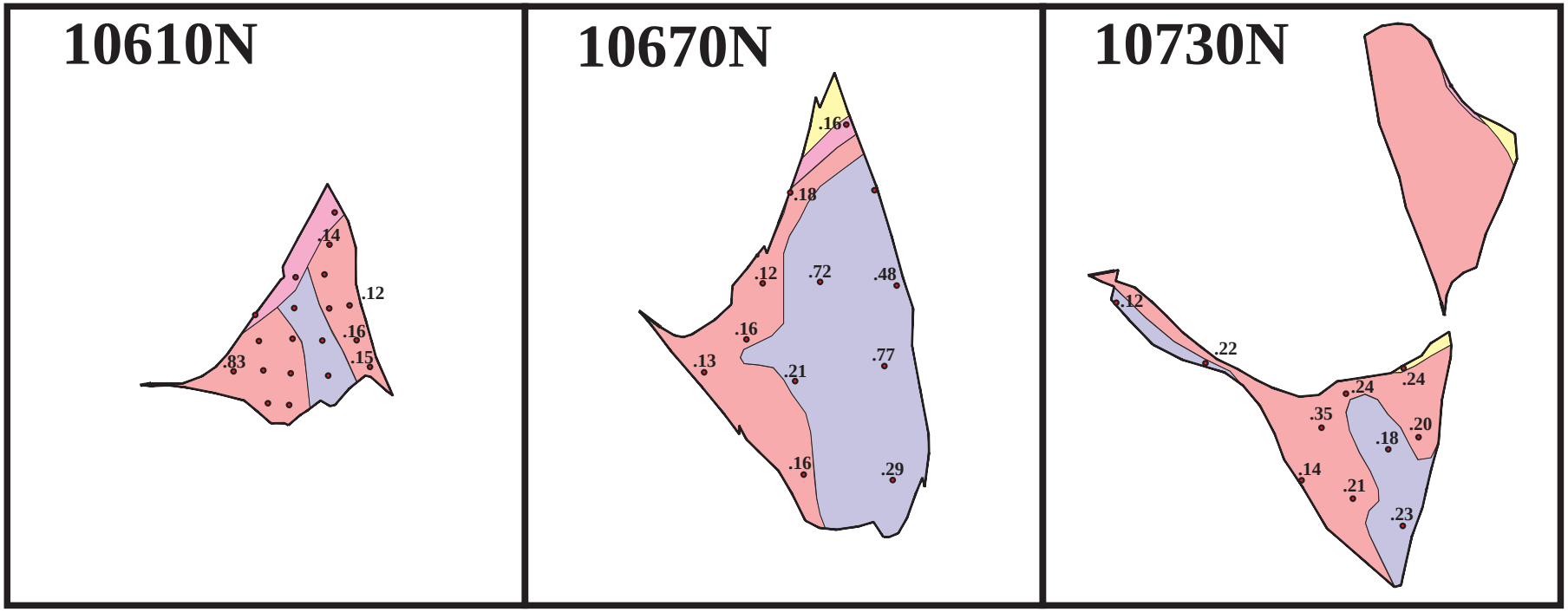

Fig. 99 - Galena %Bi analyses (normalised)

ORETYPES

- Siliceous cap (GSP)
- Baritic cap (BAR)
- Hangingwall enriched massive sulphide (HWE)
- Footwall depleted massive sulphide (FWD)

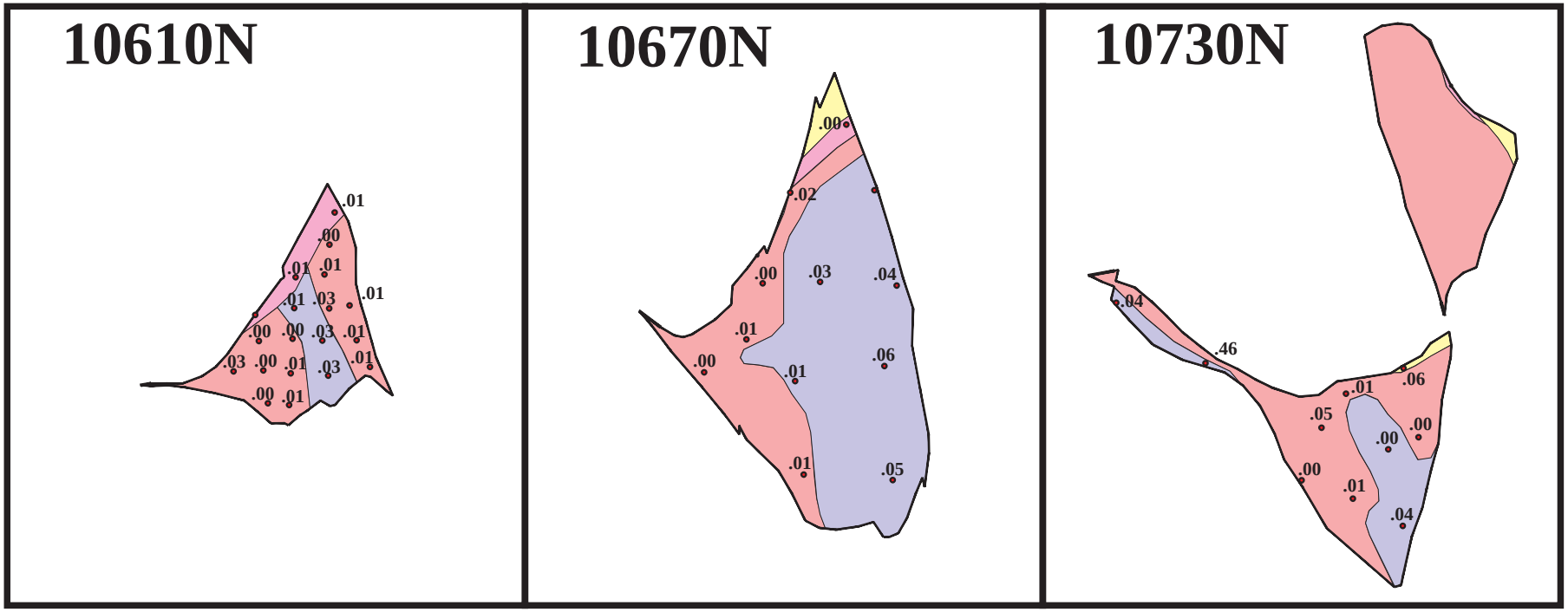

Fig. 100 - Galena %Se analyses (normalised)

ORETYPES

- Siliceous cap (GSP)
- Baritic cap (BAR)
- Hangingwall enriched massive sulphide (HWE)
- Footwall depleted massive sulphide (FWD)

6.3.4 Arsenopyrite

Arsenopyrite analyses are summarised in Tables 31-32. There are probably insufficient analyses to confidently interpret any trends of compositional variation with paragenetic sequence, but there is a tendency for Cu, Ag, Au and Pb contaminant levels to decrease, passing from earliest arsenopyrite to latest. On the other hand, Zn levels increase. This is very similar to the trends for pyrite (see above 6.3.1). The %Se levels are consistently high, with an S:Se ratio of 166 (cf. pyrite 6570).

There are clearly too few samples analysed to comment on zonation of arsenopyrite composition. Selenium distribution is shown on Fig. 101, but no trends are observed.

Table 31 - Summary of microprobe analyses of arsenopyrite by mintex (blank=not analysed)

Mintex	No.of analyses	Volume fraction	Normalised composition											
			%S	%Fe	%Co	%Ni	%Cu	%Zn	%As	%Se	%Ag	%Au	%Pb	%TOTAL
AsC	7	0.275	20.1	34.6	0.00	0.00	0.05	0.04	45.0	0.15	0.01	0.11	0.15	100
AsD	18	0.289	20.7	34.5	0.01	0.00	0.04	0.10	44.6	0.12	0.01	0.01	0.07	100
AsG	7	0.012	20.6	35.2			0.04		44.0	0.10	0.01	0.08		100
AsI	6	0.396	20.7	34.0	0.03	0.00	0.04	0.12	45.1	0.13	0.01	0.01		100
AsJ	3	0.029	20.8	34.8	0.03	0.00	0.01	0.17	44.2	0.16	0.00	0.00	0.00	100
All analyses weighted by global volume%		**1.000**	**20.54**	**34.33**	**0.017**	**0.003**	**0.043**	**0.093**	**44.87**	**0.131**	**0.010**	**0.037**	**0.060**	**100**

Table 32 - Summary of microprobe analyses of arsenopyrite by sample (blank=not analysed)

Sample	No.of analyses	Ars'pyrite Volume%	Normalised composition											
			%S	%Fe	%Co	%Ni	%Cu	%Zn	%As	%Se	%Ag	%Au	%Pb	%TOTAL
61-449-59.0	2	0.6	20.0	34.1	0.00	0.00		0.22	45.4	0.09	0.03		0.04	100
61-450-72.2	3	9.6	21.6	34.6	0.01	0.00		0.03	43.6	0.11	0.01		0.07	100
61-452-44.1	1	1.6	21.2	34.7			0.12		43.9	0.06	0.00	0.00		100
61-452-57.3	2	0.6	21.5	35.0			0.01		43.3	0.04	0.04	0.14		100
61-452-71.8	3	1.6	20.5	35.3			0.00		43.9	0.20	0.01	0.10		100
61-452-84.6	7	11.0	20.4	35.0			0.03		44.4	0.10	0.00	0.04		100
61-454-58.9	3	5.0	20.5	35.4			0.01		43.9	0.13	0.01	0.01		100
61-455-61.6	2	1.2	20.3	31.0			0.06		48.3	0.19	0.03	0.03		100
67-231-16.3	5	7.0	20.3	34.5	0.01	0.01		0.12	44.9	0.12	0.01		0.08	100
67-382-96.1	1	0.1	20.1	33.8	0.00	0.00		0.17	45.7	0.15	0.00		0.00	100
67-385-39.9	4	4.6	20.1	35.0	0.01	0.00		0.00	44.6	0.12	0.01		0.16	100
73-157-6.3	1	0.1	21.3	34.3	0.03	0.00		0.17	44.1	0.14	0.00		0.00	100
73-347-20.4	10	27.6	20.8	33.9	0.01	0.00	0.06	0.07	45.1	0.14	0.01	0.01	0.10	100
73-357-77.4	1	0.2	20.6	34.1	0.00	0.01		0.00	45.0	0.12	0.02		0.16	100
All analyses weighted by As volume% per sample			**20.72**	**34.42**	**0.010**	**0.001**	**0.047**	**0.065**	**44.64**	**0.125**	**0.009**	**0.022**	**0.096**	**100**

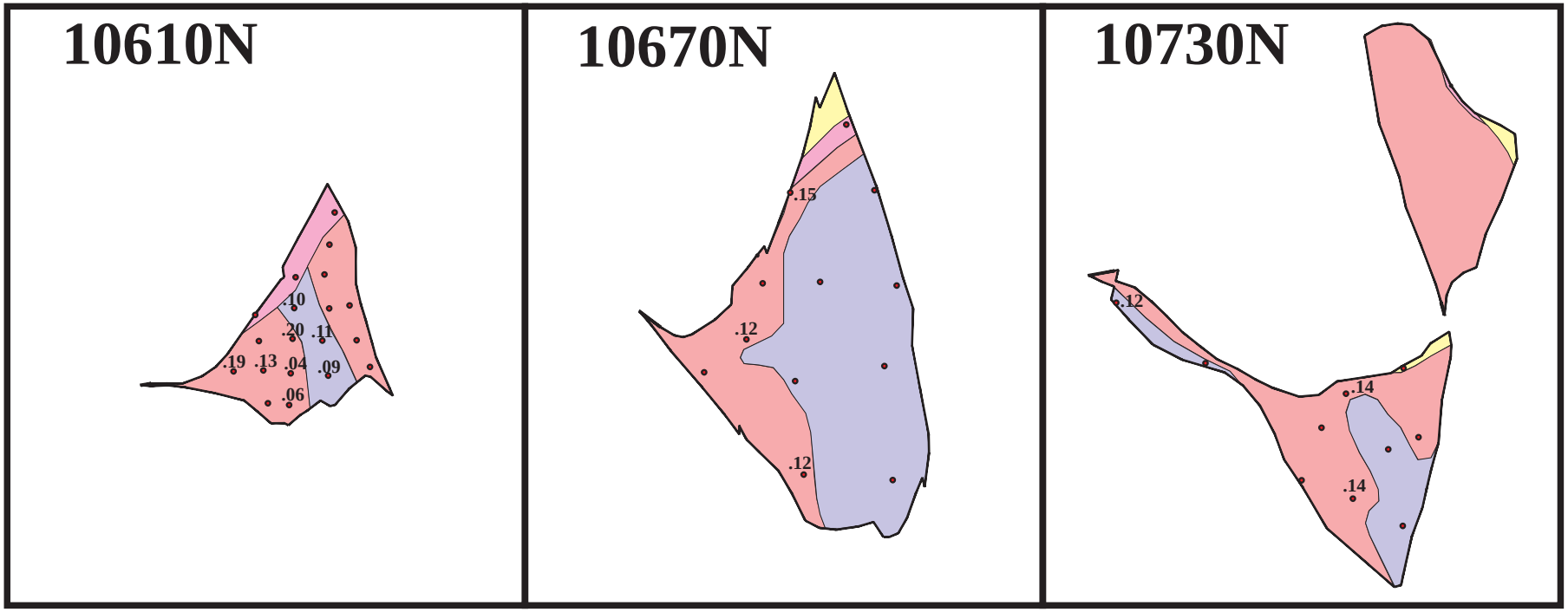

Fig. 101 - Arsenopyrite %Se analyses (normalised)

ORETYPES

- Siliceous cap (GSP)
- Baritic cap (BAR)
- Hangingwall enriched massive sulphide (HWE)
- Footwall depleted massive sulphide (FWD)

6.3.5 Chalcopyrite

Chalcopyrite analyses are summarised in Tables 33-34. Contamination in the beam area by sphalerite was a significant problem, particularly with the fine-grained CpA blebs. No texturally aligned trends are apparent. Table 34 shows considerable variation in trace element content between samples but as Figs. 102-103 show, no spatial structure can be interpreted. The variability is probably due to submicroscopic contaminant mineral inclusions and/or poor count statistics for the microanalysis.

Table 33 - Summary of microprobe analyses of chalcopyrite by mintex

Mintex	No.of analyses	Volume fraction	Normalised composition								
			%S	%Fe	%Cu	%Zn	%As	%Ag	%Sb	%Bi	%Total
CpE	34	0.234	35.3	29.8	33.8	0.97	0.03	0.01	0.01	0.06	100
CpF	13	0.263	35.8	29.9	34.1	0.09	0.04	0.00	0.01	0.08	100
CpG	10	0.234	35.9	30.1	33.9	0.02	0.02	0.02	0.00	0.09	100
CpH	10	0.251	35.7	29.6	34.3	0.05	0.25	0.02	0.02	0.06	100
CpI	6	0.019	36.0	29.9	33.8	0.12	0.07	0.03	0.01	0.10	100
All analyses weighted by global volume%		**1.000**	**35.70**	**29.82**	**34.03**	**0.269**	**0.087**	**0.015**	**0.012**	**0.071**	**100**

Table 34 - Summary of microprobe analyses of chalcopyrite by sample

Sample	No.of analyses	Chal'pyrite Volume%	Normalised composition								
			%S	%Fe	%Cu	%Zn	%As	%Ag	%Sb	%Bi	%Total
61-443-76.7	2	0.2	35.9	30.0	33.8	0.07	0.15	0.01	0.01	0.14	100
61-449-59.0	4	2.4	34.8	30.1	34.3	0.78	0.09	0.02	0.01	0.00	100
61-449-89.6	2	0.4	36.1	29.9	33.3	0.55	0.08	0.00	0.01	0.03	100
61-450-85.9	1	0.4	34.5	29.3	34.3	1.63	0.23	0.00	0.01	0.00	100
61-451-99.7	7	2.8	34.4	29.9	34.8	0.73	0.04	0.01	0.01	0.08	100
61-451-112.3	3	1.4	35.5	29.8	33.2	1.45	0.00	0.01	0.01	0.00	100
61-451-125.9	1	0.2	34.5	29.9	34.7	0.82	0.00	0.02	0.04	0.00	100
61-455-61.6	5	1.2	35.5	30.1	33.2	1.06	0.00	0.03	0.01	0.12	100
67-209-42.8	4	0.1	35.4	30.4	33.9	0.20	0.02	0.03	0.01	0.09	100
67-231-16.3	6	0.4	35.8	30.0	33.7	0.01	0.31	0.02	0.01	0.12	100
67-377-59.4	9	8.8	35.6	30.1	33.7	0.49	0.01	0.01	0.02	0.07	100
67-377-126.0	2	2.0	35.3	30.3	34.2	0.14	0.08	0.00	0.02	0.00	100
67-378-70.8	2	1.0	35.9	29.5	33.6	1.01	0.00	0.01	0.00	0.00	100
67-382-17.3	2	0.2	35.4	30.1	33.6	0.58	0.04	0.03	0.01	0.12	100
67-382-96.1	1	0.2	35.9	30.1	33.9	0.02	0.03	0.00	0.03	0.00	100
67-385-39.9	2	0.4	35.4	29.9	33.2	1.43	0.02	0.03	0.00	0.02	100
73-050-356.7	1	0.2	36.1	29.1	32.4	2.25	0.04	0.00	0.00	0.00	100
73-151-21.1	7	0.6	36.3	28.6	34.6	0.33	0.06	0.01	0.01	0.04	100
73-347-20.4	7	3.0	35.5	29.6	34.5	0.12	0.05	0.02	0.02	0.13	100
73-348-30.8	2	0.1	36.3	30.1	33.4	0.02	0.05	0.00	0.01	0.10	100
73-357-77.4	6	2.4	36.5	29.7	33.8	0.01	0.03	0.01	0.01	0.02	100
All analyses weighted by Cp volume% per sample			**35.47**	**29.92**	**33.95**	**0.551**	**0.040**	**0.011**	**0.013**	**0.057**	**100**

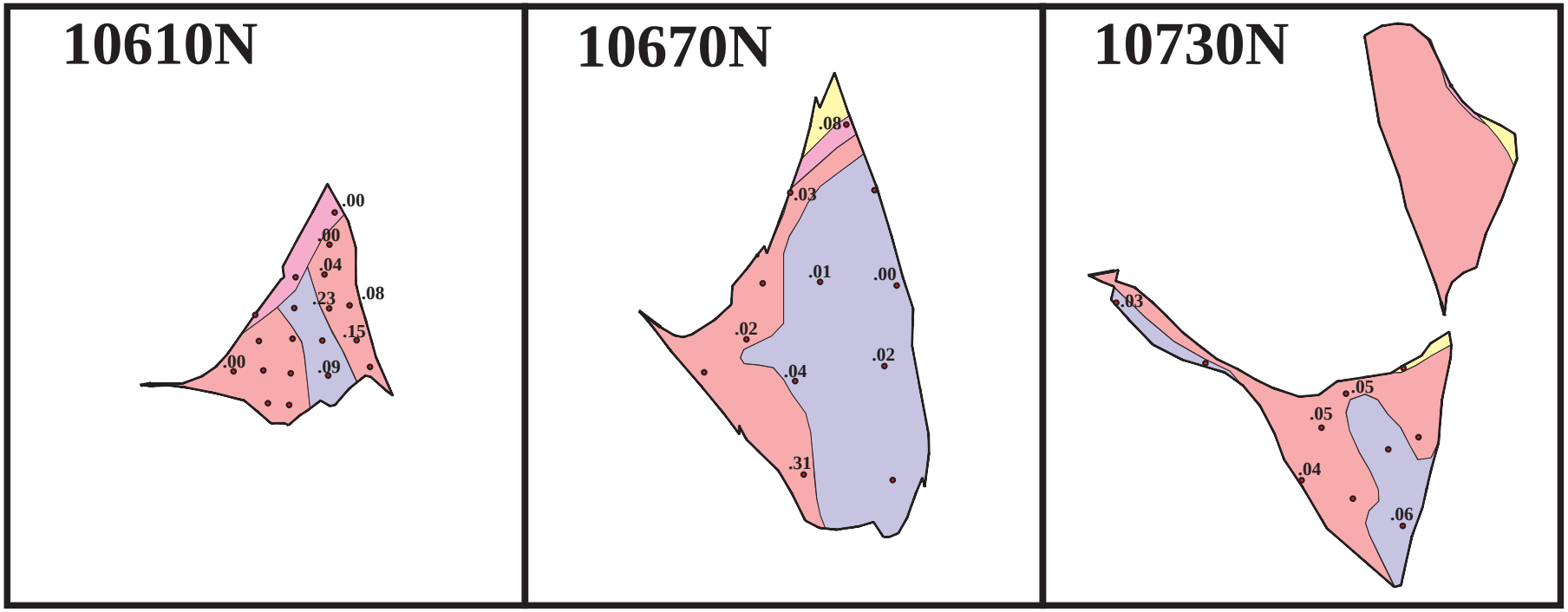

Fig. 102 - Chalcopyrite %As analyses (normalised)

ORETYPES

- Siliceous cap (GSP)
- Baritic cap (BAR)
- Hangingwall enriched massive sulphide (HWE)
- Footwall depleted massive sulphide (FWD)

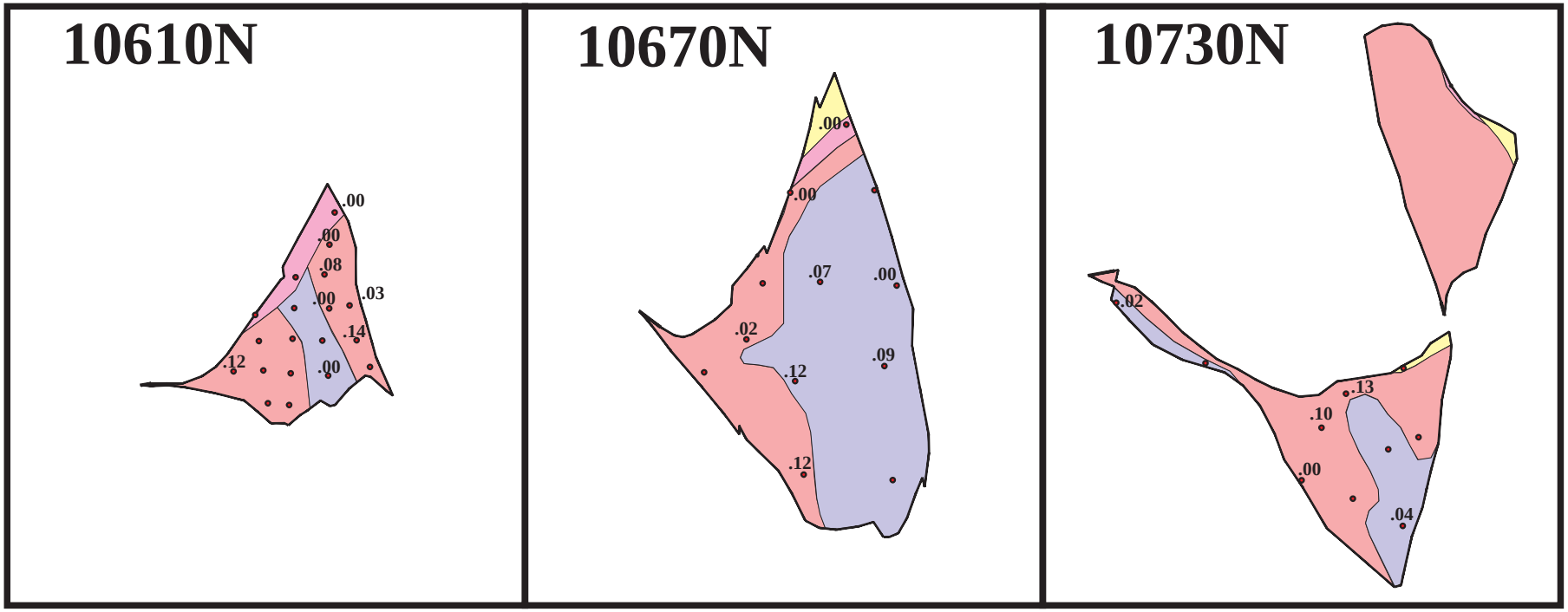

Fig. 103 - Chalcopyrite %Bi analyses (normalised)

ORETYPES

- Siliceous cap (GSP)
- Baritic cap (BAR)
- Hangingwall enriched massive sulphide (HWE)
- Footwall depleted massive sulphide (FWD)

6.3.6 Tetrahedrite

Tetrahedrite analyses are summarised in Tables 35-36. Stoichiometry has been normalised to 13 sulphur atoms to coincide with the accepted tetrahedrite composition (Criddle and Stanley, 1986) of $Cu_{12}Sb_4S_{13}$ (with substitution of Cu by Fe, Zn and Ag, and of Sb by As to form tennantite $Cu_{12}As_4S_{13}$).

At Hellyer, there is considerable compositional variation (Fig. 104-105), as is normally the case for minerals from the tetrahedrite-tennantite series.

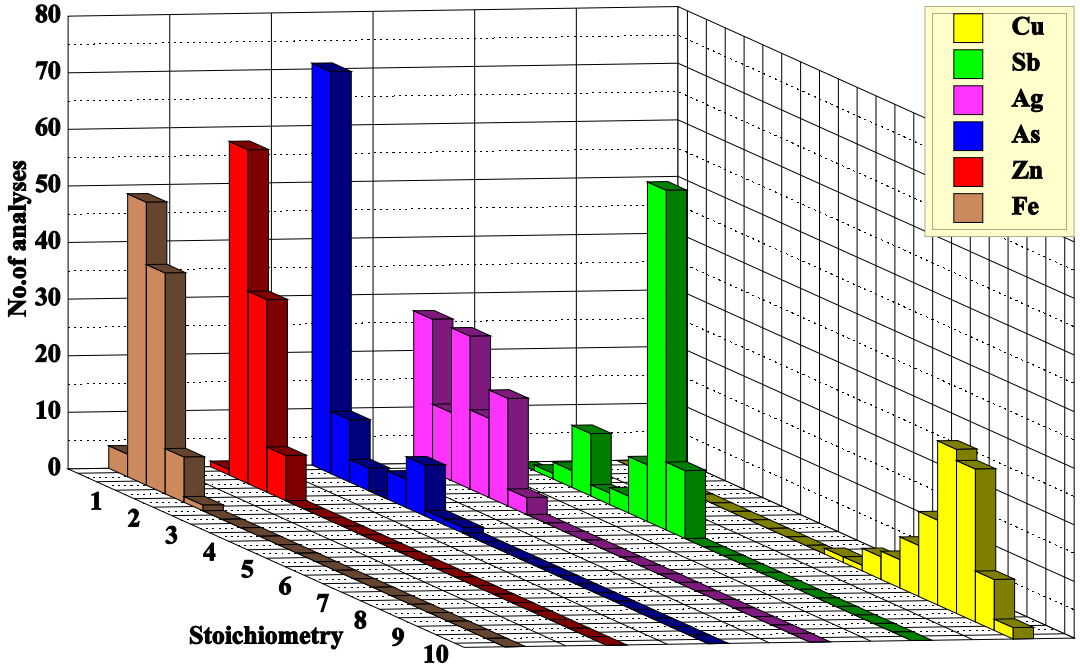

Figure 104 - Tetrahedrite compositional variation from 102 microprobe analyses. Stoichiometry for each metal has been calculated assuming 13 sulphur atoms. The class interval for each histogram is 0.5 atom.

Substitution of the Cu_{12} position by Fe, Zn and Ag varies between 1.8 and 6.0 atoms, with no obvious grouped populations. On the other hand, two populations are evident in the Sb/As substitution sites. 86 of the 102 analyses (84%) are As-deficient (<10% by weight), argentian tetrahedrites with an average stoichiometric composition of:

$$(Cu_{8.50}Ag_{1.36})_{9.86}(Zn_{1.06}Fe_{0.99})_{2.05}(Sb_{3.76}As_{0.34})_{4.10}S_{13}.$$

Fig. 105 - Tetrahedrite composition correlation matrix. Annotation in red is the linear correlation coefficient (bold if significant). The diagonal histograms are schematic only.

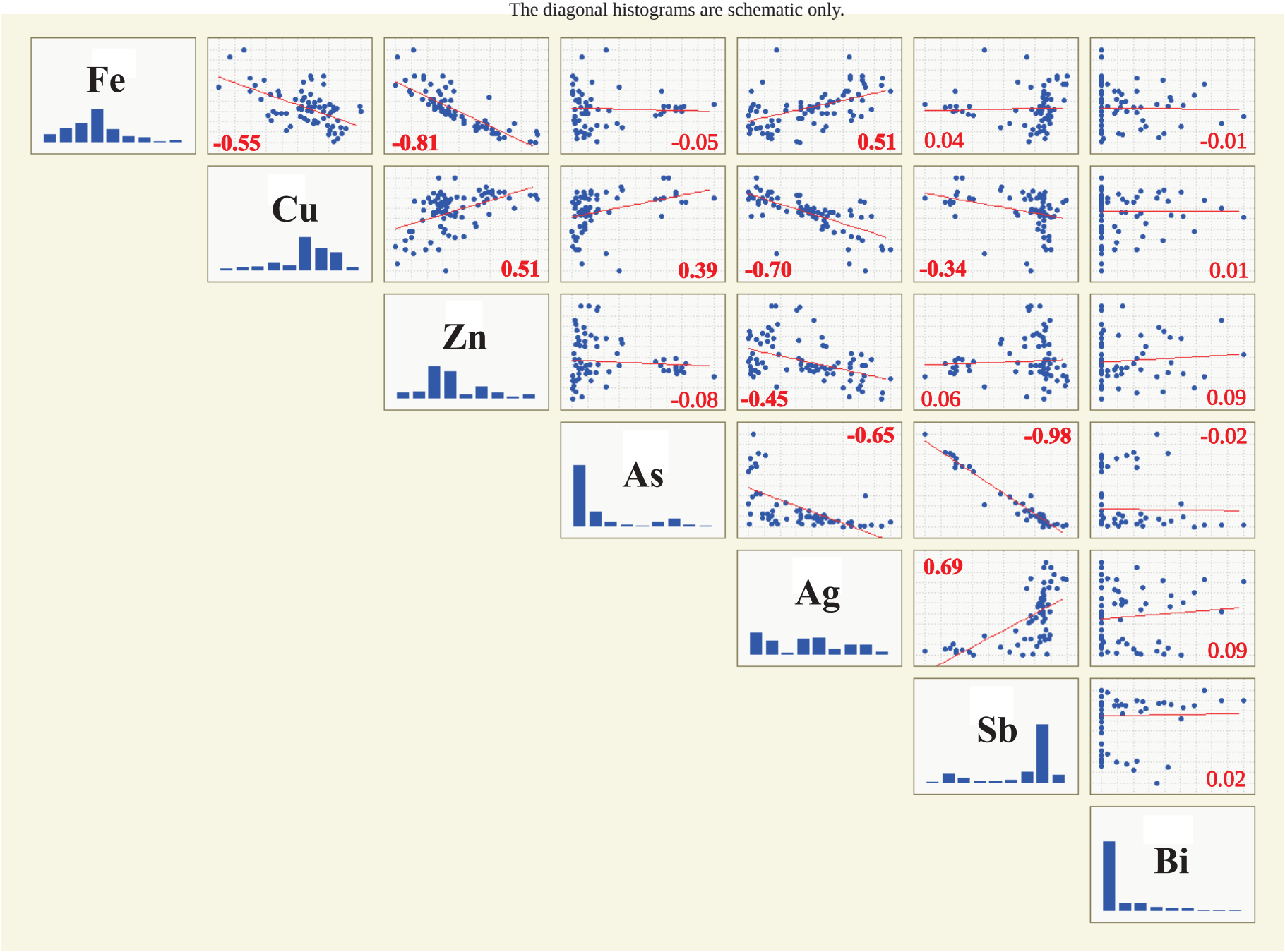

Table 35 - Summary of microprobe analyses of tetrahedrite by mintex

Mintex	No.of	Volume	Normalised composition by weight									Atomic composition normalised to 13 sulphur atoms								
	analyses	fraction	%S	%Fe	%Cu	%Zn	%As	%Ag	%Sb	%Bi	%Total	S	Fe	Cu	Zn	As	Ag	Sb	Bi	Total
TeA	6	0.022	24.75	4.41	30.43	3.68	1.36	8.66	26.57	0.14	100	13.00	1.32	8.08	0.95	0.30	1.36	3.69	0.01	28.71
TeD	33	0.646	25.26	3.23	32.64	3.86	4.36	7.33	23.26	0.06	100	13.00	0.96	8.45	0.97	0.91	1.16	3.20	0.01	28.65
TeE	32	0.228	25.03	3.42	33.05	3.73	3.70	6.85	24.18	0.04	100	13.00	1.01	8.66	0.95	0.79	1.08	3.34	0.00	28.84
TeF	14	0.047	22.93	3.88	29.96	3.69	1.16	11.47	26.83	0.08	100	13.00	1.27	8.59	1.02	0.27	1.94	4.02	0.01	30.12
TeG	6	0.028	26.07	2.68	36.87	5.36	5.64	1.09	22.08	0.21	100	13.00	0.75	9.29	1.32	1.16	0.16	2.94	0.02	28.64
TeH	6	0.009	24.40	2.23	33.45	4.89	2.47	7.47	24.94	0.14	100	13.00	0.69	8.96	1.27	0.54	1.23	3.53	0.01	29.23
TeJ	5	0.022	24.61	2.11	34.82	6.22	1.06	4.30	26.86	0.02	100	13.00	0.64	9.28	1.61	0.24	0.68	3.74	0.00	29.18
All analyses weighted by global volume%		**1.000**	**25.09**	**3.28**	**32.74**	**3.92**	**3.94**	**7.20**	**23.77**	**0.064**	**100**	**13.00**	**0.98**	**8.54**	**1.00**	**0.83**	**1.14**	**3.29**	**0.01**	**28.78**

Table 36 - Summary of microprobe analyses of tetrahedrite by sample

Sample	No.of	Tetrahed.	Normalised composition by weight									Atomic composition normalised to 13 sulphur atoms								
	analyses	Volume%	%S	%Fe	%Cu	%Zn	%As	%Ag	%Sb	%Bi	%Total	mol.S	mol.Fe	mol.Cu	mol.Zn	mol.As	mol.Ag	mol.Sb	mol.Bi	mol.total
61-442-69.0	1	0.2	27.5	4.0	38.8	3.5	18.4	1.4	6.3	0.30	100	13.0	1.1	9.3	0.8	3.7	0.2	0.8	0.0	28.9
61-443-76.7	3	0.1	25.2	2.7	31.7	4.4	5.2	8.6	22.1	0.18	100	13.0	0.8	8.2	1.1	1.1	1.3	3.1	0.0	28.7
61-449-59.0	5	0.1	25.0	2.0	35.2	6.2	1.9	3.8	25.9	0.02	100	13.0	0.6	9.2	1.6	0.4	0.6	3.6	0.0	29.0
61-449-89.6	3	0.2	27.2	3.8	37.6	3.9	14.4	2.0	11.0	0.17	100	13.0	1.0	9.1	0.9	2.9	0.3	1.4	0.0	28.6
61-451-99.7	2	2.0	26.1	3.5	40.6	4.0	11.6	1.6	12.6	0.00	100	13.0	1.0	10.2	1.0	2.5	0.2	1.7	0.0	29.5
61-451-125.9	1	0.1	23.6	2.3	31.5	6.1	0.3	8.2	27.5	0.55	100	13.0	0.7	8.8	1.7	0.1	1.3	4.0	0.0	29.6
61-452-44.1	4	0.1	23.6	3.6	30.8	3.4	0.8	11.0	26.6	0.13	100	13.0	1.1	8.5	0.9	0.2	1.8	3.9	0.0	29.5
61-452-57.3	2	0.1	23.6	3.9	30.9	4.3	0.9	9.4	26.7	0.20	100	13.0	1.2	8.6	1.2	0.2	1.5	3.9	0.0	29.6
61-452-97.6	3	0.1	25.5	1.9	37.4	5.5	4.2	2.4	23.1	0.00	100	13.0	0.6	9.6	1.4	0.9	0.4	3.1	0.0	29.0
61-454-45.0	5	0.2	21.8	4.3	30.2	2.8	0.2	12.8	27.9	0.09	100	13.0	1.5	9.1	0.8	0.1	2.3	4.4	0.0	31.1
61-454-71.3	2	0.1	22.5	4.8	29.9	3.0	0.3	11.9	27.5	0.00	100	13.0	1.6	8.7	0.9	0.1	2.0	4.2	0.0	30.5
61-454-82.3	4	0.1	23.4	2.0	31.8	5.4	1.6	10.1	25.5	0.16	100	13.0	0.6	8.9	1.5	0.4	1.7	3.7	0.0	29.8
67-231-16.3	5	0.2	24.2	4.3	27.2	2.4	0.2	14.3	27.2	0.10	100	13.0	1.3	7.4	0.6	0.1	2.3	3.8	0.0	28.5
67-377-59.4	3	0.4	25.3	2.0	37.0	5.7	2.3	0.7	26.6	0.30	100	13.0	0.6	9.6	1.4	0.5	0.1	3.6	0.0	28.9
67-377-126.0	3	0.2	24.7	1.8	35.6	5.6	1.7	3.0	27.6	0.12	100	13.0	0.5	9.4	1.4	0.4	0.5	3.8	0.0	29.1
67-382-96.1	8	1.6	26.9	3.5	38.0	4.3	11.4	1.2	14.7	0.06	100	13.0	1.0	9.3	1.0	2.4	0.2	1.9	0.0	28.6
67-384-59.7	2	0.1	24.9	5.9	25.7	2.1	0.9	13.8	26.7	0.14	100	13.0	1.8	6.8	0.5	0.2	2.1	3.7	0.0	28.1
67-385-21.6	2	0.1	24.5	2.6	34.7	5.2	0.9	5.0	27.2	0.00	100	13.0	0.8	9.3	1.4	0.2	0.8	3.8	0.0	29.2
73-050-356.7	6	0.2	24.2	3.9	25.8	3.4	1.3	14.0	27.4	0.05	100	13.0	1.2	7.0	0.9	0.3	2.2	3.9	0.0	28.5
73-347-20.4	20	3.8	24.4	3.3	32.0	3.5	1.8	8.2	26.7	0.03	100	13.0	1.0	8.6	0.9	0.4	1.3	3.8	0.0	29.0
73-348-30.8	3	0.2	25.0	2.9	33.6	4.4	0.7	4.4	28.9	0.00	100	13.0	0.9	8.8	1.1	0.2	0.7	3.9	0.0	28.6
73-349-8.0	1	0.1	26.5	5.4	34.3	4.2	2.5	2.5	24.5	0.00	100	13.0	1.5	8.5	1.0	0.5	0.4	3.2	0.0	28.1
73-351-36.7	6	0.1	25.9	3.7	32.2	3.9	2.0	6.4	25.9	0.00	100	13.0	1.0	8.2	1.0	0.4	1.0	3.5	0.0	28.1
73-355-30.6	3	0.8	26.9	3.0	37.7	4.4	9.2	0.9	17.9	0.00	100	13.0	0.8	9.2	1.1	1.9	0.1	2.3	0.0	28.4
73-357-77.4	5	0.1	24.8	2.8	29.7	3.9	1.3	10.2	27.2	0.01	100	13.0	0.8	7.9	1.0	0.3	1.6	3.8	0.0	28.4
All analyses weighted by Te volume% per sample			**25.34**	**3.34**	**35.02**	**3.98**	**5.89**	**5.11**	**21.25**	**0.057**	**100**	**13.00**	**0.99**	**9.05**	**1.00**	**1.24**	**0.81**	**2.92**	**0.00**	**29.01**

The remaining 16 analyses (14%) are arsenical tetrahedrites (>10% by weight) with an average stoichiometric composition of:

$$(Cu_{9.32}Ag_{0.19})_{9.51}(Zn_{0.95}Fe_{1.01})_{1.96}(Sb_{1.56}As_{2.71})_{4.27}S_{13}.$$

Table 35 shows a tendency for Hellyer tetrahedrites to contain: less Fe and Ag, and more Cu and Zn, passing from early to late textural sites. As and Sb have no distinct correlation with tetrahedrite texture. The highest Ag content (averaging 11.5%Ag by weight) occurs in the TeF mintex, as fine-grained blebs in the massive annealed sphalerite. The lowest Ag content (averaging 1.1%Ag by weight) occurs in the TeG mintex, as interstitial infillings to the recrystallised pyrite euhedra.

In a spatial sense, interpretation of tetrahedrite compositional zonation is effected by the lack of analyses from the FWD, where tetrahedrite is rare. Fe content (Fig. 106) is highest in the Ag-rich portions of the HWE and in one analysis from the GSP. Conversely, Fe content is consistently low in the BAR and FWD. Cu content (Fig. 107) is quite variable, no zonation pattern can be recognised. Zn content (Fig. 108) shows a reverse zonation to Fe, with highest values in the BAR and FWD and lowest values in the Ag-rich HWE. As content (Fig. 109) shows an unusual cluster of high values occurring as Devonian pull-apart infills on section 10610N adjacent to the Jack Fault. Elsewhere, As content is predominantly low. Ag content (Fig. 110) clearly shows concentration in the HWE (*senso stricto,* by definition!) and is mostly low in the FWD. The BAR zone has variable Ag content. Sb content (Fig. 111) shows a reverse zonation to As. Sb values are consistent, apart from the area on section 10610N adjacent to the Jack Fault where Sb content is low.

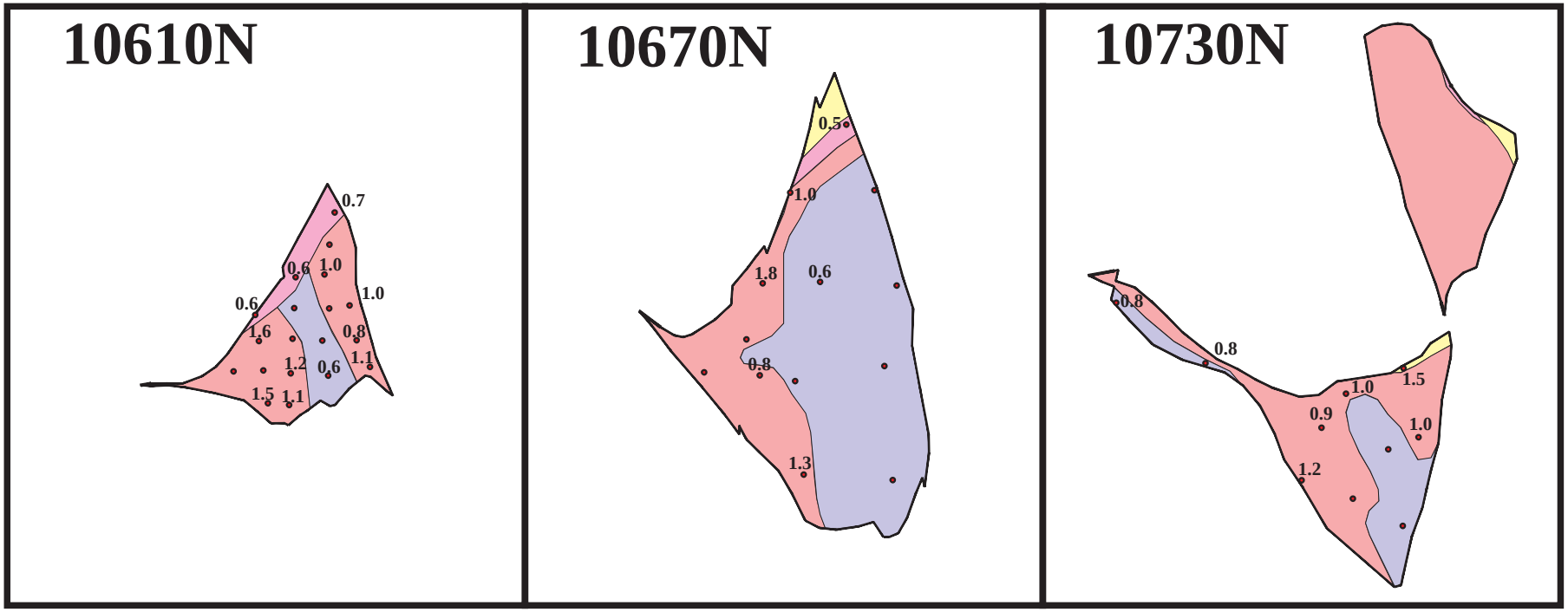

Fig. 106 - Tetrahedrite Fe stoichiometry (normalised to 13 S atoms)

ORETYPES

- Siliceous cap (GSP)
- Baritic cap (BAR)
- Hangingwall enriched massive sulphide (HWE)
- Footwall depleted massive sulphide (FWD)

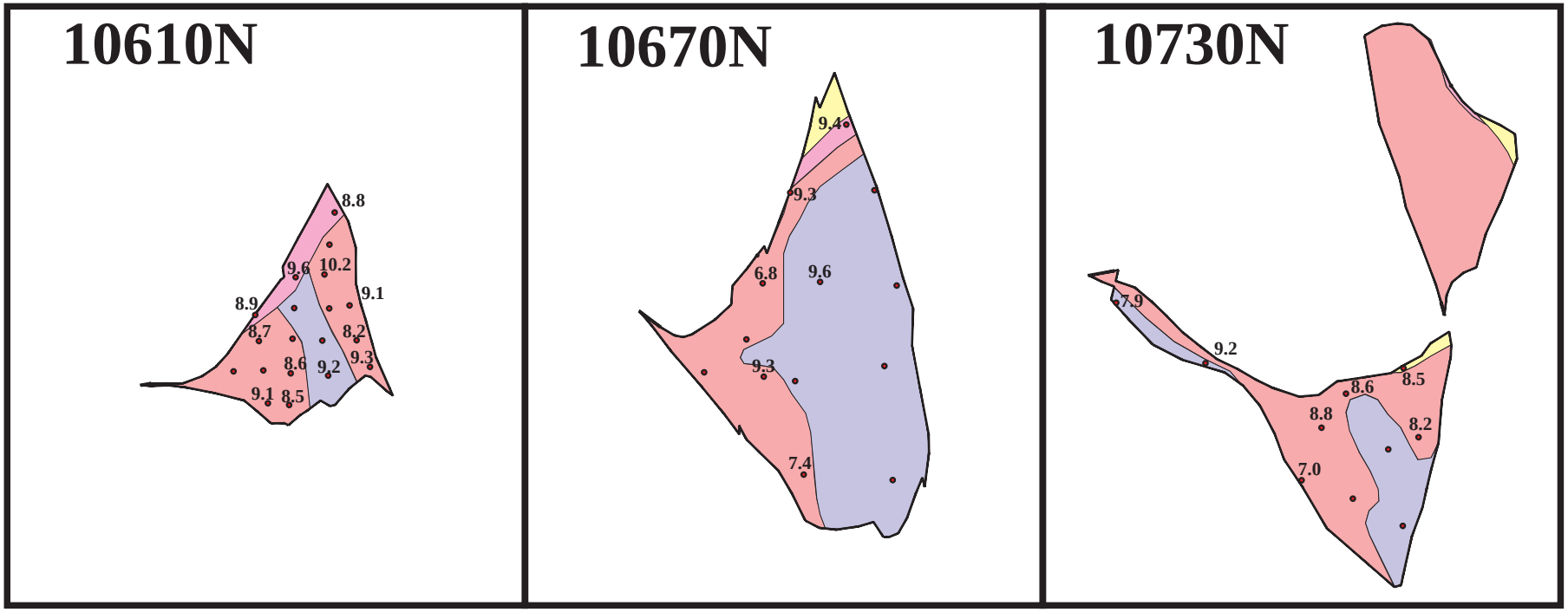

Fig. 107 - Tetrahedrite Cu stoichiometry (normalised to 13 S atoms)

ORETYPES

- Siliceous cap (GSP)
- Baritic cap (BAR)
- Hangingwall enriched massive sulphide (HWE)
- Footwall depleted massive sulphide (FWD)

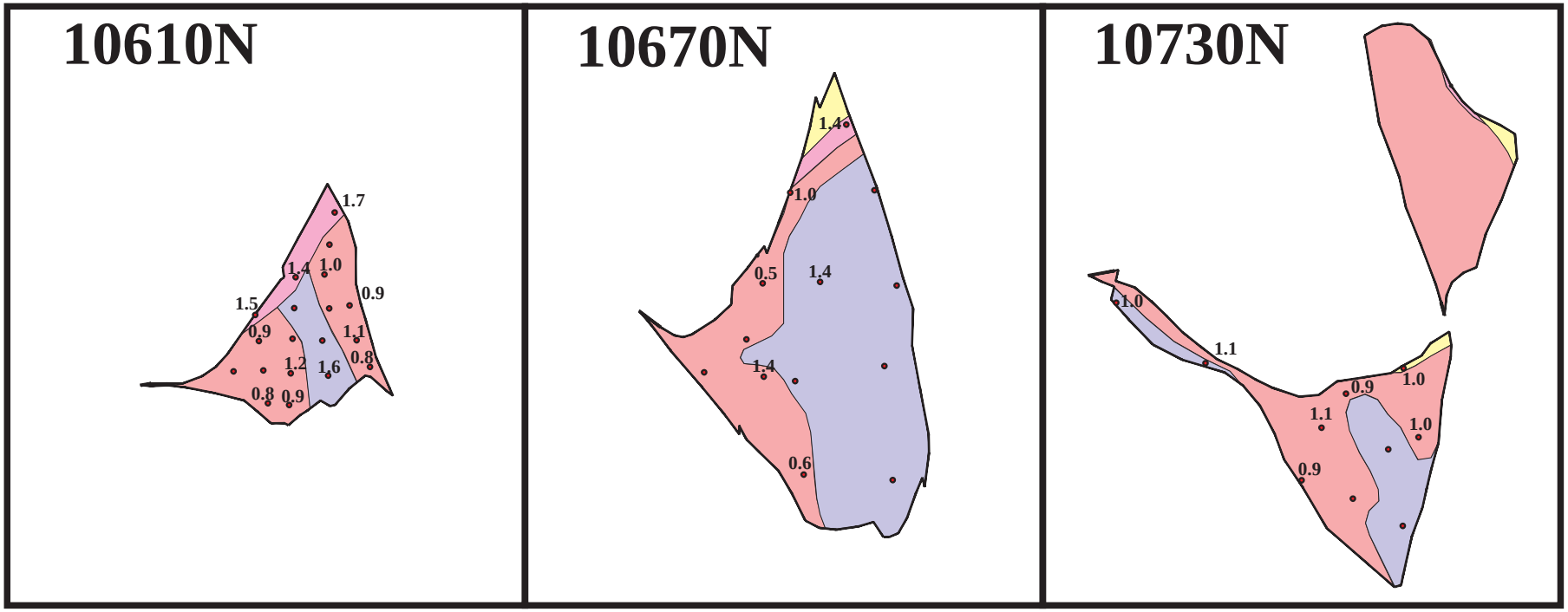

Fig. 108 - Tetrahedrite Zn stoichiometry (normalised to 13 S atoms)

ORETYPES

- Siliceous cap (GSP)
- Baritic cap (BAR)
- Hangingwall enriched massive sulphide (HWE)
- Footwall depleted massive sulphide (FWD)

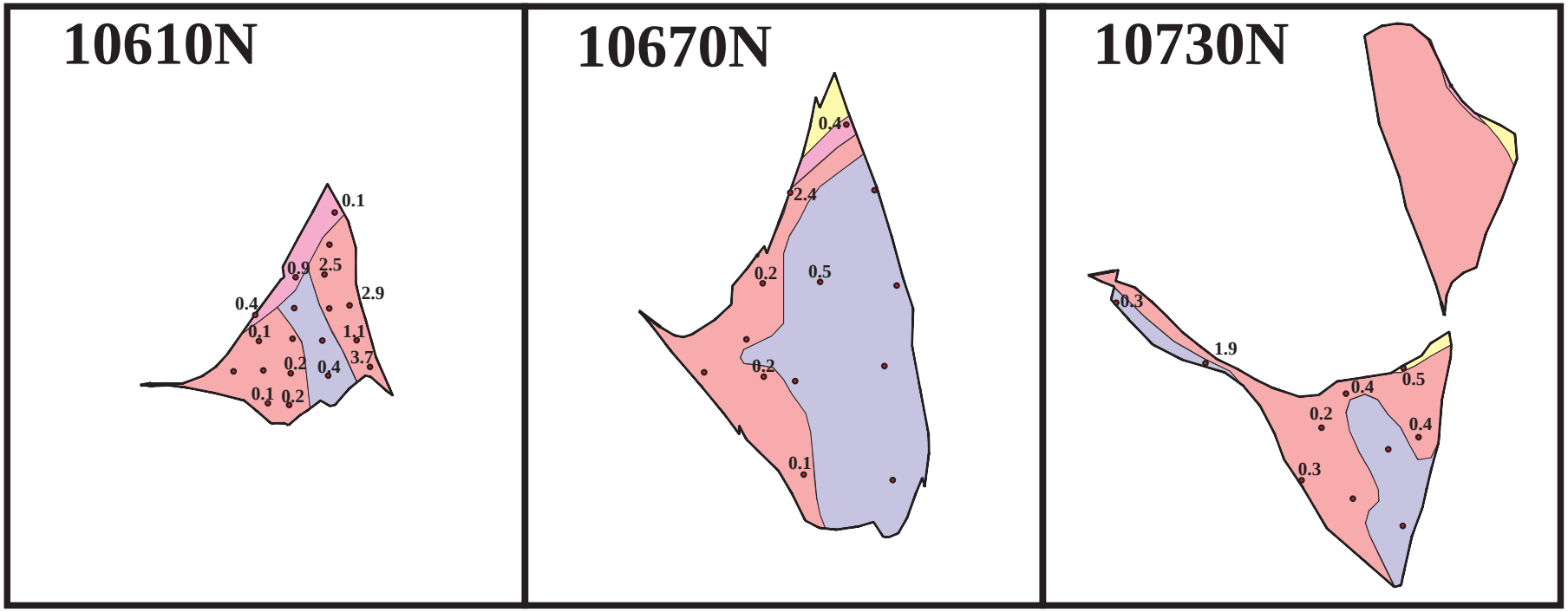

Fig. 109 - Tetrahedrite As stoichiometry (normalised to 13 S atoms)

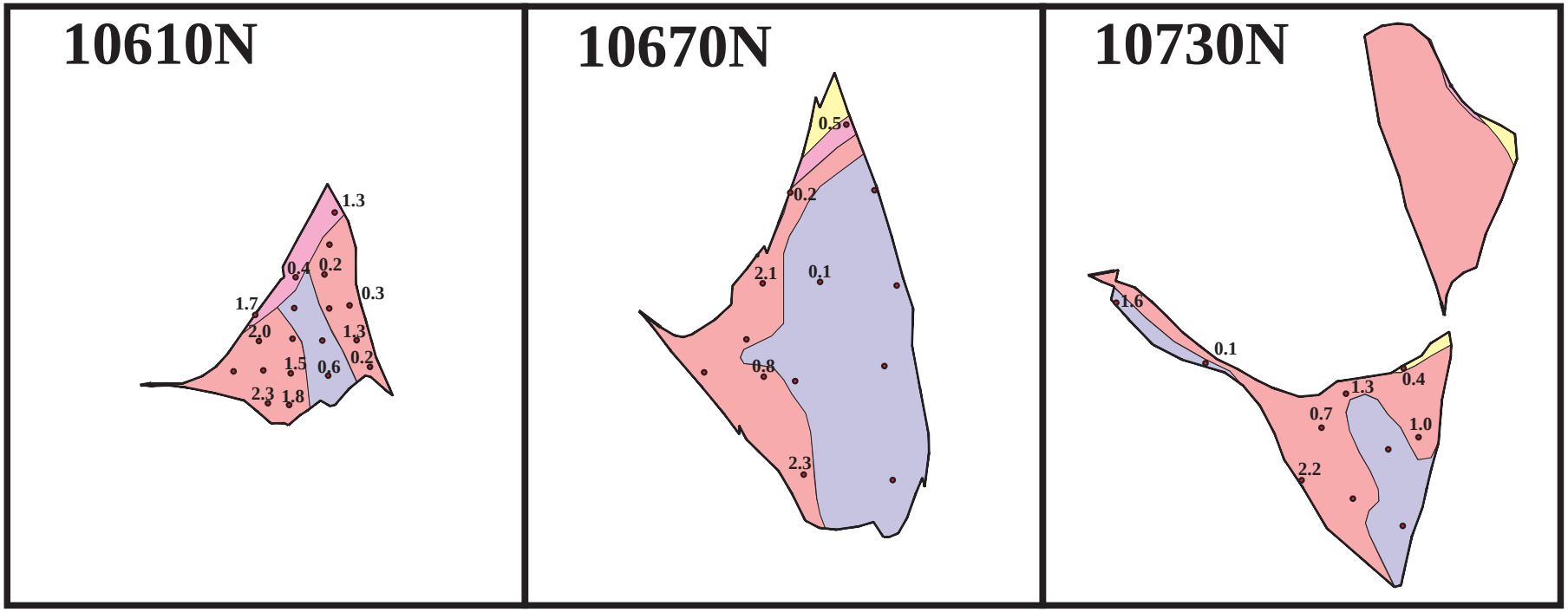

Fig. 110 - Tetrahedrite Ag stoichiometry (normalised to 13 S atoms)

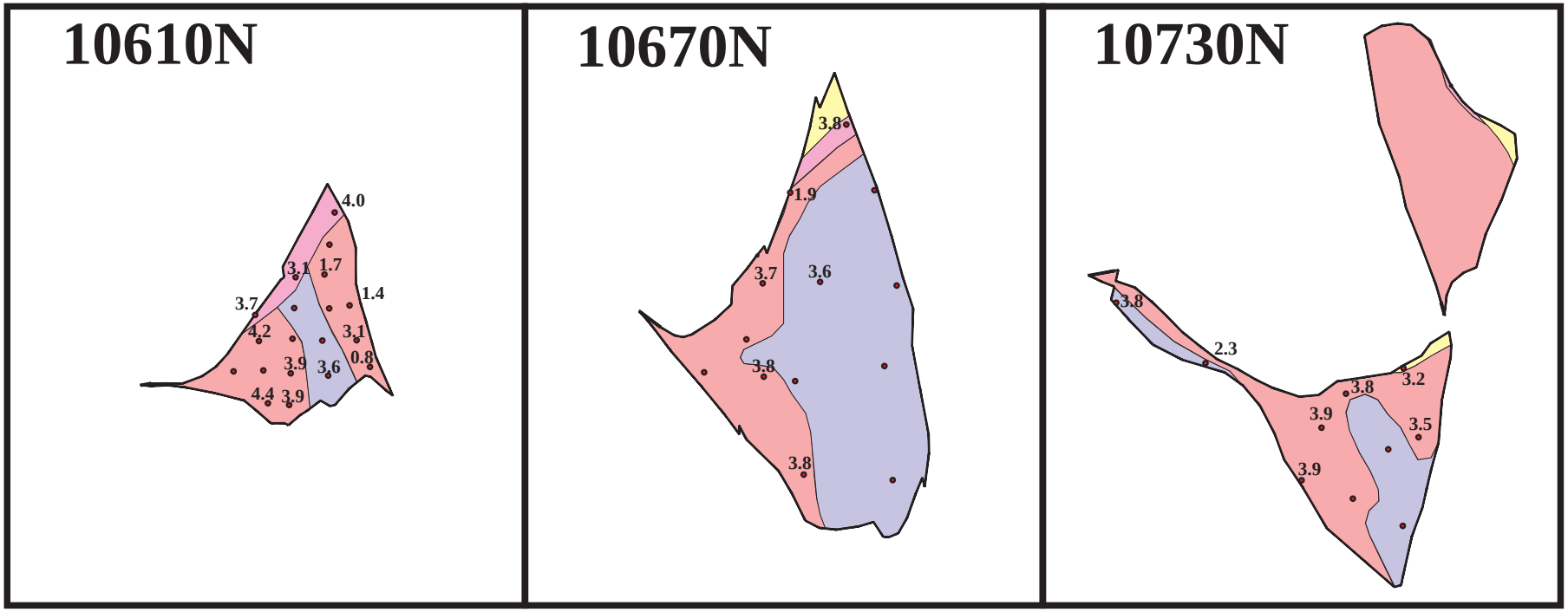

Fig. 111 - Tetrahedrite Sb stoichiometry (normalised to 13 S atoms)

6.3.7 Minor opaque minerals

Bournonite

Six analyses from two samples on 10610N section average:

19.6%S, 0.18%Fe, 12.6%Cu, 0.02%Ag, 24.3%Sb, 43.3%Pb by weight

which can be normalised stoichiometrically to 3 sulphur atoms as $\mathbf{Pb_{1.02}(Cu_{0.97}Fe_{0.02})_{0.99}Sb_{0.98}S_3}$ which approximates ideal bournonite $PbCuSbS_3$.

Two "bournonites" analysed using the PBSALT label, from one sample on 10730N section had slightly different stoichiometry of $Pb_{1.22}(Cu_{1.34}Fe_{0.02})_{1.36}Sb_{1.32}S_3$. These analyses had raw totals <93% suggesting unanalysed components (Zn, Bi?). Since re-analysis was not attempted, this mineral remains unidentified.

Pyrargyrite

Two analyses from one sample on 10670N section average:

17.4%S, 0.06%Fe, 0.87%Cu, 0.14%Zn, 0.10%As, 59.0%Ag, 22.4%Sb, 0.03%Bi by weight

which can be normalised stoichiometrically to 3 sulphur atoms as $(Ag_{3.0}Cu_{0.1}Fe_{0.1})_{3.2}Sb_{1.0}S_3$ which closely approximates ideal pyrargyrite Ag_3SbS_3.

Miargyrite

Two analyses from one sample on 10670N section after subtraction of contaminating tetrahedrite average:

21.3%S, 0.00%Fe, 0.96%Cu, 0.16%Zn, 0.04%As, 36.6%Ag, 40.9%Sb, 0.03%Bi by weight

which can be normalised stoichiometrically to 2 sulphur atoms as $Ag_{1.0}Sb_{1.0}S_2$, equivalent to ideal miargyrite.

Boulangerite

Two analyses from one sample on 10730N section average:

13.9%S, 0.14%Fe, 0.04%Cu, 0.00%Ag, 25.2%Sb, 52.5%Pb (91.8% total) by weight

which can be normalised stoichiometrically to 11 sulphur atoms as $Pb_{4.7}Sb_{3.8}S_{11}$, which is close to ideal boulangerite $Pb_5Sb_4S_{11}$.

Electrum

Six consistent analyses from one sample on 10730N section average:

28.8%Ag, 70.6%Au, 0.57%Hg by weight

which equates to a gold fineness of 710. This compares well with the average fineness of 697 and 0.52%Hg reported by Gemmell (1990a) for 17 Hellyer massive sulphide electrum grains and with an average fineness of 758 and 1.25%Hg reported by Sharpe (1991) for 15 electrum grains from the Hellyer baritic cap.

6.3.8 Barite

Barite microprobe analyses are summarised in Table 37. Strontia content shows variation up to 1.1% by weight; the BAR major mintex components (BaA, BaB) are higher in strontia than the later remobilised types. There were insufficient samples to support the marked increase in Sr content from north to south reported in the more detailed investigation by Sharpe (1991) (see section 6.4.2).

Table 37 - Summary of microprobe analyses of barite by mintex

Mintex	No.of analyses	Volume fraction	Normalised composition						
			%MgO	%SiO2	%CaO	%FeO	%SrO	%BaO	%Total
BaA	3	0.529	0.00	0.02	0.00	0.01	0.41	65.6	100
BaB	3	0.055	0.00	0.02	0.01	0.03	0.52	66.5	100
BaC	4	0.214	0.00	0.01	0.00	0.01	0.21	65.8	100
BaF	8	0.075	0.00	0.03	0.01	0.01	0.30	66.4	100
BaG	8	0.126	0.00	0.01	0.01	0.06	0.32	65.5	100
All analyses weighted by global volume%		**1.000**	**0.000**	**0.019**	**0.003**	**0.018**	**0.355**	**65.73**	**100**

6.3.9 Carbonates

Carbonate microprobe analyses are summarised in Tables 38-40. The inverse relationship between CaO and FeO, together with their respective trimodal populations (Fig. 112) allow simple subdivision of the Hellyer carbonates. Three species are present: calcite, with >45%CaO (57% of analyses); ankerite, with 25-35%CaO (30% of analyses); and siderite, with <1%CaO (13% of analyses). The texturally early carbonates (CoA, corroded rhombs in massive annealed sphalerite) are significantly FeO-rich, while the Devonian remobilised (CoK, fracture infill) carbonates are characteristically FeO-poor. The author interprets this feature to be another example of mineral refining.

Spatially, the carbonate FeO content shows very strong zonation (Fig. 113). The highest FeO content is clearly restricted to the HWE, while the lowest FeO content occurs in the FWD and in two samples from the baritic and siliceous caps. The occurrence of low FeO-carbonate in the FWD is readily explained by its tendency to occur in pull-apart fractures and intercrystal space, filled by Devonian remobilised (and refined) carbonate.

Fig. 112 - Carbonate composition correlation matrix. Annotation in red is the linear correlation coefficient (bold if significant). Diagonal histograms are schematic only.

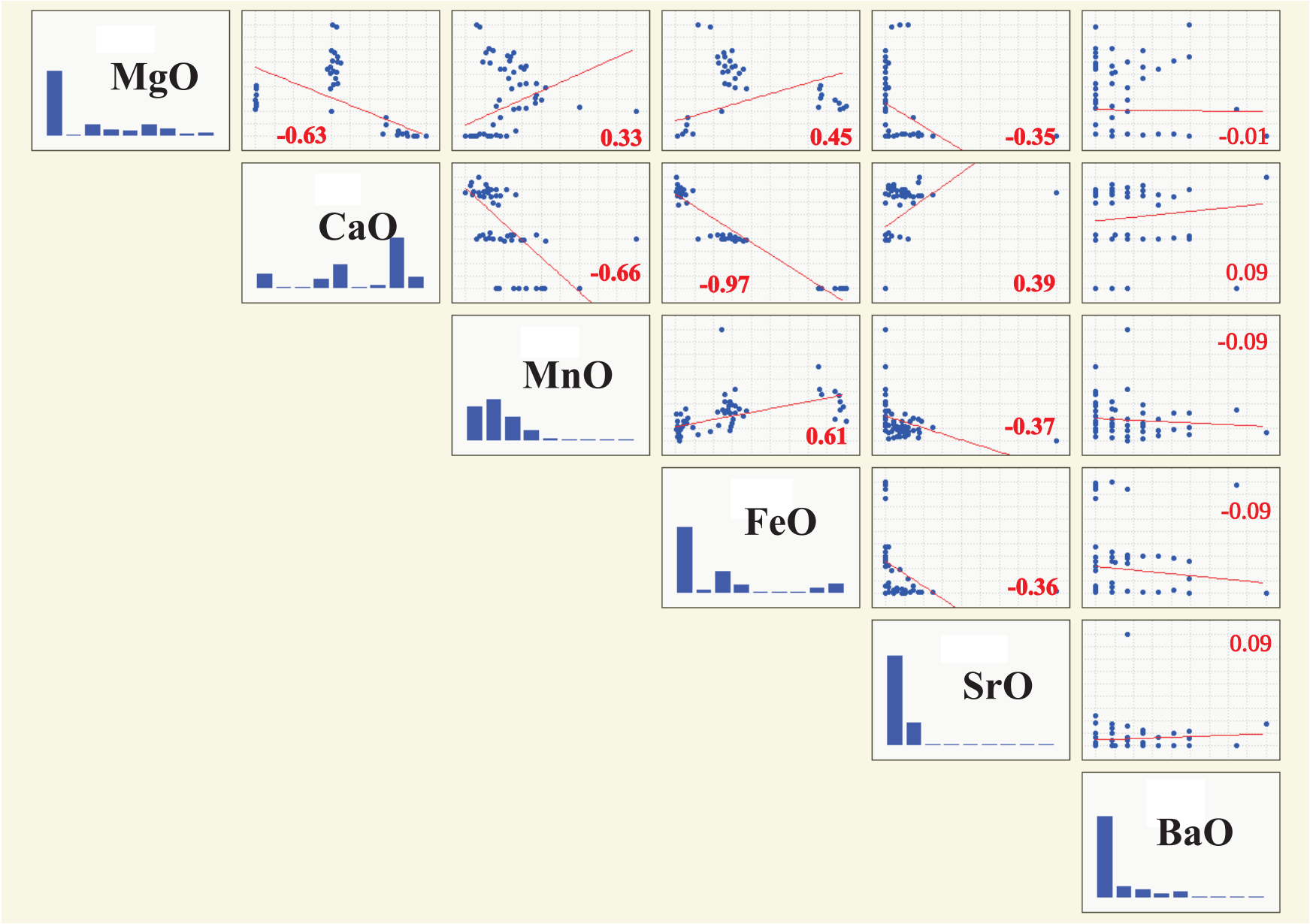

Table 38 - Summary of microprobe analyses of carbonate by species

Species	No.of analyses	Normalised composition							
		%MgO	%CaO	%MnO	%FeO	%SrO	%BaO	%CO2	%Total
Calcite (>45%CaO)	60	0.18	53.97	1.60	1.21	0.06	0.01	43.0	100
Ankerite (25-35%CaO)	31	7.52	28.73	3.42	17.82	0.01	0.01	42.5	100
Siderite (<1% CaO)	14	3.64	0.31	4.65	53.50	0.00	0.01	37.9	100

Table 39 robe analyses of carbonate by mintex

Mintex	No.of analyses			Volume fraction	Normalised composition							
	Calcite	Ankerite	Siderite		%MgO	%CaO	%MnO	%FeO	%SrO	%BaO	%CO2	%Total
CoA	7	14	7	0.057	4.39	27.60	3.92	22.40	0.01	0.01	41.7	100
CoE	8	2	2	0.374	1.74	40.38	2.72	14.31	0.04	0.01	40.8	100
CoH	3	0	0	0.010	0.04	56.91	0.51	0.16	0.03	0.02	42.3	100
CoK	20	2	4	0.320	1.11	44.10	2.27	10.84	0.07	0.01	41.6	100
CoM	18	13	0	0.238	3.75	43.59	1.70	7.34	0.04	0.02	43.6	100
CoO	3	0	0	0.002	0.54	51.85	1.60	2.57	0.08	0.01	43.4	100
All analyses weighted by global volume%				**1.000**	**2.15**	**41.78**	**2.38**	**11.84**	**0.04**	**0.01**	**41.8**	**100**

Table 40 robe analyses of carbonate by sample

Sample	No.of analyses	Carbonate Volume%	Normalised composition							
			%MgO	%CaO	%MnO	%FeO	%SrO	%BaO	%CO2	%Total
61-442-69.0	4	7.0	9.7	21.9	1.4	21.5	0.04	0.02	45.4	100
61-449-89.6	2	2.6	1.5	27.2	4.2	25.0	0.31	0.01	41.7	100
61-450-72.2	2	0.6	0.0	53.9	2.0	0.1	0.04	0.03	43.9	100
61-450-85.9	1	0.1	0.3	47.2	2.5	0.9	0.05	0.04	49.1	100
61-452-44.1	8	18.8	4.8	36.0	3.4	13.5	0.01	0.01	42.2	100
61-452-57.3	6	9.8	1.5	50.2	2.6	5.5	0.03	0.01	40.2	100
61-452-71.8	5	24.2	0.2	56.4	1.7	1.3	0.04	0.00	40.4	100
61-452-84.6	3	0.4	0.1	56.6	2.3	0.7	0.05	0.02	40.3	100
61-454-45.0	2	3.0	4.2	0.3	5.2	49.3	0.00	0.00	41.0	100
61-454-58.9	2	2.8	7.5	30.2	3.5	15.1	0.00	0.01	43.6	100
61-454-82.3	2	14.0	0.1	61.3	0.8	0.3	0.12	0.06	37.4	100
67-229-41.6	2	13.4	0.1	53.2	1.9	0.2	0.07	0.00	44.7	100
67-378-70.8	2	6.0	0.7	50.3	2.2	2.2	0.05	0.02	44.5	100
67-381-102.4	2	3.2	0.1	52.4	2.5	0.7	0.13	0.01	44.2	100
67-382-96.1	4	1.6	0.0	53.5	1.7	0.2	0.09	0.01	44.4	100
67-388-42.4	2	0.2	5.2	0.3	5.5	49.0	0.00	0.00	40.0	100
73-050-356.7	12	12.0	5.3	36.7	2.0	13.5	0.01	0.01	42.4	100
73-157-6.3	8	1.0	2.4	20.1	4.7	32.9	0.01	0.02	39.8	100
73-341-78.7	4	6.8	0.5	51.9	1.6	2.6	0.08	0.01	43.4	100
73-347-49.5	7	1.8	3.2	42.3	2.3	8.9	0.02	0.01	43.2	100
73-348-30.8	10	3.0	2.4	27.0	2.9	27.6	0.02	0.00	40.1	100
73-349-8.0	3	1.0	0.0	56.9	0.5	0.2	0.03	0.02	42.3	100
73-351-36.7	10	6.2	3.5	43.0	2.2	7.8	0.06	0.02	43.5	100
73-355-30.6	2	2.2	0.0	54.3	1.5	0.1	0.07	0.00	43.9	100
All analyses weighted by Co volume% per sample			**2.32**	**45.47**	**2.19**	**8.03**	**0.05**	**0.01**	**41.9**	**100**

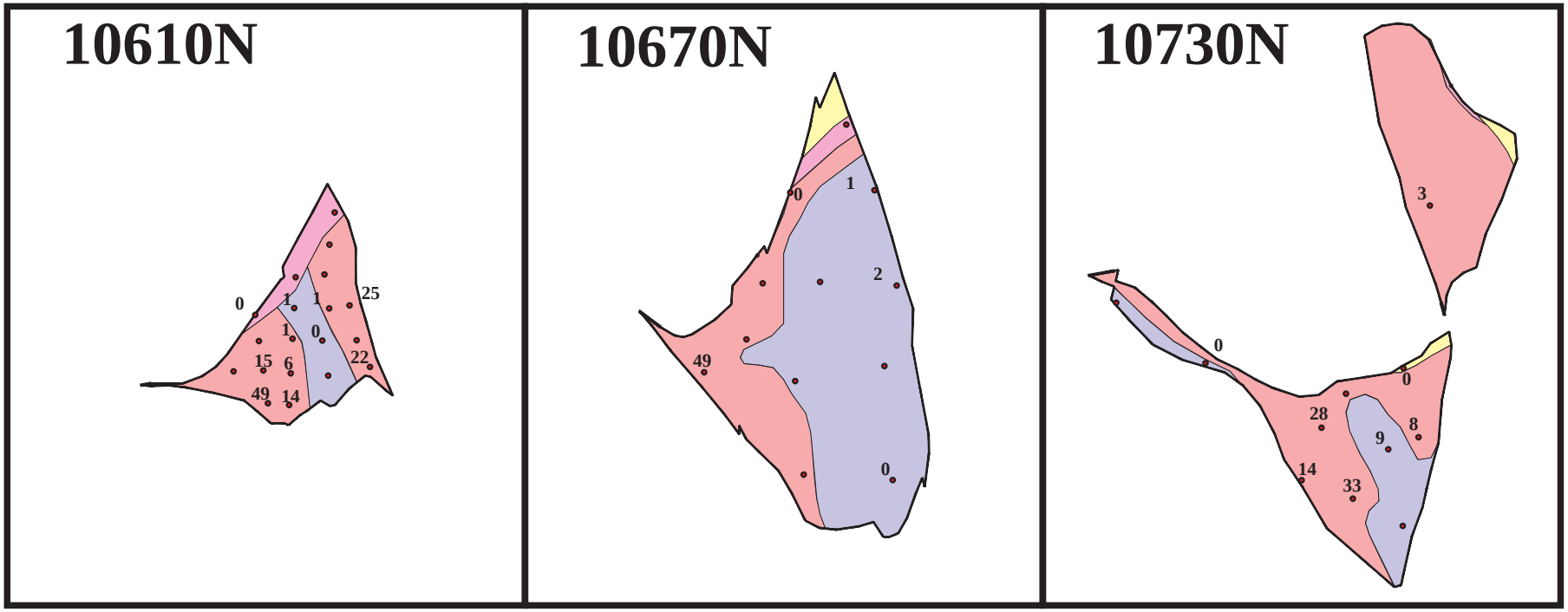

Fig. 113 - Carbonate %FeO analyses (normalised)

ORETYPES

- Siliceous cap (GSP)
- Baritic cap (BAR)
- Hangingwall enriched massive sulphide (HWE)
- Footwall depleted massive sulphide (FWD)

6.3.10 Minor gangue minerals

Chlorite

Twenty-five analyses from five samples are shown in Table 41. There are insufficient analyses from too few textural styles to interpret any zonation. These chlorites fall into the ripidolite and brunsvigite fields of Hey (1954). The Fe/(Fe+Mg) ratio (averaging 0.81), far exceeds that reported by Gemmell (1989) for the stringer zone (0.14-0.28) and the stringer envelope zone (0.44-0.46).

Hyalophane

Just one sample, immediately below the hangingwall on the eastern side of section 10730N, contained 3% by volume of an unusual feldspar. This was subsequently identified by probing (Table 42) to be the mineral hyalophane, a barium adularia. This is a most unusual occurrence - adularia is usually restricted to epithermal vein systems and is a classic indicator of boiling.

Table 41 - Microprobe analyses of chlorite (exclusively ClE mintex, blank=not analysed)

Sample	Normalised composition										Fe/(Fe+Mg)
	%MgO	%Al2O3	%SiO2	%CaO	%TiO2	%Cr2O3	%MnO	%FeO	%H2O	%Total	ratio
61-449-59.0	4.2	18.9	23.2	0.00	0.07		0.11	42.5	11.0	100	0.93
61-449-59.0	4.8	19.6	23.1	0.02	0.05		0.17	42.0	10.2	100	0.92
67-208-37.0	14.3	21.7	25.1	0.00	0.01	0.00	0.16	26.2	12.6	100	0.70
67-208-37.0	8.1	21.1	23.3	0.04	0.03	0.04	0.29	33.3	13.8	100	0.84
67-381-76.5	15.3	20.9	25.9	0.04	0.00	0.00	0.13	24.4	13.3	100	0.67
67-381-76.5	15.6	21.1	25.9	0.01	0.01	0.03	0.25	24.2	12.9	100	0.67
67-381-76.5	14.1	21.0	25.5	0.00	0.00	0.00	0.25	26.3	12.9	100	0.71
67-381-76.5	15.7	21.0	26.0	0.01	0.03	0.02	0.17	24.7	12.4	100	0.67
67-381-76.5	16.5	20.7	26.2	0.02	0.02	0.03	0.12	22.8	13.6	100	0.64
67-381-76.5	11.7	20.6	24.5	0.01	0.03	0.00	0.41	30.9	11.9	100	0.77
73-221-17.9	8.2	22.0	22.9	0.00	0.01	0.01	0.38	34.9	11.7	100	0.85
73-221-17.9	8.0	21.7	23.5	0.01	0.02	0.01	0.30	35.0	11.5	100	0.85
73-221-17.9	8.4	20.9	23.5	0.01	0.00	0.02	0.29	35.4	11.5	100	0.84
73-221-17.9	7.3	19.7	23.4	0.00	0.00	0.00	0.28	37.5	11.8	100	0.87
73-221-17.9	7.0	19.2	23.1	0.03	0.07	0.00	0.31	37.6	12.6	100	0.87
73-221-17.9	8.5	20.7	23.6	0.04	0.03	0.00	0.38	34.9	11.9	100	0.84
73-221-17.9	8.2	21.6	23.2	0.02	0.00	0.00	0.34	34.4	12.3	100	0.84
73-221-17.9	8.6	21.1	23.7	0.02	0.03	0.00	0.30	34.7	11.5	100	0.84
73-221-17.9	8.3	21.8	23.2	0.00	0.01	0.01	0.35	34.0	12.3	100	0.84
73-221-17.9	9.6	21.4	24.2	0.00	0.02	0.00	0.30	32.8	11.7	100	0.82
73-221-17.9	8.6	21.6	23.4	0.00	0.06	0.00	0.34	34.8	11.3	100	0.84
73-221-17.9	12.5	21.2	24.8	0.00	0.00	0.03	0.35	28.6	12.6	100	0.75
73-221-17.9	13.7	20.9	25.5	0.00	0.01	0.02	0.35	27.5	11.9	100	0.72
73-221-17.9	7.1	21.2	23.2	0.01	0.02	0.00	0.32	36.2	11.9	100	0.87
73-342-127.6	6.6	18.4	23.3	0.02	0.04	0.02	0.13	38.7	12.8	100	0.88
Average of all analyses	**10.0**	**20.8**	**24.1**	**0.01**	**0.02**	**0.01**	**0.27**	**32.6**	**12.1**	**100**	**0.81**

Table 42 - Microprobe analyses of hyalophane

Mintex	Normalised composition												
	%Na2O	%MgO	%Al2O3	%SiO2	%K2O	%CaO	%TiO2	%Cr2O3	%MnO	%FeO	%SrO	%BaO	%Total
HyA	0.25	0.00	24.7	51.9	8.3	0.01	0.00	0.00	0.01	0.00	0.22	14.6	100
HyA	0.26	0.00	24.7	52.0	8.5	0.00	0.00	0.00	0.00	0.10	0.16	14.3	100
HyA	0.26	0.01	25.1	50.9	7.8	0.00	0.00	0.00	0.08	0.28	0.22	15.4	100
Average of all analyses	**0.26**	**0.00**	**24.8**	**51.6**	**8.2**	**0.00**	**0.00**	**0.00**	**0.03**	**0.13**	**0.20**	**14.8**	**100**

6.4 Comparison with previous microprobe analyses

6.4.1 Ramsden et al. (1990)

Ramsden et al. (1990) document very detailed microprobe analyses from three Hellyer drill holes (HL038A, 10450N; HL070, 10650N; HL056, 10950N) from an earlier company-commissioned study to investigate the metallurgical character of the ore. Samples were selected every 2m downhole from each massive sulphide intersection and multiple analyses of sphalerite, galena, tetrahedrite and arsenopyrite were carried out. Although the holes chosen are not representative of the orebody as a whole (only surface holes had been drilled at the time of sampling), their elucidation of downhole, stratigraphic zonation can be compared to results from this study.

Ramsden et al. sphalerite analyses show lowest Fe content in the barite cap, higher values in the HWE and lower values in the FWD. This zonation is identical to that documented in this study (Table 43). Ramsden et al. correlate a high-Fe sphalerite zone in each hole near the base of the HWE, but my sampling is not detailed enough to support this.

Ramsden et al. galena analyses show considerable variation in Ag content with a tendency for highest values (up to 0.42%Ag by weight) to occur in the FWD. This is also broadly in concert with my findings.

Ramsden et al. tetrahedrite analyses show highest Ag content in the upper part of the HWE, particularly the small blebs in massive sphalerite (my TeF). This matches my findings.

Ramsden et al. arsenopyrite analyses show high Au content (up to 400ppm). My arsenopyrite Au analyses lack quality, but have similar values.

6.4.2 Sharpe (1991)

Sharpe (1991) in her study of the Hellyer baritic and siliceous caps undertook microprobe analyses of barite, carbonate, sphalerite, pyrite, arsenopyrite, galena, tetrahedrite and electrum.

Sharpe reports Sr contents of barite up to 2% by weight, with an average of 0.7% Sr. This exceeds the indicative 0.4%Sr content in the baritic cap found in this study (Table 37). However, Sharpe's sampling was far more extensive. Her lateral zonation trend of higher Sr content to the south was not tested in this study.

Sharpe baritic cap carbonate analyses are all calcites, in accordance with my findings.

Sharpe baritic cap sphalerite analyses average 2.3%Fe by weight, much higher than found in this study (Table 28; 4 samples, 27 analyses averaging 1.0%Fe). A possible explanation is that Sharpe may have included sphalerites from actual massive sulphide "slugs" from within the baritic cap, which would have higher Fe content.

Sharpe reports high As content in framboidal pyrites (up to 4.4% by weight) from both the baritic and siliceous caps. I suspect that some of Sharpe's framboidal pyrite actually may be high-As spherical colloform pyrites *[PyB, #2463]* which are not true framboids. However, my study broadly supports Sharpe's findings of contaminated primitive pyrite.

Sharpe baritic and siliceous cap galena was apparently devoid of Ag. This study also found baritic cap galena to have very low Ag content (average <300 ppm Ag). Sharpe tetrahedrite analyses show 2-3%Ag content, but my study (Table 35; 4 samples, 11 analyses) average 5.9% Ag by weight. The author has no explanation for this discrepancy. Sharpe analysed 15 electrum grains from the baritic and siliceous caps, reporting an average fineness of 758 and 1.25%Hg. My electrum analyses were from massive sulphide only, but are similar, with a fineness of 710 and 0.57%Hg.

6.5 Summary

The variations found in mineral composition at Hellyer from microprobe analyses are summarised in Table 43. Since mineral composition generally varies systematically with the textural paragenetic sequence and overall orebody zonation, there is good evidence to support a mineral refining model.

- Pyrite shows systematic reduction in Cu, Pb, Ag and As trace element content with increasing crystallinity. The arsenic expelled during lower mound pyrite recrystallisation has been shown by calculation, to comprise a significant proportion of the upper, semi-replacive arsenopyrite.
- Fe content of sphalerite generally decreases from highest values in the early colloform types to lower values in the Devonian remobilised styles.
- Galena Ag and Se content increase towards the proximal feeder zone, contrary to the general trend of most minerals which are more refined proximally.
- Tetrahedrites have variable composition, but the Ag and Fe contents decrease, while Cu and Zn contents increase, passing from early to late textural sites.
- FeO content of carbonates systematically decreases from early to late paragenetic position.

Early primitive minerals that were contaminated by "foreign" metals (as submicroscopic separate mineral species; or to a lesser extent, within the parent mineral lattice) were purged of their contaminants by repeated recrystallisation, both during the Cambrian mound building episode and also during the later Devonian deformation. The paragenetically latest textural sites are generally occupied by relatively coarse-grained minerals with minimal contaminants.

Table 43 - Summary of paragenetic and spatial variation of mineral composition

Above average content
Average or variable content
Below average content
Not available, insufficient analyses or not applicable

Mineral	Component	Textural sites			Orebody zones			
		Early	Mid	Late	GSP	BAR	HWE	FWD
Py	Cu							
	Pb							
	Zn							
	Ag							
	As							
	Se							
Sp	Fe							
	Hg							
Gn	Ag							
	Bi							
	Se							
As	Cu							
	Pb							
	Zn							
	Ag							
	Au							
	Se							
Te	Cu							
	Zn							
	Ag							
	As							
	Sb							
	Fe							
Ba	Sr							
Co	MgO							
	CaO							
	MnO							
	FeO							
	SrO							
	BaO							

7. INTERPRETATIVE GENETIC MODEL

7.1 Constraints

The genetic model for the Hellyer massive sulphide deposit presented below, represents an interpretation by the author based solely on the data collected during this study. It is largely built on the detailed microtextural relationships observed between the various minerals, in the spatial context of their stratigraphic position and proximity to the recognised core of the footwall alteration zone. The author is aware that the model presented currently lacks supporting geochemical evidence specific to the Hellyer deposit massive sulphide, (e.g. thermodynamic modelling, isotope and fluid inclusion studies) but these were never considered to be an integral part of this particular study. The author trusts that any future research on massive sulphide of the Hellyer deposit that may be based on isotope and/or fluid inclusion work will at least have a ready made paragenetic textural framework for proper sampling and interpretation.

In arriving at this interpretation, several basic precepts or axioms have been assumed. These are fundamental characteristics of most VHMS depoits, well established by previous workers, and have widespread general acceptance by the geological fraternity.

- the Hellyer deposit formed on the Cambrian seafloor by precipitation of sulphides and sulphates from venting hydrothermal solutions, in a similar manner to the modern-day analogues (Lydon, 1988; Jack, 1989; McArthur, 1990; McArthur and Dronseika, 1990; Gemmell and Large, 1992; Franklin, J.M., 1993)
- metals were transported as chloro complexes (Au as thio complexes), each with varying solubilities mainly dependent on temperature and pH (Lydon, 1988; Huston and Large, 1989; Large, 1992)
- the mineralising system underwent temporal variation of temperature, waxing

to peak intensity when the sulphide mound reached its maximum volume, then waning, as the system shut down (Pisutha-Arnond and Ohmoto, 1983; Khin Zaw et al., 1996)

- at peak intensity, isotherms within the massive sulphide mound varied between ~350°C at the footwall immediately overlying the core of the footwall feeder, and ~2°C at the hangingwall/seawater interface (Lydon, 1988; Gemmell and Large, 1992; Franklin, 1993)
- the Hellyer area underwent major compressional deformation in the Middle Devonian and brittle faulting in the Mesozoic (Berry, 1989; Corbett, 1992)

7.2 The model

7.2.1 Introduction

The Hellyer genetic model is presented in point format, as a sequential geologic history from the Late Cambrian to the present. The model is pictorially represented by a temporal series of east-west cross-sections (Figs. 114-122, 124) through the centre of the deposit and the central feeder zone (10670N/10800N).The seafloor profile in these drawings is taken from Downs' (1993) Cambrian reconstruction (his Fig. 17) and the seafloor morphology is assumed to have remained essentially unchanged during the mound building episode.

References *[in italics]* are made to mintex photomicrographs in the Appendix II textural atlas, to illustrate interpreted processes.

7.2.2 Pre-massive sulphide deposition

- In the Late Cambrian, the local seafloor, composed of calc-alkaline andesite lavas, autobreccias and volcaniclastics of the FPS (see 2.2.1 above) lay beneath about 3km of seawater (Waters, 1995).
- East-west extension formed a series of north-south grabens and half-grabens with east-west striking transfer faults (Downs, 1993) (my Fig. 11).

- This fault system tapped a deep heat source, initiating weak seawater circulation through the seafloor rocks, producing a north-south sub-vertical zone of chlorite-sericite alteration (Gemmell and Large, 1992).
- Rotation of the stress regime led to northwest-southeast extension with realignment, reactivation and dilation of the original transfer faults (Downs, 1993) (my Fig. 11).
- These reactivated northeast striking faults provided additional "plumbing" to the deep heat source, rapidly expanding the seawater circulation. Isotherms within the footwall (i.e. seafloor) rocks began to rise.
- Deeply circulating seawater infiltrated Precambrian metasediments 5km below Hellyer (Downs, 1993), converting seawater sulphate to sulphide, and leaching metals and perhaps sulphur from the basement rocks (Gemmell and Large, 1992).
- Footwall alteration became focussed at the intersection of the Central Fault with the Northwest Ridge (Fig. 11) where maximum dilation occurred. Siliceous alteration overprinted the earlier pervasive chlorite-sericite alteration (Gemmell and Large, 1992) in this zone of maximum dilation (to become the central feeder zone).

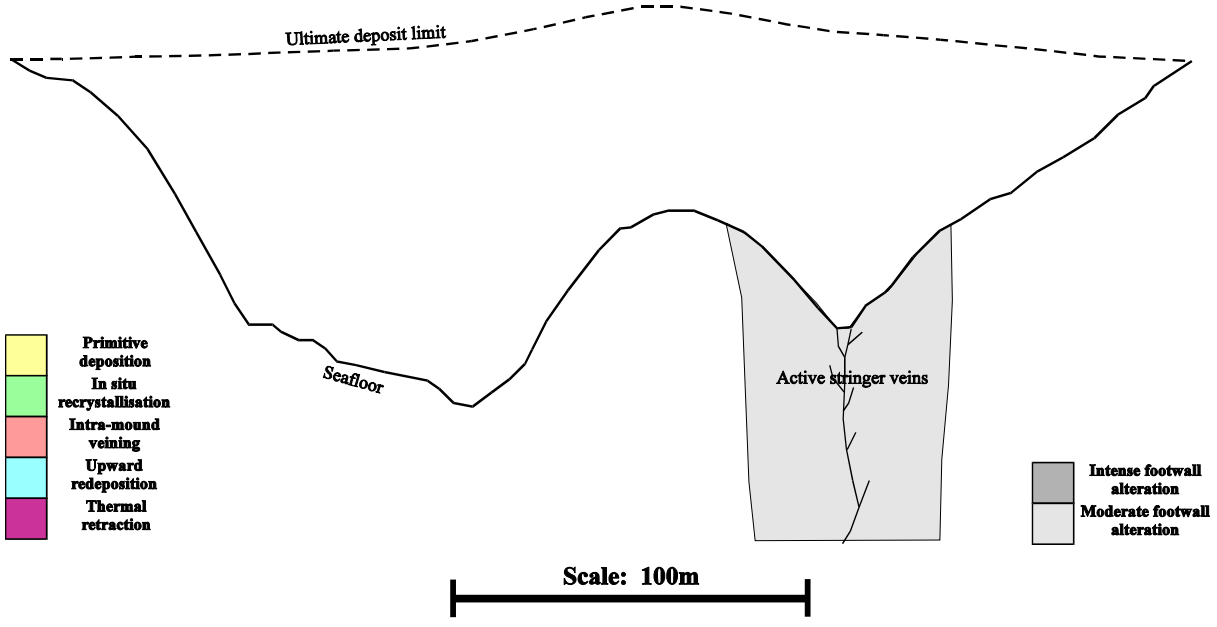

Figure 114 - Cross-section 10670N/10800N at the onset of Cambrian mineralisation

- Stage 2A stringer veins (Gemmell and Large, 1990b) of crustiform banded quartz, pyrite and dolomite with trace base metal sulphides, cut through the footwall alteration zone (Fig. 114).

7.2.3 Sulphide mound building

- Isotherms continued to rise at the main alteration focus. Stage 2B veins (Gemmell and Large, 1990b) of pyrite, chalcopyrite, galena, sphalerite, tetrahedrite-tennantite and barite cut through the siliceous alteration towards the seafloor.
- Hydrothermal solutions now charged with Si, Ca, Ba, Fe, As and some reduced S breached the seafloor and began to vent into cold, oxygenated seawater.
- Crusts of siliceous sinter (chert) with rare pyrite framboids and auriferous arsenopyrite crystals (i.e. GSP) *[Pyb, #638; AsJ, #1374]* formed on the seafloor over and adjacent to the main footwall feeders. Where SO_4^{-2} dominated, crystal aggregates of barite and anhydrite formed crusts (i.e. BAR), interdigitating with the cherty deposits (i.e. GSP) (Sharpe, 1991). Rare accumulations of hydrothermal sericite with pyrite framboids *[SeA, #3278]* also formed. Isotherms continued to rise within the footwall as the seafloor GSP and BAR deposits began to form sealing crusts (Fig. 115).

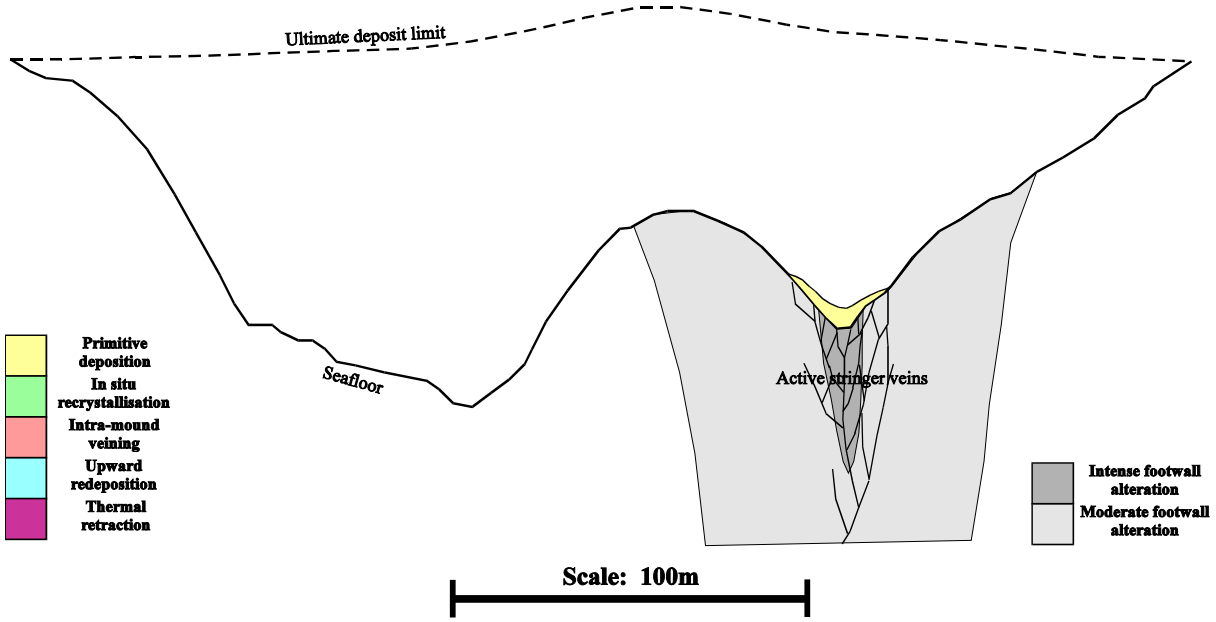

Figure 115 - Cross-section 10670N/10800N shortly after onset of Cambrian mineralisation

- Hot solutions rich in Fe and reduced S were quenched by cold seawater just beneath the GSP/BAR sealing crusts. Rapid deposition of melnikovite pyrite (contaminated with Cu, Pb, As, Ag and Au; see Table 25) as featureless masses *[PyA, #1080, #1958]* or as weakly colloform crusts *[PyA, #2147]* occurred. Less common (most likely least preserved), intricate spongy intergrowths of melnikovite and sphalerite *[PyD, #527; SpB, #528; PyF, #377]* were also precipitated.
- Drusy wurtzite crystal aggregates were deposited in local voids; these were rapidly infilled with quenched melnikovite *[SpG, #2474; PyS, #1134]*.
- As temperatures rose in the originally deposited GSP/BAR, chert, barite and anhydrite were dissolved and melnikovite was deposited in the crystal casts *[PyC, #536, #3173]* as pseudomorphs. Coeval overgrowths of melnikovite were also deposited *[PyI, #606, #3167]*. The redissolved Ba, Ca and Si moved upwards to the mound surface to redeposit new GSP/BAR crusts, although some chert was precipitated in interstitial areas beneath the top.
- Alternating bands of colloform melnikovite *[PyB, #703; PyE, #530, #533]* and high-Fe sphalerite/galena *[SpA, #1598; note galena is not present, having been remobilised]* began to develop beneath the upper mound crusts.
- As the sulphide content of the mound increased, heat was transferred to upper

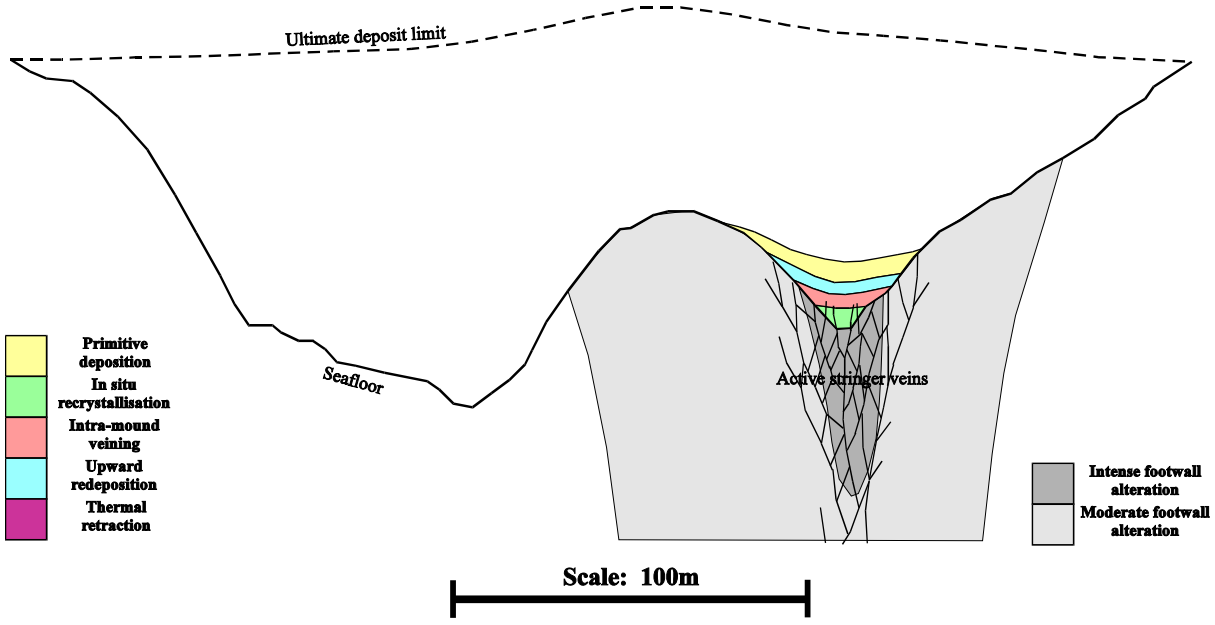

Figure 116 - Cross-section 10670N/10800N 10% through the Cambrian mineralisation

parts by solid conduction, as well as convection.

- The lower pyritic parts of the mound began to recrystallise, due to increased temperatures (Fig. 116). Initially, the original spongy melnikovite recrystallised to ultrafine-grained crystal aggregates. Some contaminants (galena and tetrahedrite) were expelled from the pyrite out into newly created interstices (void space once residing as melnikovite sponge pores) *[PyA, #1753 → PyM, #1820, #1821; PyY, #1760; PyB → PyN, #1843 → PyH, #643]*. Other contaminants (sphalerite, chalcopyrite and galena) coalesced into irregular blebs, but were trapped inside the pyrite crystals *[SpT, #972; GnA, #3105]*. Arsenopyrite, due to its crystallisation strength, formed fine-grained rhombs inside the recrystallising pyrite *[AsC, #2025]*.
- The lower pyritic zone began to crack from the "jacking" pressure of the buoyant hydrothermal solutions beneath. Sudden cracking permitted rapid transfer of solution and heat to upper parts of the mound. Walls of the cracks began to recrystallise. Symmetric crustiform banded pyrite and wurtzite crystals were deposited on the crack selvedge *[PyV, #767, frontispiece (upper left); SpG, #597]*. These cracks often cut across banding from earlier generations, producing complex "boxwork veining" (see 3.5.1 above). Eventually, most cracks were completely filled by continual deposition of pyrite, sphalerite *[SpH, #770; SpI, #2334]*, galena *[GnN, #2427]*, barite *[BaB, #382]* and quartz *[QzJ, #1888]*. This choked off the local plumbing, increasing "jacking" pressure on adjacent areas.
- Meanwhile, as the mound grew upwards, continual lower dissolution and upper redeposition continued. GSP/BAR continued to be deposited at the seawater interface with primitive melnikovite just beneath. Temperatures increased in the mound as thickness increased. Some pockets of the mound, escaped redissolution, thus preserving anomalous primitive textures.
- The pyrite, most proximal to the feeder locus, continued to recrystallise. Existing euhedral crystals grew larger *[PyL, #2841]* and more massive pyrite continued to anneal into coarser grained aggregates *[PyT, #1270]*. Original fine-grained interstitial sphalerite, galena, chalcopyrite and tetrahedrite were dissolved and the metals were transferred to higher, cooler parts of the mound

for redeposition. Most arsenopyrite was taken back into solution; however some remained trapped to grow coarser-grained crystals *[AsC, #1629]*.

- Once the mound had reached sufficient thickness to maintain a thermal equilibrium beneath the primitive crusts or carapace, large thicknesses of crustiform colloform sphalerite and wurtzite (with galena and tetrahedrite) began to deposit above the recrystallising pyrite. Slightly hotter fluids deposited pyritic layers, "interbedded" with the colloform sphalerite or interstitial to the wurtzite crystal aggregates *[SpP, #2418; PyJ, #2035; Pyd, #2323]*. Chalcopyrite disease formed in the wurtzite particularly by epitaxial growth *[CpA, #946]*. Other minerals deposited with the sphalerite/wurtzite were melnikovite *[PyA, #2799; PyP, #1929]*, magnetite *[MgA, #777]*, siderite/ankerite *[CoA, #579]*, quartz *[QzO, #778]*, sericite *[SeB, #2693]* and chlorite *[ClG, #1914]*. These large sphalerite-rich deposits were completely annealed and extended by later deformation, therefore original primary textures (e.g. colloform galena/tetrahedrite) were not preserved.
- Some of the melnikovite pseudomorphs (after sulphates) were in turn replaced by galena *[GnD, #1575]*, sphalerite *[SpM, #452]* and tetrahedrite *[TeC, #3134]*.
- Isotherms continued to rise within the sulphide mound causing the zone of recrystallised pyrite to grow upwards, and outwards from the central feeder. A significant proportion of the As released from the recrystallising pyrite was taken back into solution (see 6.3.1 above) and partially replaced pyritic areas higher in the mound *[AsD, #3116]*.
- As the base of the sphalerite/galena-rich zone came under the influence of higher temperatures, it was redissolved, with Pb and Zn transported upwards/distally to cooler parts of the mound. New pyrite/wurtzite was deposited, often overgrowing older euhedral pyrite *[PyW, #3183]*. All the temperature-dependent depositional processes moved further outwards from the central feeder zone as temperature gradually increased in the expanding mound.
- Because of steep slopes on the seafloor (southwestern and northeastern flanks of Northwest Ridge, Fig. 16), the sulphide mound could not support itself and

probable local seismic activity triggered slumping of upper sulphides into adjacent basins. Angular fragments of both sulphide rich material and barite-rich cap material rolled downslope to accumulate in the topographic lows (Plate 5d, Fig. 117). This, no doubt was a recurring process.

- The sudden loss of mound carapace and consequent pressure release caused an explosive pulse of hydrothermal fluids to vent, but rapid quenching by the cold seawater quickly formed a new sealing "scab" over the slumped zone.

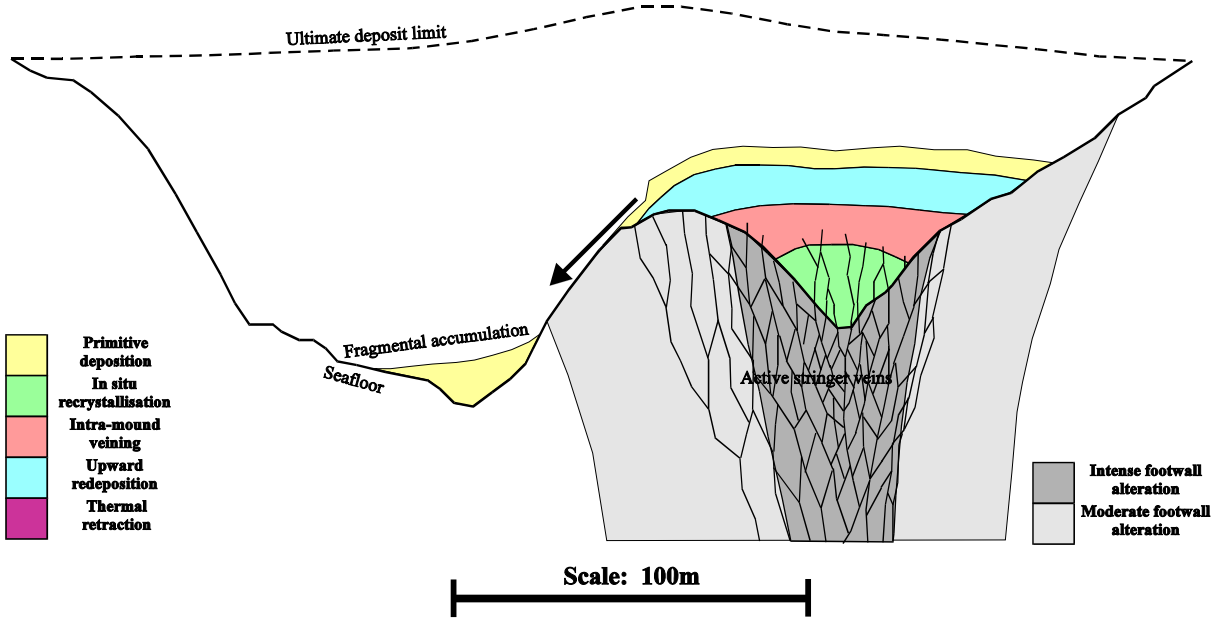

Figure 117 - Cross-section 10670N/10800N 30% through the Cambrian mineralisation

- As the system further increased in temperature, the isotherms within the sulphide mound began to take on the shape of the underlying seafloor topography. This had the effect of causing increased mound growth over the Northwest Ridge. This was all but totally compensated by repeated slumping into the adjacent basins. McArthur (1986) and Downs (1993) showed that despite irregular seafloor topography, the final surface of the sulphide mound was remarkably flat (as shown by comparatively little variation in thickness of overlying volcaniclastics).
- Over the Stage 2B vein vent site, very hot conditions caused maximum recrystallisation of pyrite (up to 1mm crystal size) and almost total refining of any base metal contaminants. These coarse-grained pyritic areas became very

permeable with up to 10% porosity, well connected between the pyrite euhedra.

- Clastic massive sulphide that accumulated in the adjacent basins from upslope slumping began to be replaced as the high temperature hydrothermal system expanded (Fig. 118). Gradual recrystallisation all but destroyed original fragmental textures, redissolving base metals for transport to the upper parts of the clastic pile. Some massive sulphide fragments were cemented by a matrix of younger massive sulphide.

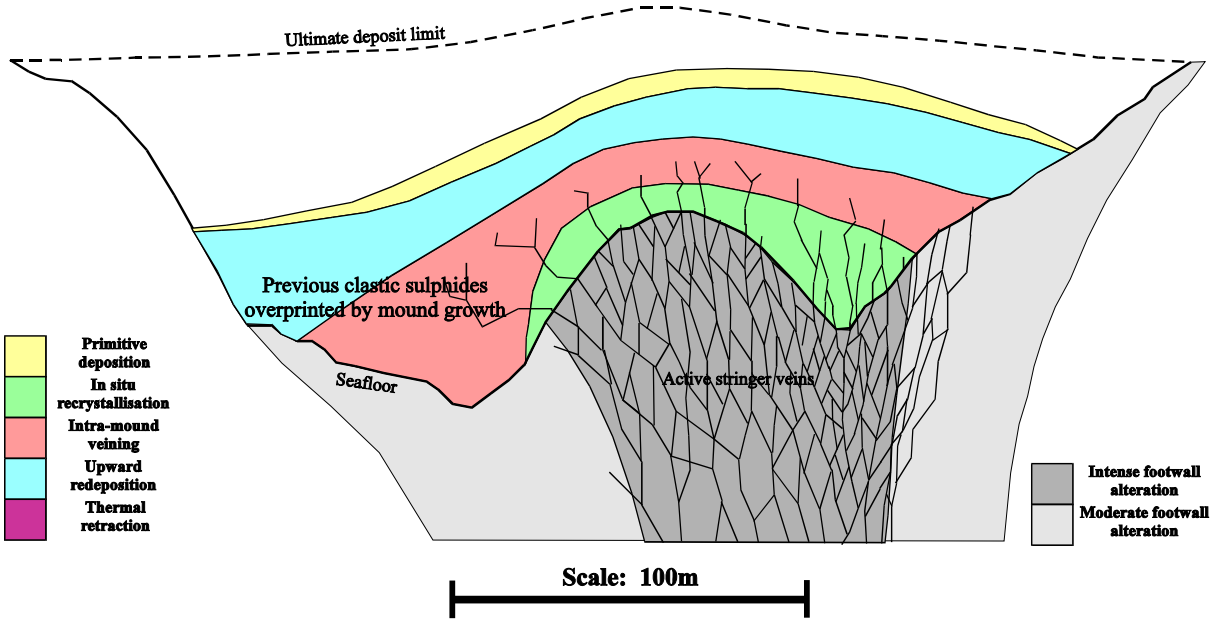

Figure 118 - Cross-section 10670N/10800N 60% through the Cambrian mineralisation

- As the mound continued to grow, occasional seismic events triggered catastrophic mass flows of mainly andesitic material, to be deposited over parts of the sulphide mound (Fig. 119). Two such mass flows were well preserved (although intensely altered and mineralised) at 10710N (Keel Zone) and 11000N (North End) by overlying sulphide deposition.

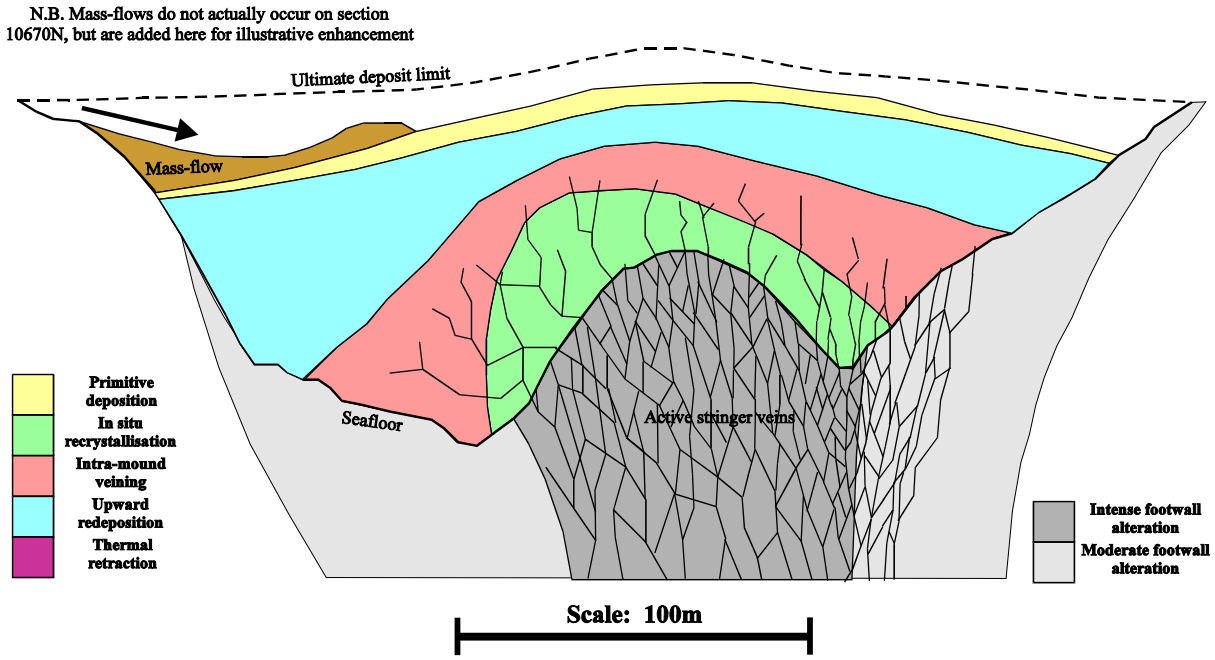

Figure 119 - Cross-section 10670N/10800N 90% through the Cambrian mineralisation

- The mound building processes described above occurred contemporaneously at smaller satellite feeders along the graben zone. Their individual sulphide deposits accumulated and interdigitated in a probable complex manner to integrate as the complete elongate deposit known today. Figure 120 shows the massive sulphide at its maximum extent.

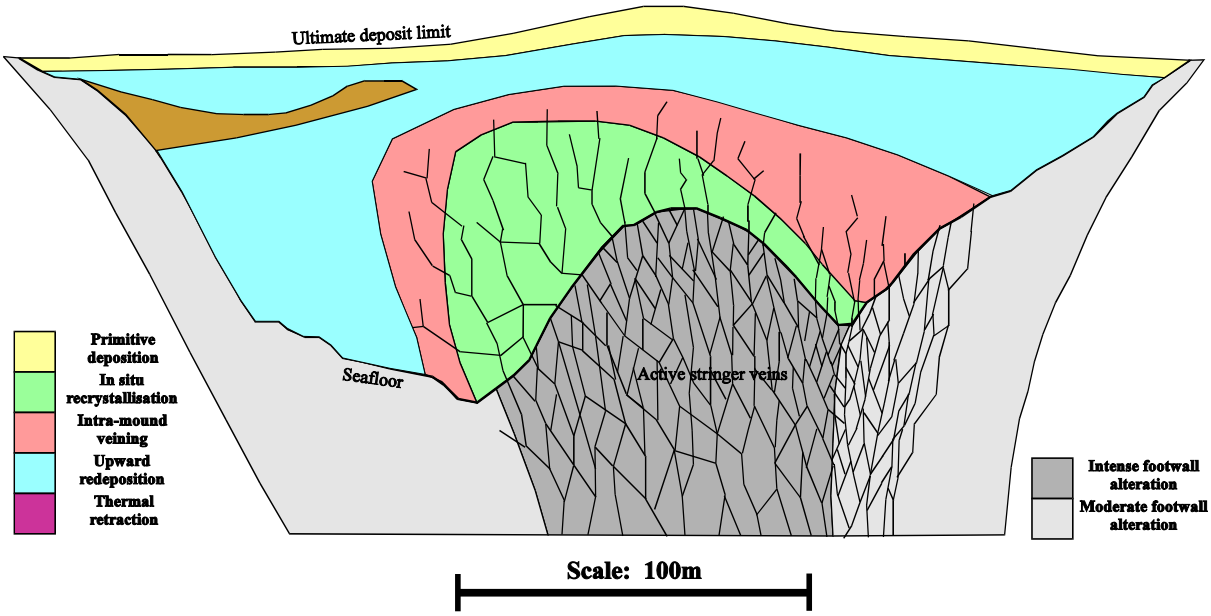

Figure 120 - Cross-section 10670N/10800N as Cambrian mineralisation reached its maximum extent

7.2.4 Thermal retraction

- As the sulphide mound reached its ultimate size, a rotation in the stress regime closed off the dilated channelways in the footwall, causing fluid flow to be drastically reduced. Isotherms within the sulphide mound began to retract.
- The zone of thermochemical conditions suitable for GSP/BAR deposition increased in thickness and additional barite and chert were deposited at or just below the mound surface, directly over the central feeder zone (Sharpe, 1991). Barite was gradually recrystallised to granoblastic aggregates *[BaC, #2629]* or very large laths *[BaA, #3243, #3253]* with interstitial quartz *[QzH, #3249-3250]*.
- Increased seismic activity associated with the new stress regime, triggered large scale mass flows to nearly bury the sulphide mound. Only the highest region of the sulphide mound over the central feeder remained uncovered (McArthur, 1986). Some sulphide material was torn off the mound surface by the mass flows to be preserved within the HVS, particularly at the southern and northern ends of the deposit. The mass flow accumulations were altered by hydrothermal fluids filtering through from the massive sulphide below. Minor amounts of Au and As, were deposited as auriferous arsenopyrite within the HVS.
- As the hydrothermal system waned, isotherms retreated towards the main feeder vents. Nevertheless, fluid flow continued, but at a much reduced rate.
- As isotherms descended, primitive chert *[QzI, #601]* , pyrite framboids *[Pyb, #1980; Pya, #2803-2804]*, recrystallised framboids *[PyZ, #2031]* and melnikovite pyrite *[PyW, #807]* were deposited in available interstitial sites (or partially replacing massive sphalerite, *[QzM, #3092])*, at increasingly greater depths within the mound, as the critical precipitation thermochemical conditions were reached.
- Further below, thermal retraction caused deposition of tetrahedrite *[TeG, #954]*, bournonite *[BoE, #439]*, galena *[GnG, #1977]*, Fe-poor sphalerite *[SpN, #812]*, chalcopyrite *[CpF, #405]* and crystalline quartz *[QzF, #2235]*

into various pyrite interstices. Pyrite overgrowths were deposited on pyrite euhedra *[Pyc, #801]*. Arsenopyrite partially replaced pyrite *[AsI, #1577]*. Gangue minerals were deposited in interstitial areas also; chlorite most distal *[ClB, #849; ClE, #794]*, then calcite-ankerite *[CoE, #915]* and lastly, sericite most proximal *[SeC, #989]*.

- Newly created deep-seated fractures tapped a basaltic magma source which rose up as northeast striking dykes, cutting through the footwall andesite, massive sulphide and overlying volcaniclastics to extrude pillowed and sheet lavas on the seafloor (Waters, 1995). The deposit was rapidly buried and thus preserved (Fig. 121).

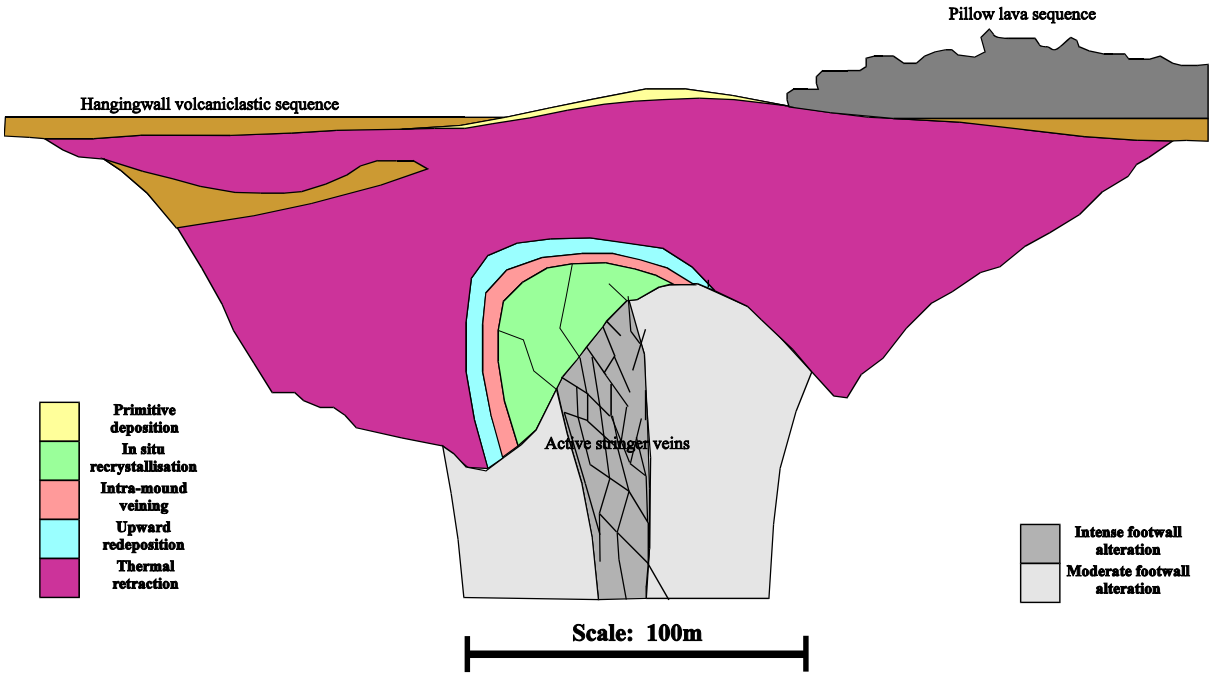

Figure 121 - Cross-section 10670N/10800N as Cambrian mineralisation commenced retraction

- Hydrothermal fluid flow continued during basalt extrusion, percolating through the pillowed lavas in particular, causing intense "fuchsite"-carbonate±pyrite alteration as a plume over the central feeder (Jack, 1989; Warren, 1989). This alteration extended to the very top of the PLS, extending laterally at the seafloor due to reduced hydrostatic pressure (Fig. 122).

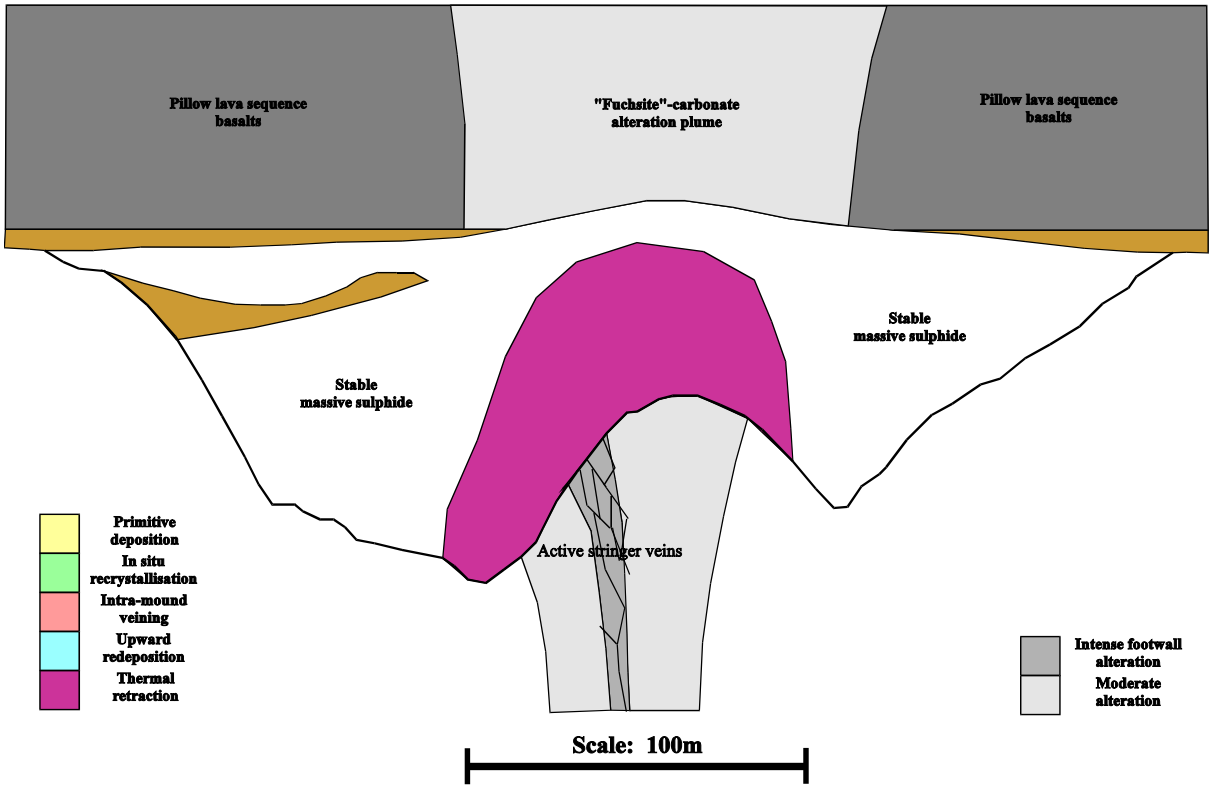

Figure 122 - Cross-section 10670N/10800N as Cambrian mineralisation came to a close

- Hydrothermal fluid flow retracted below the footwall, leaving the basal portion of the sulphide mound with unfilled interstitial voids *[VdA, #762]*. Stage 2B veins in the footwall closed off. Basalt extrusion ceased. The subsequent quiescent period saw the comparatively slow deposition of the Que River black shales (Sinclair, 1994). The Hellyer hydrothermal system became totally extinct.

The Cambrian mound building episode can be summarised by a simple diagram (Fig. 123) showing the main sulphide paragenetic categories plotted on time-proximity space (not to scale).

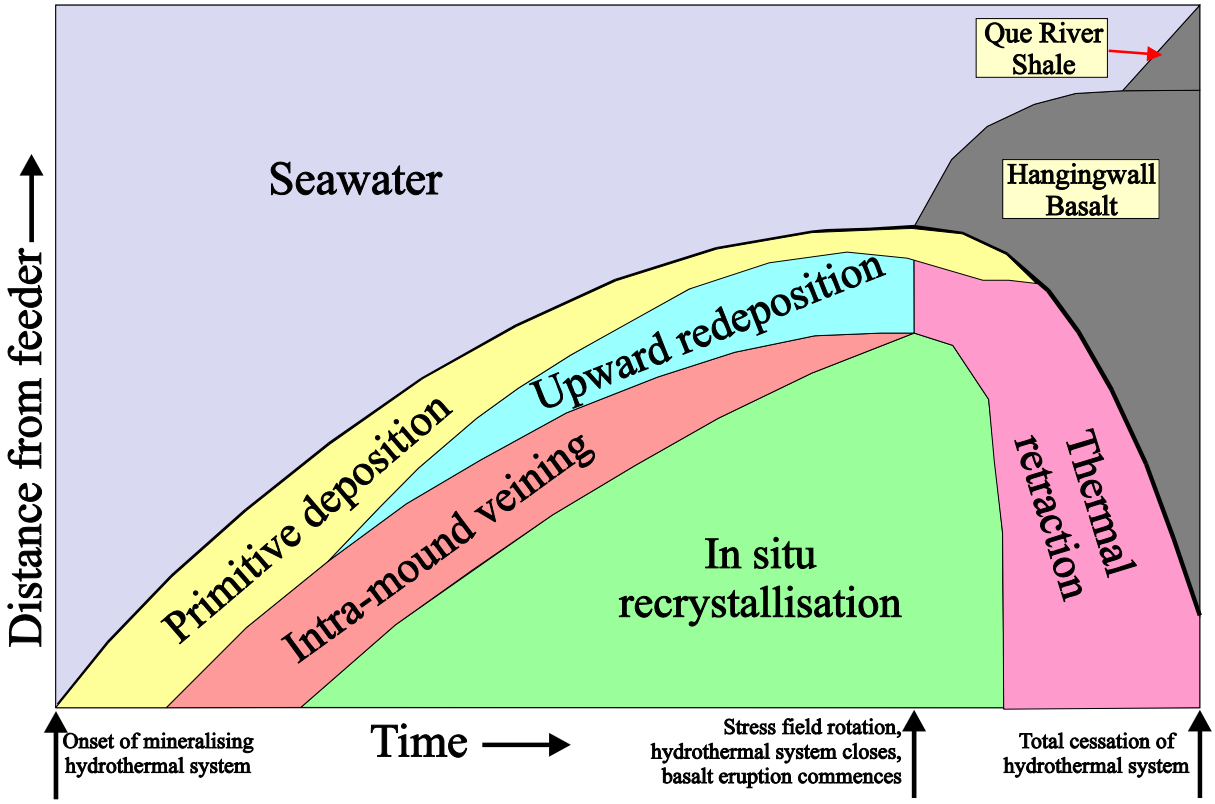

Figure 123 - Cambrian mound building processes through time against distance from the central feeder zone

The metal zonation observed in the Hellyer deposit today (Fig. 87) is predominantly controlled by the Cambrian mound building process detailed above. Later remobilisation was very local, effectively moving only a minor quantity of metal, any significant distance, from its original Cambrian position. The GSP and BAR zones are virtually perfectly preserved as they existed at the termination of the mineralising episode. The HWE zone corresponds to the "upward redeposition" and "intra-mound veining" regions, containing relict primitive material, particularly in the basal portions of the HWE (Appendix II, Fig. F), plus the distal portions of the "in situ recrystallised" region. The FWD zone corresponds to the bulk of the "in situ recrystallised" region. Both the HWE and FWD oretypes were overprinted by mineral deposition during the "thermal retraction" phase.

7.2.5 Devonian deformation

- During the Middle Devonian, east-west compression produced open upright folds in the Hellyer host rocks (Large, 1992; Downs, 1993)

- Due to rheology/competency contrasts, strain partitioning directed ductile deformation to the Sp/Gn-rich portions of the massive sulphide and the phyllosilicate-rich areas of the footwall alteration zone. Brittle tensile deformation was directed to the Py-rich part of the massive sulphide, the siliceous central feeder zone of the footwall, the adjacent relatively unaltered footwall andesites, and the overlying hangingwall basalts (Drown and Downs, 1990).
- Two locally tight synclines were produced, coinciding with original Cambrian seafloor basins (Fig. 11). Between these two synclines, an open anticline developed over the central feeder zone which extended up into the Southwell Sub-group rocks overlying Hellyer (Fig.124).
- Maximum extension within the massive sulphide occurred near the western termination where Sp/Gn-rich sulphides were compressed between rigid blocks of hangingwall basalt above, unaltered footwall andesite below and Py-rich massive sulphide/siliceous footwall to the east.
- In the siliceous cap, chert was partially recrystallised *[QzG, #2973]* and in the baritic cap, fibrous barite *[BaD, #2579]* developed. Calcite was remobilised to partially replace barite *[CoL, #2855]*.
- Within the Sp/Gn-rich massive sulphide, sphalerite was strongly annealed, while galena/tetrahedrite inclusions and the chalcopyrite disease were locally remobilised into medium-grained blebs *[SpP, #1412; GnJ, #745; TeF, #1422; CpE, #1638]*. Pyrite euhedra *[Pye, #681]* and magnetite *[MgA, #386]* were strongly corroded by sphalerite, while siderite/ankerite *[CoA, #1611]* was also corroded and partially recrystallised. Quartz remained unaffected. Pyrite bands, of any significant width, were rotated, extended and boudinaged. Crystalline pyrite bands developed tensile pull-apart fractures normal to the extension direction (nominally, the cleavage). These, and shadow zones around pyrite euhedra, were quickly filled with quartz *[QzN, #1815; QzL, #631]*, calcite/ankerite *[CoK, #2935; CoF, #1050]*, fibrous sericite *[SeD, #1355]*, fibrous chlorite *[ClF, #1064]*, fibrous barite *[BaD, #2516]*, galena *[GnL, #829; GnM, #759]*, chalcopyrite *[CpH, #875]*, tetrahedrite *[TeD, #832;*

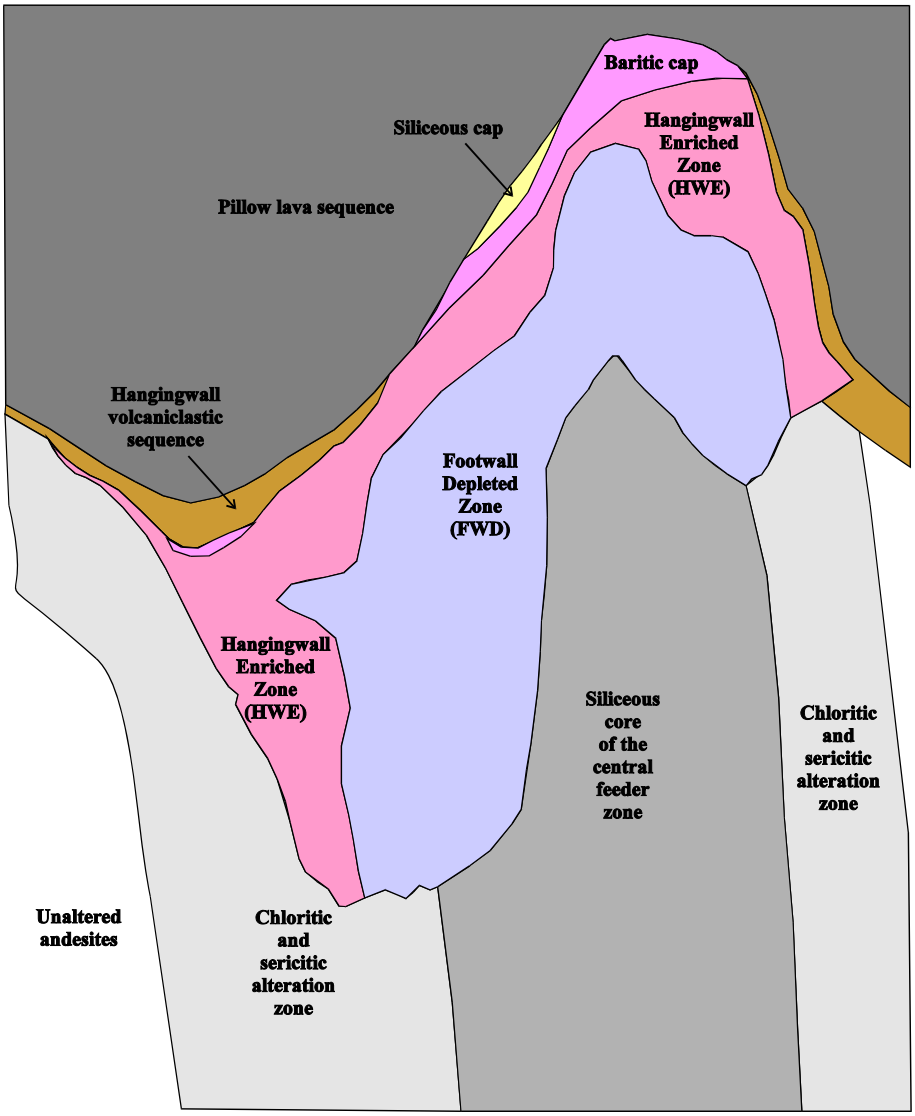

Figure 124 - Cross-section 10670N/10800N after Devonian folding

TeE, #2661], sphalerite *[SpR, #1565]* or bournonite *[BoA, #1608]*. More often than not, chalcopyrite took up positions on the selvedge of the pull-apart fractures, with sphalerite and/or galena in the centre *[CpH, #893]*. Electrum remobilised with galena into pyrite cracks and interstices *[AuB, #1464, #2735]*.

- Where remobilisation was most intense, large coarse-grained segregations of galena developed parallel to cleavage *[GnK, #2377]*. This remobilised galena often replaced sphalerite and other minerals previously filling pyrite interstices *[e.g. GnG, #411]*. Some remobilising galena is interpreted to have replaced relict spongy pyrite *[e.g. GnD, #813; GnE, #2301; GnH, #598]*.
- Devonian remobilised gangue minerals partially replaced sphalerite and galena. Quartz *[QzM]*, and calcite/ankerite *[CoM, #432]* in the most deformed areas infiltrated and replaced sphalerite and galena, but not pyrite. Remobilised

barite partially replaced sphalerite in regions near the baritic cap *[BaF, #2485]*.

- Within the strongly recrystallised pyrite-rich areas of the FWD, no cleavage or mineral fibres developed. Low-Fe sphalerite *[SpN, #1164]*, galena *[GnG, #1852]*, chalcopyrite *[CpF, #951]* and Ag-poor tetrahedrite *[TeG, #954]* were remobilised in the pyrite euhedra interstices, but there is no evidence that they were moved very far from their original interstitial sites. In the lower FWD, chalcopyrite formed coarse-grained segregations *[CpG, #1261]* containing unusual late crusts of pyrite *[Pyf, #2293; Pyg, #1112]*. Again, there appears little evidence to suggest that this chalcopyrite moved far from its original location.
- Considerable erosion of cover rocks took place from the Devonian to the Mesozoic.

7.2.6 Mesozoic deformation

- In association with sinistral movement on the Henty Fault (Berry, 1989; Downs, 1993), shallow brittle wrench faulting cut through the Hellyer area in the Mesozoic.
- One significant wrench fault, now known as the Jack Fault, reactivated one of the pre-mineralisation north-south normal graben faults (labelled EF on Fig. 11). This fault propagated north until it encountered siliceous footwall alteration, associated with the north-east striking central fault (labelled CF on Fig.11). This caused the fault to branch (Fig. 10); one major branch cutting through the siliceous alteration and massive sulphide, while the other (now known as the Silic Fault) took a more northeast trend, partially reactivating earlier Cambrian faults. Sinistral movement on the Jack (+ Silic) Fault amounted to 130m horizontally, with a 30m vertical component, east side up (McArthur and Dronseika, 1990).
- Several west-northwest striking dextral conjugate faults also propagated through the massive sulphide with sub-horizontal displacements up to 10m.
- The Mesozoic faulting event cataclasised pyrite *[Pyk, #1202]* and to a lesser

extent sphalerite *[SpV, #1205]* and chalcopyrite *[CpL, #3146]* in the FWD. The resulting interfragmental voids were filled with chlorite *[ClK, #3007]*, quartz *[Pyk, #2949]*, carbonate or tetrahedrite/chalcopyrite *[TeL, #1151]*; but mostly left empty *[Pyk, #1272; VdA, #1211]*.

- Within the HWE sphalerite-rich region, characteristic narrow microfault networks developed, filled with angular fragments of pyrite *[Pyl, #2606]*, sphalerite *[SpW, #2166]* and rare galena *[GnU, #3270]* healed by quartz *[QzQ, #2792]*.
- Several minerals were remobilised during this deformational episode. Barite, in particular was strongly mobilised into fractures parallel to the Jack Fault, cutting across earlier textures *[BaG, #2537]* and in some areas, replacing sphalerite *[BaF, #1032]*. Large sub-vertical veins up to 5m wide of massive barite cut through the massive sulphide within 50m of the Jack Fault, predominantly in the Cap Zone. Calcite also filled late cracks *[CoK, #2177]*. Narrow cracks through massive sulphide were filled with mobilised chalcopyrite *[CpK, #502]*, galena *[GnV, #2261]*, tetrahedrite *[TeJ, #1029]* and cubanite *[CbB, #2201]*. Very rare spongy crustiform pyrite with unidentified gangue needle inclusions, coated quartz-filled fractures *[Pym, #2180-2181]*.
- Previous obvious Devonian textures were overprinted by effects of the Mesozoic brittle faulting, e.g. a calcite-filled fracture cutting across a fibrous quartz shadow beard *[QzL, #626]*, fragmentation and rotation of fibrous quartz *[QzL, #2312]* or tetrahedrite-filled cracks intersecting chalcopyrite-filled pull-aparts *[TeJ, #2689]*.

7.2.7 Mesozoic to present day

- Erosion continued. Groundwaters percolated down Mesozoic faults with rare incipient dissolution of carbonates and weathering of chlorite to clay *[CyA, #2486-2487]*.
- Mankind's presence was first felt in 1983 AD, when the diamonds of an NQWL drill bit cut through massive sulphides on 10400N (Plate 2). Exploitation began.

- The economic portions of the Hellyer deposit will have been totally mined by 2000 AD. Only low grade in situ remnants and archived drill core will remain (*aside:* the author's sentiment is surely understandable, after 13 years attachment to the deposit!).

7.3 Comparison with the Kuroko refining model of Eldridge et al.

In 1983, Eldridge, Barton and Ohmoto undertook a comprehensive textural investigation of several volcanic-hosted massive sulphide deposits of the Kuroko field in northern Japan. Their interpretation of textural data (herein referred to as "the Eldridge model") represented a significant watershed in genetic understanding of this style of deposit (Ohmoto and Skinner, 1983).

Previously widely accepted models (e.g. Sato, 1973; Solomon and Walshe, 1979), postulated precipitation of ore minerals from plumes of hydrothermal fluids with simple superposition of minerals to accumulate stratified ore piles. Observed mineral zonation was interpreted to be the result of compositional variation of hydrothermal fluids.

The Eldridge model (Eldridge et al., 1983) divides the depositional history of Kuroko massive sulphides into five stages, all of which may have taken place nearly contemporaneously but at different sites within (here quoted verbatim from their abstract):

(1) "precipitation of primitive or facies 1 (black ore) minerals which are fine-grained (<50μm in size) and often colloform; sphalerite, galena, pyrite, tetrahedrite, barite with minor chalcopyrite, and quartz at the sites of mixing of hot hydrothermal fluids with cold seawater (i.e. on or near the sea floor)

(2) resolution of facies 1 minerals by hotter hydrothermal fluids, resulting in the formation of coarser grained facies 2 minerals in the lower parts and the reprecipitation of facies 1 minerals in the outer parts of the growing orebodies

(3) introduction of hotter and Cu-rich hydrothermal solutions into the ore pile, resulting in the replacement of facies 2 sulphides by facies 3 chalcopyrite (forming yellow ore) in the lower parts of the orebodies and the migration of facies 2 - and facies 1 - zones outward

(4) introduction of hotter (and undersaturated with chalcopyrite) fluids into the ore pile, resulting in the dissolution of chalcopyrite and formation of pyrite ores in the lowermost part of the ore pile and migration of chalcopyrite, facies 2, and facies 1 ore upward and outward of the ore pile

(5) precipitation of tetsusekiei (chert-hematite) ores on top of the massive ores."

Before comparing my genetic model for Hellyer with the Eldridge model for Kuroko, it is instructive to highlight some important differences between the deposits. Table 44 is sourced mainly from Ohmoto and Skinner (1983), Ohmoto (1983) and Tanimura et al. (1983) and summarises the main differences.

Care is required when comparing the two camps; the Kuroko deposits were defined with quite different economic constraints (i.e. much lower cutoff grade) and often included footwall stringer mineralisation as part of the resource. Nevertheless, it is clear there are significant differences in footwall host rocks, deposit clustering style, deposit size, grades, overall sulphide content and later deformation. Despite these differences, metal and textural zonation in both deposits is remarkably similar.

The Hellyer genetic model presented above is **very similar** to the Eldridge model. The **Eldridge facies 1 equates to the Hellyer HWE** oretype predominantly formed by the "upward redeposition" process. **Eldridge facies 2 equates to the Hellyer pyritic FWD** formed mainly by "in situ recrystallisation". Kuroko facies 3 mineralisation is not well represented at Hellyer. The differences between the two models are:

- this Hellyer model postulates that siliceous and baritic caps existed on top of the sulphide mound **throughout** the mound building episode - the Eldridge model has the siliceous cap (tetsusekiei) forming as the system wanes.

- the Hellyer model postulates significant deposition of sulphides and gangue minerals during "thermal retraction" - the Eldridge model only briefly discusses "..cooling fluids allowing reequilibration of sulphur-rich assemblages that are not encapsulated in pyrite.."

Table 44 - Summary of characteristic differences between the Kuroko (tonneage and grades from Table 2 of Tanimura et al., 1983) and Hellyer deposits

Characteristic	Kuroko	Hellyer
Age	Miocene	Cambrian
Footwall	rhyolite, dacite	andesite
Hangingwall	sediments, basalt	basalt
Deposit groupings	many clusters of several	3 (+Que River + Mt.Charter)
Tonneage Mt	2.5 (mean of 37)	16.2
Thickness m.	34	44
%Cu grade	2.1	0.4
%Pb grade	1.1	7.1
%Zn grade	4.5	13.9
%Fe grade	12.4	24.8
%Sulphide content	37	86
100Cu/(Cu+Zn)	32	3
100Zn/(Zn+Pb)	80	66
Deformation	almost nil	folding & remobilisation, brittle faulting

- the Hellyer model allows for deposition of significant primitive pyrite (melnikovite) with base metal contaminants that were gradually expelled during lower mound recrystallisation - the Eldridge model admits to a lack of detailed knowledge of the paragenesis of Kuroko pyrite
- the Hellyer model explains the occurrence of "intra-mound veins" with symmetric crustiform banding as upward extensions of footwall stringer veins

providing plumbing to the upper mound - the Eldridge model mentions in passing "..metasomatism of the black ore changing it to yellow ore along fractures (Fukazawa mine -150 level).."

- the Hellyer model postulates that seafloor topography at Hellyer played a role in the distribution of heat within the mound, therefore effecting the spatial distribution of pyrite recrystallisation
- lack of chalcopyrite at Hellyer severely downplays the Eldridge chalcopyrite replacement event
- the Hellyer mineralising system was much more focussed and more Fe-rich than the Kuroko systems resulting in more extensive high temperature recrystallisation within a very thick sulphide mound

8. CONCLUSIONS

This study has successfully investigated, and subsequently comprehensively documented, pronounced zonation within the Hellyer massive sulphide deposit. This zonation is demonstrated by variations in metal content, mineralogy, macroscopic and microscopic textures, and mineral trace element composition, surrounding the recognised core of footwall alteration. Exhaustive microtextural analysis has allowed clear distinction between the primary Cambrian mound building processes of primitive deposition, in situ recrystallisation, intra-mound veining, upward redeposition and thermal retraction, and post-mineralisation deformational overprints. These overprints, while accounting for a significant proportion of the identified textural types, are interpreted to be relatively local, remobilising phenomena that did not appreciably alter the original Cambrian metal zonation of Fe→Cu→Zn→Pb→Ag→Au→As→Ba (from proximal→distal).

The postulated genetic model for Hellyer is very similar to the mound refining model proposed by Eldridge et al. (1983) for the Kuroko massive sulphide deposits of Japan. Despite important geological differences between the Kuroko camp and Hellyer, zonation as exhibited by metal, mineral and textural patterns, is almost identical. The Hellyer model extends the validity and scope of the Eldridge model, by providing better 3-dimensional sampling representivity, analytical evidence of individual mineral refining and an alternative explanation for the occurrence of low-temperature mineral suites in the lower mound, by means of thermal retraction deposition.

REFERENCES

Aberfoyle Resources Limited, 1987, Hellyer expansion project - Feasibility study: Ore Reserves Vol.I, unpub. report, 37pp.

Aberfoyle Resources Limited, 1996, Hellyer ore reserves as at 30th June 1995, unpub. report, 42pp.

Alt, J.C. and Wei-Teh Jiang, 1991, Hydrothermally precipitated mixed-layer illite-smectite in recent massive sulfide deposits from the sea floor, *Geology*, vol.19, pp.570-573.

Barton, P.B., 1978, Some ore textures involving sphalerite from the Furotobe Mine, Akita Prefecture, Japan, *Mining Geol.*, vol.28, pp.293-300.

Berry, R.F., 1989, The history of movement on the Henty fault zone, western Tasmania: an analysis of fault striations, *Aust. Journ. Earth Sci.*, vol.36, pp.189-206.

Binks, C.J., 1980, Explorers of western Tasmania, Mary Fisher, 264p.

Corbett, K.D., 1992, Stratigraphic-volcanic setting of massive sulfide deposits in the Cambrian Mount Read Volcanics, Tasmania, *Econ. Geol.*, vol.87, pp.564-586

Craig, J.R. and Vaughan, D.J., 1981. *Ore microscopy and ore petrography*, John Wiley & Sons, 406p.

Crawford, A.J., Corbett, K.D. and Everard, J.L., 1992, Geochemistry of the Cambrian volcanic-hosted massive sulfide-rich Mount Read Volcanics, Tasmania, and some tectonic implications, *Econ. Geol.*, vol.87, pp.597-619.

Criddle, A.J. and Stanley, C.J. (eds.), 1986, The quantitative data file for ore minerals, British Museum (Natural History), 420p.

David, M., 1977, *Geostatistical Ore Reserve Estimation*, Elsevier, New York, 364p.

Downs, R.C., 1990, Geological mapping and logging at Hellyer, *Mine Geologists' Conference*, Mt.Isa, Australia, October 1990, Australas. Inst. Min. Metall., pp.1-7.

Downs, R.C., 1993, Syn-depositional fault controls on the Hellyer volcanic-hosted massive sulphide deposit, Unpub. M.Econ.Geol. thesis, Univ. Tasmania, 62p.

Drown, C.G. and Downs, R.C., 1990, Deformational style and strain partitioning at the Hellyer volcanogenic massive sulphide deposit [abs.], in *Gondwana Terranes and Resources,* 10th Australian Geological Convention, Hobart, Australia, February 1990, Geol. Soc. Aust., Abs. no.25, pp.176-177.

Drown, C.G. and Richardson, S.M., 1990, Hellyer massive sulphide deposit, in *Gondwana*

Terranes and Resources, 10th Australian Geological Convention, Hobart, Australia, February 1990, Geol. Soc. Aust., Excursion Guide E1, 8p.

Eadie, E.T., 1987, The downhole EM response of the Hellyer ore deposit, *Expl. Geophys.*, vol.18, pp.255-264.

Eadie, E.T., 1988, Discovery and geology of Que River and Hellyer, in *Australas. Inst. Min. Metall.* Annual Conference, July 1988.

Eadie, E.T. and Silic, J., 1984, The application of geophysics in the discovery of the Hellyer ore deposit, in *AMIRA Technical Meeting, Exploration, Minerals and Petroleum,* Melbourne 1984, pp.11-14 (AMIRA Limited: Melbourne)

Eadie, E.T., Silic, J. and Jack, D.J., 1985, The application of geophysics to the discovery of the Hellyer ore deposit, Tasmania, *Aust. Soc. Expl. Geophys.*, 20, nos.2-3, pp.207-209.

Edwards, A.B., 1947, *Textures of the ore minerals,* Aust. Inst. Min. Metall., Melbourne.

Eldridge, C.S., Barton, P.B. and Ohmoto, H., 1983, Mineral textures and their bearing on formation of the Kuroko orebodies, *Econ. Geol.*, Mono.5, pp.241-281.

Franklin, J.M., 1993, Volcanic-associated massive sulphide deposits, in *Mineral Deposit Modeling*, (Eds. Kirkham, R.V., Sinclair, W.D., Thorpe, R.I. and Duke, J.M.), Geol. Assoc. Canada, Special Paper 40, pp.315-334.

Franklin, J.M., Sangster, D.F. and Lydon, J.W., 1981, Volcanic-associated massive sulfide deposits, *Econ. Geol.*, 75th Anniv. Vol., pp.485-627.

Gemmell, J.B., 1988, Hellyer Stringer Zone Project, Progress Report No.1, Unpub. report, University of Tasmania, December 1988, 8p.

Gemmell, J.B., 1989, Hellyer Stringer Zone Project, Progress Report No.2, Unpub. report, University of Tasmania, June 1989, 14p.

Gemmell, J.B., 1990a, Hellyer gold study - preliminary results, Unpub. report, University of Tasmania, April 1990, 16p.

Gemmell, J.B., 1990b, Hellyer Stringer Zone Project, Progress Report No.3, Unpub. report, University of Tasmania, May 1990, 14p.

Gemmell, J.B., 1991, Evolution of the alteration zone and stringer system beneath the Hellyer volcanogenic massive sulfide deposit, Tasmania, Australia, [abs.], in *Meet. Geol. Assoc. Canada*, Toronto, Canada, January 1991.

Gemmell, J.B. and Large, R.R., 1990a, Geologic evolution of the stringer zone underlying the Hellyer volcanogenic sulphide deposit, Tasmania, in *Pacific Rim Congress Proc.*, vol.II,

Gold Coast, Queensland, Australia, May 1990, pp.385-392.

Gemmell, J.B. and Large, R.R., 1990b, Stringer system and alteration zones underlying the Hellyer volcanic-hosted massive sulphide deposit, Tasmania, Australia, *Econ. Geol.*, vol.87, pp.620-649.

Gemmell, J.B., Large, R.R. and Barreiro, B., 1990, δ34S and Pb isotope study of the stringer zone beneath the Hellyer sulphide deposit, Tasmania [abs.], in *7th International Conference on Geochronology and Isotope Geology*, Canberra, Australia, September 1990.

Gemmell, J.B., Large, R.R., McArthur, G.J., Drown, C.G. and Downs, R.C., 1990, Formation of the alteration pipe and stringer zone beneath the Hellyer massive sulphide deposit, Tasmania [abs.], in *Gondwana Terranes and Resources*, 10th Australian Geological Convention, Hobart, Australia, February 1990, Geol. Soc. Aust., Abs. no.25, pp.8-9.

Gemmell, J.B. and Large, R.R., 1992, Stringer system and alteration zones underlying the Hellyer volcanic-hosted massive sulfide deposit, Tasmania, Australia, *Econ. Geol.*, vol.87, pp.620-649.

Hey, M.H., 1954, A new review of the chlorites, *Min. Mag.*, vol.30, p277.

Hudspeth, J.W., 1986, A gravity survey of the Hellyer deposit, in *The Mount Read Volcanics and associated ore deposits* (Ed. Large, R.R.), pp.45-48 (Geol. Soc. Aust., Tas. Div.: Hobart).

Huston, D.L. and Large, R.R., 1987, Genetic and exploration significance of the zinc ratio (100Zn/(Zn+Pb)) in massive sulfide systems, *Econ. Geol.*, vol.82, pp.1521-1539.

Huston, D.L. and Large, R.R., 1989, A chemical model for the concentration of gold in volcanogenic massive sulphide deposits, *Ore Geology Rev.*, Vol.4, No.3, pp.171-200.

Jack, D.J., 1989, Hellyer host rock alteration, unpub. M.Sc. thesis, Univ. Tasmania, 181p.

Jack, D.J., 1990, Geochemistry and alteration of the hangingwall basalts to the Hellyer volcanogenic massive sulphide deposit, Tasmania [abs.], in *Gondwana Terranes and Resources*, 10th Australian Geological Convention, Hobart, Australia, February 1990, Geol. Soc. Aust., Abs. no.25, pp.7.

Jago, J.B., 1979, Tasmanian Cambrian biostratigraphy - a preliminary report, *Geol. Soc. Aust. Jour.*, vol.26, pp.223-230.

Khin Zaw, Gemmell, J.B., Large, R.R., Mernagh, T.P. and Ryan, C.G., 1996, Evolution and source of ore fluids in the stringer system, Hellyer VHMS deposit, Tasmania, Australia: evidence of hydrothermal ore genesis, *Ore Geol. Reviews*, vol.10, pp.251-278.

Komyshan, P., 1986, Geology of the Hellyer-Mt.Charter area, in *The Mount Read Volcanics and associated ore deposits* (Ed. Large, R.R.), pp.11-19 (Geol. Soc. Aust., Tas. Div.: Hobart).

Large, R.R., 1977, Chemical evolution and zonation of massive sulfide deposits in volcanic terrains, *Econ. Geol.*, vol.72, pp.549-572.

Large, R.R., 1992, Australian volcanic-hosted massive sulfide deposits: features, styles, and genetic models, *Econ. Geol.*, vol.87, pp.471-510.

Lees, T., Khin Zaw, Large, R.R. and Huston, D.L., 1990, Rosebery and Hercules copper-lead-zinc deposits, in *Geology of the Mineral Deposits of Australia and Papua New Guinea,* (Ed. Hughes, F.E.), Australas. Inst. Min. Metall., Monograph no.14, pp.1241-1247.

Lydon, J.W., 1988, Ore deposit models #14. Volcanogenic massive sulphide deposits Part 2: Genetic models, *Geosci. Canada*, vol.15, No.1, pp.43-65.

McArthur, G.J., 1986, The Hellyer massive sulphide deposit, in *Cambrian Mt. Read Volcanics and associated ore deposits* (Ed. Large, R.R.), pp.144-148 (Geol. Soc. Aust., Tas. Div.: Hobart).

McArthur, G.J., 1988, Using geology to control geostatistics in the Hellyer deposit, *Math. Geol.*, vol.20, no.4, pp.343-366.

McArthur, G.J., 1990, Metal and textural zonation in the Hellyer massive sulphide deposit [abs.], in *Gondwana Terranes and Resources,* 10th Australian Geological Convention, Hobart, Australia, February 1990, Geol. Soc. Aust., Abs. no.25, pp.108-109.

McArthur, G.J. and Dronseika, E.V., 1990, The Que River and Hellyer volcanogenic Ag-Pb-Zn sulphide deposits, in *Geology of the Mineral Deposits of Australia and Papua New Guinea,* (Ed. Hughes, F.E.), Australas. Inst. Min. Metall., Monograph no.14, pp.1229-1239.

McArthur, G.J. and Kuipers, A.J., 1990, Computer methods for mine geology at Hellyer, *Mine Geologists' Conference,* Mt.Isa, Australia, October 1990, Australas. Inst. Min. Metall., pp.49-55.

McPhie, J. and Allen, R.L., 1992, Facies architecture of mineralized submarine volcanic sequences: Cambrian Mount Read Volcanics, Western Tasmania, *Econ. Geol.*, vol.87, pp.587-596.

Offler, R. and Whitford, D.J., 1992, Wall-rock alteration and metamorphism of a volcanic-hosted massive sulfide deposit at Que River, Tasmania: petrology and mineralogy, *Econ. Geol.*, vol.87, pp.686-705.

Ohmoto, H., 1983, Geologic setting of the Kuroko deposits, Japan: part I - geologic history of the Green Tuff region, *Econ. Geol.*, Mono.5, pp.9-24.

Ohmoto, H. and Skinner, B.J., 1983, The Kuroko and related volcanogenic massive sulfide deposits: introduction and summary of new findings, *Econ. Geol.*, Mono.5, pp.1-8.

Pisutha-Arnond, V. and Ohmoto, H., 1983, Thermal history, and chemical and isotopic compositions of the ore-forming fluids responsible for the Kuroko massive sulfide deposits in the Hokuroku District of Japan, *Econ. Geol.*, Mono.5, pp523-558.

Ramdohr, P., 1980, *The ore minerals and their intergrowths*, 2nd edition, Pergamon, 1205p.

Ramsden, A.R., Kinealy, K.M., Creelman, R.A. and French, D.H., 1990, Precious- and base-metal mineralogy of the Hellyer volcanogenic Ag-Pb-Zn sulphide deposit, northwest Tasmania - a study by electron microprobe, in *Sulphide Deposits - Their Origin and Processing*, (Ed. Gray, P.M.J., Bowyer, G.J., Castle, J.F., Vaughan, D.J. and Warner, N.A.), The Inst. Min. Metall., pp.49-71.

Read, J.J., 1989, Seismic reflection investigations of the Hellyer orebody and Que-Hellyer Volcanics, northwest Tasmania, *Expl. Geophys.*, vol.20, nos.1-2, pp.159-162.

Richmond, G.D. and Lai, K.F., 1988, Metallurgical development of the Hellyer ore, *Third Mill Operators' Conference*, Cobar, Australia, May 1988, Australas. Inst. Min. Metall., pp.9-14.

Sato, T., 1973, A chloride complex model for Kuroko mineralisation, *Geochem. Journ. (Japan)*, vol.8, pp27-35.

Schneiderhöhn, H., 1952, *Erzmikroskopisches Praktikum*, Stuttgart, 274p.

Scott, D., 1988, Stratigraphic and volcanogenic analysis of the Hellyer Upper Rhyolite Sequence, Western Tasmania, B.App.Sc thesis, University of Technology Sydney , 92p.

Sharpe, R.A., 1991, The distribution, mineralogy and paragenesis of the Hellyer baritic and siliceous caps, Unpub. B.Sc. (Hons.) thesis, Univ. Tasmania, Australia, 114p.

Silic, J. and Eadie, E.T., 1989, DHEM: The Que-Hellyer Volcanics experience, *Expl. Geophys.*, vol.20, nos.1-2, pp.65-69.

Silic, J., Eadie, E.T. and Jack, D.J., 1985, Application of time-domain electromagnetic methods in the discovery of the Hellyer deposit, Tasmania, Australia, *SEG 55th Annual Int. Mtg. & Exposition, 1985*, Expanded abstracts, pp.241-243.

Sinclair, B.J., 1994, Geology and geochemistry of the Que River Shale, Western Tasmania, unpub. B.Sc.(Hons.) thesis, Univ. Tasmania, 114p.

Singer, D.A., 1995, World class base and precious metal deposits - a quantitative analysis, *Econ. Geol.*, vol.90, pp.88-104.

Sise, J.R. and Jack, D.J., 1984, Exploration case history of the Hellyer deposit [abs.], in *Mineral Exploration and Tectonic Processes in Tasmania* (Ed. Baillie, P.W. and Collins, P.L.F., Geol. Soc. Aust. Tas. Div., Hobart, November 1984).

Skey, E.H., 1984, Dualism in the discovery of the Que River and Hellyer polymetallic sulphide deposits in western Tasmania [abs.], Geol. Soc. Aust., 12, pp.489-491.

Solomon, M. and Walshe, J.L., 1979, The formation of massive sulfide deposits on the sea floor, *Econ. Geol.*, vol.74, pp.797-813.

Spear, F.S., 1993, *Metamorphic phase equilibria and pressure-temperature-time paths*, Mineral. Soc. Amer., Washington D.C., 799p.

Staff of Aberfoyle Resources, 1989, Exploration case history of the discovery of the Hellyer polymetallic massive sulphide deposit, in *Geology and Mineral Resources of Tasmania* (Ed. Burrett, C.F. and Martin, E.L.), Geol. Soc. Aust., pp.430-434.

Staff of Aberfoyle Resources, 1990, Geology and discovery of the Que River and Hellyer polymetallic sulphide ores, Tasmania, in *Geological Aspects of the Discovery of Some Important Mineral Deposits in Australia*, (Ed. Glasson, K.R. and Rattigan, J.H.), Australas. Inst. Min. Metall., Monograph no.17, pp.187-196.

Sweeney, R.E. and Kaplan, J.R., 1973, Pyrite framboid formation: laboratory synthesis and marine sediments, *Econ. Geol.*, vol.68, pp.618-634.

Tanimura, S., Date, J., Takahashi, T. and Ohmoto, H., 1983, Geologic setting of the Kuroko deposits, Japan: part II - stratigraphy and structure of the Hokuroku district, *Econ. Geol.*, Mono.5, pp.24-38.

Warren, W., 1989, Sulphides in the hanging wall basalts of the Hellyer massive sulphide deposit, Unpub. B.App.Sc. thesis, Univ. Technol. Sydney, Aust., 100p.

Waters, J., 1990, Styles of sedimentation and volcanism within the Que-Hellyer Volcanics [Abs.], in *Gondwana Terranes and Resources*, 10th Australian Geological Convention, Hobart, Australia, February 1990, Geol. Soc. Aust., Abs. no.25, pp.32-33.

Waters, J., 1995, Volcanology and sedimentology of the host succession to VHMS style mineralisation within the Cambrian Que-Hellyer Volcanics, northwestern Tasmania, Unpub. Ph.D. thesis, Monash Univ., Australia, 303p.

Waters, J. and Wallace, D.B., 1992, Volcanology and sedimentology of the host succession

to the Hellyer and Que River volcanic-hosted massive sulfide deposits, northwestern Tasmania, *Econ. Geol.,* vol.87, pp.650-666.

Webster, S.S. and Skey, E.H., 1979, Geophysical and geochemical case history of the Que River Deposit, Tasmania, Australia, in *Geophysics and Geochemistry in the Search for Metallic Ores,*ed. P.J.Hood, Geological Survey of Canada: Ottawa, pp697-720.

Weston, A.J., Molinia, A.B. and Viney, K.G., 1988, Hellyer's exploration development, in *Underground Operators' Conference,* Mt.Isa, June 1988, The Australas. Inst. Min. Metall. NW Qld. Branch, pp.67-73.

Whitford, D.J. and Craven, S.J., 1986, Strontium isotopic studies at Que River and Hellyer, in *The Mount Read Volcanics and associated ore deposits* (Ed. Large, R.R.), pp.87-88 (Geol. Soc. Aust., Tas. Div.: Hobart).

Whitford, D.J., Sun, S.S. and Togashi, Y., 1982, Petrological and geochemical studies at Que River: Part 3, *CSIRO Inst. Earth Resources,* Restr. Inv. Rept. 13324R, 29p.

Wiggins, L.B. and Craig, J.R., 1980, Reconnaissance of the Cu-Fe-Zn-S system: Sphalerite phase relationships, *Econ. Geol.,* vol.75, pp742-752.